Study of the mass composition of cosmic rays with the Underground Muon Detector of AMIGA

Zur Erlangung des akademischen Grades eines

Doktors der Naturwissenschaften (Dr. rer. nat.)

von der KIT-Fakultät für Physik des
Karlsruher Instituts für Technologie (KIT)

und der

Universidad Nacional de San Martín (UNSAM)

angenommene

Dissertation

von

Lic. Joaquín de Jesús

aus Buenos Aires

Study of the mass composition of cosmic rays with the Underground Muon Detector of AMIGA

For the attainment of the academic degree of

Doctorate in Science

from the

Karlsruher Institut für Technologie (KIT)

and the

Universidad Nacional de San Martín (UNSAM)

presented

Dissertation

of

Lic. Joaquín de Jesús

of Buenos Aires

Day of the oral examination: 25.04.2025

Referee: Prof. Dr. Juan Manuel Figueira

Co-referee: Prof. Dr. Ralph Engel

Supervisor: Dr. Federico Sanchez, Dr. Darko Veberič

Study of the mass composition of cosmic rays with the Underground Muon Detector of AMIGA

Tesis presentada para optar por el título de

Doctor en Astrofísica

del Instituto de Tecnología "Prof. Jorge A. Sábato" de la
Universidad Nacional de San Martín (UNSAM)

y del

Karlsruher Institut für Technologie (KIT)

por

Lic. Joaquín de Jesús

de Buenos Aires

Fecha de la defensa oral: 25.04.2025

Director: Prof. Dr. Juan Manuel Figueira

Co-director: Prof. Dr. Ralph Engel

Colaborador: Dr. Federico Sanchez, Dr. Darko Veberič

Abstract

Despite several decades of study, the origin of ultra-high-energy cosmic rays (UHECRs)—ionized nuclei from outer space bombarding the Earth's atmosphere at energies above 10^{17} eV—remains a key open question in astroparticle physics. Their enormous energies, exceeding by orders of magnitude those achievable in the most powerful human-made particle accelerators, are indicative of the most violent and extreme processes in our universe. Since their flux is extremely low, UHECRs can only be detected indirectly by measuring the extensive air showers (EAS) of secondary particles they produce when interacting with an air nucleus. Consequently, the energy, arrival direction and mass composition must be inferred from the signals that EAS produce in large ground-based detectors such as the Pierre Auger Observatory. In particular, the mass composition is of utmost importance, as it would help to constrain astrophysical scenarios explaining the origin and sources of these extremely energetic particles. One of the most mass-sensitive EAS observables is the number of muons produced in the shower, which can be directly sampled by underground segmented scintillator detectors, such as the Underground Muon Detector (UMD) of the Pierre Auger Observatory.

In this work, we present a measurement of the muon content of air showers within the energy range $10^{17.5}$ eV to $10^{18.9}$ eV using the Underground Muon Detector (UMD) of the Pierre Auger Observatory. We revisited and improved the existing procedure for reconstructing the lateral distribution function (LDF) of muons at the individual event level. The likelihood model used to fit the LDF was extended to account for detector effects—such as detector noise, inefficiency, and corner-clipping muons—by introducing probabilistic models with physical motivation. In addition, we developed a novel data-driven method to quantify and correct for corner-clipping muons—inclined muons that can generate signals in adjacent segments, leading to overcounting. Previously, this effect was addressed solely through simulations; in this work, we demonstrate how it can be studied and corrected using data. The framework developed here, both for the likelihood model and the corner-clipping correction, is generally applicable to any type of segmented detector.

The muon content measured in this work was compared to air shower simulations to infer the mass composition. The energy-dependent trend of the inferred mass is consistent with that observed using another mass-sensitive observable—the depth of shower maximum, X_{max}—indicating a transition from heavy to light elements from $10^{17.5}$ eV up to $\sim 10^{18.4}$ eV, where a break toward heavier elements is observed. However, the absolute mass is systematically heavier than that predicted from X_{max}. This discrepancy between the inferred mass from these two observables has been observed in other experiments and is interpreted as a muon deficit in simulations. This suggests that current hadronic models used to simulate air showers—tuned to LHC data and extrapolated to higher energies—do not consistently reproduce all aspects of EAS. We find that the discrepancy between the inferred mass of the two observables remains relatively constant with energy up to $10^{18.4}$

eV but gradually increases beyond that point. Although the number of events above $10^{18.4}$ eV is still low, our results suggest that the muon deficit may become more pronounced at these energies, providing valuable insights for model builders seeking to improve hadronic interaction models.

Zusammenfassung

Trotz mehrerer Jahrzehnte der Forschung bleibt der Ursprung der kosmischen Strahlen mit ultrahohen Energien (UHECR) – ionisierte Atomkerne aus dem Weltraum, die mit Energien über 10^{17} eV auf die Erdatmosphäre treffen – eine zentrale, offene Frage in der Astroteilchenphysik. Ihre Energien liegen um mehrere Größenordnungen über den Werten, die in den leistungsstärksten, von Menschen geschaffenen Teilchenbeschleunigern erreichbar sind. Diese deuten auf die gewaltigsten und extremsten Prozesse in unserem Universum hin. Da ihr Fluss extrem gering ist, können UHECR nur indirekt nachgewiesen werden, indem man die ausgedehnten Luftschauer (EAS) sekundärer Teilchen misst, die sie bei der Wechselwirkung mit einem weiteren Teilchen in der Atmosphäre erzeugen. Folglich können die Energie, die Ankunftsrichtung und die Massenkomposition aus den Signalen der EAS abgeleitet werden, die in großen bodengebundenen Experimenten wie dem Pierre-Auger-Observatorium, gemessen werden. Insbesondere die Massenkomposition ist von größter Bedeutung, da sie helfen könnte, astrophysikalische Szenarien zur Erklärung des Ursprungs und der Quellen dieser extrem energiereichen Teilchen einzugrenzen.

Eine der massensensitivsten EAS-Observablen ist die Anzahl der im Schauer erzeugten Myonen, die direkt mit unterirdischen, segmentierten Szintillationsdetektoren gemessen werden kann, wie dem Untergrund Myonen Detektor (UMD) des Pierre-Auger-Observatoriums. In dieser Arbeit präsentieren wir eine Messung des Myonengehalts von Luftschauern im Energiebereich von $10^{17.5}$ eV bis $10^{18.9}$ eV unter Verwendung des UMD des Pierre-Auger-Observatoriums. Wir haben das bestehende Verfahren zur Rekonstruktion der lateralen Verteilungsfunktion (LDF) der Myonen pro Einzelereignissen überarbeitet und verbessert. Das für die Anpassung der LDF verwendete Wahrscheinlichkeitsmodell wurde erweitert, um Detektoreffekte – wie Detektorrauschen, Ineffizienz und randstreifende Myonen – durch die Einführung physikalisch motivierter probabilistischer Modelle zu berücksichtigen. Darüber hinaus haben wir eine neuartige, datenbasierte Methode zur Quantifizierung und Korrektur von randstreifende Myonen – geneigte Myonen, die Signale in benachbarten Segmenten erzeugen und so zu einer Überzählung führen können, entwickelt. Bisher wurde dieser Effekt ausschließlich durch Simulationen behandelt; in dieser Arbeit zeigen wir, wie er mit experimentellen Daten untersucht und korrigiert werden kann. Das hier entwickelte methodische Konzept ist, sowohl für das Wahrscheinlichkeitsmodell als auch für die Randstreifen-Korrektur, allgemein auf jede Art von segmentierten Detektoren anwendbar.

Der in dieser Arbeit gemessene Myonengehalt wurde mit Luftschauer-Simulationen verglichen, um die Massenkomposition zu bestimmen. Der energieabhängige Verlauf der abgeleiteten Masse ist konsistent mit dem einer anderen massensensitiven Observablen – der Tiefe des Schauermaximums, $X_{\max}$ – und zeigt einen Übergang von schweren zu leichten Elementen im Bereich von $10^{17.5}$ eV bis etwa $10^{18.4}$ eV, wo eine Abweichung hin zu schwereren Elementen auftritt. Die absolute Masse ist jedoch systematisch schwerer als diejenige, die

aus X_{max} vorhergesagt wird. Die Diskrepanz zwischen der aus beiden Observablen abgeleiteten Masse wurde auch in anderen Experimenten beobachtet und wird als Myonendefizit in Simulationen interpretiert. Dies deutet darauf hin, dass die derzeitigen hadronischen Modelle zur Simulation von Luftschauern – die mit LHC-Daten kalibriert und auf höhere Energien extrapoliert wurden – nicht alle Aspekte der EAS konsistent wiedergeben. Wir stellen fest, dass die Diskrepanz zwischen den aus beiden Observablen abgeleiteten Massen bis $10^{18.4}$ eV relativ konstant bleibt, darüber hinaus jedoch allmählich zunimmt. Obwohl die Anzahl der Ereignisse über $10^{18.4}$ eV noch gering ist, legen unsere Ergebnisse nahe, dass sich das Myonendefizit bei diesen Energien weiter verstärken könnte, was wertvolle Einblicke für Entwickler von Modellen liefert, die hadronische Wechselwirkungsmodelle verbessern möchten.

Resumen

A pesar de varias décadas de estudio, el origen de los rayos cósmicos de ultra-alta energía —núcleos ionizados provenientes del espacio exterior que bombardean la atmósfera terrestre con energías superiores a 10^{17} eV—sigue siendo una de las principales cuestiones abiertas en la física de astropartículas. Sus enormes energías, que superan en órdenes de magnitud a las alcanzadas en los aceleradores de partículas más potentes construidos por el ser humano, son indicativas de los procesos más violentos y extremos de nuestro universo. Dado que su flujo es extremadamente bajo, los rayos cósmicos de ultra-alta energía solo pueden detectarse de manera indirecta mediante la medición de las extensas cascadas atmosféricas de partículas secundarias que producen al interactuar con un núcleo del aire. Por lo tanto, su energía, dirección de llegada y composición en masa (esto es, qué especie nuclear es la que generó la lluvia de partículas) deben inferirse a partir de las señales que los cascadas atmosféricas generan en grandes detectores terrestres, como el Observatorio Pierre Auger. En particular, la composición en masa es de gran importancia, ya que permitiría restringir los escenarios astrofísicos que explican el origen y las fuentes de estas partículas extremadamente energéticas.

Uno de los observables más sensibles a la composición en masa en las cascadas atmosféricas es el número de muones producidos en la cascada, los cuales pueden ser medidos directamente mediante detectores subterráneos segmentados de centelleo, como el Detector de Muones Subterráneo (UMD, por sus siglas en inglés) del Observatorio Pierre Auger. En este trabajo, presentamos una medición del contenido de muones en las cascadas atmosféricas dentro del rango de energía de $10^{17.5}$ eV a $10^{18.9}$ eV utilizando el UMD del Observatorio Pierre Auger. Revisamos y mejoramos el procedimiento existente para reconstruir la función de distribución lateral de los muones a nivel de evento individual. El modelo de verosimilitud utilizado para ajustar la distribución lateral fue ampliado para incluir los efectos del detector—como el ruido, la ineficiencia y los muones *corner-clipping*—mediante la introducción de modelos probabilísticos con una motivación física. Además, desarrollamos un novedoso método basado en datos para cuantificar y corregir la presencia de muones *corner-clipping*—muones inclinados que pueden generar señales en segmentos adyacentes, dando lugar a un sobreconteo. Hasta ahora, este efecto se abordaba únicamente mediante simulaciones; en este trabajo, demostramos cómo puede estudiarse y corregirse utilizando datos experimentales. El marco metodológico desarrollado aquí, tanto para el modelo de verosimilitud como para la corrección del efecto *corner-clipping*, es aplicable en general a cualquier tipo de detector segmentado.

El contenido de muones medido en este trabajo se comparó con simulaciones de cascadas atmosféricas para inferir la composición en masa. La tendencia de la composición en función de la energía es consistente con la observada utilizando otro observable sensible a la masa del primario—la profundidad atmosférica del máximo de la cascada, $X_{\max}$—indicando una

transición de elementos pesados a ligeros desde $10^{17.5}$ eV hasta aproximadamente $10^{18.4}$ eV, donde se observa un cambio hacia elementos más pesados. Sin embargo, la masa absoluta inferida es sistemáticamente más pesada que la predicha a partir de X_{max}. Esta discrepancia entre la composición inferida a partir de ambos observables ha sido observada en otros experimentos y se interpreta como un déficit de muones en las simulaciones. Esto sugiere que los modelos hadrónicos actuales utilizados para simular los cascadas atmosféricas—calibrados con datos del LHC y extrapolados a energías más altas—no reproducen de manera consistente todos los aspectos de las cascadas. Encontramos que la discrepancia entre ambos observables se mantiene relativamente constante con la energía hasta $10^{18.4}$ eV, pero aumenta gradualmente más allá de ese punto. Aunque el número de eventos por encima de $10^{18.4}$ eV sigue siendo bajo, nuestros resultados sugieren que el déficit de muones podría volverse más pronunciado a estas energías, proporcionando información valiosa para el desarrollo y mejora de los modelos de interacciones hadrónicas.

Contents

Chapter 1

Introduction

Particles of extraterrestrial origin are constantly bombarding our atmosphere. This cosmic beam is composed of several types of particles, both neutral and charged, spanning various orders of magnitude in energy. Some of them are ionized nuclei with tremendous amounts of energy, which can reach macroscopic energies of up to 10^{20} eV. These so-called ultra-high-energy cosmic rays (UHECRs) are of particular interest. On one hand, their very existence challenges our understanding of acceleration mechanisms for charged particles and suggests that they must be accelerated in the most violent and extreme processes in our universe. On the other hand, they can reach energies far beyond those achievable in the most powerful human-made particle accelerators, providing a unique opportunity for particle physicists to study particle interactions in an otherwise inaccessible energy region.

Despite being known for more than half a century, fundamental questions such as their origin, mass composition, and acceleration mechanisms are still not entirely understood. Their detection is challenging because UHECRs are very rare: they exhibit a steeply falling energy spectrum, with a flux of approximately 10 particles per km^2 per day at 10^{17} eV. At 10^{20} eV, their flux decreases to 1 particle per km^2 per century. In practice, such a low flux means that for energies above $\sim 10^{15}$ eV, cosmic rays can only be indirectly measured by observing the extensive air showers (EAS) they produce when interacting with air nuclei. These showers, which can cover an area of tens of km^2 at the highest energies, are detected by large ground-based arrays of detectors.

Determining the mass composition (i.e., their nuclear mass A) of these particles as a function of energy is of utmost importance to disentangle between astrophysical scenarios for the origin and acceleration of cosmic rays that can fit equally well the existing data. The two main mass-sensitive observables from EAS are the atmospheric depth where the shower reaches its maximum development, $X_{\max}$, and the number of muons N_μ (see Chapter 2). To interpret their measurements in terms of the nuclear mass, data has to be compared to expectations from air shower simulations of different nuclear species. These simulations, in turn, depend on hadronic models that extrapolate accelerator data to the highest energies, leading to large systematic uncertainties.

Since $X_{\max}$ is linked to the better-understood electromagnetic component of extensive air showers (EAS), its interpretation is less influenced by uncertainties in hadronic models, making it the most reliable and widely used observable for composition studies. However, its measurement is constrained by lower statistics, as it necessitates dedicated fluorescence telescopes, which can only operate during moonless nights with favorable weather conditions.

In contrast, the muonic component of air showers can be measured with higher statistics using shielded muon detectors, such as the Underground Muon Detector (UMD) at the Pierre

1

Auger Observatory, or by analyzing highly inclined air showers, where the majority of the electromagnetic component is absorbed in the atmosphere, utilizing unshielded detectors [1, 2]. However, interpreting these measurements is more challenging due to the greater uncertainty associated with muons, as they originate from the hadronic component of the shower, which is more susceptible to model uncertainties.

Several experiments have reported that the composition inferred from muon measurements consistently suggests a heavier composition, which does not align with the composition predicted from X_{max} observations, indicating that these two observables are not consistently reproduced by current hadronic models. This discrepancy has led to the hypothesis of a muon deficit in simulations, giving rise to the so-called *muon puzzle*, a topic that has generated substantial research in recent years (see Ref. [3] for a comprehensive review). Resolving or further constraining this puzzle would not only make it possible to use muons as a mass composition estimator with larger datasets and improved statistical significance, providing insight into astrophysical scenarios for ultra-high-energy cosmic rays (UHECRs), but it would also enhance our understanding of hadronic physics at energies far beyond those achievable in man-made accelerators, making a significant contribution to the field of particle physics.

Key aspects of the muon puzzle remain unresolved. The energy threshold at which the muon deficit begins, its energy dependence, and the extent of the deficit are still unclear. Additionally, although many experiments report a muon deficit in their data, this is not the case to all of them [3, 4]. In this context of uncertainty, further measurements are essential to clarify the situation. In this work, we present a measurement of the muon content of air showers in the energy range $10^{17.5}$ eV $< E < 10^{18.9}$ eV with the UMD of the Pierre Auger Observatory.

The muon content in this work is obtained on an event-by-event basis by fitting a muon lateral distribution function (LDF) through a maximum likelihood maximization (log-likelihood minimization). In Chapter 4, we begin by optimizing the existing detector likelihood, extending it to account for effects that can bias the muon estimator of a segmented detector like the UMD. These effects include detector noise, inefficiency, and corner-clipping muons. The inclusion of these effects, which are common to any segmented detector, is achieved using suitable probabilistic models that depend on parameters that are physically motivated, easy to interpret, and measurable in the laboratory with standard instrumentation.

For the UMD case, corner-clipping muons are the dominant effect. These are inclined muons that can generate signals in adjacent segments, leading to overcounting. In Chapter 5, we present a data-driven method to quantify and correct for the corner-clipping effect. This approach allows the effect, which until now could only be characterized through simulations, to be quantified and accounted for using data for the first time.

In Chapter 6, we assess how the improvements developed in the previous chapters impact the LDF reconstruction using both data and full detector simulations, particularly how these improvements compare to the existing reconstruction procedure. Additionally, we introduce a method to fit the core position, which improves the quality of the fit for showers that land very close to a detector.

The evolution of the muon content with energy is presented and discussed in Chapter 7. We interpret the measurements in terms of mass composition and discuss their energy-dependent trends. Moreover, we assess the compatibility of these results with the inferred composition from X_{max} measurements and provide an estimate on the muon deficit. We compare our results—both the absolute number of muons, using the so-called *z*-scale, and the shape of the LDF—to other experiments and previous results reported by the UMD.

Chapter 2

Cosmic rays

Despite being known to humanity for more than 70 years, several key aspects of ultrahigh-energy cosmic rays (UHECRs)—ionized nuclei bombarding the Earth's atmosphere with energies above $E \sim 10^{17}$ eV—remain a mystery. The astrophysical sources, as well as the acceleration and propagation mechanisms, and mass composition of these extremely energetic particles —whose energies exceed by orders of magnitude those achieved in human-made accelerators— are still not entirely understood. Given their extremely low flux, UHECRs can only be detected indirectly by observing Extensive Air Showers (EAS)—cascades of billions of secondary particles generated when a UHECR interacts with the atmosphere. As a result, the energy, arrival direction, and primary mass of UHECRs must be inferred by analyzing the signals produced by EAS in large ground-based detectors.

In this chapter, we summarize the current knowledge on UHECRs. In Section 2.1, the UHECR energy spectrum observed at Earth is presented, and its main features are discussed. The currently accepted acceleration and propagation mechanisms, as well as potential sources for UHECRs, are presented in Section 2.2. The main features of EAS are presented in Section 2.3, whereas the muon puzzle—the discrepancy between the observed and expected number of muons in EAS—is introduced in Section 2.4.

2.1   Energy spectrum at Earth

The energy spectrum of cosmic rays (CRs) at Earth spans from $\sim 10^9$ eV up to 10^{20} eV, covering approximately eleven decades in energy. The differential flux over this large energy range decreases steeply and can be well described by broken power laws, $\frac{d\Phi}{dE} \propto E^{-\gamma}$, with the spectral index γ varying between 2.6 and 3.3 in different energy ranges. The energies at which the spectral index changes are significant, as they give rise to features in the spectrum associated with variations in the elemental composition of the cosmic-ray beam. In turn, these changes in mass composition are directly related to modifications in the sources, acceleration, and/or propagation mechanisms of CRs. Thus, understanding the features in the all-particle spectrum requires a comprehensive picture of the underlying astrophysical scenario in which cosmic rays are accelerated and propagated.

The differential flux of the all-particle CR spectrum, as measured by several experiments, is shown in Fig. 2.1. The steeply falling flux is multiplied by $E^{2.6}$ to flatten the spectrum and reveal more clearly discontinuities in the spectral index. Three main features are visible which are named in analogy to the anatomy of a human leg: (i) the softening at $E_{\mathrm{knee}} \sim 4 \times 10^{15}$ eV, known as the *knee*; (ii) another softening, dubbed the *second knee*, at $E_{\mathrm{2nd\ knee}} \sim 10^{17}$
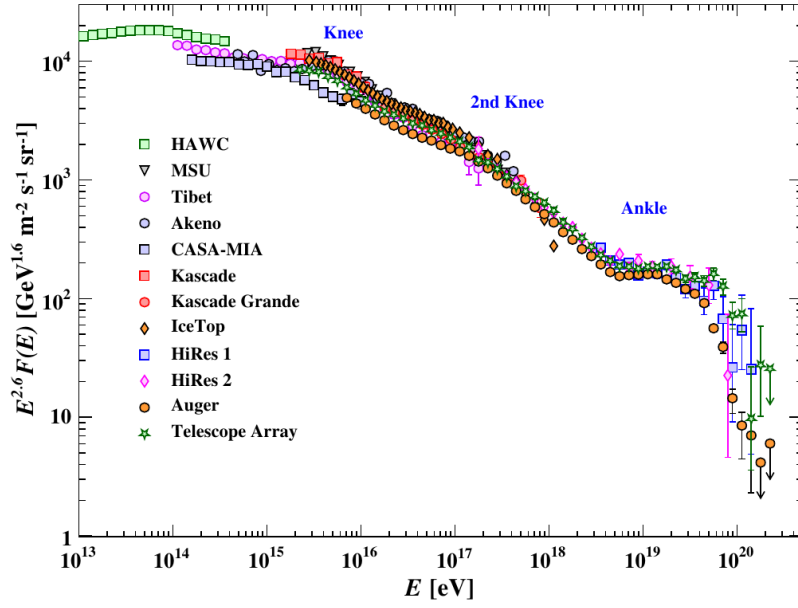
Figure 2.1: Scaled all-particle flux as measured by several experiments. Figure extracted from Ref. [6]

eV; and (iii) a hardening, referred to as the *ankle*, at $E_{ankle} \sim 5 \times 10^{18}$ eV. Lastly, a strong flux suppression is visible for energies greater than 4×10^{19} eV.

Although significant advances in the understanding of CRs have been made in the last few decades, the origin of the features of the all-particle spectrum is still not entirely understood. The current consensus is that CRs up to the knee are of galactic origin, accelerated through a first-order Fermi mechanism (Section 2.2.1) in supernova remnants (SNRs) (Section 2.2.2), whereas those above the ankle are of extragalactic origin. Although this idea has long been proposed—since the Larmor radius of a particle with energies above the ankle is larger than the size of the galaxy—it was only recently confirmed by the observation of a large-scale dipolar anisotropy, pointing outside the galactic plane, in the arrival direction of cosmic rays with $E > 8 \times 10^{18}$ eV by the Pierre Auger Observatory [5]. The transition between galactic and extragalactic CRs is thus expected to occur within the energies of $\sim 10^{15}$ eV to $\sim 10^{18.5}$ eV, although the details of how this transition occurs is still a matter of debate.

The flux of cosmic rays below $\sim 10^{14}$ eV is high enough to be detected directly by balloon- or satellite-based detectors in the upper atmosphere (or even outside it). These devices not only allow for the measurement of cosmic ray energy but also for the determination of its nuclear type, enabling the measurement of a flux discriminated by element. Some examples of this kind of experiments are PAMELA [7], CREAM [8] and AMS [9].

Due to their low flux, cosmic rays with energies greater than $\sim 10^{14}$ eV can only be detected indirectly by observing extensive air showers (EAS)—cascades of billions of secondary particles generated when a CR interacts with the atmosphere (Section 2.3). As a result, the energy, arrival direction, and primary mass (or, more precisely, the natural logarithm of the nuclear mass) of CRs must be inferred by analyzing the signals produced by EAS in large ground-based detectors. This can be achieved by measuring the radiation produced as the shower particles interact with the atmosphere, notably Cherenkov or fluorescence emission, using dedicated telescopes; or by detecting the footprint of air showers on the ground with surface detectors, which are comprised of arrays of water-Cherenkov or scintillator detectors. Historically, air shower experiments focused on only one of these detection techniques, employing either telescopes or surface detectors. State-of-the-art experiments, such as the

Telescope Array [10] in the Northern Hemisphere and the Pierre Auger Observatory [11] in the Southern Hemisphere, use hybrid designs that combine large surface detectors with fluorescence telescopes, leveraging the benefits of both techniques. Details on the the Pierre Auger Observatory and its reconstruction techniques are given in Chapter 3.

2.2 Acceleration, propagation and potential sources of UHECRs

2.2.1 Diffusive shock acceleration

The most commonly accepted acceleration mechanism for cosmic rays is through diffusive shock acceleration, also known as first-order Fermi acceleration. In this mechanism, a particle interacts multiple times with a shock front, like the ones generated in a supernova explosion, gradually gaining energy in each interaction by a constant fractional amount, leading to a stochastic multiplication process. The interaction with the shock front occurs as the particle moves back and forth across the shock front, interacting with magnetic irregularities with the plasma. If the shock front moves with a velocity v_{shock}, the average energy gain ΔE by a particle after one interaction can be shown to be [12]

$$\frac{\Delta E}{E} = \frac{4}{3}\beta, \tag{2.1}$$

where E is the energy of the particle before the interaction and $\beta = v_{\text{shock}}/c$, with c the speed of light. The fact that the energy gain is of first order in β gives this process the name of first-order Fermi acceleration[1]. After n interactions, the energy of a particle with initial energy E_0 is

$$E_n = E_0(1 + \frac{4}{3}\beta)^n. \tag{2.2}$$

In turn, Eq. (2.2) can be rearranged to obtain the number of encounters needed to reach an energy E_n:

$$n = \frac{\ln(E_n/E_0)}{\ln(1 + 4\beta/3)}. \tag{2.3}$$

Not all particles remain in the acceleration process indefinetely. If p_{esc} is the escape probability of a particle in one interaction, it follows that the probability of remaining is $1 - p_{\text{esc}}$. Thus, the probability of remaining in the acceleration region after n interactions is $(1 - p_{\text{esc}})^n$. Therefore, we can obtain the number of particles with energies $E > E_n$ as

$$N(E > E_n) = \sum_{m=n}^{\infty}(1 - p_{\text{esc}})^m = \frac{(1 - p_{\text{esc}})^n}{p_{\text{esc}}}. \tag{2.4}$$

Substituing Eq. (2.3) into Eq. (2.4) and simplifying the expression, we obtain

$$N(E > E_n) \propto \frac{1}{p_{\text{esc}}}\left(\frac{E}{E_0}\right)^{-\gamma}, \tag{2.5}$$

where $\gamma = -\frac{\ln(1-p_{\text{esc}})}{\ln(1+4\beta/3)}$. In this way, a power-law spectrum is obtained, as observed for cosmic rays.

---

[1]Fermi initially conceived diffusive acceleration through magnetized plasma in interstellar clouds [13], which led to a fractional gain per encounter $\frac{\Delta E}{E} \propto \beta^2$. Since the energy gain scales with β^2, this process is known as second-order Fermi acceleration. Since $\beta << 1$, this mechanism is significantly less efficient compared to first-order mechanisms, and the required confinement time to reach cosmic-ray energies would be impractically long. Therefore, although it also leads to a power-law spectrum, first-order Fermi acceleration is currently the standard process invoked for cosmic-ray acceleration.
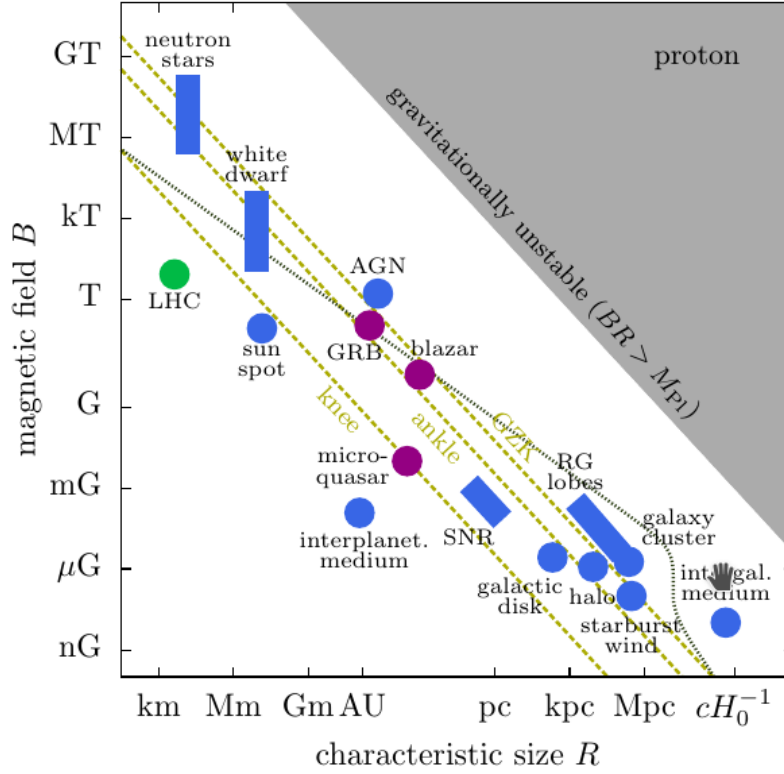
Figure 2.2: Hillas plot, in which potential sources are placed organized depending on their magentic field B and size R. The dashed lines indicate the lower limits for cosmic accelerators of protons at the knee ($\sim 10^{15}$ eV), ankle ($\sim 10^{18.5}$ eV) and the GZK suppresion ($\sim 10^{19.6}$ eV). Figure extracted from Ref. [15]

2.2.2 Potential sources

As discussed in the previous section, the widely accepted mechanism for cosmic-ray acceleration is the gradual acceleration through the diffusive shock mechanism. To identify which objects could serve as cosmic accelerators, and the maximum energy to which cosmic rays could be accelerated through this process, Hillas introduced a useful approach [14]. A necessary condition for a particle to be accelerated in an astrophysical object of size R and magnetic field B is that it remains confined within the object. If the Larmor radius of the particle exceeds R, the particle escapes. Thus, an estimate of the maximum energy a cosmic ray of charge Z can reach is obtained by equating its Larmor radius to the size of the object:

$$E_{\max} \propto ZBR. \tag{2.6}$$

In Fig. 2.2, an adapted version of the so-called Hillas plot is shown, where various astrophysical objects are organized in the $B - R$ plane to assess their viability as cosmic-ray sources. The dashed lines indicate the location in the plane of a source capable of accelerating protons to different energies at which characteristic features of the all-particle spectrum are observed. A source lying below a given line is ruled out as a candidate for producing protons at that energy. Heavier nuclei with charge Z can reach energies up to Z times higher than protons within the same sources. As observerd in Fig. 2.2, there are several candidates for ultra-high-energy (UHECRs) cosmic rays with energies $E \gtrsim 10^{18}$ eV. For multiple reasons, supernova-remnants (SNRs) are currently accepted as the most likely sources for galactic cosmic rays [16]. However, SNRs cannot explain the highest energies cosmic rays above the ankle, which are of extragalactic origin. Active galactic nuclei (AGNs) and gamma-ray

bursts (GRBs) are promising candidates for extragalactic sources of the the highest-energy cosmic rays.

2.2.3   Propagation

While propagating from their sources to Earth, cosmic rays can interact with cosmic magnetic fields, which affect their direction and arrival time but not their energy or composition. Additionally, interactions with the cosmic background can influence all these properties. Regarding deflections in magnetic fields, since the Larmor radius of a charged particle is inversely proportional to its charge and directly proportional to its momentum (which, in the relativistic regime, is approximately its energy, $p \approx E$), it follows that lighter, less charged particles (e.g., protons) experience less deviation than heavier, more highly charged nuclei (e.g., iron). Likewise, higher-energy particles undergo smaller deflections compared to low-energy particles. For this reason, detecting light particles at the highest energies is crucial, as they can trace back to their sources, paving the way for charged-particle astronomy. However, current composition-sensitive observables indicate an increasingly heavier composition at the highest energies. Therefore, achieving mass discrimination at the event level is of paramount importance. To address this, the Pierre Auger Observatory, the world's largest cosmic-ray observatory, has recently undergone an upgrade aimed, among other goals, at detecting this (presumably subdominant) light component at the highest energies (see Chapter 3).

The main energy losses at the highest energies come from interaction of cosmic rays with photons from the cosmic microwave backogrund (CMB). For protons, the main processes are photo-pion production and electron-positron pair production (also called Bethe-Heitler process). Photopion production occurs when the interaction with the CMB produces a Δ resonance, leading to pion production. One possible channel is

$$p + \gamma_{\mathrm{CMB}} \to \Delta^+ \to p + \pi^0, \tag{2.7}$$

leading to a neutral pion carrying approximately 10-20% of the initial energy of the proton, contributing significantly to the energy loss.

The π^0 decays promptly into two gamma rays ($\pi^0 \to \gamma + \gamma$). Thus, if protons were dominant at ultra-high energies, a diffuse flux of ultra-high-energy *cosmogenic* gamma rays ($\sim 10^{18}$ eV) would be expected on Earth as a product of proton propagation. The observation of such a gamma-ray flux on Earth would favor a proton-dominated composition at the highest energies. However, the predicted flux is small, and no direct observation of ultra-high-energy gamma rays has yet been achieved, allowing only upper limits on the integral flux to be obtained. Leading observatories, such as the Pierre Auger Observatory, are currently reaching the exposure necessary to rule out whether such a flux exists.

Another channel is

$$p + \gamma_{\mathrm{CMB}} \to \Delta^+ \to n + \pi^+, \tag{2.8}$$

which results in a charged pion. Since the neutron β-decays into a proton, the final state leads to a proton with an effective energy loss, similarly to Eq. (2.7). The pion decays into a muon which, in turn, decays into a positron. All these decays lead to neutrinos. Therefore, in addition to the ultra-high-energy gamma ray flux predicted from Eq. (2.7), a diffuse flux of cosmogenic high-energy neutrinos is also expected in a proton-dominated scenario.

In addition to photopion production, protons can lose energy through electron-positron pair production, given by the process

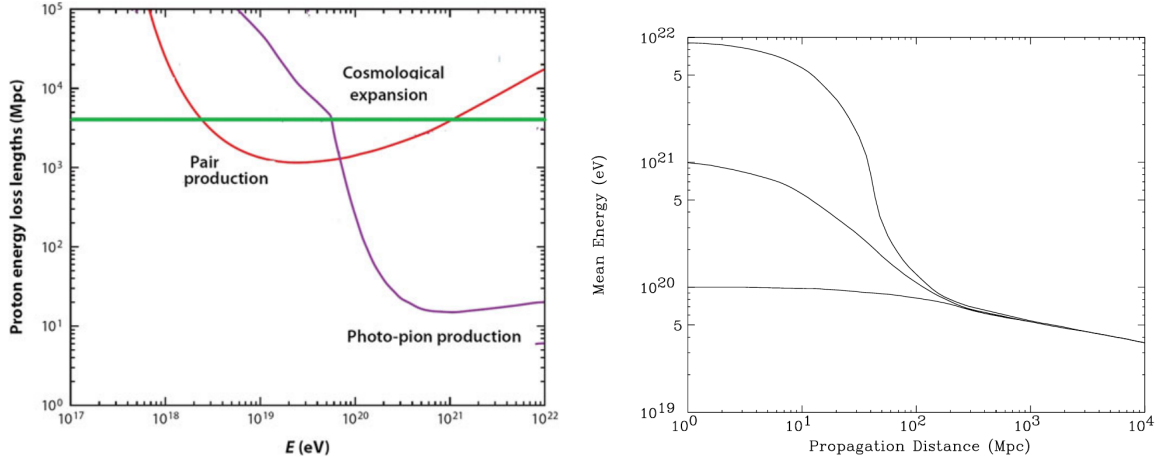$$p + \gamma_{\mathrm{CMB}} \to p + e^+ + e^-. \tag{2.9}$$

Figure 2.3: *Left*: Energy loss length for pair production and photo-pion production as a function of proton energy. The cosmological energy loss, produced by the adiabatic loss due to the expansion of the Universe is also shown as a green line. Taken from Ref. [17] *Right*: Energy of a proton as a function of its propagation distance. Beyond ~ 100 Mpc, all protons converge to energies below 10^{20} due to (mainly) photo-pion energy losses. From Ref. [20]

The energy loss length, defined as $x_{\text{loss}} = \frac{1}{E}\frac{dE}{dX}$, for photo-pion and pair production as a function of proton energy is depicted in the left panel of Fig. 2.3. The threshold energy for pair production is $E \sim 2 \times 10^{18}$ eV [17], where its loss length drops down to ~ 1000 Mpc. The threshold of the photo-pion production is $E_{\text{th}} \sim 10^{20}$ eV [17], and above this threshold, it becomes the dominant process, with a loss length of $\sim 10 - 100$ Mpc. As a result, the distance traveled without significant energy loss shortens considerably. If ultra-high-energy protons must travel cosmological distances, their flux above this energy should therefore be suppressed, giving rise to the so-called Greisen, Kuzmin, and Zatsepin (GZK) suppression [18, 19]. Furthermore, this also implies that if cosmic rays with energies $E > E_{\text{th}}$ are observed, their sources must lie within a distance $l \lesssim x_{\text{loss}}$, defining the so-called GZK horizon. Indeed, in the right panel of Fig. 2.3, the mean energy of a proton with various initial energies is shown as a function of its propagation distance. For proton sources beyond ~ 100 Mpc, the proton energy falls below 10^{20} eV due to energy losses from photo-pion production, regardless of its initial energy. Whether the observed suppression in the UHECR spectrum is caused by the GZK effect or due to the sources reaching their maximum acceleration is still a matter of debate.

For nuclei with $A > 1$, although photo-pion[2] and pair production are still possible, photo-disintegration, where a nucleus absorbs a photon and splits into smaller parts in its deexcitation, becomes the dominant process, given by

$$X_A + \gamma_{\text{CMB}} \rightarrow X_{A-k} + k, \tag{2.10}$$

Three main processes contribute to photodisintegration of nuclei upon interaction with CMB photons, namely, the Giant Dipolar Resonance (for photon energies of $\epsilon \sim 8 - 30$ MeV), the Quasi Deuteron process ($\epsilon \sim 20 - 150$ MeV) and the Baryonic Resonance ($\epsilon \sim 150$ MeV) [21].

The concept of GZK horizon (an effective distance below which sources with $E > E_{\text{th}}$ must lie), initially conceived for protons, can be extended to heavier nuclei considering. Remarkably, and by coincidence, the effective suppresion due to energy loss effects (assuming a power-law injection spectrum) is similar for proton and iron [12].

---

[2]Being a sub-dominant process for heavy nuclei, the expected flux of γ rays and neutrinos is consequently smaller than the one predicted in a proton-dominated scenario.

2.3 Extensive Air Showers

Due to their low flux, the detection of cosmic rays with energies above $\sim 10^{14}$ eV relies on observing the showers of particles they generate when interacting with the atmosphere, known as extensive air showers (EAS). Therefore, in order to infer the main properties of the primary cosmic rays, a profound understanding of the processes involved in the generation of EAS is necessary. In this section, we discuss the relevant aspects of air shower physics.

The particles within an EAS can be broadly categorized into three components: the *electromagnetic* component, consisting of photons, electrons, and positrons; the *hadronic* component, composed mainly of pions, protons, antiprotons, and neutrons; and the *muonic* component, consisting of muons and antimuons originating from the decay of hadrons (primarily charged pions) and, to a lesser extent, from the electromagnetic component through photonuclear interactions. Since muons can travel long distances before decaying, they can reach the ground and be detected, serving as a probe of the hadronic component.

The main processes involving the electromagnetic component are Bremsstrahlung ($e \rightarrow e + \gamma$) and pair production ($\gamma \rightarrow e^+ + e^-$), while photonuclear interactions with atmospheric nuclei are subdominant. Neglecting the latter, Heitler developed a simplified yet useful model to gain insight into the electromagnetic cascade [22]. The left panel of Fig. 2.4 illustrates a purely electromagnetic shower, i.e., one initiated by a photon or an electron[3]. A primary photon of energy E_0 reaches the atmosphere and undergoes pair production. After travelling a characteristic *splitting length* $d = \lambda_{\rm em} \ln 2$, where $\lambda_{\rm em}$ is the radiation length in the medium, the electrons produces a photon through Bremsstrahlung[4]. Again, after transversing d, photons undergo pair production and electrons undergo Bremsstrahlung, generating a multiplicative process. In each split, we assume the energy of each particle is divided equally: electrons lose half of their energy through Bremsstrahlung, and those produced via pair production carry half of the photon's energy. Thus, after n interactions, the shower energy is distributed equally among all particles. After n generations, the number of particles N, the energy per particle E_n, and the trasversed matter X are given by:

$$
\begin{aligned}
N_n &= 2^n, \\
E_n &= E_0/2^n, \\
X_n &= n\, d.
\end{aligned}
\tag{2.11}
$$

The multiplication stops when the energy per particle reaches a critical energy $\xi_{\rm em} = 84$ MeV at which ionization losses becomes dominant for electrons, causing the shower to start dying out. The generation n_c at which the critical energy is reached is obtained by equating $E_n = \xi_{\rm em}$, yielding $n_c = \ln(E/\xi_{\rm em})/\ln 2$. By inserting n_c in the expressions of Eq. (2.11), the values at the maximum shower development are obtained:

$$
\begin{aligned}
N_{\rm max} &= E_0/\xi_{\rm em}, \\
X_{\rm max} &= \lambda_{\rm em} \ln(E_0/\xi_{\rm em}).
\end{aligned}
\tag{2.12}
$$

Remarkably, although the number of electrons is overestimated (in reality, there are more photons than electrons, as multiple photons can be emitted through Bremmsstrahlung), this simplified model correctly predicts that $N_{\rm max} \propto E_0$ and $X_{\rm max} \propto \ln E_0$, in agreement with cascade theory and detailed Monte Carlo simulations.

The Heitler model was extended to hadronic-initiated cascades by Mathews in Ref. [23], giving rise to the so-called Heitler-Mathews model. Let us first assume the simplest case,

---

[3]We refer to both electrons and positrons generically as electrons.

[4]d is the distance after which the electron looses half of its energy by radiation, as needed by Heitler's assumption that electrons lose half of their energy in each generation.
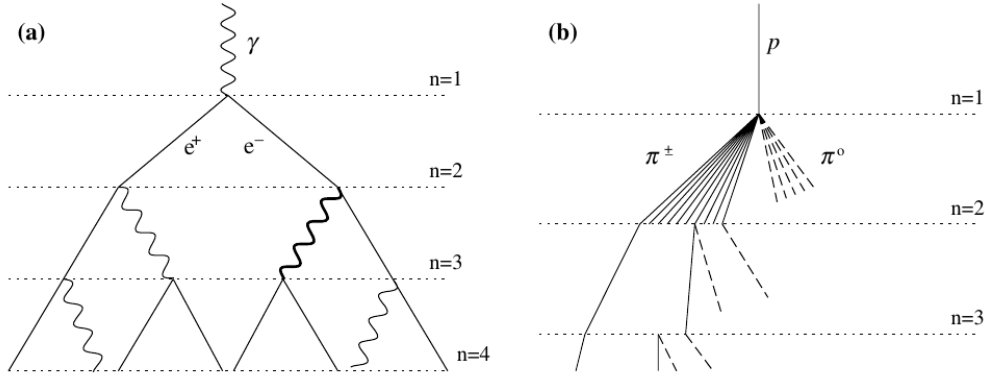
Figure 2.4: Schematics of a purely electromagnetic shower (left) and a hadron-initiated shower (right) in the framework of the Heitler and Heitler-Mathews models, respectively. Figure extracted from Ref. [23]

i.e., a proton primary of energy E_0. The situation is illustrated in the right panel of Fig. 2.4. In this case, the atmosphere is divided into layers of $d = \lambda_I \ln 2$, where $\lambda_I \sim 120 \text{ gcm}^{-2}$ is the interaction length of pions in air. After each generation, a number of N_{mult} pions are produced, of which α are charged and $\alpha - 1$ are neutral, yielding $N_{\text{ch}} = \alpha N_{\text{mult}}$ and $N_0 = (\alpha - 1)N_{\text{mult}}$. The quantity N_{mult} is known as multiplicity. The neutral pions decay promptly to two photons via $\pi^0 \to \gamma + \gamma$, fueling the electromagnetic cascade. These photons are then treated with the Heitler framework described before for electromagnetic showers. On the other hand, the charged pions interact again after traversing d, generating a multiplicative process. Assuming that the energy is evenly distributed among all particles, the energy per particle in the generation n is given by $E_n = E_0/N_{\text{mult}}^n$. The total number of charged pions at this point is $N_{\pi^\pm} = N_{\text{ch}}^n$. This process continues until the energy per particle falls below a critical energy ξ, where the decay of charged pions becomes dominant over interaction. The generation n_{dec} at which this occurs is obtained by equating $E_n = \xi$, which leads to $n_{\text{dec}} = \frac{\ln(E_0/\xi)}{\ln N_{\text{mult}}}$. At this point, we assume all charged pions decay into muons. Therefore, we obtain $N_\mu = N_{\text{ch}}^{n_{\text{dec}}}$ as the number of muons in the shower, which can be written as

$$N_\mu = \left(\frac{E_0}{\xi}\right)^\beta, \tag{2.13}$$

with $\beta = \frac{\ln(\alpha N_{\text{mult}})}{\ln N_{\text{mult}}}$. In the simplified model of Mathews, $\alpha = 2/3$ and $N_{\text{mult}} = 15$, which gives $\beta \approx 0.85$. When fitted with detailed Monte Carlo simulations, it is found $\beta \approx 0.87 - 0.93$.

It is also intructive to write the energies carried away by the hadronic (E_{had}) and electromagnetic cascade (E_{EM}) at a given generation n:

$$\begin{aligned} E_{\text{had}} &= \left(\frac{2}{3}\right)^n E_0, \\ E_{\text{EM}} &= \left[1 - \left(\frac{2}{3}\right)^n\right] E_0. \end{aligned} \tag{2.14}$$

After $n \approx 6$, about 90% of the initial energy is carried away in the electromagnetic cascade and lost through ionization losses in the atmosphere [12]. This energy dissipated in the atmosphere is relevant, as it can be used to infer the shower energy in a nearly calorimetric way through the use of fluorescence telescopes (see Section 3.2).

If only the photons produced in the first interaction via the $\pi^0 \to 2\gamma$ decay are considered, an estimate of the X_{max} of the electromagnetic component of proton showers can be

derived assuming an electromagnetic cascade from a photon with energy $E_0/(2N_{\text{mult}})$ (the factor 2 accounts for the two photons) using Eq. (2.12) [12]:

$$X^p_{\text{max}} \approx \lambda_p + X^\gamma_{\text{max}}(E_0/(2N_{\text{mult}})) = \lambda_p + \lambda_{\text{em}} \ln\left(\frac{E_0}{2N_{\text{mult}}\xi_{\text{em}}}\right), \quad (2.15)$$

where λ_p is the interaction length of protons in air, which needs to be added since the photons originate in the first interaction.

To extend the model to nuclei with mass $A > 1$, the superposition model is invoked, in which a nucleus with energy E_0 and A nucleons is considered as A independent nucleons, each with energy E_0/A. This approach is motivated by the fact that the binding energy of ~ 5 MeV per nucleon is much smaller than the typical interaction energies involved in air showers. Thus, the number of muons N^A_μ and depth of shower maximum X^A_{max} for a nucleus with mass A and energy E_0 are estimated by substituing E_0 with E_0/A and mutliplying by A in Eq. (2.13), and by substituing E_0 with E_0/A in Eq. (2.15):

$$N^A_\mu = A\left(\frac{E_0/A}{\xi}\right)^\beta = A^{1-\beta}\left(\frac{E_0}{\xi}\right)^\beta, \quad (2.16)$$

$$X^A_{\text{max}} = \lambda_p + \lambda_{\text{em}} \ln\left(\frac{E_0/A}{2N_{\text{mult}}\xi_{\text{em}}}\right) = X^p_{\text{max}} - \lambda_{\text{em}} \ln A. \quad (2.17)$$

From Eq. (2.16) and Eq. (2.17), it follows that both the number of muons and the depth of the shower maximum are mass-sensitive observables.

The Heitler-Mathews model provides a framework to convert measurements of X_{max} and N_μ to the mean logarithmic mass. Rearranging Eq. (2.16) and Eq. (2.17), we get

$$\langle \ln A \rangle = \ln 56 \, \frac{\langle \ln N^{\text{A}}_\mu \rangle - \langle \ln N^p_\mu \rangle}{\langle \ln N^{\text{Fe}}_\mu \rangle - \langle \ln N^p_\mu \rangle}, \quad (2.18)$$

$$\langle \ln A \rangle = \ln 56 \, \frac{\langle X^{\text{A}}_{\text{max}} \rangle - \langle X^p_{\text{max}} \rangle}{\langle X^{\text{Fe}}_{\text{max}} \rangle - \langle X^p_{\text{max}} \rangle}. \quad (2.19)$$

Commonly, experiments do not measure the total number of muons in an air shower but rather a quantity that is proportional to it, in which case Eq. (2.16) and Eq. (2.18) still holds. In the context of this work, this quantity is the muon density lateral distribution evaluated at a reference distance of 450 m from the shower core, ρ_{450}. In Chapter 6, we revisit and improve the method to fit the muon density lateral distribution.

Lastly, although the simplified models described above provide conceptual insight into the main features of EAS, full Monte Carlo codes are available to simulate air showers and are widely used by various observatories to interpret their measurements. The most commonly used are CORSIKA [24], AIRES [25], and CONEX [26]. These codes implement different hadronic models. The most common high-energy hadronic models are EPOS-LHC [27, 28], QGSJetII-04 [29], and SIBYLL [30], referred to as post-LHC models since they are tuned to LHC measurements, whereas the most popular low-energy models include UrQMD [31] and FLUKA [32].

2.4 Mass composition and the Muon Puzzle

The determination of the mass composition of UHECRs is particularly relevant, as several astrophysical scenarios—differing in their assumed mass composition—can equally well explain the existing data. For example, to explain the mass composition and all-particle

spectrum observed above the ankle, different scenarios can be invoked, namely, a maximum-rigidity or a photodisintegration scenario. A maximum-rigidity scenario implies that the suppression of the spectrum is due to sources reaching their maximum acceleration limit. Different nuclear species can be accelerated up to a maximum energy proportional to their charge (Eq. (2.6)), and their flux is subsequently suppressed beyond this limit. The suppression of the all-particle flux is thus interpreted as the maximum energy achieved by a heavy, strongly charged component. On the other hand, a photodisintegration scenario suggests that heavy nuclei are accelerated at the sources to energies beyond the GZK limit and undergo photodisintegration during their journey to Earth. In this framework, the suppression is a consequence of propagation effects, and the presence of a light component in the highest-energy cosmic-ray flux results from photodisintegration reactions. In both cases, a mixed composition is required within this energy range, disfavouring the long-standing paradigm of a proton- or helium-dominated flux at the highest energies. In reality, a combination of both scenarios can occur, with a predominance of the maximum-rigidity scenario, as suggested by the latest combined fit to X_{max} distributions and energy spectrum measurements from the Pierre Auger Observatory [33].

The conversion of air shower observables into the mean logarithmic mass, $\langle \ln A \rangle$, relies on EAS simulations (see Section 2.3). These simulations, in turn, depend on hadronic models that extrapolate accelerator data into unexplored regions of phase space, particularly at the highest energies and in the forward region. As a result, the inferred composition is strongly model-dependent. A comprehensive understanding of EAS is therefore essential for interpreting mass composition measurements from UHECR observatories, thereby bridging the fields of UHECR research and high-energy particle physics.

The two main shower observables sensitive to the primary mass are X_{max} and N_μ. Since X_{max} is associated with the better-understood electromagnetic component of EAS, its interpretation is less affected by hadronic model uncertainties, making it the most reliable and widely used observable for composition studies. However, its measurement is limited by poorer statistics, as it requires dedicated fluorescence telescopes that operate only on moonless nights with favorable weather conditions (Section 3.2).

On the other hand, the muonic component of air showers can be sampled with high statistics using shielded muon detectors, such as the Underground Muon Detector of the Pierre Auger Observatory, or by analyzing very inclined air showers, where most of the electromagnetic component is attenuated in the atmosphere, with unshielded detectors [1, 2]. However, its interpretation is subject to greater uncertainties, as muons originate from the hadronic component of the shower, which is more strongly affected by model uncertainties.

Furthermore, several experiments have reported that the inferred composition from muon measurements (Eq. (2.18)) is systematically heavier and not compatible with the composition predicted from X_{max} observations (Eq. (2.19)). This discrepancy has led to the interpretation of a muon deficit in simulations (equivalently, a muon surplus in data), giving rise to the so-called *muon puzzle*, which has been the subject of intense study in recent years (see Ref. [3] for a recent and extensive review). Solving or further constraining this puzzle will not only enable the use of muons as a mass composition estimator, with larger datasets and higher statistical significance to constrain astrophysical scenarios for UHECRs, but will also shed light on hadronic physics at energies far beyond those achieved in human-made accelerators, making a significant contribution to particle physics.

Several key features of the muon puzzle are still to be understood. The energy at which the muon deficit begins, as well as its energy dependence and magnitude, remains unclear. Moreover, although a large number of experiments report a deficit, this is not true for all of them [3, 4]. In this uncertain scenario, more measurements—preferably conducted over a wide energy range with the same energy scale—are needed to provide a clearer picture. In

this work, we present a muon measurement within the energies $10^{17.5}$ eV $< E < 10^{18.9}$ eV. In Section 7.6, we compare the muon content obtained in this work with that expected from $X_{\max}$ measurements and assess the discrepancy between them. Our results are compared with other muon measurements from different observatories in Section 7.8.

2.5 Summary

In this chapter, the main aspects related to high- and ultra-high-energy cosmic rays were outlined. We presented the energy spectrum of cosmic rays at Earth and its main features in Section 2.1. The acceleration mechanisms, potential sources, and propagation effects in the extragalactic medium were discussed in Section 2.2. Diffusive shock acceleration via a first-order Fermi mechanism—the currently widely accepted and most commonly invoked acceleration process for cosmic rays—was described in Section 2.2.1. Within this acceleration mechanism, potential sources were identified using the so-called Hillas diagram (Fig. 2.2) in Section 2.2.2. Propagation effects, notably the interaction of cosmic rays with the cosmic microwave background and its implications for protons and nuclei, were discussed in Section 2.2.3. The main features of extensive air showers, produced upon the interaction of a cosmic ray with the atmosphere, were presented in Section 2.3. Two simple models were introduced to provide insight into air shower development: the Heitler model for electromagnetic showers and the Heitler-Mathews model for hadronic showers. In particular, we showed that both $X_{\max}$ and N_μ are two mass-sensitive obervables that can be used to infer the mass composition of cosmic rays. Lastly, the inconsistency between the mass composition inferred from $X_{\max}$ and muon measurements —leading to the interpretion of a muon deficit in simulations— was presented in Section 2.4.

Chapter 3

The Pierre Auger Observatory

The Pierre Auger Observatory, located in Malargüe, Argentina, is the largest facility dedicated to the detection and study of ultra-high-energy cosmic rays (UHECRs). Successfully operating for more than 20 years, it was a pioneer in its hybrid design, observing air showers both with a Surface Detector (SD)—a large ground-based array of water-Cherenkov detectors (WCDs)—and a Fluorescence Detector (FD), a set of 24 telescopes overlooking the SD array.

Operating nearly 100% of the time, the SD measures the footprint of shower particles on the ground, and its vast surface ensures unprecedented exposure and statistics. The FD, with a duty cycle of approximately 15%, operates only during moonless nights with favorable weather conditions, providing a quasi-calorimetric and nearly model-independent estimate of the shower energy. It also measures the depth of the shower maximum, the most reliable and widely used mass-sensitive observable. By cross-calibrating the SD and FD, the complementary benefits of both detectors become evident, allowing for energy estimation of air showers with high statistics and low systematic uncertainties. The main characteristics and data reconstruction procedure of the SD are presented in Section 3.1, while the main features of the FD are described in Section 3.2

In its second phase of operation, the Observatory recently underwent a major upgrade, known as AugerPrime, to enhance its sensitivity to the primary mass. The main components of this upgrade are presented in Section 3.3, with a more detailed discussion of the Underground Muon Detector, as it is the primary detector used in this thesis.

3.1 The Surface Detector

The Surface Detector (SD) consists of an array of 1660 water-Cherenkov detectors (WCD) ordered in three nested triangular grids with spacing of 1500 m (SD-1500), 750 m (SD-750) and 433 m (SD-433). The SD-1500 covers an area of 3000 km^2 and provides an energy threshold for air-showers of $10^{18.5}$ eV whereas the SD-750 comprises an area of 23.5 km^2 with an energy threshold of $10^{17.5}$ eV. Lastly, the SD-433 encloses a smaller area of 1.9 km^2 and is suitable for air-showers of energies above $10^{16.5}$ eV. A sketch of the SD array is shown in Fig. 3.1.

3.1.1 SD station and trigger system

Each WCD, referred to as a SD station, consists of a cylindrical tank with a top surface area of 10 m^2, filled with highly purified water up to a height of 1.2 m and enclosed by a diffusely
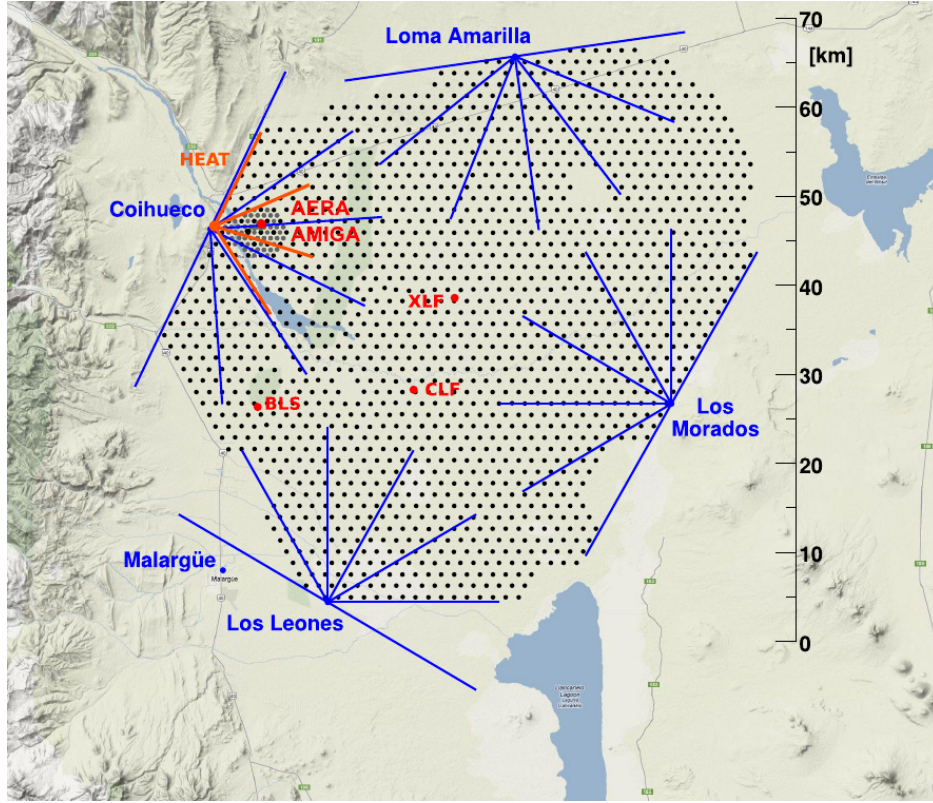
Figure 3.1: Layout of the Pierre Auger Observatory. Black dots indicate the position of the water-Cherenkov detectors of the Surface Detector. The 30° azimuthal field of view of each of the 24 FD telescopes across the four sites is displayed with blue lines (see Section 3.2).

reflective liner. The water volume is monitored from above by three 9-inch photomultiplier tubes (PMTs), which detect Cherenkov light generated as charged particles traverse the water. Each PMT produces two signals, both of which are time-stamped using GPS with an absolute accuracy of approximately 12 ns. The signals are digitized at a rate of 40 MHz with 10-bit resolution by Flash Analog-to-Digital Converters (FADCs). The low-gain signal is directly extracted from the PMT anode, whereas the high-gain signal originates from the final dynode and undergoes amplification, making it about 32 times stronger than the low-gain signal, thereby extending the overall dynamic range. Each station operates independently, powered by a solar energy system that supplies electricity to both the PMTs and the station's electronics. A photograph of a SD station is shown in Fig. 3.2.

The data acquisition of the SD relies on a hierarchical set of triggers, ranging from the station level to the array level [34]. The first and second-level triggers, referred to as T1 and T2, respectively, are generated locally at each station. Two T1 triggers, designed to function in a complementary manner, are implemented in the station electronics. The first trigger, known as T1-Threshold (T1-Th), is primarily sensitive to muons and is activated when all three PMTs exceed a predefined threshold. The second trigger, referred to as Time-Over-Threshold (T1-ToT), is designed to be more sensitive to electromagnetic particles. It is triggered when at least two PMTs surpass a lower threshold within a minimum time window.

All T1-ToT triggers are promoted to the T2 level, whereas T1-Th triggers are only promoted if all three PMTs exceed a higher threshold. The WCDs continuously transmit the timestamp and type of T2 triggers to the central data acquisition system (CDAS) of the Observatory, which scans for air-shower events by identifying spatial and temporal correlations
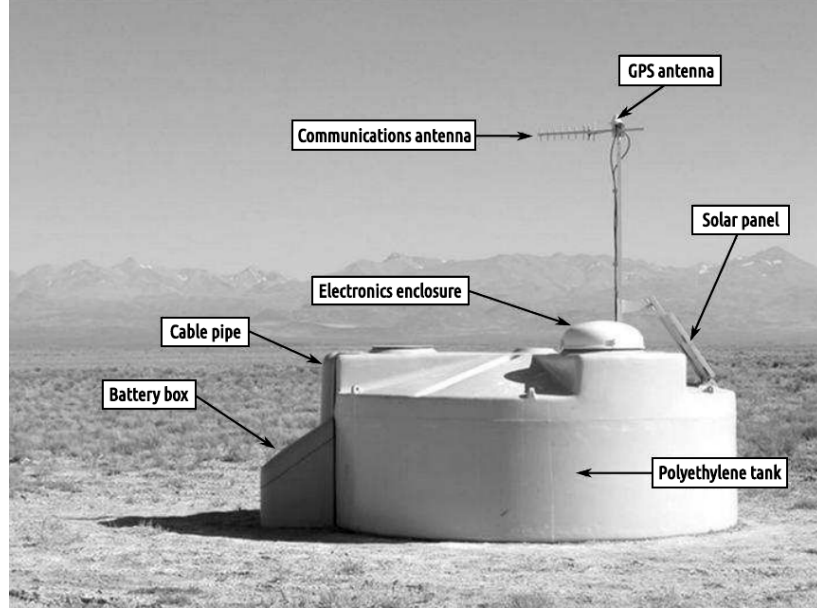
Figure 3.2: Picture of a WCD indicating its most relevant components. Taken from Ref. [35].
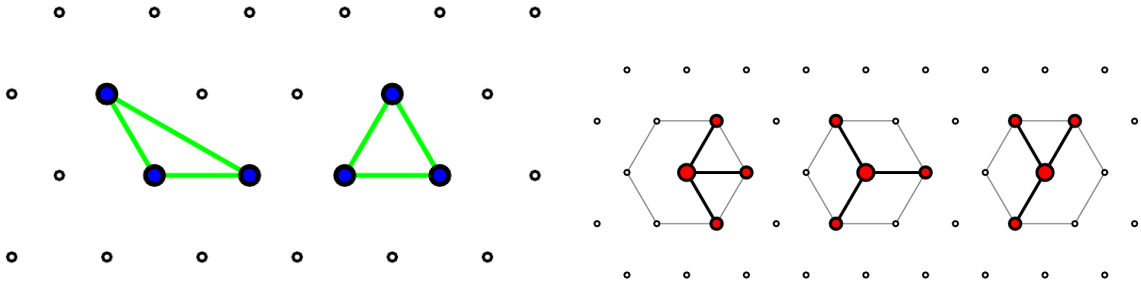

Figure 3.3: Possible T4 configurations (with addition of all the symmetry transformations of a triangular grid). The left (right) panel shows the 3ToT (4C1) trigger. Taken from Ref. [36].

between them. If such correlations are detected, a third-level trigger, referred to as T3, is issued to the participating stations (which, by definition, have T2 triggers) as well as adjacent stations (which may have either T1 or T2 triggers). These station then respond sending their data for permanent storage.

The next set of triggers is applied offline to the stored T3 data. The fourth-level trigger, known as T4, serves as the physics trigger and is designed to select genuine air showers while filtering out background T3 events caused by random coincidences between stations. Two configurations qualify as T4, as shown in Fig. 3.3. The 3ToT condition requires three neighboring stations, arranged in a triangular pattern, to pass the T2-ToT trigger. In contrast, the 4C1 condition requires four neighboring stations, with no specific requirements on the type of T2 trigger. In both configurations, the timing of the participating stations must be consistent with a shower front propagating at the speed of light

Lastly, a fiducial trigger, known as 6T5, is applied with the goal of ensuring that the air shower is well contained within the array, thereby guaranteeing a reliable reconstruction of the impact point of the shower on the ground. This trigger requires that the station with the largest signal be surrounded by a set of working (i.e., non-broken) stations.

3.1.2   SD reconstruction

In this section, we summarize the main aspects of the SD reconstruction procedure, which is thoroughly described in Ref. [37].

The first step of the reconstruction consists of estimating the signal deposited by the shower particles in each station. To this end, in each time bin, the trace of every working PMT is averaged (the high gain is used if it is not saturated, otherwise the low-gain trace is used). The charge generated in the station is obtained by integrating the average trace between the start and stop times of the signal, previously determined using only the high-gain channel, and converted into units of Vertical Equivalent Muon (VEM), the mean charge deposited by a vertical muon in the tank. The VEM is obtained for each PMT in every station by constantly recording the charge generated by background particles, from which muons generate a distinguishable peak.

The geometry of the shower, namely the impact point of the shower $\vec{x}_c$ on the ground—the so-called shower core—and its arrival direction $\hat{a}$, is estimated through an iterative procedure. An initial estimate of $\vec{x}_c$ is obtained as the signal-weighted center of mass of the participating stations, known as the barycenter of the event. Then, $\hat{a}$, anchored at the barycenter, is estimated by fitting a shower plane front propagating at the speed of light to the start times of the signals from the three neighboring stations with the highest average signal. At this stage, accidental stations that are not part of the event but are triggered by background particles coinciding with the shower front are identified by requiring a delay relative to the shower front that is not within $[-2\,\mu s, +1\,\mu s]$ and are subsequently discarded. Using these initial values, a more refined estimate of $\hat{a}$ is obtained by fitting a time model that accounts for the curvature of the shower front. The radius of curvature is left as a free parameter if enough stations are available; otherwise, it is fixed to a parameterized value obtained from events where it could be reliably fitted.

The next step involves determining the shower size, defined as the expected signal $S(r_{\mathrm{opt}})$ at an optimal distance r_{opt}. This is obtained by fitting a lateral distribution function (LDF), which describes the fall-off of station signals as a function of the distance to the shower axis, using a log-likelihood minimization. For the case of the Surface Detector (SD) of the Pierre Auger Observatory, the LDF model corresponds to a modified Nishimura-Kamata-Greisen (NKG) function, given by

$$S(r) = S(r_{\mathrm{opt}}) \left(\frac{r}{r_{\mathrm{opt}}} \right)^{\beta} \left(\frac{r + r_{\mathrm{s}}}{r_{\mathrm{opt}} + r_{\mathrm{s}}} \right)^{\beta+\gamma} , \qquad (3.1)$$

where $r_{\mathrm{s}} = 700$ m is fixed, $S(r_{\mathrm{opt}})$ is a free parameter, and β and γ are fixed to data-driven parameterized values unless enough stations with appropiate spacing are available. The core position $\vec{x}_c$, intially estimated as the barycenter, is also left free during the LDF fit. The optimal distance is chosen to minimize the uncertainty due to incomplete knowledge of the true shape of the LDF, and depends mainly on the grid type and spacing between detectors [38]. For the SD-1500, this corresponds to $r_{\mathrm{opt}} = 1000$ m, wheras for the SD-750 is $r_{\mathrm{opt}} = 450$ m. Thus, the shower size estimators are referred to as $S(1000)$ ($S(450)$) for the SD-1500 (SD-750) arrays. In Fig. 3.4, an example LDF fit for an event is displayed.

Lastly, the zenith angle dependence of the shower size needs to be removed, as an identical shower arriving from an inclined direction traverses a larger amount of atmosphere than a vertical one, producing smaller signals in the WCDs due to atmospheric attenuation. To this end, an attenuation correction $f_{\mathrm{att}}(\theta)$ is derived using the Constant Intensity Cut (CIC) method [39, 40], allowing the shower size $S(r_{\mathrm{opt}})$ of a shower arriving at a zenith angle θ to
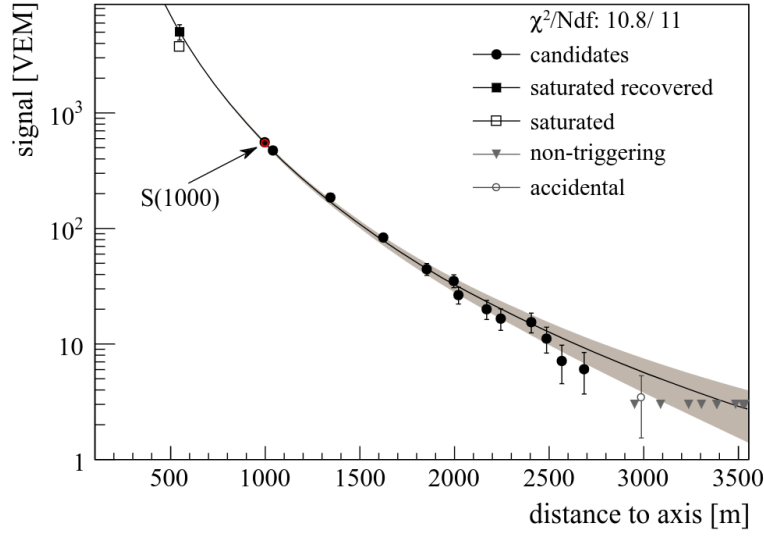
Figure 3.4: Example of an LDF fit of the SD. Taken from Ref. [11].

be converted into $S_{\theta_{\text{ref}}}$, the shower size it would have produced had it arrived at a reference angle of θ_{ref}, via

$$S_{\theta_{\text{ref}}} = \frac{S(r_{\text{opt}})}{f_{\text{att}}(\theta)}. \tag{3.2}$$

The reference angle is chosen to coincide with the median of the zenith angle distribution of the data: $38°$ for the SD-1500 (covering a range of $0° \leq \theta \leq 60°$) and $35°$ for the SD-750 (ranging from $0° \leq \theta \leq 55°$). The attenuation-corrected shower sizes are then S_{38} and S_{35} for the SD-1500 and SD-750 arrays, respectively.

The attenuation-corrected shower sizes are used to estimate the shower energy through calibration with the FD, which provides a quasi-calorimetric measurement of the shower energy (see Section 3.2). Using high-quality events independently reconstructed by both the SD and FD, the SD observables S_{38} and S_{35} are related to the FD energy E_{FD} via a calibration curve given by

$$E_{\text{FD}} = A \left(S_{38}/\text{VEM}\right)^B, \tag{3.3}$$

where A and B are fit parameters obtained through a log-likelihood minimization procedure [41]. The correlation between the SD energy estimators (S_{38} and S_{35}) and the FD energy, along with the corresponding fits to Eq. (3.3), are displayed in Fig. 3.5. In this way, the S_{38} and S_{35} obtained with the SD, which operates with a nearly 100% duty cycle, can be used to estimate the shower energy even when the FD is not operational.

3.2 The Fluoresence Detector

The FD consists of 24 telescopes arranged across 4 sites (Los Leones, Los Morados, Loma Amarilla, and Coihueco; see Fig. 3.1) overlooking the SD array. Operating nearly 15% of the time, during moonless nights with favorable weather conditions, the FD measures the longitudinal development of air showers with energies greater than 3×10^{18} eV by detecting the fluorescence light emitted by nitrogen molecules, which are excited by the shower particles as the shower develops through the atmosphere. Each site is comprised of 6 independent telescopes, each providing a field of view of $30° \times 30°$ in both azimuth and elevation, giving each site a $180°$ azimuthal field of view.
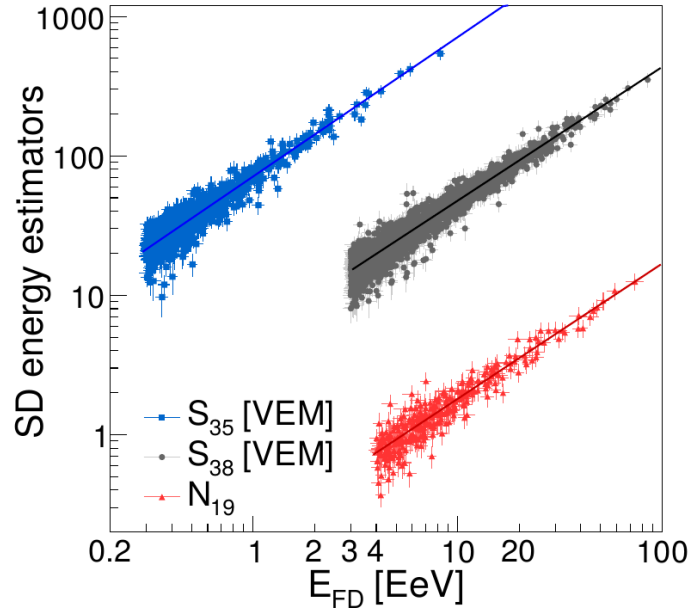
Figure 3.5: Correlation between the SD energy estimates, S_{38} and S_{35}, and the FD energy. The correlation with the SD estimate N_{19} used for air showers with $\theta > 60°$ and the FD energy is also shown. Lines indicate fits to Fig. 3.5. Taken from Ref. [42].
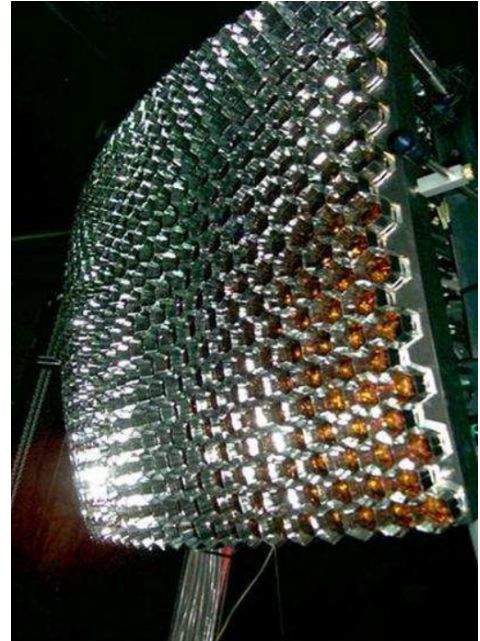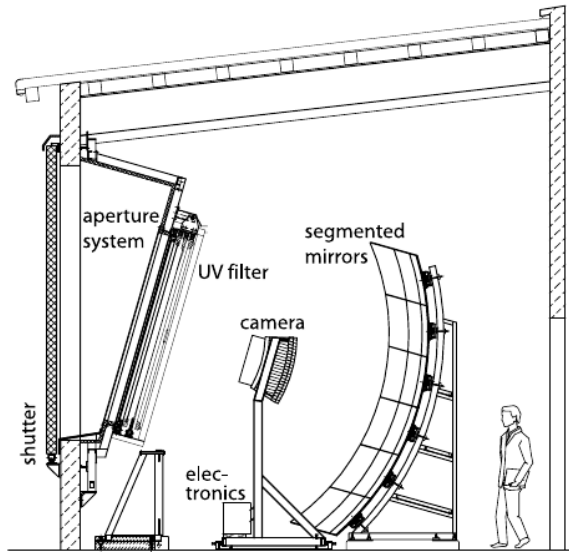

Figure 3.6: *Left*: Skematich view of an FD telescope and its main components. *Right*: Picture of an FD camera and its 440 PMTs. Taken from Ref. [43]

The main elements of the detection system of an FD telescope are a circular aperture, a mirror and a camera composed of a matrix of 440 photomultiplier tubes (PMTs), known as pixels, located on the focal surface of the mirror. The camera pixels are arranged in a matrix of 22 rows by 20 columns. Additionally, an UV filter is used to reduce background and enhance the signal-to-noise ratio. A skematich view of an FD telescope and a picture of its camera are shown in Fig. 3.6.
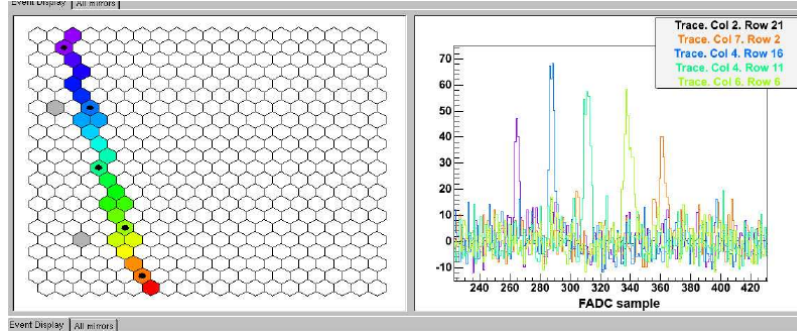
Figure 3.7: Example of an air-shower event as seen by the camera of an FD telescope taken from Ref. [43]. *Left*: The pattern of activated PMTs with its timing color-coded. *Right*: Time-dependent signals of the participating pixels. Each pixel reaches its maximum signal at different times as the shower develops.

The flux of fluorescence photons produced by the shower, entering through the aperture, is reflected in the mirror and focused on the telescope camera, producing a time-dependent profile in the signals of the PMTs, as displayed in Fig. 3.7. Utilizing the timing of the PMT signals in the FD telescopes, the shower geometry is reconstructed. If measurements from the SD tanks are available, they are also included to improve the shower geometry estimation.

Then, the time-dependent signals of the FD pixels are projected onto the shower axis, and a profile of the energy deposition of the shower particles per slant depth (dE/dX) as a function of the slant depth X is obtained. This profile is fitted with a Gaisser-Hillas function:

$$f_{\text{GH}}(X) = \left(\frac{dE}{dX}\right)_{\text{max}} \left(\frac{X - X_0}{X\text{max} - X_0}\right)^{(X_{\text{max}} - X_0)/\lambda} e^{(X_{\text{max}} - X)/\lambda}, \tag{3.4}$$

where $\left(\frac{dE}{dX}\right)_{\text{max}}$ is the maximum energy deposition, X_0 and λ are shape parameters, and X_{max} is the depth of the shower maximum.

Since approximately 90% of the shower energy is transferred into the excitation of air molecules, the integral of the profile is used as an estimator of the shower's calorimetric energy. The final estimate of the shower energy is obtained by applying a correction of $\sim 10\%$ to account for the so-called invisible energy—the energy carried away by neutrinos and muons that cannot be detected by the fluorescence light technique. A three-dimensional schematic view of a hybrid event, along with its energy deposition profile and its fit to Eq. (3.4) , is shown in Fig. 3.8.

Lastly, three high-elevation telescopes, known as High-Elevation Auger Telescopes (HEAT), are also operative in Coihueco [45]. The larger inclination of HEAT, covering an elevation from $30°$ to $58°$, allows to measure showers of lower energies that develop at a higher altitude. Overlooking the SD-750 array, it extended the energy of high-quality hybrid events down to $10^{17.2}$ eV.

3.3 AugerPrime

As discussed in Chapter 2, having sensitivity to the primary mass on an event-by-event basis is crucial for disentangling astrophysical scenarios for sources and acceleration mechanisms of UHECRs. To enhance its sensitivity to the primary mass, the Observatory recently underwent an upgrade known as AugerPrime, which includes several enhancements, such as the installation of scintillator and radio detectors on top of the WCDs, the replacement of the WCD electronics, the addition of a small photomultiplier tube to the WCDs, and the
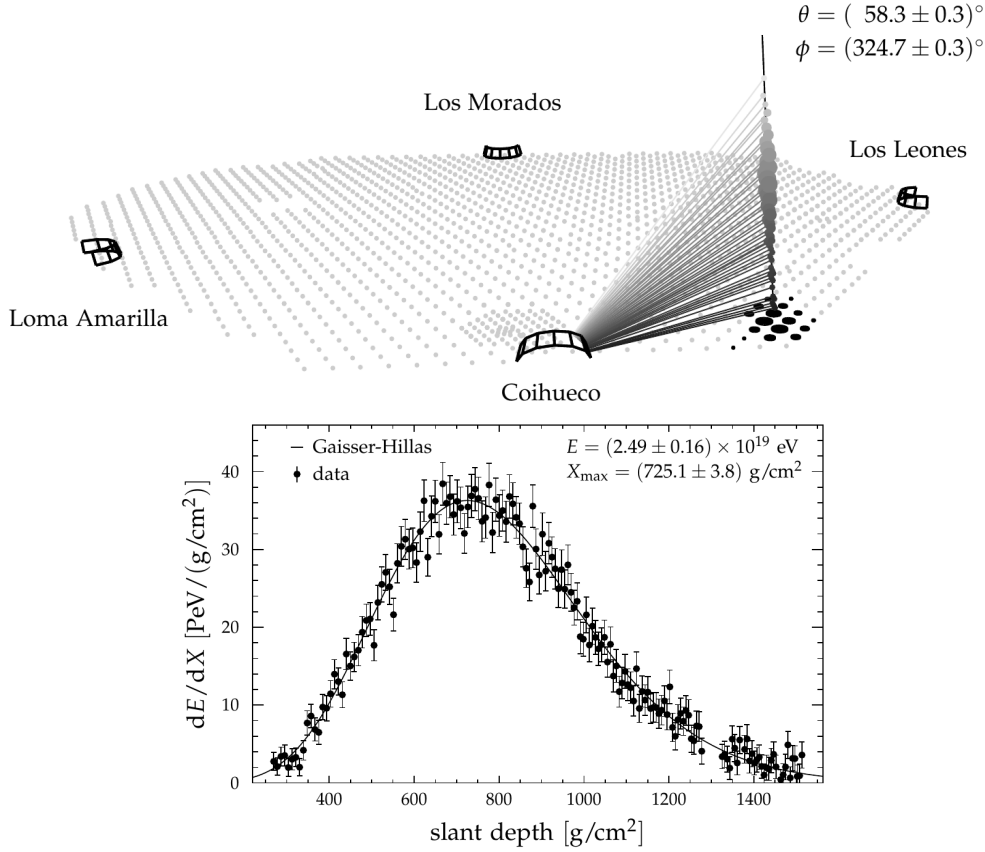
Figure 3.8: A three dimensional view of a hybrid event (upper panel) and its longitudinal profile together with its fit to Eq. (3.4) (lower panel). Taken from Ref. [44].

deployment of the Underground Muon Detector (UMD). In this section, we briefly describe each of these components of AugerPrime, focusing on the UMD, as it is the main detector used in this thesis.

3.3.1 Surface Scintillator Detector

As part of the AugerPrime upgrade, each Surface Detector (SD) station was equipped with a Scintillator Surface Detector (SSD), placed above the existing water-Cherenkov detector. This addition enhances the ability to distinguish between the electromagnetic and muonic components of extensive air showers, improving mass composition measurements.

The SSD consists of two scintillator modules with a total detection area of 3.8 m², built from extruded polystyrene strips. These strips contain wavelength-shifting (WLS) fibers, which guide the light produced when charged particles traverse the detector to a single PMT for signal detection. The SSD's response differs from that of the WCD: while the SSD is equally sensitive to both electromagnetic and muonic particles, the WCD has a higher sensitivity to muons. By combining the signals from both detectors, the separate contributions of these components can be estimated [46, 47].

3.3.2 Small photomultiplier tube and upgraded electronics

The WCDs are being upgraded to enhance their dynamic range and overall performance. A key improvement is the addition of a small photomultiplier tube (SPMT), the Hamamatsu R8619-22, which has a diameter of less than 30 mm—significantly smaller than the ~23

cm standard PMTs. This new SPMT will allow the SD stations to accurately measure large signals that would otherwise saturate the existing PMTs, improving the capability of the detector to record events occurring closer to the shower axis [48, 49].

Additionally, the electronics of the WCDs are being upgraded. The original unified board (UB), which has six channels, a 40 MHz sampling frequency, and a 10-bit ADC, is being replaced by an upgraded unified board (UUB). This new board features 10 channels, a higher sampling frequency of 120 MHz, and a 12-bit ADC, accommodating the additional signals from the SPMT and scintillator detectors, also enabling communication with the radio and underground muon detectors. With these enhancements, the dynamic range of the SD stations will be extended to match the upper limits of the scintillator detectors, ensuring both systems saturate at approximately the same distance from the shower axis—around 250 m for showers with energies of $\sim 10^{20}$ eV. Furthermore, the increased sampling rate of the UUB will lead to finer digitization of the detector signals, enhancing the overall performance of the WCDs.

The operation of the WCDs with the UBs is known as Phase 1 of the Observatory, whereas the current operation with UUBs is referred to as Phase 2.

3.3.3 Radio detector

Coherent radio emission in the frequency band 30–80 MHz also occurs as the shower develops through the atmosphere, primarily due to the deflection of electrons and positrons in the geomagnetic field. A time-dependent negative charge excess present in the air shower also contributes, but subdominantly. As radio emission stems from the electromagnetic component of air-showers, it potentially provides an alternative way to access to X_{max} and to the calorimetric energy of the shower.

Part of the AugePrime upgrade includes integrating radio detection to enhance its sensitivity to the nuclear mass particularly for inclined air showers, as these produce large radio footprints that can be detected with sparsed arrays of radio antennas. This technique has been validated by the Auger Engineering Radio Array (AERA) [50, 51].

Unlike the Fluorescence Detector (FD), which operates only on moonless nights, the new Radio Detector (RD) will have an almost 100% duty cycle, ensuring continuous data collection. This feature, combined with its low cost, makes radio detection a valuable addition to AugerPrime. The RD will be particularly effective in the zenith angle range of 65° to 85°, where the SSD upgrade is less effective, providing improved mass composition measurements. With its deployment recently finished, the RD consists of dual-polarized Short Aperiodic Loaded Loop Antennas (SALLAs) installed on each SD-1500 station and triggered by the corresponding SD station [52].

3.3.4 Underground Muon Detector

The Underground Muon Detector (UMD) is part of the low-energy enhancement of the Observatory known as *Auger Muons and Infill for the Ground Array* (AMIGA) [53] and is being deployed in the SD-750 and SD-433 arrays. It consists of an array of plastic scintillator muon counters buried 2.3 m underground near a WCD. The UMD operates in slave mode with the WCD, relying on the latter to provide the trigger for data acquisition. The soil above the detector absorbs the electromagnetic component of air showers and imposes an energy cut of ~ 1 GeV for vertical muons. Each UMD station comprises three modules, made of 10 m^2 of plastic scintillator, giving a total active area of 30 m^2 per station. A scheme of a UMD station is shown in Fig. 3.9.

A UMD module is divided into 64 strips, each measuring 400 cm in length, 4 cm in width, and 1 cm in thickness, with embedded wavelength-shifting (WLS) optical fibers connected to
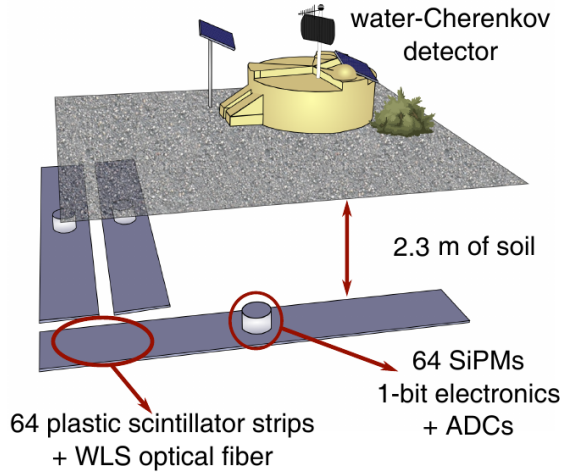
Figure 3.9: Scheme (left) and photograph of the deployment (right) of a UMD station.
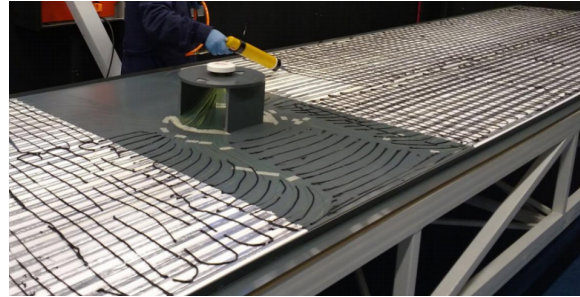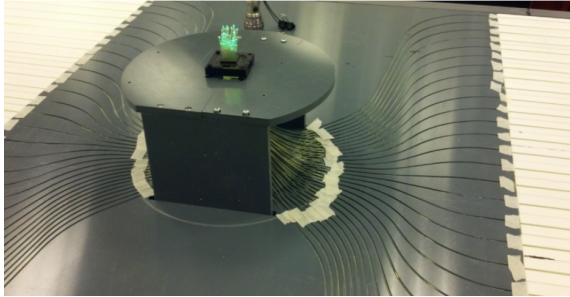

Figure 3.10: *Left*: Picture of the 64 optical fibers arranged before coupling to the SiPM array. *Right*: Photograph of UMD module under construction before closing the PVC casing. Both pictures were extracted from Ref. [54].

an array of 64 silicon photomultipliers (SiPMs). These strips are organized into two identical panels of 32. The fibers converge into a central dome between the panels, which houses the SiPM array and electronics. To ensure protection from environmental factors and soil, modules are enclosed in a PVC container before being buried. A picture of a UMD module under construction is shown in Fig. 3.10.

Scintillator strips and optical fibers

The detection mechanism of the scintillator detector relies on fluorescence light emission. The scintillator bars used in the UMD are manufactured at the Fermi National Accelerator Laboratory [55] and made of commercial Dow Styron 663W polystyrene, doped with fluorescent chemicals PPO (2,5-diphenyloxazole) and POPOP (1,4-bis(5-phenyloxazole-2-yl)benzene) in weight fractions of 1% and 0.03%, respectively. The strips are further coated with a 0.25 mm polystyrene reflective layer containing 12% TiO_2, which helps prevent photon loss. The purpose of the doping materials is to enhance photon production when a charged particle passes through the strip. When a charged particle traverses the scintillator, the base polystyrene emits ultraviolet photons, which would be attenuated within a few millimeters if no doping materials were present. These photons are absorbed and re-emitted by the first dopant (PPO), which has a longer attenuation length. Subsequently, the second dopant (POPOP) absorbs the ultraviolet photons and re-emits light at approximately 420 nm. A simplified scheme showing the processes inside the scintillator is shown in the upper-left panel of Fig. 3.11.
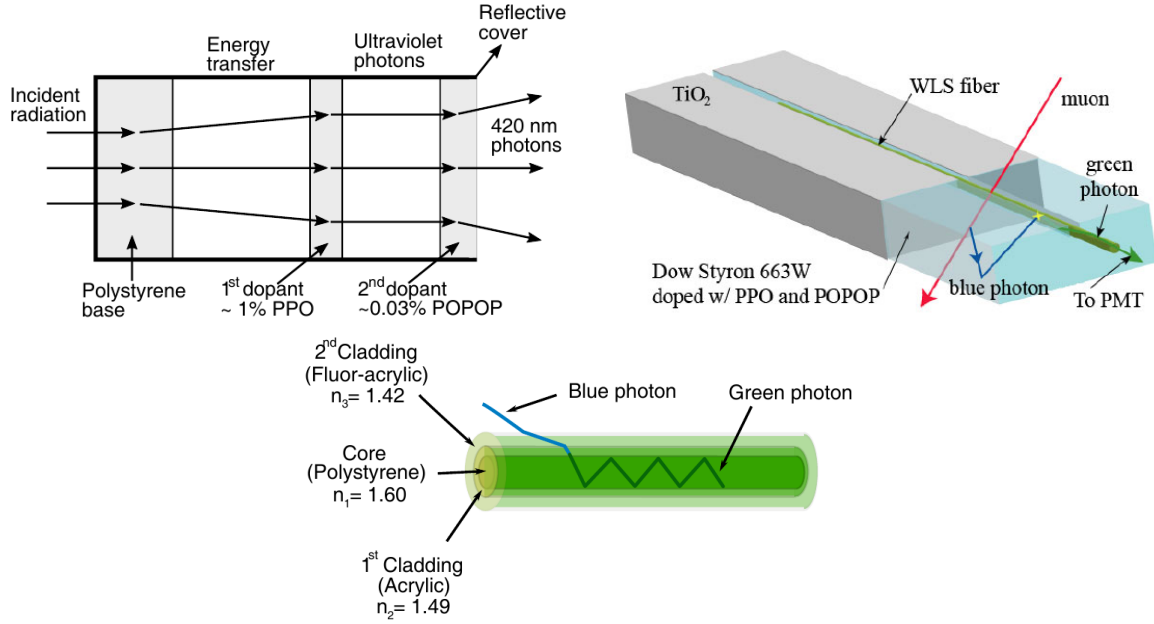
Figure 3.11: *Upper left*: Simplified scheme of the processes inside the material of a UMD scintillator strip. *Upper right*: Scheme of a strips with a WLS fiber. *Lower panel*: Detail of a WLS fiber utilized in the detector. The upper-left and lower figures were taken from Ref. [54], whereas the upper-right was extracted from Ref. [56].

With these doping materials, photons can travel between 5 and 25 cm along the strip before being absorbed. Since the strips are 4 m long, optical fibers are required to efficiently transport these photons to a photomultiplier. To this end, the Saint-Gobain BCF-99-29AMC multi-clad WLS fibers are used. Blue photons generated in the scintillator are absorbed, re-emitted as green photons ($\lambda \sim 500$ nm), and transported by the fiber over several meters to the SiPM. Schemes showing the scintillator and fiber are displayed in Fig. 3.11.

Silicon photomultipliers (SiPMs)

SiPMs (Silicon Photomultipliers) are solid-state detectors composed of arrays of avalanche photodiodes (APDs) connected in series with a resistor, with each APD-resistor tandem known as a cell. These micro-cells are arranged in a parallel configuration, as shown in the left panel of Fig. 3.12. The SiPM used in the UMD is the HAMAMATSU S13361-2050NE-08, consisting of 1584 cells. These cells are operated in Geiger mode, where a reverse voltage is applied to the diodes, larger than the breakdown voltage, to initiate the avalanche process. When a photon strikes a cell, it triggers an electron-hole pair, and the electric field accelerates these carriers, leading to multiplication (avalanche) and generating an electric current. The process is quenched by the resistor to prevent it from becoming self-sustaining. The output signal at the SiPM anode that results from the triggering of a single cell is known as a photon-equivalent (PE) signal, and the number of triggered cells in a SiPM is referred to as the number of PEs. A set of PE signals from a UMD SiPM measured at the laboratory is displayed in the right panel of Fig. 3.12.

Modes of acquisition

In order to increase the dynamic range of the UMD, two complementary modes of operation are implemented in the modules: the *binary* mode (sometimes also known as *counter* mode) and the analog-to-digital converter (ADC) mode (sometimes also referred to as *integrator* or
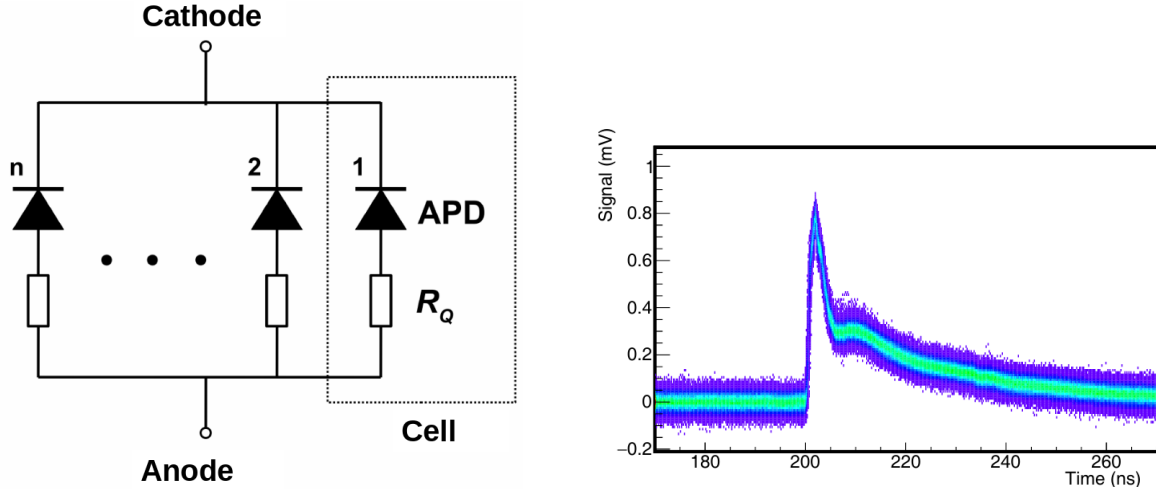
Figure 3.12: *Left*: Simplified scheme of a SiPM composed of *n* cells. Adapted from Ref. [57]. *Right*: Photo-equivalent signals measured at the laboratory. Taken from Ref. [54]

calorimetric mode). These modes operate simultaneously and measure the same particles. A schematic of the electronics chain of the two working modes can be found in Fig. 3.13.

The binary mode, designed for sampling low muon densities, relies on detector segmentation and processes each of the 64 SiPM signals independently. The output of each SiPM is processed by a dedicated channel in one of two 32-channel application-specific integrated circuits (ASICs), in this case, CITIROCs manufactured by WEEROC. A channel consists of a pre-amplifier, fast shaper, and discriminator, whose output signal is sampled at 320 MHz (3.125 ns sample time) with a Field-Programmable Gate Array (FPGA) into a 6.4 μs-long trace of 2048 bits. In each bit, a "1" or "0" is recorded depending on whether the discriminator signal was above or below the discriminator threshold, which is set at 2.5 PEs to reject most of the SiPM dark noise [58, 59]. Muons typically generate sequences of seven or eight consecutive"1"s in the trace, whereas detector noise ("1"s caused by spurious light emission in the scintillator or background particles) generate mostly patterns of three or fewer consecutive"1"s. Thus, muons in each bar are identified as a sequence of four or more consecutive "1"s, a condition known as *muon pattern* [59]. A simulated example of the response of one channel to a single muon is shown in the left panel of Fig. 3.14. The total number of bars exhibiting a muon pattern, *k*, is used to estimate the number of muons in each module and reconstruct the lateral distribution function of muons in this mode. In Chapter 4, we revisit the reconstruction procedure for this mode and propose new probabilistic models that extend and improve the existing likelihood to account for effects such as corner-clipping muons, detector noise, and inefficiency.

On the other hand, the ADC mode, designed for high muon densities, treats the module as a whole independent of detector segmentation. In this mode, the 64 SiPM signals are summed and subsequently amplified with high- and low-gain amplifiers. The amplified signals are digitized with two ADCs at a sampling time of 6.25 ns, producing two waveforms of 1024 samples. The number of muons is then obtained by dividing the charge of these signals by the mean charge of a single vertical muon. Although the ADC mode is not used to analyze and produce high-level physics results in this thesis, it is considered in Appendix I to analyze the overall long-term performance of the detector and validate its expected behavior regarding fiber attenuation.
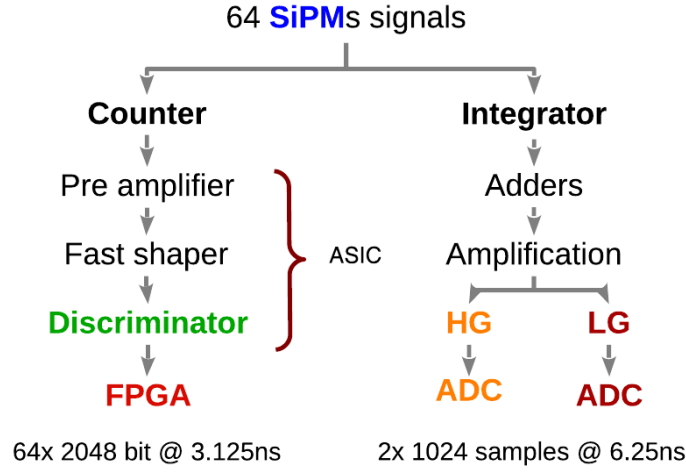
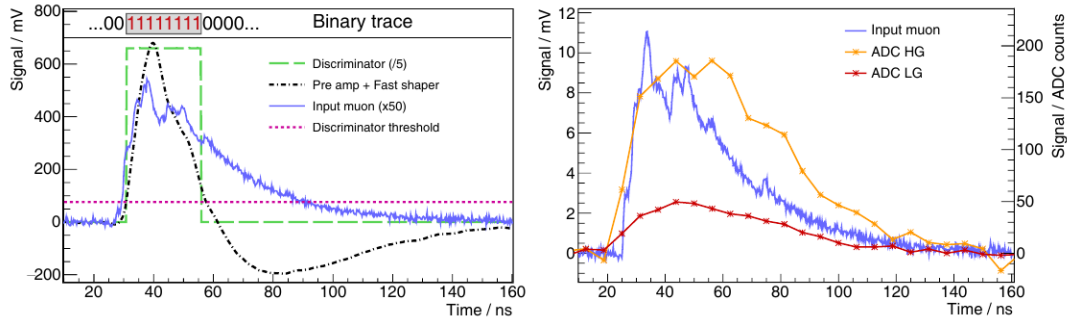**Figure 3.13:** Schematics of the electronics of the two acquisition modes of the UMD. From Ref. [54].

Figure 3.14: Simulated signal of a single-muon as seen by the binary (left) and ADC (right) mode. From Ref. [60].

Engineering array and current status

During the engineering array of the UMD, the muon detectors used multi-anode PMTs as photodetectors [61]. With this prototype, first physics results were published with one year of acquisition, spanning from October 2015 to October 2016, revealing a muon deficit within $10^{17.3}$ eV $< E < 10^{18.3}$ eV, ranging from 38% to 50% depending on the hadronic model used [62]. After several considerations, PMTs were replaced by SiPMs for the final design of the detector, as described above. Since then, UMD modules have been deployed in the SD-750 and SD-433 arrays at varying paces, with deployment still ongoing. Currently, the entire SD-433 array and half of the SD-750 array are fully operational with UMDs. The results obtained in this thesis with the final design of the UMD operating with SiPMs will be compared to those obtained with the engineering array in Section 7.7.

3.4 Summary

In this chapter, the main components of the Pierre Auger Observatory were introduced. The key aspects of the Surface Detector were discussed in Section 3.1, while those of the Fluorescence Detector were summarized in Section 3.2. The recent upgrade, known as AugerPrime, which aims to enhance the Observatory's sensitivity to the nuclear mass of primary particles,

was described in Section 3.3. The Underground Muon Detector, a central component of this thesis, was presented in greater detail in Section 3.3.4.

Chapter 4

Accounting for detector effects in the single-detector likelihood

A segmented detector like the UMD is affected by several factors that, if not accounted for, can bias the analysis of its signal. Such effects are pile-up, inefficiency, corner-clipping muons and detector noise.

Probability distributions to model the signals of a segmented detector, and the corresponding estimators of the number of muons, accounting only for pile-up, were developed in Refs. [63, 64]. In previous analyses of the UMD, the bias introduced in this estimators by the remaining effects, being the corner-clipping muons the most important, was parameterized with simulations to correct for them in data.

In this chapter, we extend the probability distributions of the signal of a segmented detector to take into consideration detector inefficiency, corner-clipping muons and detector noise. We do so by modeling each of these effects with easy probablistic models, which in turn depend on parameters that can be measured in the laboratory. In this way, the influence of the detector simulations in the data analysis is minimized while providing a transparent, easy-interpretable and more realistic model for the signal of a segmented detector.

This chapter is organized as follows: in Section 4.1 we present the probabilistic models and the necessary modifications to the existing likelihoods to account for detector inefficiency, noise, and corner-clipping muons. We additionally perform toy Monte-Carlo simulations to assess the accuracy of the new distributions and the performance of the new estimators. In Section 4.2, we discuss how to apply the formality derived in the previous section to the particular case of the Underground Muon Detector of the Pierre Auger Observatory. Finally, in Section 4.3, we compare two methods to calculate an uncertainty interval for the expected number of muons in a detector making use of the new likelihoods.

4.1 Single module likelihood

During an air shower event, several strips can be activated in a module. The number of activated strips k is the main raw observable from which an estimator of the number of impinging muons has to be constructed. At this point it is necessary to make a distinction between *expected* and *actual* number of impinging muons. A module of area A located at a shower plane distance r in an air shower event of zenith angle θ has a number of expected muons given by

$$\mu = \rho(r)A\cos(\theta), \tag{4.1}$$

where $\rho(r)$ is the muon lateral distribution function (MLDF) evaluated at r. The actual number of impinging muons N_μ in a given module fluctuates as a Poisson variable with parameter μ. Note that N_μ is an integer number, while μ is a real number. A probability distribution for the observable k can be related to N_μ or μ, depending on which parameter one is interested in estimating. In mathematical terms, we write $P(k|N_\mu)$ or $P(k|\mu)$, respectively. Obtaining such distributions is the first, fundamental step of any reconstruction procedure, as for a given measured k, they corresponds to the likelihood of the parameter N_μ or μ. We will refer to such distributions as the *single-module* or *single-detector likelihoods* .

In order to get an accurate distribution for k it is necessary to account for several effects that are characteristic of any segmented counter, such as

- **Pile-up**. This is caused by muons transversing the same scintillation bar in the event, leading to undercounting.

- **Corner-clipping muons**. These are inclined muons that activate two neighboring bars, leading to overcounting[1]. The activation of the bars can be produced by the same muon or by knock-on electrons generated by ionization of the soil as the muon travels though it. This source of bias is correlated with the shower geometry: inclined events are more affected by these muons than more vertical ones. Also, for a given zenith angle, the effect is larger for modules that are more perpendicular to the shower axis, see Fig. 4.1.

- **Detector inefficiency**. Some muons, especially those hitting far from the SiPM, may not produce enough photons to generate a muon pattern, giving rise to muon underestimation. From laboratory measurements, an efficiency of $\sim 98.5\%$ was established for a UMD scintillation bar [60].

- **Detector noise**. Even when no particles hit a strip, a muon pattern can be found in its binary trace. This is caused by the optical fiber-scintillation bar system, which can produce spontaneous light emission. Although the counting strategy defining a muon pattern was chosen to reject most of this noise, it is not possible to eliminate this irreducible source of background entirely [59]. However, the impact of this overcounting effect is rather small: a single strip has a probability of 0.1% of being activated by noise in a 6.4 μs trace, which translates into a probability of 5% of having one bar activated in a 64-strip module.

In the following sections, we will propose suitable probabilistic models to gradually include these effects until a final expression for $P(k|N_\mu)$ and $P(k|\mu)$ is achieved.

4.1.1 Pile-up

We start by considering only the pile-up effect, meaning that no corner-clipping muons are considered and a 100%-efficient, noise-free detector is assumed. Such idealized case was studied in Refs. [63–65]. For illustrative purposes, it is helpful to follow the analogy presented in Ref. [66], in which the problem of counting particles in a segmented detector is compared to a "ball in boxes" experiment. In this analogy, the balls represent the number of particles N_μ and the boxes the number of segments n_s (n_s=64 for the UMD modules). One experiment consists of assigning each ball (particle) a random box (segment). After one realization, each box can be either occupied (one or more ball inside, which corresponds to a strip with a muon pattern in its trace) or empty (no balls in the box, corresponding to a strip

---

[1]We note that a muon can pass through two neighboring bars but activate only one of them, or very rarely none. In this work, we use the term "corner-clipping" only to refer to muons that do activate adjacent bars.
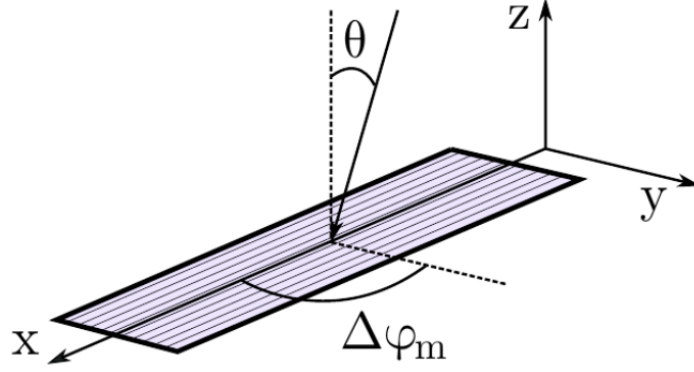
Figure 4.1: Geometry of the shower as seen by a UMD module.

with no pattern). The total number of occupied boxes then corresponds to the total number of segments on, k. Finally, we recall that N_μ is a realization of a Poisson experiment with mean μ.

Under these conditions, the probability distribution of k for a fixed N_μ was derived in Ref. [64]. The corresponding distribution for fixed μ was found in Ref. [63]. They are given by

$$P(k|N_\mu) = L(N_\mu) = \binom{n_s}{k} S(N_\mu, k) \frac{k!}{n_s^{N_\mu}} \tag{4.2}$$

$$P(k|\mu) = L(\mu) = \binom{n_s}{k} e^{-\mu} (e^{\mu/n_s} - 1)^k \tag{4.3}$$

where $S(N_\mu, k)$ is the Stirling number of second kind given by

$$S(N_\mu, k) = \frac{1}{k!} \sum_{j=0}^{k} \binom{k}{j} (-1)^k (k-j)^{N_\mu}.$$

For a given k, equations 4.2 and 4.3 represent the likelihood of N_μ and μ respectively. Thus, maximum likelihood estimators can be obtained by maximizing those expressions for fixed k. For μ we have

$$\hat{\mu} = -n_s \ln(1 - k/n_s). \tag{4.4}$$

For N_μ, no analytical expression can be obtained. A good approximation to the maximum likelihood estimator was obtained in Ref. [64]:

$$\hat{N}_\mu \cong \frac{\ln(1 - k/n_s)}{\ln(1 - 1/n_s)}. \tag{4.5}$$

Note that the two estimators are very similar as $-n_s \cong \frac{1}{\ln(1-1/n_s)}$. Also note that they are not defined for saturated modules ($k = n_s$).

It is interesting to analyze the expected bias for the estimators in this simple case. We consider here the case of $\hat{\mu}$ as an analytical expression is available. Furthermore, this is the more relevant case as it links the MLDF model (Eq. (4.1)) to the observed k, which is particularly important for MLDF fitting. However, we stress that the bias of $\hat{N}_\mu$ is qualitatively similar and all the conclusions extracted for $\hat{\mu}$ will be valid for $\hat{N}_\mu$ as well. We recall that the bias of an estimator is defined as

$$B[\hat{\mu}](\mu) = E[\hat{\mu}] - \mu, \tag{4.6}$$

where $E[\hat{\mu}]$ is the expected value of the estimator, given by

$$E[\hat{\mu}] = -n_s E[\ln(1 - k/n_s)], \tag{4.7}$$

and, in turn,

$$E[\ln(1 - k/n_s)] = \sum_{k=0}^{n_s-1} \ln(1 - k/n_s) \frac{P(k|\mu)}{C(\mu)} = h_{n_s}(\mu), \tag{4.8}$$

where $P(k|\mu)$ is given by Eq. (4.3) and $C(\mu) = \sum_{k=0}^{n_s-1} P(k|\mu)$ is a normalization factor so that $\frac{P(k|\mu)}{C(\mu)}$ adds to 1 in the range $0 \leq k \leq n_s - 1$. This is necessary since $\hat{\mu}$ is defined only up to $k = n_s - 1$ while $P(k|\mu)$ is defined up to $k = n_s$. In this way, calculation of the expected bias reduces to numerically computing $h_{n_s}(\mu)$. We can write Eq. (4.6) as

$$B(\mu) = -n_s h_{n_s}(\mu) - \mu. \tag{4.9}$$

The relative bias is given by

$$b(\mu) = B(\mu)/\mu = \frac{-n_s h_{n_s}(\mu) - \mu}{\mu}. \tag{4.10}$$

In Fig. 4.2 the relative bias is shown as function of μ for different number of segments n_s. It is important to highlight that the bias is never actually zero. The overall bias decreases as the number of segments increases. This is expected since an ideal Poisson counter, for which a null bias is awaited, can be thought as a segmented counter in the limit $n_s \to \infty$. For a fixed n_s, the qualitative behaviour of the bias is the same: the bias is minimum for small μ (more formally, when $\mu \ll n_s$), regime in which the segmented counter resembles the most to an ideal Poisson counter, and increases until it reaches a maximum at $\mu_{\max}$ (this maximum is not visible in the Figure for $n_s = 128$ and $n_s = 256$) above which it drops rapidly as the probability of saturation $P(k = n_s|\mu)$ becomes increasingly important.

Following the criterion adopted in Ref. [63], we define the saturation value μ_{sat} as the value of μ such that the probability of saturation is 0.01. Mathematically, $P(k = n_s|\mu_{\text{sat}}) = 0.01$, which yields

$$\mu_{sat} = -n_s \ln(1 - 0.01^{1/n_s}).$$

The saturation values for $n_s = 32$ and $n_s = 64$ are shown as vertical dashed lines in Fig. 4.2. Note that μ_{sat} is a proxy of $\mu_{\max}$. Naturally, μ_{sat} increases with n_s, which simply reflects the fact that a counter with more segments allows to measure larger values of μ before saturation.

From now on, unless explicitly stated, a segmentation of $n_s = 64$ will be assumed, since it corresponds to the UMD case. We will refer to this bias of the pile-up estimator as an *intrinsic* or *segmentation* bias, to stress that even in the most simple model of our detector, when no other sources of bias are considered, there is an irreducible bias in the estimators arising only from the segmentation of the detector.
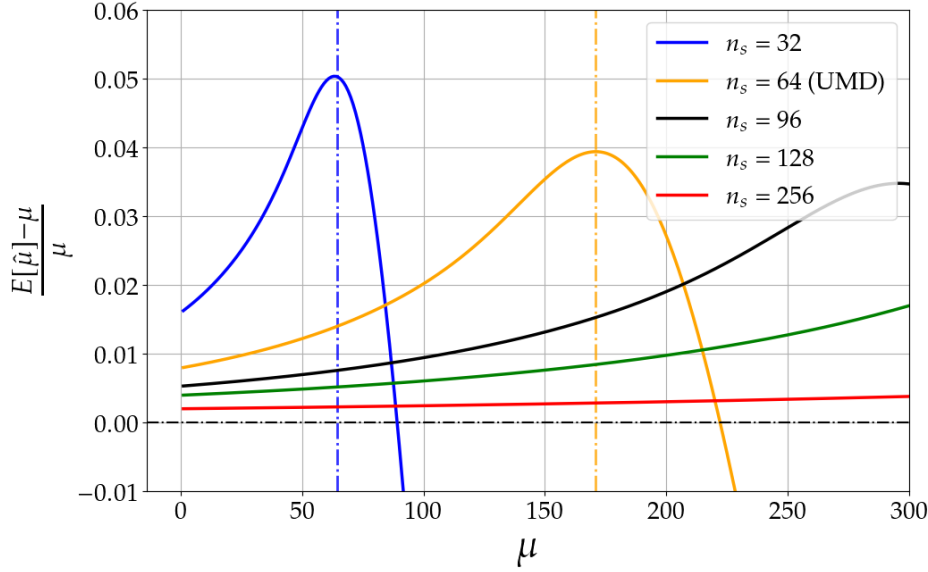
Figure 4.2: Relative bias of $\hat{\mu}$ (Eq. (4.10)) as a function of the true value μ for different segmentations n_s. Dashed vertical lines represent the saturation value (eq. 4.1.1).

4.1.2 Corner-clipping muons

The distributions of eqs. 4.2 and 4.3 were obtained under the assumption that each particle can activate only one strip. However, corner-clipping muons can activate two neighboring bars. In addition, a strip that was activated due to a corner-clipping muon can also be hit by a different muon during the event. In other words, corner-clipping signals can pile-up with "real", single-muon signals. Therefore, we can think that the overall result of the corner-clipping effect is to increase the number of effective particles. Following the "ball in boxes" analogy, whenever a module is affected by corner-clipping muons, we have an effective, larger number of balls to distribute in the boxes[2].

In order to account for this, we model the corner-clipping effect as a binomial process. This means that we assume that the number of muons that produce overcounting n_{cc} is a binomial variable with N_μ trials and p_{cc} success probability. Here, p_{cc} is the single-muon corner-clipping probability, namely, the probability of one muon to activate two neighboring bars. As discussed in Section 4.1, p_{cc} is expected to depend on the zenith angle of the shower and the relative orientation of the module wrt the shower axis[3], $p_{cc} = p_{cc}(\theta, \Delta\phi)$. In Chapter 5 we present a method to obtain p_{cc} in a data-driven way. The effective number of particles N_{eff} is then

$$N_{eff} = N_\mu + n_{cc}. \tag{4.11}$$

Since $N_\mu \sim \text{Poisson}(\mu)$, it follows that $n_{cc} \sim \text{Poisson}(\mu \times p_{cc})$ and $E[N_{eff}] = \mu(1 + p_{cc})$. We will assume $N_{eff} \sim \text{Poisson}(\mu_{eff})$ with $\mu_{eff} = \mu(1 + p_{cc})$. Although not formally true, since N_μ and n_{cc} are not independent, we will show that this assumption provides a simple working model for our purposes. We investigate the difference between this assumption and the true, more complicated distribution for N_{eff} in Appendix A. Thus, by making the substitutions

---

[2]Another way of thinking it is that the number of balls is not actually the number of particles, but the number of muon patterns, and now a muon is allowed to generate two muon patterns.

[3]More accurately would be to parameterize p_{cc} in terms of the zenith and the azimuth angles of the muon, θ_μ and ϕ_μ respectively. However, this information is not accesible in real data, so we make the approximation $\theta_\mu \sim \theta_{shower}$ and $\phi_\mu \sim \phi_{shower}$.

$$N_\mu \longrightarrow N_{\text{eff}}$$
$$\mu \longrightarrow \mu_{\text{eff}}, \tag{4.12}$$

the probability distributions of eqs. 4.2 and 4.3 can be modified to take into consideration the corner-clipping effect:

$$P(k|N_\mu) = L(N_\mu) = \sum_{n_{\text{cc}}=0}^{N_\mu} \binom{n_s}{k} S(N_\mu + n_{\text{cc}}, k) \frac{k!}{n_s^{N_\mu+n_{\text{cc}}}} \times P(n_{\text{cc}}) \tag{4.13}$$

$$P(k|\mu) = L(\mu) = \binom{n_s}{k} e^{-\mu(1+p_{\text{cc}})} \left(e^{\mu(1+p_{\text{cc}})/n_s} - 1 \right)^k, \tag{4.14}$$

where

$$P(n_{\text{cc}}) = \binom{N_\mu}{n_{\text{cc}}} p_{\text{cc}}^{n_{\text{cc}}} (1 - p_{\text{cc}})^{N_\mu - n_{\text{cc}}}$$

is the probability of having n_{cc} corner-clipping muons. Note that in the transition from Eq. (4.2) to Eq. (4.13) we need to weight for the probability of a given n_{cc}, $P(n_{\text{cc}})$, and to sum over all the possibilities, from no corner-clipping muons ($n_{\text{cc}} = 0$) to all of the muons producing overcounting ($n_{\text{cc}} = N_\mu$). The maximum likelihood estimator for μ is now given by

$$\hat{\mu} = \frac{-n_s}{1 + p_{\text{cc}}} \ln(1 - k/n_s). \tag{4.15}$$

Inspired in Eq. (4.15), the approximate estimator for N_μ of Eq. (4.5) is modified accordingly:

$$\hat{N}_\mu \cong \frac{1}{(1 + p_{\text{cc}})} \frac{\ln(1 - k/n_s)}{\ln(1 - 1/n_s)}. \tag{4.16}$$

The effect of incorporating p_{cc} is shown in Figs. 4.3 and 4.4. As visible in Fig. 4.3, when $p_{\text{cc}} \neq 0$, $P(k)$ is shifted towards larger values, meaning that when a module is affected by corner-clipping muons, a greater number of activated bars is expected. Naturally, this translates into the likelihoods, as depicted in Fig. 4.4: for the same number of observed activated bars, the estimators for N_μ and μ are displaced towards lower values when $p_{\text{cc}} \neq 0$.

In Fig. 4.5, the relative bias of the estimator $\hat{\mu}$ of eq. 4.15 is shown as function of μ for different p_{cc} values. It is apparent that the effect of the corner-clipping is to lower the maximum number of μ that can be sampled by the detector before saturation. In other words, μ_{sat} decreases with p_{cc}. Indeed, calculating μ_{sat} using eq. 4.14 now yields

$$\mu_{sat} = -\frac{n_s}{1 + p_{\text{cc}}} \ln(1 - 0.01^{1/n_s}). \tag{4.17}$$

4.1.3 Detector efficiency

A similar reasoning than the one presented in the previous section can be applied to take the detector inefficiency into account in the single-module likelihood. By including the detector inefficiency in the model, we allow a new possible outcome to the injection of a single muon in the detector. When a muon hits the detector, one out of three outcomes may occur: (i) it remains undetected with probability p_I, (ii) it produces overcounting with probability p_{cc} or (iii) it activates a single strip with probability $1 - p_I - p_{cc}$. Thus, when injecting N_μ muons,
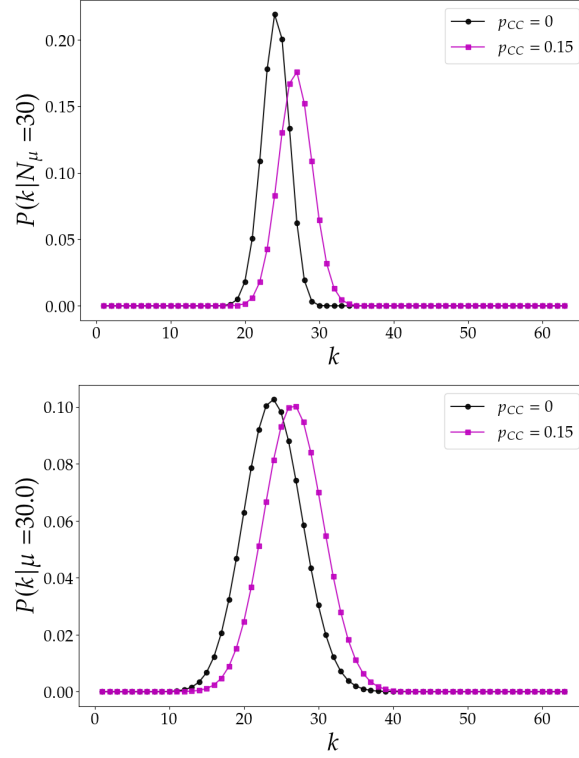
Figure 4.3: Probability distribution of k for $N_\mu = 30$ (left) and $\mu = 30$ (right). Black curves correspond to the case $p_{cc} = 0$ (eqs. 4.2 and 4.3) and magenta curves correspond to $p_{cc} = 0.15$ (eqs. 4.13 and 4.14).

the joint probability of having n_I undetected muons and n_{cc} corner-clipping muons is given by a multinomial distribution with N_μ trials

$$P(n_I, n_{cc}|N_\mu) = \frac{N_\mu!}{n_I! n_{cc}! (N_\mu - n_I - n_{cc})!} p_I^{n_I} p_{cc}^{n_{cc}} (1 - p_I - p_{cc})^{N_\mu - n_I - n_{cc}}. \tag{4.18}$$

The effective quantities are then

$$N_{\text{eff}} = N_\mu + n_{cc} - n_I$$
$$\mu_{\text{eff}} = \mu(1 + p_{cc} - p_I),$$

which leads to the following distributions

$$P(k|N_\mu) = L(N_\mu) = \sum_{n_I, n_{cc}} \binom{n_s}{k} S(N_\mu + n_{cc} - n_I, k) \frac{k!}{n_s^{N_\mu + n_{cc} - n_I}} \times P(n_I, n_{cc}|N_\mu) \tag{4.19}$$

$$P(k|\mu) = L(\mu) = \binom{n_s}{k} e^{-\mu(1 + p_{cc} - p_I)} \left(e^{\mu(1 + p_{cc} - p_I)/n_s} - 1\right)^k, \tag{4.20}$$

where the sum in Eq. (4.19) goes over all (n_I, n_{cc}) such that $n_I + n_{cc} \leq N_\mu$. The maximum likelihood estimators are obtained by making the substitution $(1 + p_{cc}) \longrightarrow (1 + p_{cc} - p_I)$ in Eqs. 4.15 and 4.16:
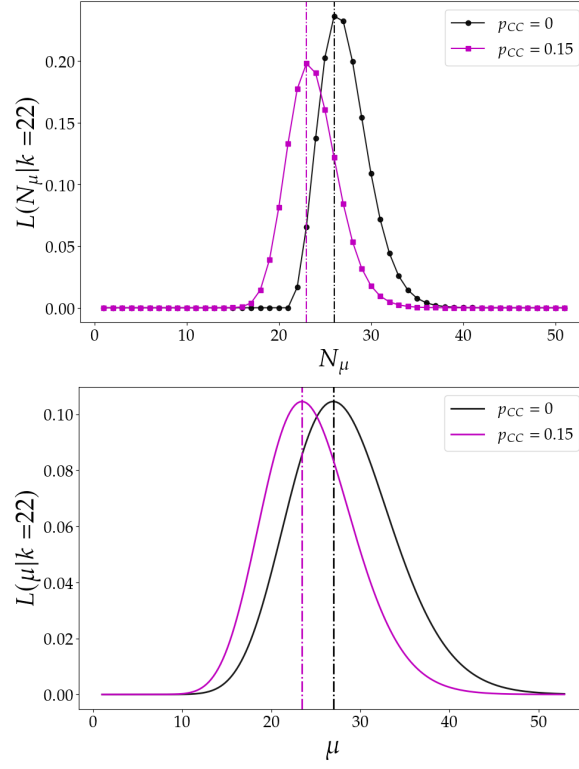
Figure 4.4: Likelihood of N_μ (*left*) and μ (*right*) for an observed value of $k = 22$. Black curves correspond to the case $p_{cc} = 0$ (eqs. 4.2 and 4.3) and magenta curves correspond to $p_{cc} = 0.15$ (eqs. 4.13 and 4.14). Dashed lines are the corresponding maximum likelihood estimators.
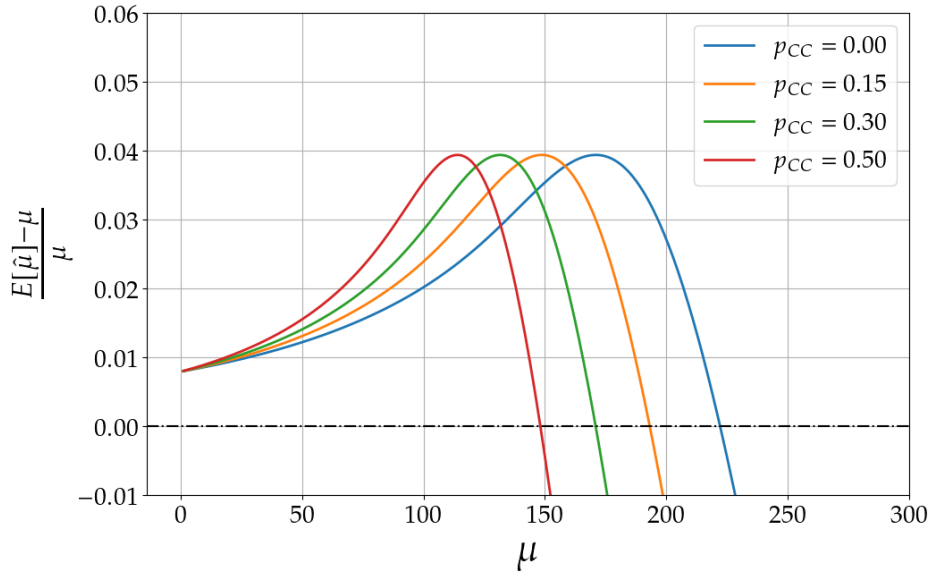

Figure 4.5: Relative bias of $\hat{\mu}$ as a function of the true value μ for different p_{cc} values.

$$\hat{\mu} = \frac{-n_s}{1 + p_{cc} - p_I} \ln(1 - k/n_s) \tag{4.21}$$

$$\hat{N}_\mu = \frac{1}{(1 + p_{cc} - p_I)} \frac{\ln(1 - k/n_s)}{\ln(1 - 1/n_s)}. \tag{4.22}$$

Note that if $p_I = 0$, the distributions and estimators obtained in the previous section are recovered. In order to test the validity of the distributions of Eqs. 4.19 and 4.20, and the perfomance of the estimators of Eqs. 4.21 and 4.22, a toy Monte-Carlo experiment was performed. It consisted of the following steps:

- For testing Eq. (4.20) and Eq. (4.21) we consider a fixed μ, and the number of muons N_μ was sampled from a Poisson distribution with parameter μ. To test Eq. (4.19) and Eq. (4.22), N_μ was fixed.

- The number of corner-clipping and undetected muons, n_I and n_{cc}, were sampled from the multinomial distribution of Eq. (4.18). The number of muons that activated a single bar is given by $n_1 = N_\mu - n_I - n_{cc}$.

- For each of the $n_1 + n_{cc}$ muons, a strip was assigned by sampling a random integer between 1 and 64.

- For each of the n_{cc} muons, a neighboring strip was randomly chosen. If the initial strip was in a border of the detector (strips 1, 32, 33 or 64), only one neighboring bar is available and the possibility of not activating a bar was taken into account.

- Finally, the total number of bars k is obtained and Eqs. 4.21 and 4.22 can be evaluated and compared to the true μ or N_μ, respectively.

This procedure was repeated 10000 times for various values of μ and N_μ.

In Fig. 4.6 the distribution of k obtained by the Monte-Carlo simulation for several N_μ values is compared to Eq. (4.19) for $p_I = 2\%$ and $p_{cc} = \{0\%, 15\%\}$. As discussed later, these correspond to realistic values for the UMD. The same comparison is observed using an extreme (unrealistic) value of $p_I = 80\%$ in Fig. 4.7, only for the purpose of testing the model in a different region of the phase space. In all cases, a perfect agreement between the simulation and the expected distribution is observed.

The same analysis for various values of μ can be found in Figs. 4.8 and 4.9. A very good agreement between the simulation and Eq. (4.20) for all μ is seen in Fig. 4.8. For the extreme case of $p_I = 80\%$, some discrepancy between the model and the Monte-Carlo experiment is observed when $p_{cc} \neq 0$, particularly for small values of μ (lower panel of Fig. 4.9). The fact that this discepancy exists for the distributions of μ and not for N_μ is due to the distribution of Eq. (4.19) being exact[4]. As mentioned in the previous section, for Eq. (4.20) to be exact, N_{eff} needs to be Poissonian with mean μ_{eff}, which is not formally true (see Appendix A). Nevertheless, we stress that for realistic values of p_I and p_{cc} for the UMD this proves to be a useful model.

Interestingly, when $p_{cc} = 0$ (upper panel of Fig. 4.9), a perfect agreement between the simulation and the expected distribution is apparent. It can be shown that in this particular case, N_{eff} do follow a Poisson distribution with parameter $\mu(1 - p_I)$ and therefore Eq. (4.20) is exact. More generally: if $N \sim \text{Poiss}(\mu)$ and $K \sim \text{Binom}(n = N, p)$, then $M_- = N - K \sim \text{Poiss}(\mu(1 - p))$ but $M_+ = M + K \not\sim \text{Poiss}(\mu(1 + p))$, which explains why when $p_{cc} = 0$ Eq. (4.20) is exact but when $p_I = 0$ and $p_{cc} \neq 0$ is not. See Appendix A for details.

The relative bias of the estimator of Eq. (4.21) as function of μ obtained in the simulation is displayed in Fig. 4.10. The bias gradually increases with μ until a maximum around $\sim 5\%$ is reached, above which the bias monotonically decreases due to detector saturation, as expected according to what was dicussed in Section 4.1.1. Also corresponding to expectations,

---

[4]A priori, the only difference between the distibution and the simulation in this case may arise only from border effects since strips in the edges only posses one neighbor. This effect is taken into account in the simulation but not in the model. This however proves to be negligible considering the excellent agreement between the model and the Monte-Carlo experiment.
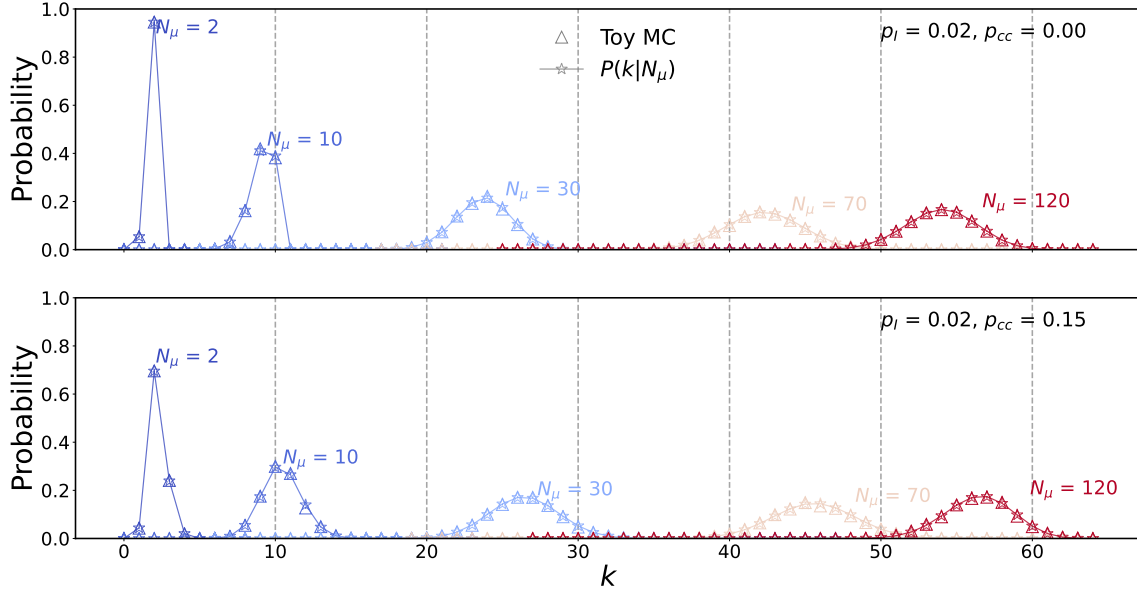
Figure 4.6: Distribution of the number of triggered bars k with $p_I = 2\%$ for different N_μ as obtained by the toy Monte-Carlo experiment and by Eq. (4.19). Upper plot corresponds to $p_{cc} = 0$ and lower to $p_{cc} = 15\%$.

Figure 4.7: Distribution of the number of triggered bars k with $p_I = 80\%$ for different N_μ as obtained by the toy Monte-Carlo experiment and by Eq. (4.19). Upper plot corresponds to $p_{cc} = 0$ and lower to $p_{cc} = 15\%$.
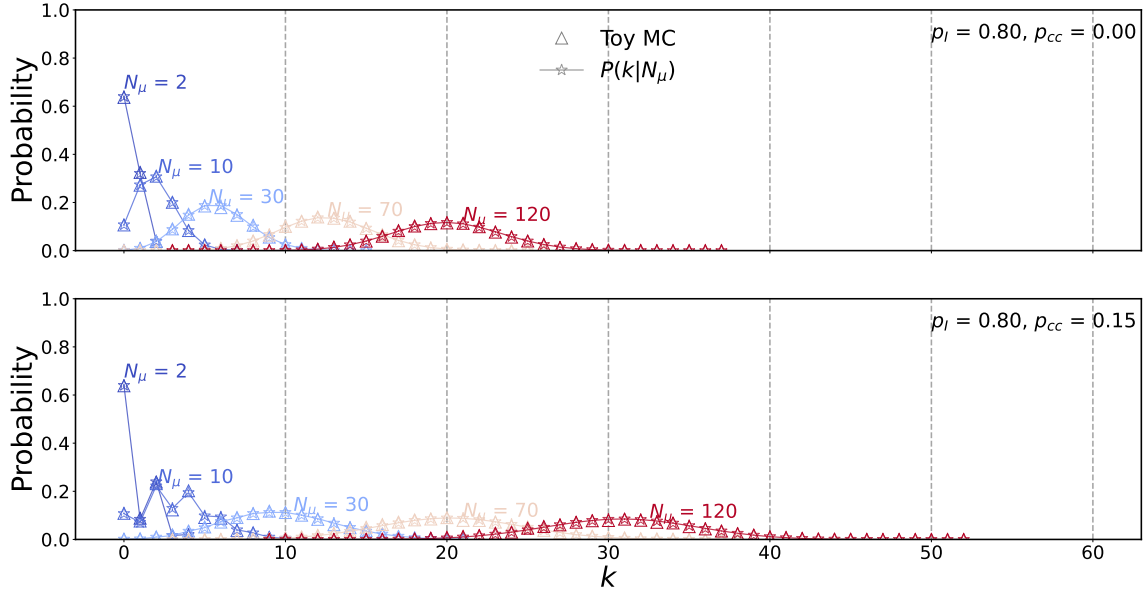
the effect of having $p_{cc} \neq 0$ is to shift this maximum towards smaller values of μ. In Fig. 4.11, the same analysis for Eq. (4.22) is presented, showing the same behaviour.

4.1.4 Detector noise

As mentioned in Section 4.1, a muon pattern can be found in the binary trace of a strip in the absence of particles. This phenomenom, leading to overcounting, is produced by
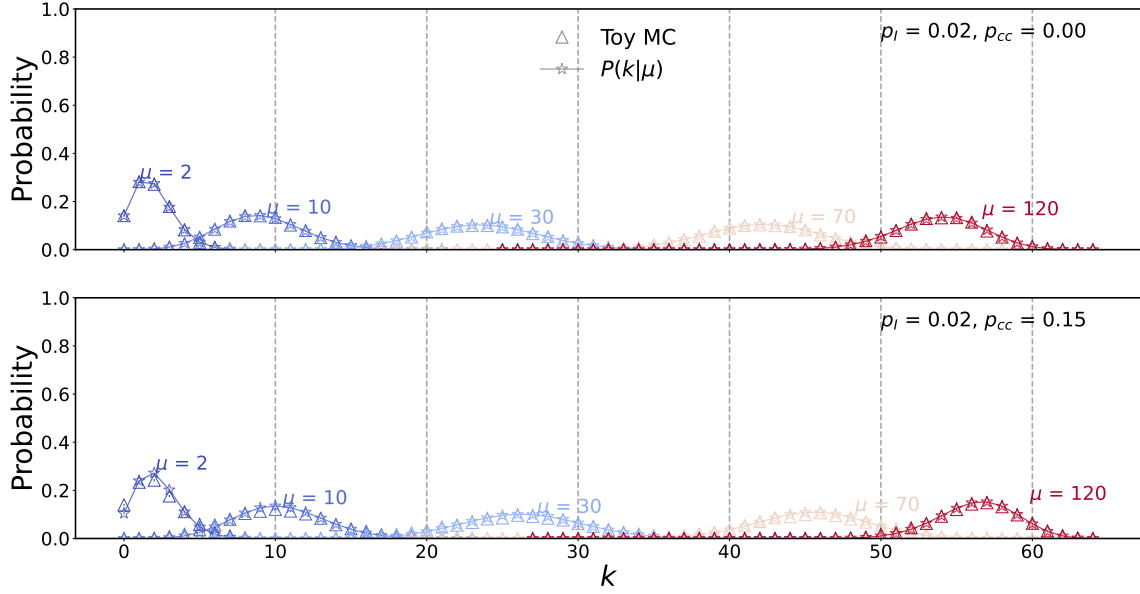
Figure 4.8: Distribution of the number of triggered bars k with $p_I = 2\%$ for different μ as obtained by the toy Monte-Carlo experiment and by Eq. (4.20). Upper plot corresponds to $p_{cc} = 0$ and lower to $p_{cc} = 15\%$.

Figure 4.9: Distribution of the number of triggered bars k with $p_I = 80\%$ for different μ as obtained by the toy Monte-Carlo experiment and by Eq. (4.20). Upper plot corresponds to $p_{cc} = 0$ and lower to $p_{cc} = 15\%$.
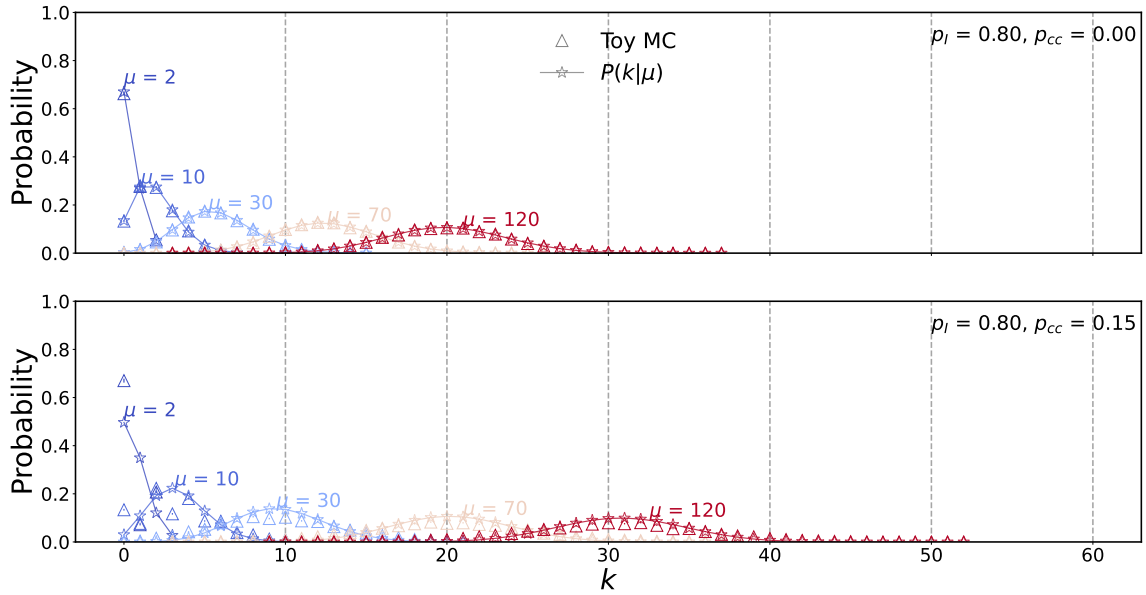
spontaneous light emission in the scintillator-fiber system and constitutes an irreducible source of background noise.

A strip that was activated due to noise can subsequently be activated by a muon. In other words, a noise signal can pile up with single-muon signals. Hence, we can treat this effect as increasing the number of effective particles to be distributed in the segments of the detector. We can write the number of effective particles as

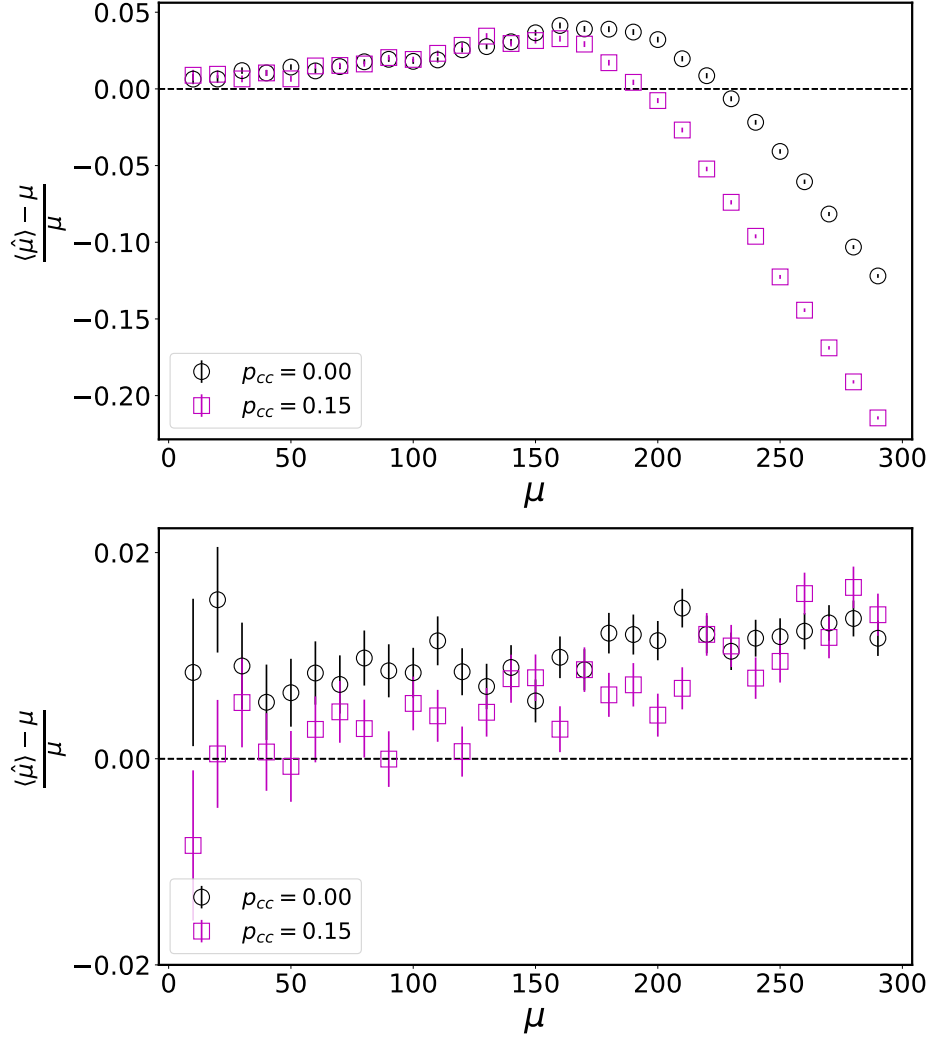$$N_{\text{eff}} = N_\mu + n_{\text{cc}} - n_{\text{I}} + n_0,$$

Figure 4.10: Bias of estimator of Eq. (4.21) as function of μ for $p_{cc} = \{0\%, 15\%\}$. The upper pannel corresponds to $p_I = 2\%$ and the lower to $p_I = 80\%$.

where n_0 is the number of bars activated due to noise in the detector during the event.

Defining the noise probability p_n as the probability of a single strip to have a muon pattern produced by noise in a 6.4 μs-long trace, it follows that n_0 follows a binomial distribution with n_s trials and p_n success probability. For $P(k|N_\mu)$ we can write:

$$P(k|N_\mu) = \sum_{n_0=0}^{n_s} \sum_{n_I, n_{cc}} \binom{n_s}{k} S(N_\mu + n_{cc} - n_I + n_0, k) \frac{k!}{n_s^{N_\mu + n_{cc} - n_I + n_0}} P(n_I, n_{cc}|N_\mu)P(n_0). \quad (4.23)$$

We note that n_0 is fundamentally different than the previous cases as it does not correlates with N_μ: even when $N_\mu = 0$, and hence $n_{cc} = n_I = 0$, n_0 can be non-zero. This implies that $P(k|N_\mu = 0) = P(k|\mu = 0) = \text{Binom}(n_s, p_n)$. Furthermore, for this reason, there is no μ_{eff} such that the substitution $\mu \longrightarrow \mu_{\text{eff}}$ leads to $P(k|\mu)$. Thus, a different strategy needs to be considered.

To derive a distribution for a fixed μ, it is necessary to follow the reasoning in Ref. [63] that allowed to obtain Eq. (4.3). For this purpose, we consider $p_{cc} = p_I = 0$ as they can be straightforwardly included later by substituing $\mu \longrightarrow \mu(1 + p_{cc} - p_I)$.
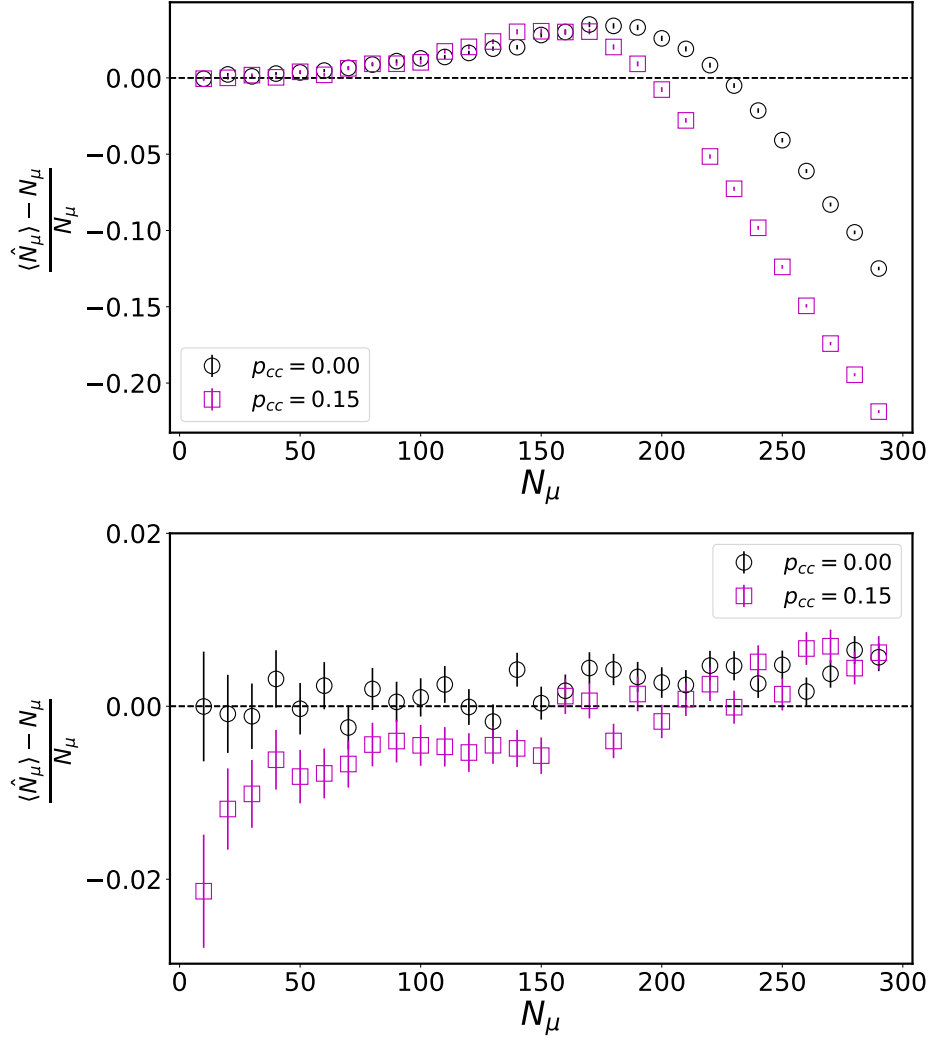
Figure 4.11: Bias of estimator of Eq. (4.22) as function of N_μ for $p_{cc} = \{0\%, 15\%\}$. The upper pannel corresponds to $p_I = 2\%$ and the lower to $p_I = 80\%$.

Since the number of muons impinging in the detector fluctuates as a Poisson with parameter μ, the number of muons m hitting a single bar fluctuates as a Poisson with mean μ/n_s. Thus, the probability of a single bar to be hit by one or more muons is given by $p_\mu = P(m \geq 1) = 1 - P(m = 0) = 1 - e^{-\mu/n_s}$. If we assume a perfectly efficient detector, then p_μ constitutes the success probability of a bar to be activated by muons in an event. Therefore, $P(k|\mu) = \text{Binom}(n_s, p_\mu)$, which leads to Eq. (4.3).

In addition to being hit by muons, a bar can be activated due to noise. Consequently, $p = p(\text{muons}) + p(\text{noise}) - p(\text{muons and noise}) = p_\mu + p_n - p_\mu p_n = (1 - e^{-\mu/n_s})(1 - p_n) + p_n$. Therefore,

$$P(k|\mu) = L(\mu) = \text{Binom}(n_s, (1 - e^{-\mu/n_s})(1 - p_n) + p_n). \tag{4.24}$$

We note that, as expected, $P(k|\mu = 0) = \text{Binom}(n_s, p_n)$.
The new maximum likelihood estimator is given by

$$\hat{\mu} = \begin{cases} 0 & k \leq n_s\, p_n \\ -\frac{n_s}{1 + p_{cc} - p_I} \ln\left(1 - \frac{k/n_s - p_n}{1 - p_n}\right) & n_s\, p_n \leq k < n_s \end{cases} \tag{4.25}$$
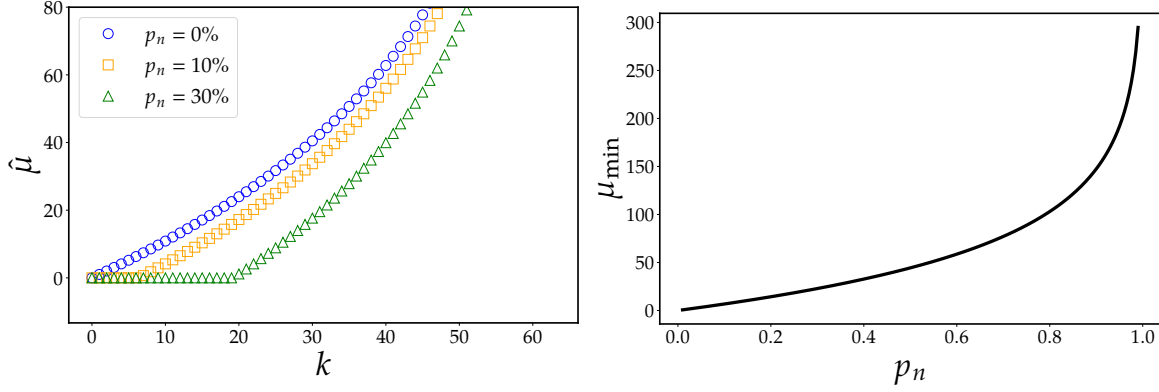
Figure 4.12: *Left*: Maximum likelihood estimator for μ as function of k for different noise probabilities. *Right*: $\mu_{\min}$ as function of p_n. In all cases, $p_{cc} = p_I = 0$.

where we have included p_I and p_{cc}. We observe that when $p_n = 0$ the previous estimator is recovered. The expression for $\hat{N}_\mu$ is obtained by replacing $-n_s \longrightarrow 1/(\ln(1 - 1/n_s))$ in Eq. (4.25).

We note that there is a $k_{\min} = n_s\, p_n$ such that if $k \leq k_{\min}$ then $\hat{\mu} = 0$. This is necessary to be explicitly written in Eq. (4.25) because otherwise would yield $\hat{\mu} < 0$. It is relevant to highlight that $k_{\min}$ is the expected value of the noise distribution $\text{Binom}(n_s, p_n)$. In other words, if k is less than the expected number of activated bars due to noise, nothing can be said about μ. Therefore, the consequence of including the detector noise in the model is the appearance of a detection limit $\mu_{\min}$. A criteria based on the probability of activating $k > k_{\min}$ only due to muons can be adopted to define a minimum value $\mu_{\min}$ that can be measured by the detector. We define such criteria by requesting the probability of activating a single bar due to muons to be larger than due to noise, i.e., $p_\mu > p_n$. Thus, we define $\mu_{\min}$ in the limiting case $p_\mu|_{\mu_{\min}} = p_n$. We obtain

$$\mu_{\min} = -\frac{n_s}{1 + p_{cc} - p_I} \ln(1 - p_n). \tag{4.26}$$

In the left panel of Fig. 4.12, the estimator of Eq. (4.25) as function of k for different values of p_n is displayed, in which the increasing behaviour of $k_{\min}$ with p_n is apparent. The minimum $\mu_{\min}$ as function of p_n is shown in the right panel of the same Figure.

To assess the accuracy of the distributions of 4.23 and 4.24, a new step was added to the Monte-Carlo simulation described in Section 4.1.3. It consisted of sampling the number of bars activated due to noise n_0 from a binomial distribution with n_s trials and p_n probability. Then, a random integer for each of the n_0 bars was assigned to obtain the strip id. In Fig. 4.13, the distributions of Eqs. 4.23 and 4.24 are compared to the simulation results for $p_n = \{0\%, 10\%\}$ and various values of N_μ. In order to focus on the impact of p_n, p_I and p_{cc} were set to 0. The agreement between the simulation and the model is evident. As expected, for a fixed N_μ, the distribution is shifted towars larger values of k when $p_n \neq 0$. The same analysis for μ is displayed in Fig. 4.14, leading to the same conclusions.

Lastly, the bias of the estimator of Eq. (4.25) as function of μ is shown for different values of p_n in Fig. 4.15. Again, the values of p_I and p_{cc} were set to 0 to study the influence of p_n alone. Vertical arrows show the corresponding $\mu_{\min}$ for each p_n. A new feature is visible, namely, an increase in the bias for $\mu < \mu_{\min}$. As already discussed, the detector becomes insensitive to μ below this limit.
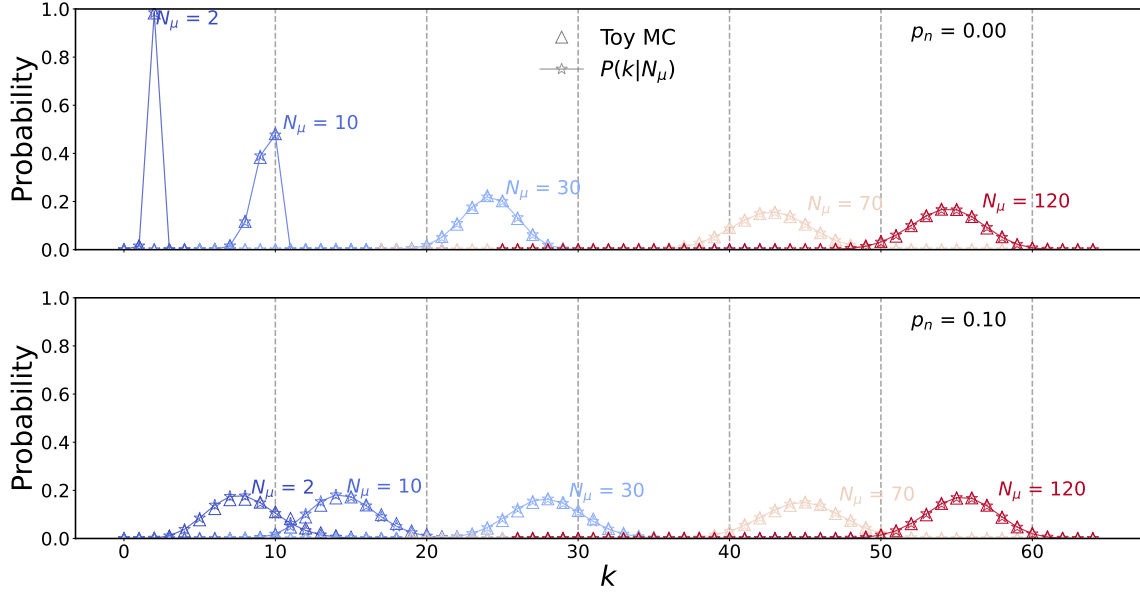
Figure 4.13: Distribution of the number of triggered bars k as obtained by the Monte-Carlo simulation and by Eq. (4.23) for $p_n = 0\%$ (upper panel) and $p_n = 10\%$ (lower pannel). In both cases, $p_{cc} = p_I = 0$.

Figure 4.14: Distribution of the number of triggered bars k as obtained by the Monte-Carlo simulation and by Eq. (4.24) for $p_n = 0\%$ (upper panel) and $p_n = 10\%$ (lower pannel). In both cases, $p_{cc} = p_I = 0$.
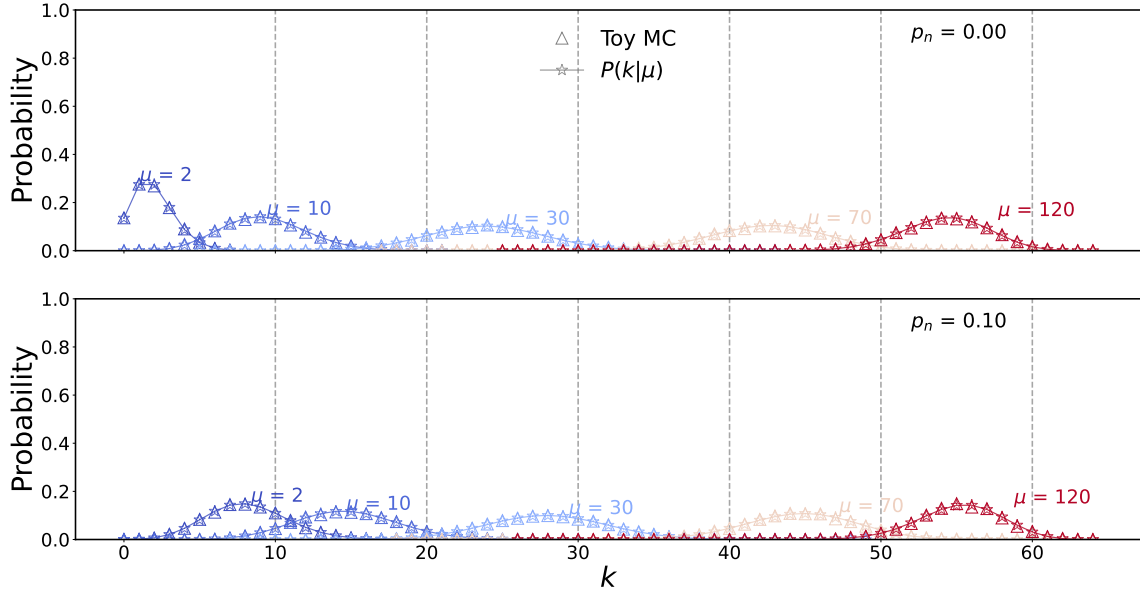
4.2 Application to the UMD case

In the preceding sections, the detector inefficiency, corner-clipping muons and detector noise were included in the single-module likelihood. The key idea was to treat these effects as increasing or decreasing the number of effective particles in the detector. In this way, the distributions and estimators derived in Refs. [63, 64] for an idealized 100% efficient, noise-free detector that is not affected by corner-clipping muons, could be extended to include these effects.
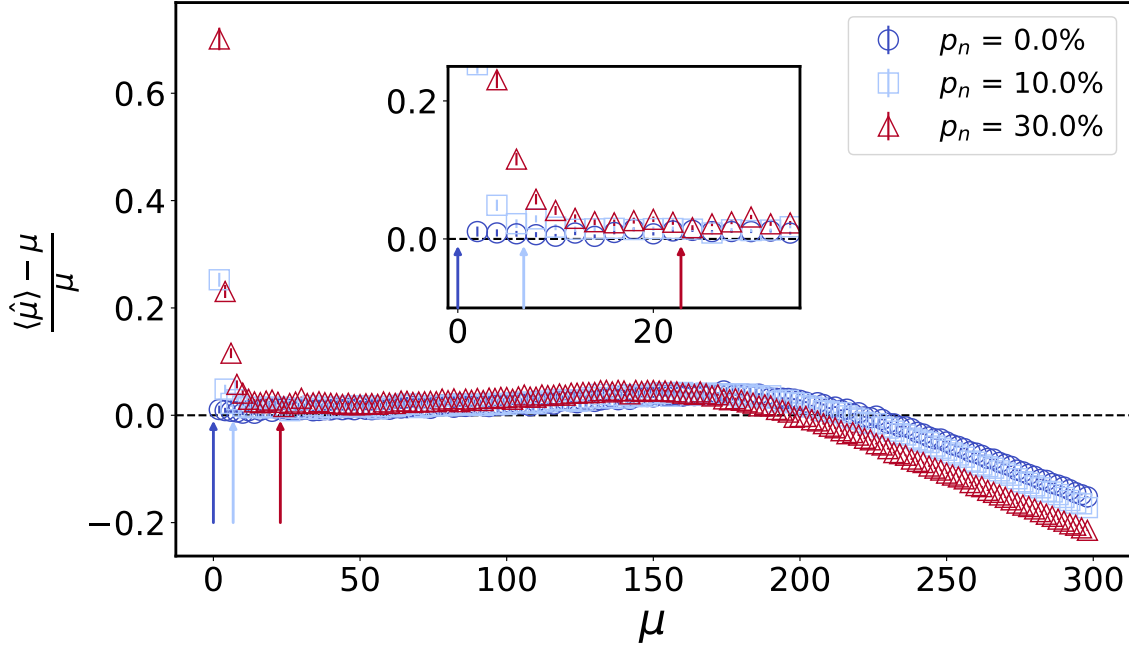
Figure 4.15: Bias of $\hat{\mu}$ (Eq. (4.25)) as function of μ for different p_n values obtained by the Monte-Carlo simulation. Vertical arrows indicate the minimum μ (Eq. (4.26)) for each p_n. Values of p_{cc} and p_I were set to 0.

It is relevant to stress that all the formality derived is generally valid to any kind of segmented detector. The only ingredients that are needed are the single-particle inefficiency and corner-clipping probability, p_I and p_{cc} respectively, and the detector noise probability p_n. We highlight that all these probabilities can be measured in the laboratory. For instance, p_I and p_{cc} could be obtained by using a muon telescope to trigger the acquisition in the detector. Thus, the probabilities could be computed using the fraction of muon triggers that were followed by the activation of 0, 1 or 2 (neighboring) bars. Furthermore, if the telescope is able to reconstruct the trajectory of the muon, the dependence of these probabilites with the zenith angle of the muon could be determined.

For the UMD, the efficiency of a single bar[5] for mostly vertical muons was found to be $\sim 98.5\%$ [60]. Due to the increased track length, the efficiency is expected to be further increased for more inclined muons. Therefore, we neglect this effect and use $p_I = 0\%$.

For the p_{cc}, there is no measurement available. We present in Chapter 5 a data-driven way to estimate this probability.

The detector noise was charaterized during the development phase of the UMD. However, the value of p_n for the UMD is not reported directly. Instead, in Ref. [59], it is reported that the probability of activating only one bar in a module due to noise is 5%. Therefore, we can obtain p_n by requesting $\text{Binom}_{k=1}(n_s, p_n) = 5\%$, which yields $p_n = 0.1\%$. Such a small value leads to a very small correction in the likelihood and in the estimators. Thus, for practical purposes, we set $p_n = 0\%$.

Considering these approximations, the expressions that will be used from now on for the likelihoods and estimators are reduced to the ones derived in Section 4.1.2.

---

[5]We note that this is not strictly what is assumed in the model we developed as this measurement was done with a single bar. However, the value obtained for the efficiency with this setup is large enough to reasonably assume that a muon injected in the detector would very rarely activate zero bars.
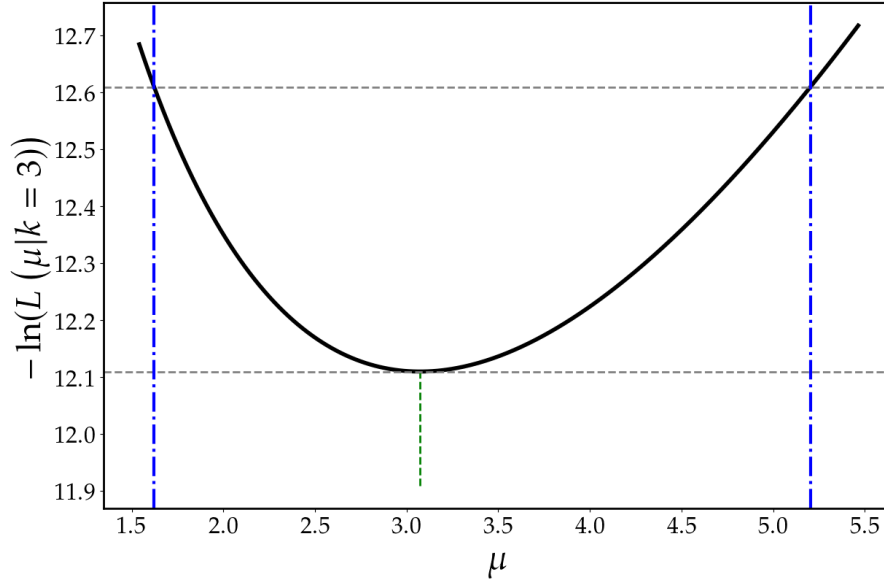
Figure 4.16: Graphical representation of the procedure to obtain the 1σ interval for μ for a measured $k = 3$ and $p_{cc} = 0$. Horizontal grey dashed lines correspond to the l_{min} and $l_{min} + 0.5$ levels. Vertical blue lines denote the interval obtained by the method. $\hat{\mu}$ is represented by a green dashed line.

4.3 Error estimation of μ

In Section 4.1.2, modified likelihoods were proposed to account for the corner-clipping effect which lead to new maximum likelihood estimators both for N_μ and μ, given by Eqs. 4.16 and 4.15, respectively. In this section, we deal with the task of determining an uncertainty interval to the point estimation of μ. We focus only on μ as its asociated likelihood Eq. (4.14), which is needed for the interval estimation, already accounts for sampling Poissonian fluctuations by construction.

A common practice is to provide an interval with 68.2% confidence level, usually referred as a 1σ interval in analogy to the gaussian case. Two recipies to construct a 1σ confidence interval for μ were tested, namely the log-likelihood contour (LLC) and the Feldman-Cousins (FC) procedure.

The LLC procedure to obtain a $n\sigma$ interval consists in finding the (μ_1, μ_2) interval such that $l_{min} + \frac{n^2}{2} = -\ln(L(\hat{\mu})) + \frac{n^2}{2}$. As a consequence of the Wilks theorem, it can be shown that in the limit of a large sample the coverage of such an interval tends to the desired confidence level (e.g. 68.2%, 95%, 99% for $n = 1, 2, 3$, respectively, also in analogy to the Gaussian case). An example of the procedure to obtain the 1σ interval for a measured value of $k = 3$ and $p_{cc} = 0$ is shown in Fig. 4.16. The resuling interval is denoted by vertical blue dashed-dotted lines and corresponds to $(\mu_1, \mu_2) = (1.6, 5.2)$. It is important to note that for $1 \le k \le 63$, the interval provided by this recipe is assymetric and one would typically report $\hat{\mu}_{\sigma_-}^{\sigma_+}$ after a measured k, where $\sigma_+ = \mu_2 - \hat{\mu}$ and $\sigma_- = \hat{\mu} - \mu_1$.

Special care should be taken when $k = 0$ or $k = 64$. For the former case, $\hat{\mu} = 0$ and the log-likelihood is $l(\mu|k = 0) = \mu$, thus leading to an interval $(0, 0.5)$. Note that since $\mu > 0$, only an upper limit can be provided in this case. As we will see next, this interval is not optimal as it does not provides the correct coverage. For the saturated case $k = 64$, the log-likelihood does not reaches a minimum and only a lower limit to μ can be established [63].

The FC method is built upon the Neyman's construction to find confidence intervals [67]. The Neyman's procedure is considered the most robust way of finding confidence intervals as it assures the right coverage by construction, usually at the cost of being computationally expensive. For a discrete variable, like in our case, it assures that the coverage is equal or greater than the desired confidence level. However, the Neyman's construction has a degree of freedom as it does not unambiguously leads to an interval, so a criteria must be adopted by the experimenter. Depending on the chosen criteria, different intervals with the same coverage can be obtained given the same measurement. Feldman and Cousins proposed a criteria based on the likelihood ratio of the measurements and it has become a standard in the High-Energy Physics community since its publication. For a description of the procedure, see the original publication, Ref [68]. More details on the implementation of the method to our particular problem can be found in Appendix C.

In the left panel of Fig. 4.17, the maximum likelihood estimator $\hat{\mu}$ (Eq. (4.4)) for each k can be found. The 1σ interval given by the LLC (FC) method is displayed with blue (magenta) full (dashed) lines and triangle (square) markers. The ratio between the length of the two intervals is shown on the right panel of the same Figure. The FC intervals are always larger than the ones given by the LLC method in order to assure a coverage equal or larger than the desired 68.2%.

A toy Monte-Carlo experiment was performed to assess the coverage of the intervals. For the FC case, this only provides a sanity check as the method guarantees equal or larger coverages than the desired one by construction[6]. For the LLC intervals, however, the desired coverage is only guaranteed in the large sample limit, so this toy experiment serves to know its true performance. One experiment consisted on generating 10000 random k values for a fixed μ usinq Eq. (4.14) with $p_{cc} = 0$. For each generated k, the corresponding μ interval was computed. Finally, the coverage is obtained as the fraction of times this interval contained the true value of μ. This scheme was repeated for $0.1 \leq \mu \leq 10$ with a step of $\Delta\mu = 0.1$ and for $10 \leq \mu \leq 200$ with a step of $\Delta\mu = 1$.

The calculated coverages as function of μ are shown in Fig. 4.18, in which the typical pattern of monotonous behaviour interrupted by abrupt discontinuities characteristic of intervals constructed with discrete variables is visible. It is apparent that the FC intervals have always larger or equal coverage than the nominal 68.2% (marked as a horizontal dashed line) as expected, while the LLC values fluctuates around this value. In the inset plot a zoom to small values of μ is shown. For the smallest values of μ, namely $\mu < 0.4$, the LLC intervals show a large coverage compatible with the FC intervals. This can be explained by the fact that for these μ, the most likely outcome is to have $k = 0$ and therefore the LLC interval $(0, 0.5)$ contains the true μ the vast majority of the trials. When $\mu > 0.5$, the LLC does not contain anymore the true μ although $k = 0$ remains the most probably outcome, causing the abrupt drop in the coverage to values below 50%. As μ increases, positive values of k becomes increasingly likely (and $k = 0$ increasingly unlikely) and the impact of this undesired behaviour of the LLC interval for $k = 0$ vanishes, leading to reasonable coverages around 68.2%.

The error estimation of μ has to be computed for each UMD module in the event during runtime in the reconstruction chain of the UMD in Offline . If there were no corner-clipping (i.e., $p_{cc} = 0$), the FC intervals could be computed beforehand for each of the 64 possible values of k and stored in a look-up table, thus avoiding its costly calculation during runtime. Unfortunately, since $p_{cc} \neq 0$, the single-module likelihood depends both on k and on the arrival the direction (θ, ϕ) of the shower, so the uncertainty interval needs to be unavoidably computed during runtime. In a trade-off between reasonable computing time and coverage

---

[6]The true coverage can also be analitically calculated during the construction of the intervals, so the toy Monte-Carlo results can be compared to this as well, see Appendix C
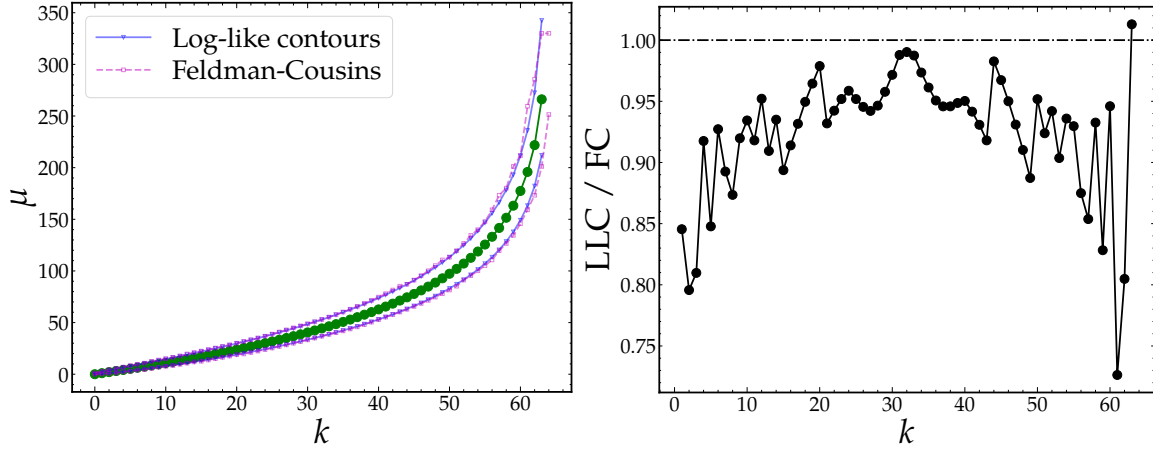
Figure 4.17: *Left:* Maximum likelihood estimator $\hat{\mu}$ (green markers) and 1σ intervals obtained by the LLC (blue triangles) and the FC (magenta squares) methods for each possible value of k. *Right:* Quotient between the lenghts of the FC and LLC intervals. Horizontal dashed line marks the unity.
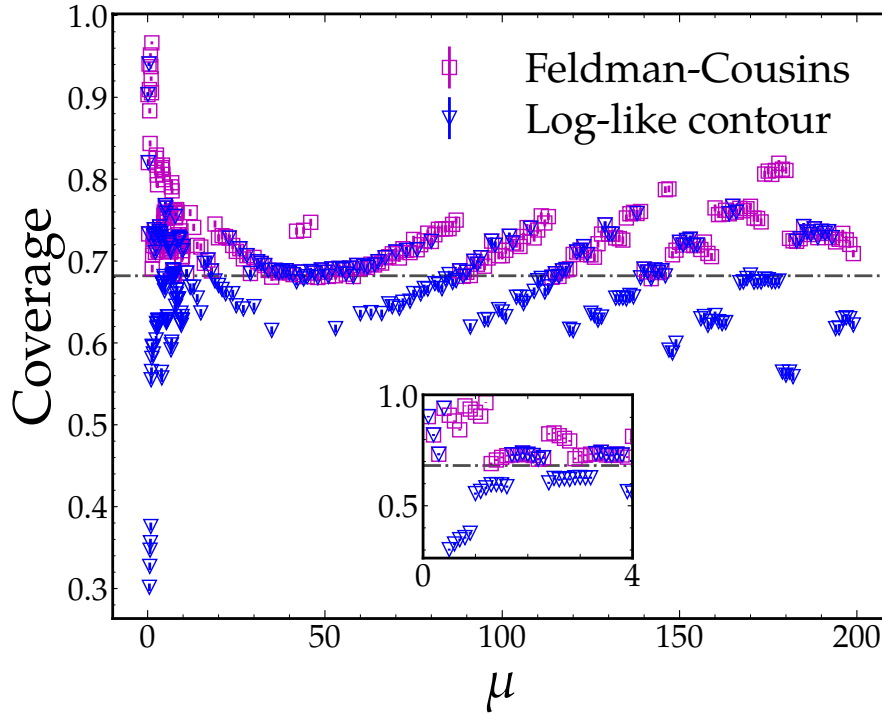

Figure 4.18: Coverages of the FC and the LLC method obtained by the toy Monte-Carlo experiment as function of the true μ. Horizontal dashed line marks the 68.2% value.

values, we use the FC interval only in the case of $k = 0$. Regardless of the value of p_{cc} of the module, we assign the more conservative interval computed for $p_{cc} = 0$, which yields $(\mu_1, \mu_2) = (0, 1.28)$. For $1 \leq k \leq 63$, the LLC interval, calculated during runtime, is used.

Finally, it is instructive to compare the length of the LLC uncertainty interval with that of a Poisson interval. For a given $\hat{\mu}$, the error assuming a Poisson distribution is $\sigma_{\text{Poisson}} = \sqrt{\hat{\mu}}$. Since the LLC gives assymetric errors, we take the error as the average $\sigma_{\text{LLC}} = \frac{\sigma_+ + \sigma_-}{2}$. In Fig. 4.19, we show the relative errors $\sigma_{\text{Poisson}}/\hat{\mu}$ and $\sigma_{\text{LLC}}/\hat{\mu}$ as function of $\hat{\mu}$. For small $\hat{\mu}$, the two error estimates are close to each other, indicating that in the limit of low number
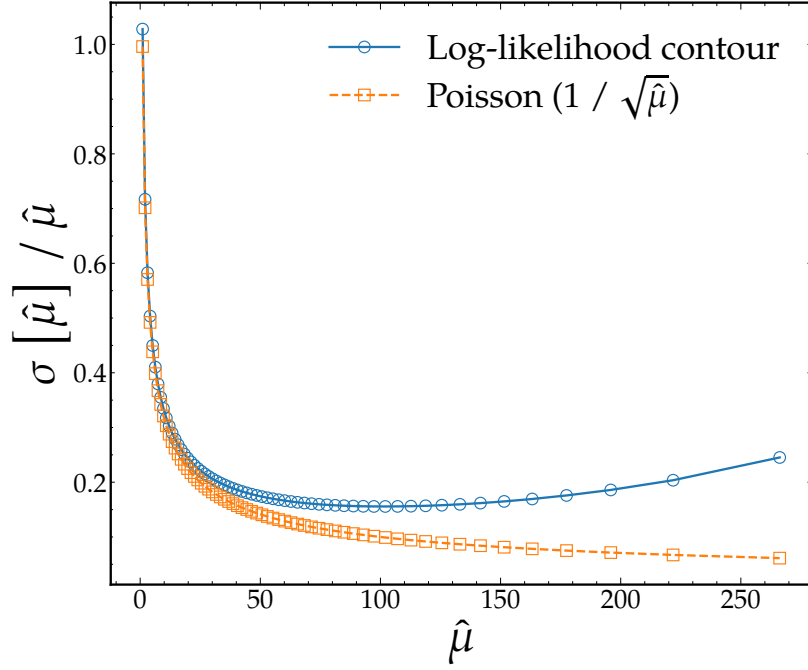
Figure 4.19: Comparison of the relative error of $\hat{\mu}$ assuming a Poisson distribution and the one obtained by the log-likelihood contour method.

of muons, Poissonian fluctutations are the dominating source of fluctuations. However, the two curves start to differ as $\hat{\mu}$ increases, the one corresponding to the LLC case being above the Poisson curve. The relative error of a Poisson estimate tends to zero as the number of counts increases, whereas the relative error given by the LLC reaches a minimum around $\hat{\mu} \sim 50$, after which start to increase again. Indeed, as the number of muons increases, the fluctutations due to the segmentation of the detector start to dominate and the assumption of a Poisson process would underestimate the uncertainties.

Since detectors close to the shower core are exposed to larger number of muons, assuming a Poisson likelihood would give these detectors the largest weight in the muon LDF fitting process. As it will be shown in Section 6.2.3, this can heavily bias the fit. In addition, the underestimation of the signal fluctutations of the detectors lead to underestimation of the uncertainties in the muon LDF fit parameters. Despite this being already noted in Ref. [63], the official reconstruction of the UMD implemented in the $\overline{\text{Offline}}$ software was still using the Poisson likelihood. In Chapter 6, we implement in $\overline{\text{Offline}}$ the likelihood model developed in this chapter and compare its performance to the existing Poisson likelihood.

4.4 Summary

In this chapter, the likelihoods of an idealized segmented detector, developed in Ref. [63] for fixed μ and in Ref. [64] for fixed N_μ, were extended to take into consideration detector effects, such as detector inefficiency, noise and corner-clipping muons. This was achieved by proposing suitable and easy-interpretable probabilistic models for each effect and by thinking in terms of effective number of particles: each effect contributes to decreasing (inefficiency) or increasing (noise and corner-clipping) this effective number.

The key ingredients are the single-muon inefficiency probability, p_I, the corner-clipping probability, p_{cc}, and the single-bar noise probability p_n. All of these can be straightforwardly

measured in the laboratory. With these parameters, the final probablity distributions for N_μ and μ were presented in Eq. (4.23) and Eq. (4.24), respectively.

With Monte-Carlo simulations, we showed that the derived distributions provide an accurate representation of the detector signal. We additionally demonstrated that the new maximum likelihood estimators have reasonable biases. In particular, a new and fundamentally different feature arises when the noise is included in the likelihood: the presence of a detection limit. If the number of activated bars is less than the expected number of bars due to noise, a negative value is predicted by the estimators and nothing can be said about μ or N_μ.

Subsequently, the formality derived for a general segmented detector was applied to the UMD case. We obtained p_I and p_n from existing references and concluded that these effects are negligible for the UMD and could be neglected for practical purposes. Although no laboratory measurement is available for p_cc, we present in the next chapter a data-driven method to estimate it. As will be shown, the corner-clipping effect is the dominant effect above inefficiency and noise, and it is considered in the UMD likelihood.

Finally, with the new likelihood, we tested two methods to compute an error interval for μ, namely, the log-likelihood contour method and the Feldman-Cousins approach. We tested the coverage of the two intervals with a toy Monte-Carlo simulation. The Feldman-Cousins approach yields, by construction, equal or larger coverages than the desired nominal value of 68.2%, but at the cost of a rather expensive calculation. On the other hand, the LLC intervals are more easily calculated. The coverage provided by this method is sometimes smaller than 68.2% but in most of the cases remains reasonably close. The exception to this is the case where zero bars are activated. Thus, it was decided to use the Feldman-Cousins interval only when zero bars are activated, and the LLC intervals for the rest of the cases.

5

Data-driven method to estimate the corner-clipping probability

In the previous chapter, the single-detector likelihood of an idealized segmented detector was extended to take into consideration the detector inefficiency, noise and the corner-clipping muons. In this way, a more realistic model of a segmented detector could be achieved.

The inclusion of these effects was accomplished by introducing new and easily-interpretable parameters: the single-muon inefficiency probability p_I, the single-bar noise probability p_n and the single-muon corner-clipping probability p_{cc}. For the UMD case, it was shown that p_I and p_n could be neglected, with p_{cc} being the only relevant quantity to consider. Since no laboratory measurement of such parameter is available, it is necessary to develop a reliable method to estimate it. In this chapter we present a data-driven approach to obtain p_{cc}.

The chapter is organized as follows: In Section 5.1 we describe the method and apply it to simulations. We further use the simulations to compare the estimated and true p_{cc}, and to assess the bias of the corner-clipping corrected estimator $\hat{N}_\mu$. Finally, in Section 5.2, we apply the method to data and compare the estimated p_{cc} with the one obtained in simulations.

5.1   Description of the method and validation with simulations

First, it is necessary to consider the detector in terms of halves, as they are the most irreducible units of material in which a particle can be injected. We will refer to the half containing strips 1 to 32 as half 1, and the half containing strips 33 to 64 as half 2. In addition, we will denote the number of activated bars in one half as $\tilde{k}$. Thus, the total number of triggered bars in a module can be written as $k = \tilde{k}_1 + \tilde{k}_2$, where $\tilde{k}_1$ and $\tilde{k}_2$ correspond to the number of triggered bars in half 1 and 2, respectively.

When a single muon is injected into a half, three outcomes are possible: no bar is activated, a single bar is activated or two neighboring bars are activated. If we call $N_{1\mu}$ the number of times in which only a single muon was injected into a half, we can write

$$N_{1\mu} = N_0 + N_{1\text{-bar}} + N_{cc}, \tag{5.1}$$

where N_0, $N_{1\text{-bar}}$ and N_{cc} are the number of times in which zero, one and two neighboring bars were activated, respectively. Thus, we can write

$$p_{cc} = \frac{N_{cc}}{N_{1\mu}}. \tag{5.2}$$

If we neglect detector inefficiency, which is a reasonable assumption given the large detection efficiency measured with a single bar [60], we can approximate $N_{1\mu} \cong N_{\text{1-bar}} + N_{\text{cc}}$. Therefore, we have

$$p_{\text{cc}}(\theta, \Delta\phi) = \frac{N_{\text{cc}}(\theta, \Delta\phi)}{N_{\text{1-bar}}(\theta, \Delta\phi) + N_{\text{cc}}(\theta, \Delta\phi)}, \qquad (5.3)$$

where we explicitly indicate the dependence with θ and $\Delta\phi$. Since counting the number of modules halves with only one activated bar is straightforward, estimating p_{cc} reduces to estimating N_{cc}.

We begin by considering the number of UMD modules halves with only two activated bars (i.e. $\tilde{k} = 2$), which we call $N_{\text{2-bars}}$:

$$N_{\text{2-bars}} = N_{\text{neigh}} + N_{\text{non-neigh}}, \qquad (5.4)$$

where N_{neigh} and $N_{\text{non-neigh}}$ are the number of halves in which the two bars were neighboring and non-neighboring, respectively. We can write

$$N_{\text{neigh}} = N_{\text{cc}} + N_{2\mu}, \qquad (5.5)$$

where $N_{2\mu}$ is the number of times in which the neighboring pair of bars were activated due to two different muons. Thus, it is necessary a way to obtain N_{cc} from N_{neigh}, discriminating the corner-clipping from the two-muons case. For that purpose, the timing information of the signals can be exploited.

We call Δt the absolute difference between the start times of the two signals involved[1]. In Fig. 5.1, we show the histograms of the Δt values for halves with $\tilde{k} = 2$ using a set of simulated showers. These showers correspond to the EPOS-LHC discrete library described in Section 7.5. We separate the neighboring and the non-neighboring case into two different histograms. In addition to the expected fact that the non-neighboring histogram has a larger number of entries, it is apparent that the neighboring histogram shows a distinctive peak for small Δt that is not present in the non-neighboring case. We further split the neighboring case into two categories: the corner-clipping case, obtained by requesting a single muon injected, and the two-muons case. The former is displayed in the green filled histogram and the latter in the grey filled histogram in the same figure. Since the two signals are generated by the same muon, the corner-clipping values accumulate in the small Δt ($\Delta t \lesssim 5$) region, with extremely few exceptions caused by the activation of a neighboring bar due to a non-muonic uncorrelated particle. We conclude that the Δt distribution of the neighboring case is the sum of two distributions: one, peaked at small Δt values generated by corner-clipping muons, and the other caused by two different muons randomly hitting two neighboring bars. Furthermore, we expect the two-muons case to have the same Δt distribution than the non-neighboring case as they both correspond to the same underlying process, namely, two muons hitting two different bars. Thus, any statistically significant deviation between the distributions of the neighboring and the non-neighboring case can be attributed to the corner-clipping muons alone. We will use this to estimate N_{cc}.

We start with a probabilistic argument by computing the probability of having two neighboring bars by chance. The probability of activating the i-th bar is $p(i) = 1/\tilde{n}_s$ and the probability of activating the neighboring bar $i + 1$ given that the i-th was activated is $p(i + 1|i) = 1/(\tilde{n}_s - 1)$, where $\tilde{n}_s = n_s/2 = 32$ is the segmentation of one modules half. Thus, given the condition that two (and only two) bars are activated, the probability of them being neighboring just by chance is given by

---

[1]The start time is the time of the first "1" of the muon pattern.

$$p_{2\mu}^{\text{exp}} = 2 \sum_{i=1}^{\tilde{n}_s - 1} p(i)p(i+1|i) = \frac{2}{\tilde{n}_s - 1} = 6.45\%, \tag{5.6}$$

where a factor 2 comes from considering that i and $i+1$ are exchangable. The subindex 2μ is to emphasize that this situation corresponds to two different muons that randomly hit two neighboring bars and the supraindex is to indicate that this is an expected value using only a probabilistic consideration. Therefore, in the absence of corner-clipping muons (i.e. sufficiently large Δt), we expect the quotient $\frac{N_{\text{neigh}}}{N_{\text{neigh}} + N_{\text{non-neigh}}}$ to be equal to $p_{2\mu}^{\text{exp}}$. We refer to the quotient calculated for large Δt as $p_{2\mu}^{\text{meas}}$, where the supraindex indicates that is a measured value extracted from data.

In Fig. 5.2, this fraction is displayed for each Δt, computed dividing the blue histogram and the sum of the blue and orange histogram in Fig. 5.1 for each bin. The dashed grey line corresponds to $p_{2\mu}^{\text{exp}}$, while the dotted magenta line indicates $p_{2\mu}^{\text{meas}}$, calculated as the fraction $\frac{N_{\text{neigh}}}{N_{\text{neigh}} + N_{\text{non-neigh}}}$ using only pairs of strips with $\Delta t > 6$. It is apparent that in this regime the neighboring fraction remains constant and that $p_{2\mu}^{\text{meas}}$ and $p_{2\mu}^{\text{exp}}$ are consistent.

In contrast, for $\Delta t < 6$, a rapid increase in the neighboring fraction is observed as a consequence of the corner-clipping effect. In this regime, we can estimate the number of pairs that correspond to the two-muons case by using $p_{2\mu}$. For each Δt, we have

$$\hat{N}_{2\mu} = p_{2\mu} \left(N_{\text{neigh}} + N_{\text{non-neigh}} \right). \tag{5.7}$$

Therefore, an estimate for N_{cc} is obtained by replacing $\hat{N}_{2\mu}$ in Eq. (5.5):

$$\hat{N}_{cc}(\Delta t) = N_{\text{neigh}}(\Delta t) - \hat{N}_{2\mu}(\Delta t) = N_{\text{neigh}}(\Delta t) - p_{2\mu} \left(N_{\text{neigh}}(\Delta t) + N_{\text{non-neigh}}(\Delta t) \right), \tag{5.8}$$

where we have explicitly indicated that the equation holds for each Δt.

In Fig. 5.3, the estimations obtained by eqs. 5.7 and 5.8 are displayed along with the same histograms shown in Fig. 5.1. The measured $p_{2\mu}$ value was used in eqs. 5.7 and 5.8. A high degree of agreement between the estimations and the true histograms can be seen.

In order to get an estimate of the total number of corner-clipping muons, as needed in Eq. (5.3), we sum over all $\Delta t \leq 5$:

$$\hat{N}_{cc}^{\text{tot}} = \sum_{\Delta t = 0}^{5} \hat{N}_{cc}(\Delta t).$$

Thus, an estimator $\hat{p}_{\text{cc}}$ can be constructed by replacing N_{cc} by $\hat{N}_{cc}^{\text{tot}}$ in Eq. (5.3).

By applying this procedure in bins of $(\theta, \Delta\phi)$ the angular dependence of $\hat{p}_{\text{cc}}$ can be obtained. The result is shown in Fig. 5.4. As expected, $\hat{p}_{\text{cc}}$ increases with θ and, for a fixed θ, it increases as $\Delta\phi$ approaches to $90°$ (or equivalenty, as $|\sin(\Delta\phi)|$ approaches to 1). For a fixed θ, we fit

$$p_{cc}(\theta, \Delta\phi) = m(\theta) \left(|\sin \Delta\phi| - 0.5 \right) + b(\theta). \tag{5.9}$$

In turn, we fit the evolution of the slope and intercept with θ with linear functions in $\sec\theta$,

$$\begin{aligned} m(\theta) &= m_0 + m_1(\sec\theta - 1.2), \\ b(\theta) &= b_0 + b_1(\sec\theta - 1.2). \end{aligned} \tag{5.10}$$
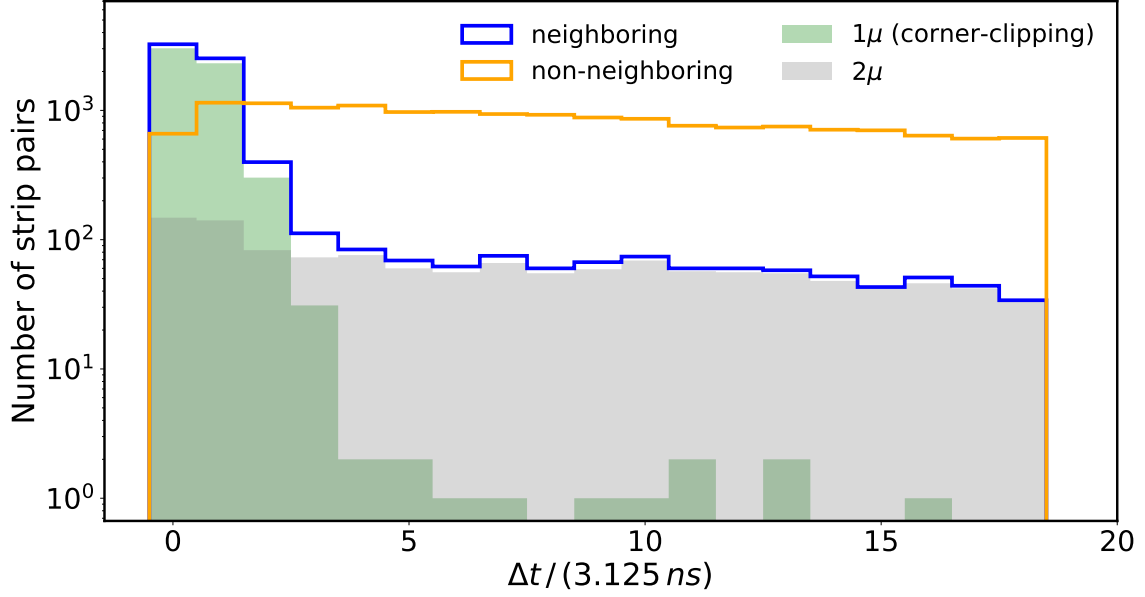
The results of such fits are displayed in Fig. 5.6.

Figure 5.1: Histograms of Δt values for modules halves with $\tilde{k} = 2$. Blue (orange) corresponds to the (non-)neighboring case. The green filled histogram corresponds to the true corner-clipping muons, identified by simultaneously requesting the condition of a single muon injected and two neighboring bars with muon pattern. The grey filled histogram shows the case in which two muons activate two neighboring bars by chance.
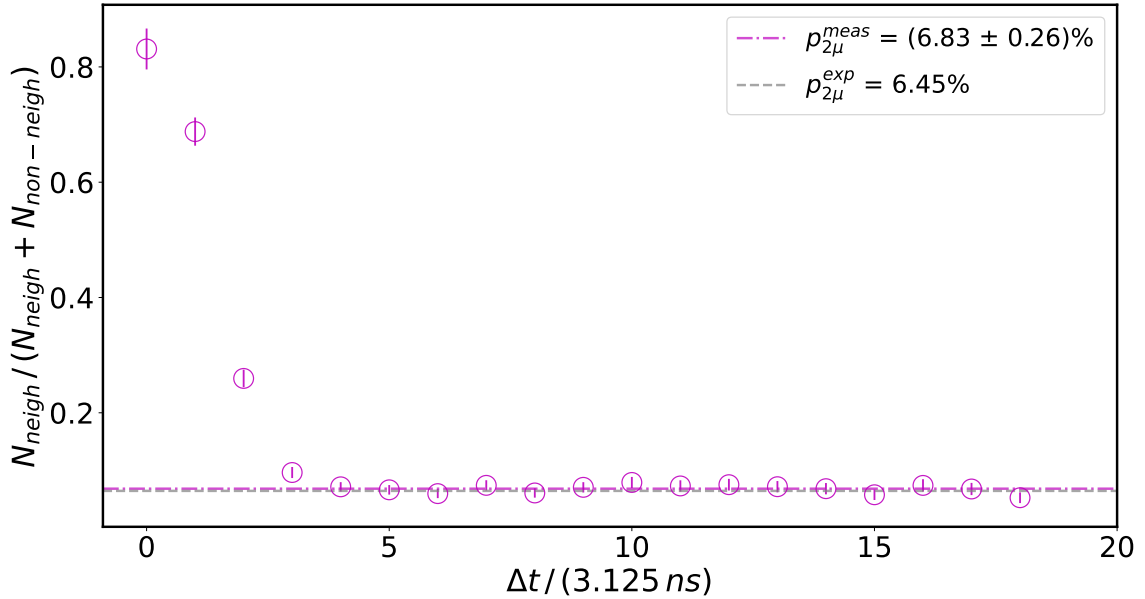

Figure 5.2: Fraction of neighboring pairs for each Δt, obtained by dividing the neighboring histogram by the sum of the neighboring and non-neighboring histograms of Fig. 5.1. Grey dashed line represents the expected value of the fraction in the absence of corner-clipping muons (Eq. (5.6)). Magenta dashed line corresponds to the neighboring fraction using only pairs with $\Delta t > 6$.

The true p_{cc}, calculated using the true values of N_{cc} and $N_{1\mu}$, is compared to the estimated $\hat{p}_{cc}$ in Fig. 5.5. It is clear that the proposed method offers a satisfactory estimator of the corner-clipping probability.
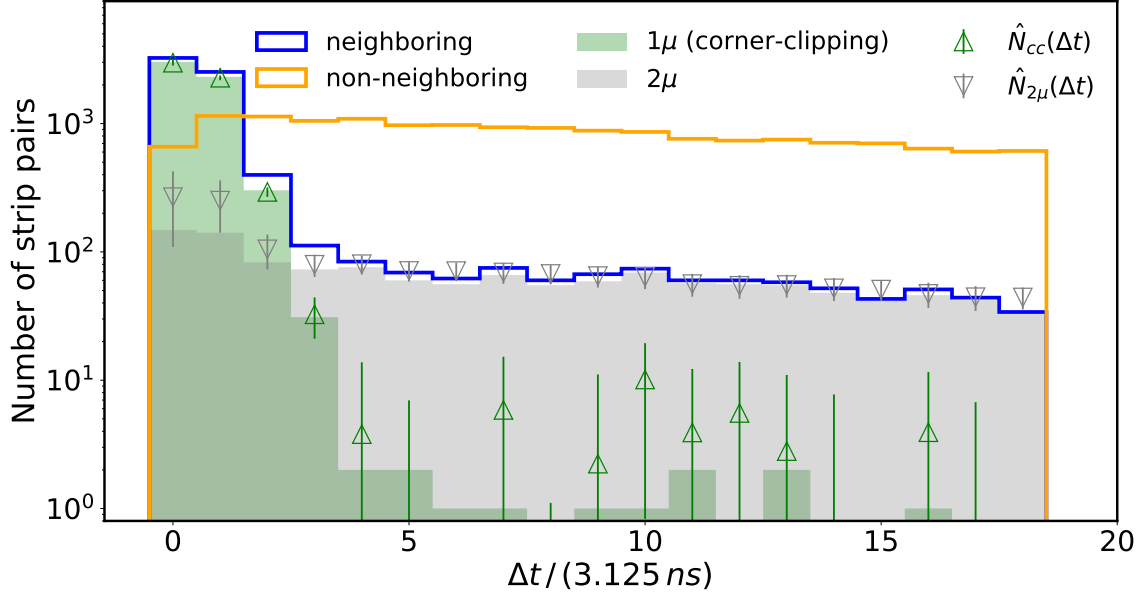
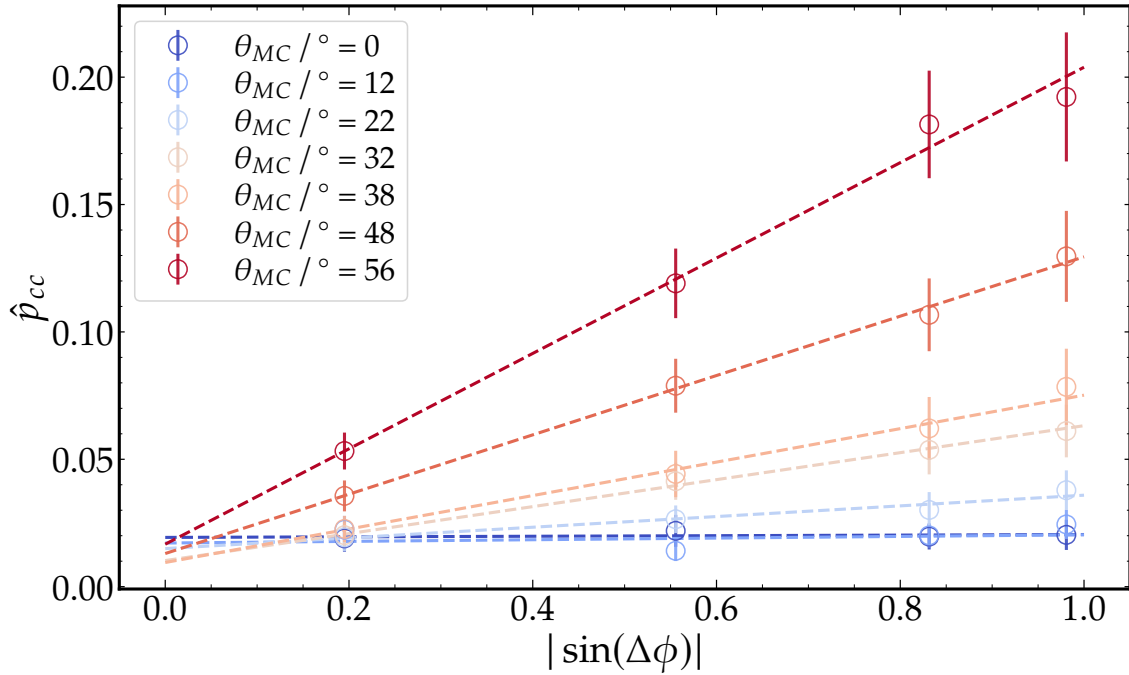**Figure 5.3:** Same as in Fig. 5.1 together with estimations from eqs. 5.7 and 5.8

Figure 5.4: Estimated corner-clipping probability as function of $|\sin \Delta\phi|$ for six different zenith angles. Dashed lines correspond to fits to the model of Eq. (5.9).

As a final step, it is necessary to validate the performance of the estimator of Eq. (4.16) combined with the parameterization of $\hat{p}_{cc}$ given by Eqs. 5.9 and 5.10 using realistic full detector simulations. In Fig. 5.7, the relative bias of the estimator as a function of the distance to the shower core is displayed using air-shower simulations of proton primaries with $\lg(E/\,\mathrm{eV}) = 18$ and EPOS-LHC as hadronic model. For brevity, only the most vertical ($\theta = 0°$) and inclined ($\theta = 48°$) zenith angles are shown. The same plot for iron primaries is visible in Fig. 5.8.
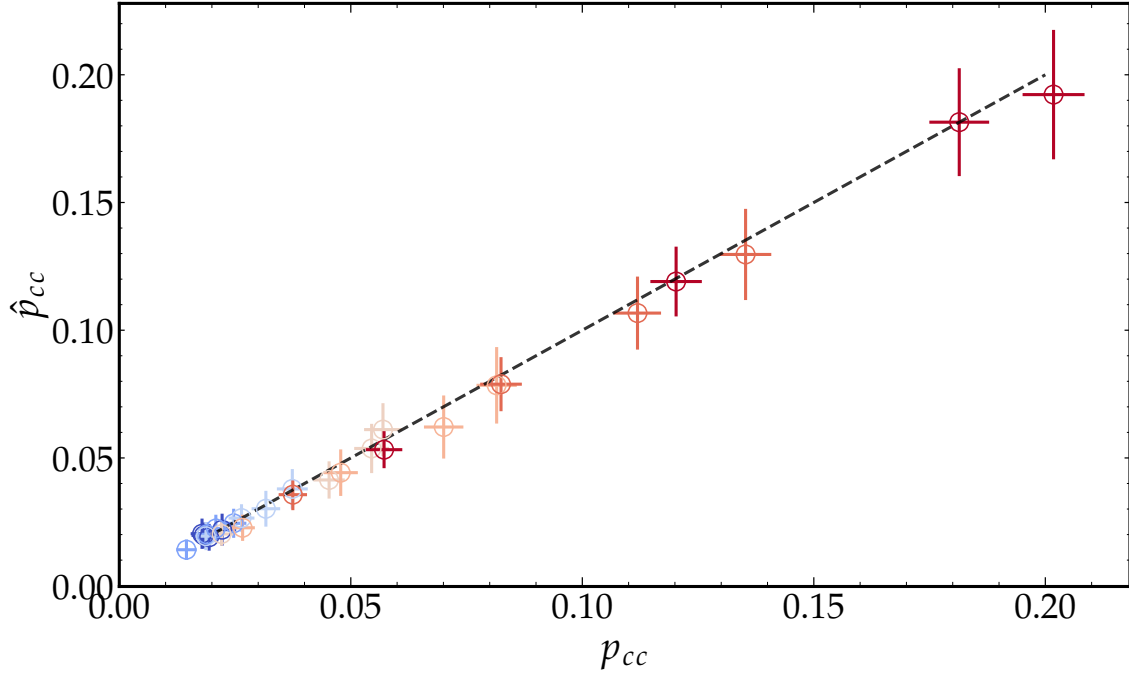
Figure 5.5: Comparison between estimated and true corner-clipping probability. The dashed line indicates the identity function.
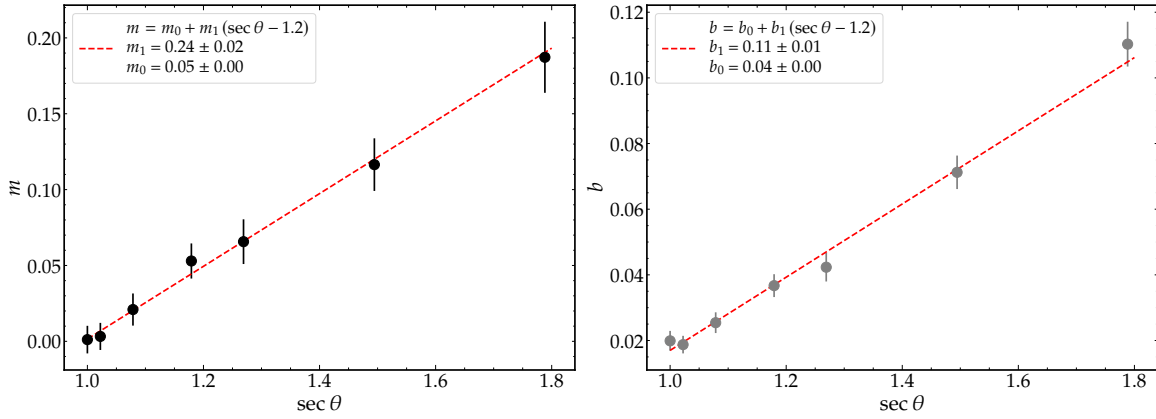

Figure 5.6: Evolution of the slope (left) and intercept (right) of the model Eq. (5.9) as a function of $\sec \theta$. Red dashed lines correspond to the linear fit of Eq. (5.10).

The same conclusions can be extracted for both primaries. Firstly, it is worth noting that the bias is reasonably constant in the entire range of r values. Secondly, since the corner-clipping effect is minimum for $\theta = 0°$, the difference between the corner-clipping-corrected (circles) and uncorrected (squares) estimator is not very large in this case. In contrast, for $\theta = 48°$, the uncorrected estimator shows a bias of $\sim 12\%$, while the corrected one presents a reduced bias of $\sim 2.5\%$. Lastly, the residual bias of $\sim 2.5\%$ that remains in the corrected estimator can be attributed to the simplifications involved in the modeling of the corner-clipping effect. Further, even in the idealized Monte Carlo simulations shown in Section 4.1.3, in which the the corner-clipping effect is indeed simulated as a binomial process with a defined p_{cc}, a residual bias is still visible (see Fig. 4.10 and Fig. 4.11) as expected from the segmentation bias of the detector discussed in Section 4.1.1 (see Fig. 4.2 and Fig. 4.5). For
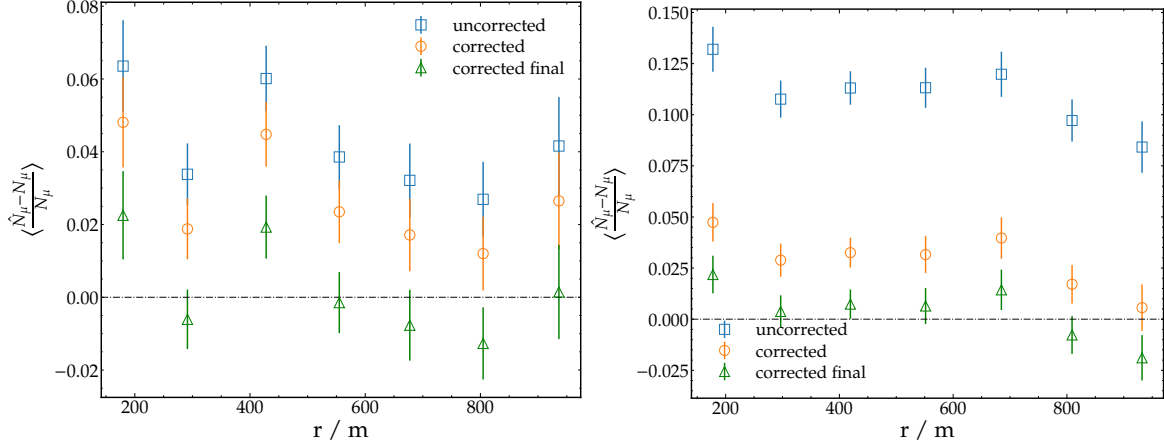
Figure 5.7: Mean relative bias of different estimators of N_μ between $100 \leq r/m \leq 1000$ for proton simulations with $\lg(E/\text{eV}) = 18$ and EPOS-LHC as hadronic model. Square markers correspond to Eq. (4.5), circular to Eq. (4.16) and triangular to Eq. (5.11). Left (right) plot corresponds to $\theta = 0°$ ($\theta = 48°$). The $\hat{p}_{cc}$ values given by the parameterization of Eqs. 5.9 and 5.10 are used. Error bars correspond to the standard deviation of the mean. Horizontal dashed line marks the null bias.

this reason, a final global, zenith- and azimuth-independent correction can be applied to the estimator,

$$\hat{N}_\mu = \frac{1}{1.025} \left(\frac{1}{(1+p_{cc})} \frac{\ln(1-k/n_s)}{\ln(1-1/n_s)} \right). \tag{5.11}$$

The bias of the estimator of Eq. (5.11), represented as triangular markers in Fig. 5.7 and Fig. 5.8, is now centered around zero as desired.

Finally, the mean relative bias over $100 \leq r/m \leq 1000$ of Eq. (4.16) and Eq. (5.11) as function of θ for all primaries and energies is shown in Fig. 5.9. It is evident that the uncorrected estimator shows an increasing bias with θ, while the corrected one shows a flat bias centered in zero. We conclude that $\hat{p}_{cc}$ succesfully captures the behaviour of the bias caused by corner-clipping muons with the zenith angle. This conclusion holds also for air showers simulated with QGSJetII-04 as hadronic model, as shown in Appendix D.

5.2 Application of the method to data

The neighboring and non-neighboring histograms for data along with the estimations calculated with Eqs. 5.7 and 5.8 are displayed in Fig. 5.10. Like in simulations (Fig. 5.3), the signature of the corner-clipping muons is visible in the neighboring histogram as an excess of entries for $\Delta t \lesssim 5$[2]. Furthermore, the same behaviour observed in simulations for the fraction of neighboring pairs (Fig. 5.2) is present in data, as shown in in Fig. 5.11. The fraction remains constant for $\Delta t > 6$ with a value consistent with $p_{2\mu}^{\text{exp}}$, while it increases rapidly for small Δt values as a consequence of the corner-clipping muons.

The estimated corner-clipping probability as function of $|\sin \Delta\phi|$ for different zenith angle bins, together with the fits to Eq. (5.9), is presented in Fig. 5.12. To facilitate the comparison between data and simulations, the zenith bins were selected so that their center was close to one of the discrete zenith angles in the simulation library. Similar to what was found

---

[2]In Appendix B, we use the corner-clipping muons to study the time response of the detector.
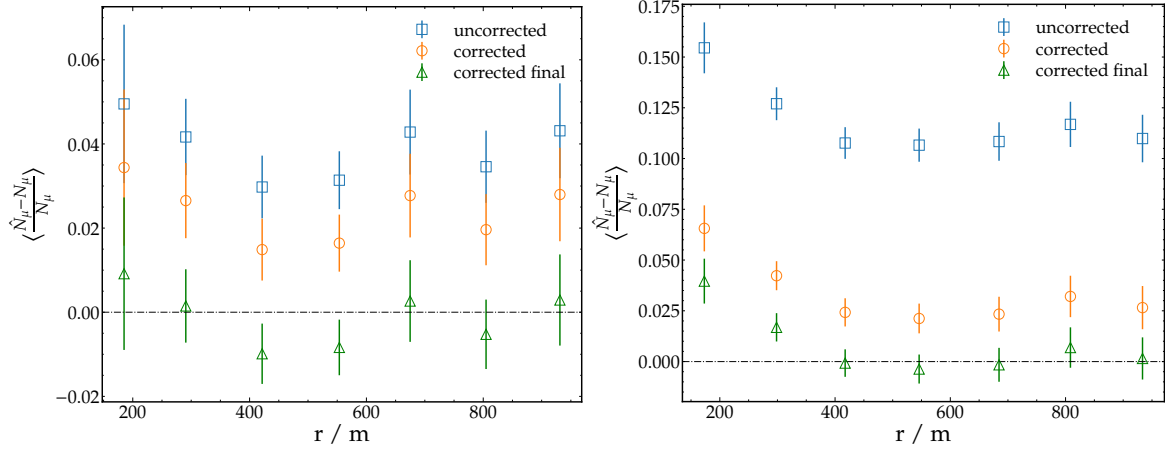
Figure 5.8: Mean relative bias of different estimators of N_μ between $100 \leq r/m \leq 1000$ for iron simulations with $\lg(E/\text{eV}) = 18$ and EPOS-LHC as hadronic model. Square markers correspond to Eq. (4.5), circular to Eq. (4.16) and triangular to Eq. (5.11). Left (right) plot corresponds to $\theta = 0°$ ($\theta = 48°$). The $\hat{p}_{cc}$ values given by the parameterization of Eqs. 5.9 and 5.10 are used. Error bars correspond to the standard deviation of the mean. Horizontal dashed line marks the null bias.
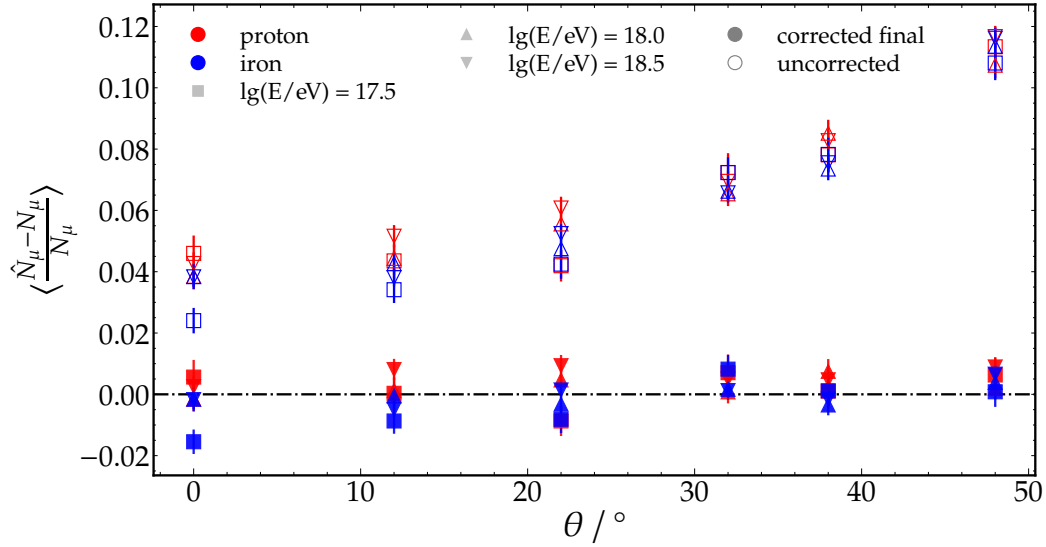

Figure 5.9: Mean relative bias over $100 \leq r/m \leq 1000$ of estimators of Eq. (4.5) (unfilled markers) and Eq. (5.11) (filled markers). Different markers shape corresponds to different energies, while different colors indicate different primaries.

in simulations, and in agreement with what is expected for corner-clipping muons, $\hat{p}_{cc}$ increases both with θ and $|\sin\Delta\phi|$. In addition, m and b also show a linear behaviour in $\sec\theta$, as shown in Fig. 5.13. This result constitutes the first quantification of the corner-clipping effect using data.

The comparison between data and simulations of $\hat{p}_{cc}$ for each $(\theta, |\sin\Delta\phi|)$ bin is displayed in Fig. 5.14. The corresponding comparison of the parameters m and b is shown in Fig. 5.15. Particularly for the most inclined zenith angles, a slight discrepancy is observed between the $\hat{p}_{cc}$ values found in data and simulations, which is also reflected in the evolution of m and b with $\sec\theta$.

These differences might be ultimately attributed to some simplifications present in the simulation of the detector. For example, the scintillator-fiber-electronics system, whose response was tuned to a handful of laboratory measurements, is the same for all the detectors in the simulated array—an assumption that is too optimistic for real detectors in the field, for which variations between different modules are expected. As a result, different strips in the field would respond slightly different to the same energy deposition. Similarly, differences between the noise levels and efficiency between bars can also impact the outcome of this analysis.

Due to this difference between data and simulations, throughout this work we will use the parameterization of $\hat{p}_{cc}$ of Fig. 5.6 for simulations and the one of Fig. 5.13 for data.

Nevertheless, it is necessary to stress that this discrepancy is not highly significant as it does not represent a large impact in the final corner-clipping correction. To ilustrate this, we can compare the maximum likelihood estimator of Eq. (4.15) using the $\hat{p}_{cc}$ found for data with that of simulations. To assess the worst-case scenario, we use the values of the $(\theta, |\sin \Delta\phi|)$ bin for which the difference between data and simulations is the largest. This corresponds to $(\theta = 48°, |\sin(78.75°)| = 0.98)$, $\hat{p}_{cc}^{data} = 0.10$ and $\hat{p}_{cc}^{sim} = 0.13$. Thus,

$$\frac{\hat{\mu}_{data}}{\hat{\mu}_{sim}} = \frac{1 + \hat{p}_{cc}^{sim}}{1 + \hat{p}_{cc}^{data}} = 1.03.$$

Therefore, the largest discrepancy between the $\hat{p}_{cc}$ values implies only a 3% impact in the final correction.

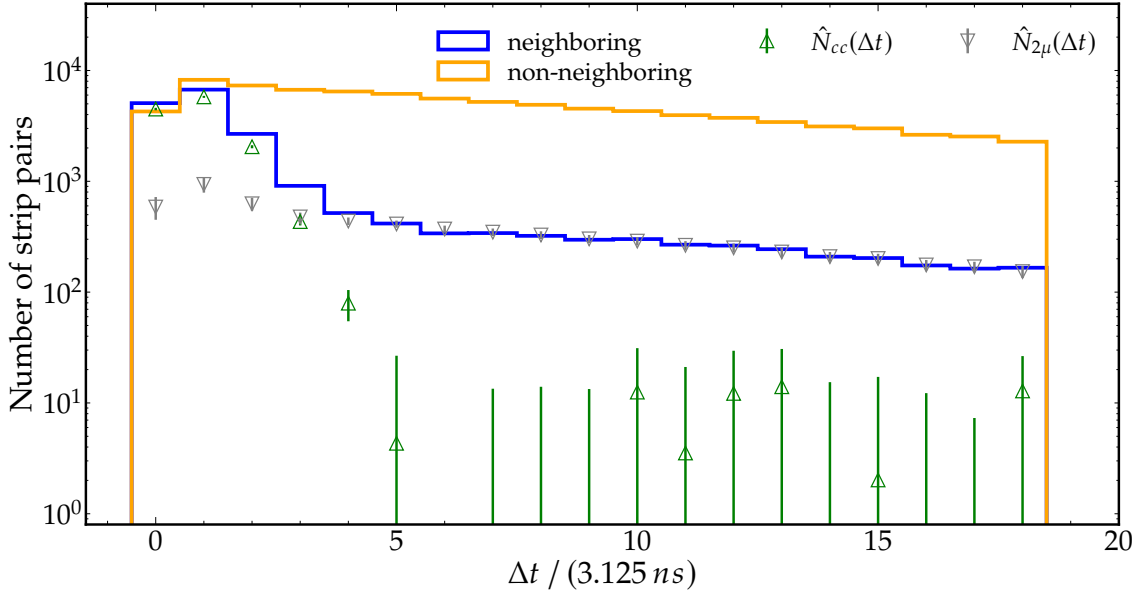**Figure 5.10:** Histograms of Δt for the neighboring (blue) and non-neighboring (orange) case using data. Unfilled markers correspond to the estimations obtained by eqs. 5.7 and 5.8.
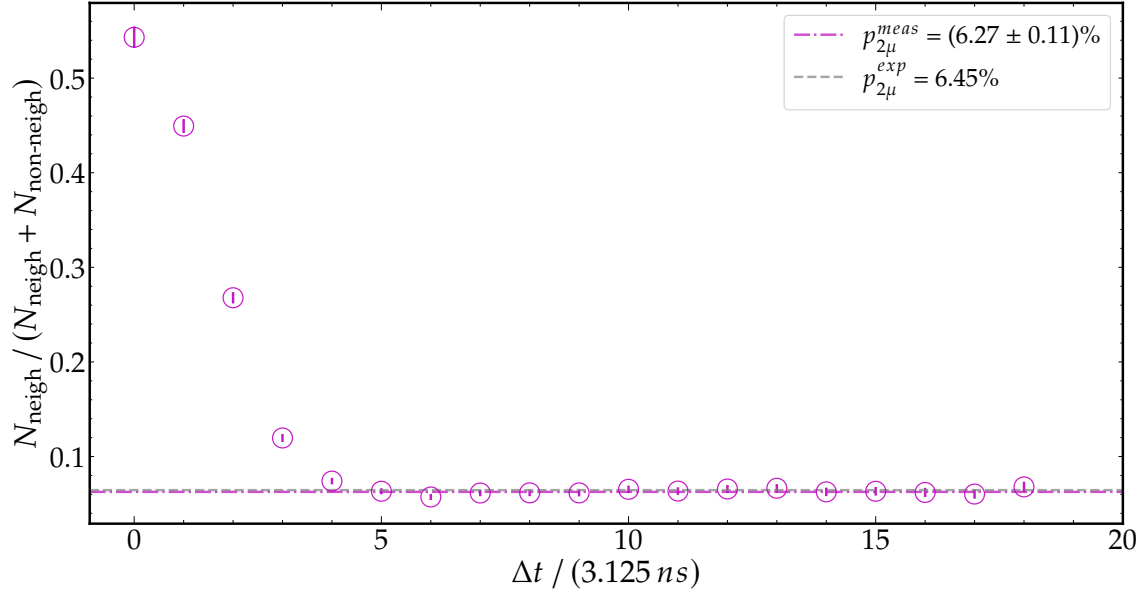
Figure 5.11: Fraction of neighboring pairs for data, obtained by dividing the neighboring histogram by the sum of the neighboring and non-neighboring histograms of Fig. 5.10. Grey dashed line represents the expected value of the fraction in the absence of corner-clipping muons (Eq. (5.6)). Magenta dashed line corresponds to the neighboring fraction using only pairs with $\Delta t > 6$.
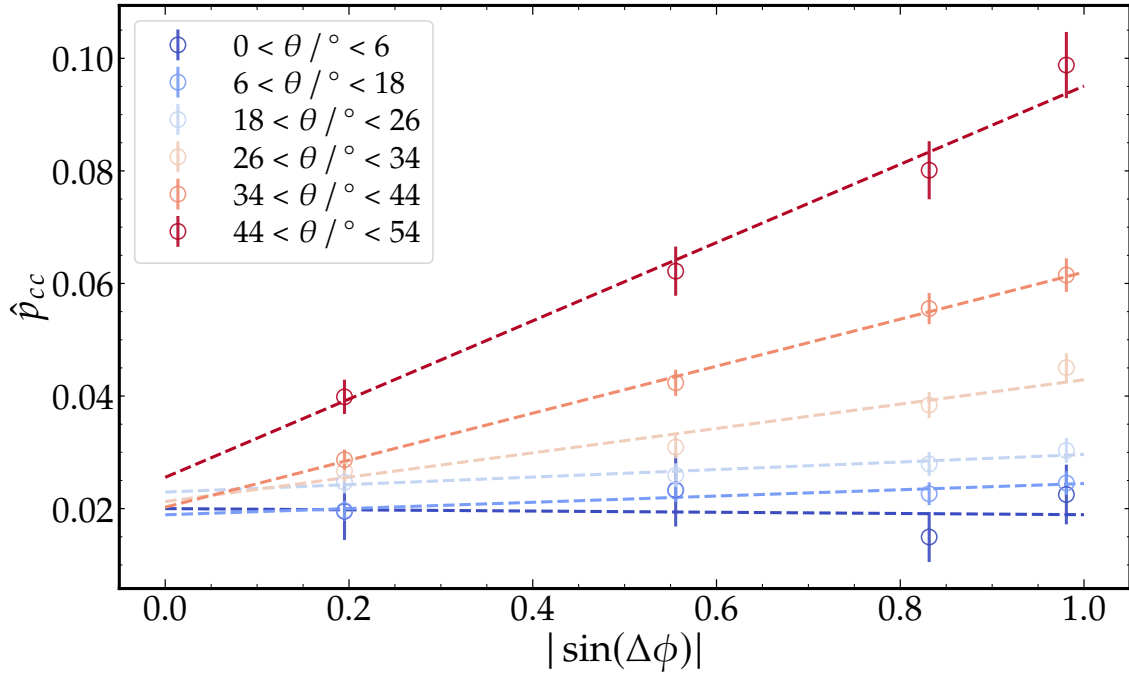

Figure 5.12: Estimated corner-clipping probability as function of $|\sin \Delta\phi|$ for six different zenith angle bins of data. Dashed lines correspond to fits to the model of Eq. (5.9).
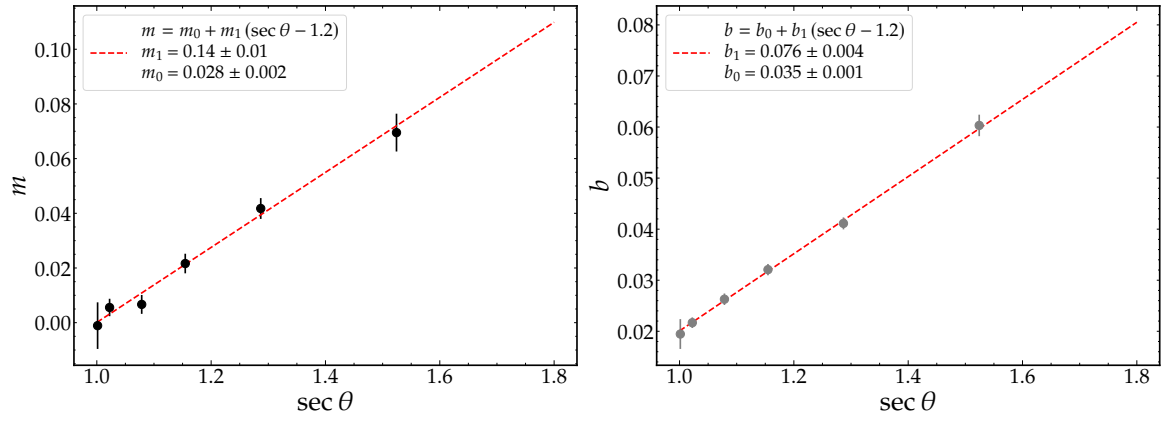
Figure 5.13: Evolution of the slope (left) and intercept (right) of the model Eq. (5.9) as function of $\sec\theta$ for data. Red dashed lines correspond to the linear fit of Eq. (5.10).
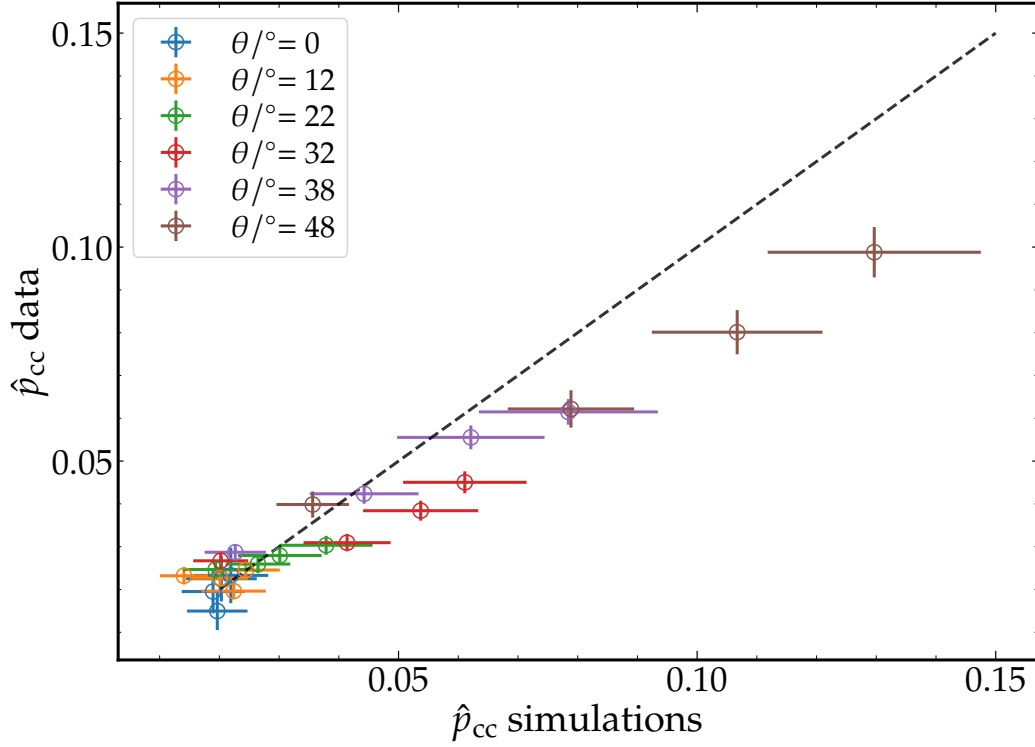
Figure 5.14: Comparison between the $\hat{p}_{cc}$ values obtained in data and simulations. The black dashed line represents the identity function.
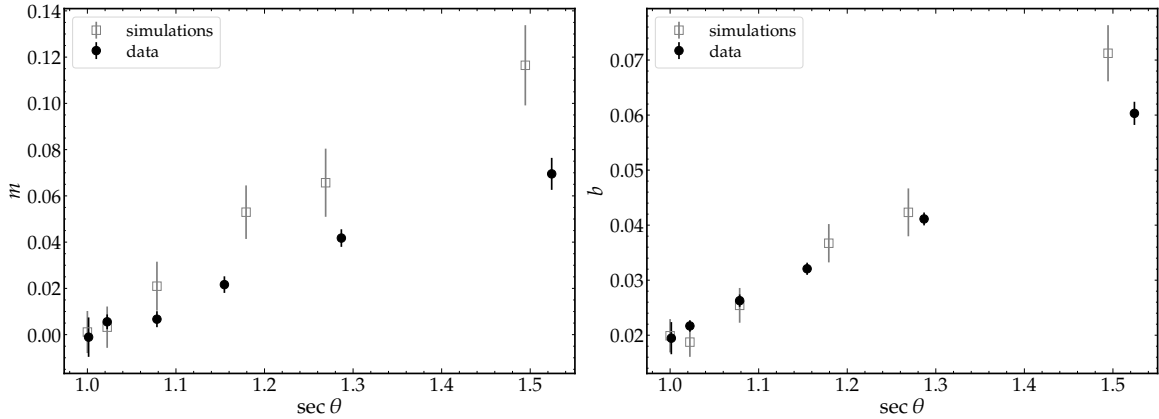
Figure 5.15: Evolution of the slope (left) and intercept (right) of the model Eq. (5.9) as function of $\sec\theta$ for data and simulations.

5.3   Comparison to previous work

As already mentioned, in previous works the corner-clipping effect was corrected for by parameterizing the mean bias of $\hat{N}_\mu$ as a function of θ and $\Delta\phi$ using simulations. This approach was used in Refs. [54, 69, 70]. In Ref. [70], the parameterization had also a dependence on the uncorrected number of muons. It is worth noting that these are end-to-end parameterizations and therefore account for all other source of biases included in the simulation (segmentation, inefficiency, noise).

In Ref. [69], a detector simulation with PMTs as photodetector was used, making the comparison to our parameterization not possible. In Refs. [54, 70], SiPMs were used and therefore a comparison can in principle be made. However, the detector simulation used in Ref. [54] was faulty, yielding overestimated signals in the UMD [71], which in turn overestimated the mean bias. Thus, a comparison to the parameterization found there is meaningless. This issue was corrected in a later version of Offline .

The latest work using SiPM was the one in Ref. [70], for which the detector simulation in Offline was the same used in this work. Therefore, a comparison can be made to our results.

First, it is necessary to describe the reconstruction procedure to estimate the number of muons used in Ref. [70], which differs to the one used in this thesis[3]. The procedure consists in doing an estimation in each of the 2048 time bins. For a given time bin j, the number of bars k_j with a muon pattern that started in that bin is computed. The estimated number of muons in that bin is obtained by the formula

$$\frac{\ln(1 - k_j / (n_s - n_j^{\text{inh}}))}{\ln(1 - 1 / (n_s - n_j^{\text{inh}}))},$$

where n_j^{inh} is the total number of inhibited channels in that bin, which correspond to the number of bars that presented a muon pattern earlier in the trace and are considered dead. We note that this corresponds to Eq. (4.5) but with a modified segmentation $n_s - n_j^{\text{inh}}$. The total number of muons in the detector for the event is then obtained by summing over all the time bins

$$\tilde{N}_\mu^{\text{uncorr}} = \sum_{j=1}^{2048} \frac{\ln(1 - k_j / (n_s - n_j^{\text{inh}}))}{\ln(1 - 1 / (n_s - n_j^{\text{inh}}))}, \tag{5.12}$$

where the superscript is to highlight that this estimator is not yet corrected for corner-clipping and other sources of biases.

As opposed to Eq. (4.5), the estimator of Eq. (5.12) depends on the arrival time distribution of the muons through the k_j's. Thus, a different intrinsic bias between the two is expected (see e.g. Fig. 8 of Ref. [66]). The bias-corrected estimator is obtained by

$$\tilde{N}_\mu^{\text{corr}} = \begin{cases} \tilde{N}_\mu^{\text{uncorr}} & \text{if } \tilde{N}_\mu^{\text{uncorr}} < 1.01 \\ \frac{\tilde{N}_\mu^{\text{uncorr}}}{1 + f_{\text{bias}}(\theta, \Delta\phi, \tilde{N}_\mu^{\text{uncorr}})} & \text{if } \tilde{N}_\mu^{\text{uncorr}} \geq 1.01 \end{cases} \tag{5.13}$$

where f_{bias} is the bias correction, obtained by parameterizating the mean relative bias of $\tilde{N}_\mu^{\text{uncorr}}$ as function of θ, $\Delta\phi$ and $\tilde{N}_\mu^{\text{uncorr}}$. The limit 1.01 was set to allow for numerical inaccuracies. f_{bias} is given by

$$\begin{aligned} f_{\text{bias}}(\theta, \Delta\phi, \tilde{N}_\mu^{\text{uncorr}}) &= a(\theta) + b(\theta) |\sin \Delta\phi| + c(\theta) \lg(\tilde{N}_\mu^{\text{uncorr}}) \\ a(\theta) &= 0.094 - 0.021 \sin^2 \theta \\ b(\theta) &= -0.34 + 0.34 \sec \theta \\ c(\theta) &= -0.038 + 0.002 \sin^2 \theta. \end{aligned} \tag{5.14}$$

For consistency in the notation, let us call Eq. (4.5) and Eq. (5.11) as N_μ^{uncorr} and N_μ^{corr}, respectively. To compare the performance of N_μ^{uncorr} and N_μ^{corr} to that of $\tilde{N}_\mu^{\text{uncorr}}$ and $\tilde{N}_\mu^{\text{corr}}$, we used a set of proton showers of 10^{18} eV, using EPOS-LHC as the hadronic interaction model. We reconstructed the number of muons in each module with Eqs. 4.5, 5.11, 5.12 and

---

[3]A more in-depth discussion on the differences can be found in Section 6.1

5.13, and compare their outcome to the true number of injected muons to assess the bias. For the comparison to be fair, we used the p_{cc} obtained for simulations when applying 5.11.

In Fig. 5.16, the relative bias as a function of r for all the estimators is shown for the zenith angles $\theta/° = \{0, 32, 38, 48\}$. It is apparent that the uncorrected and corrected estimators used in this work (Eqs. 4.5 and 5.11, respectively) are compatible to those developed in Ref. [70] (Eqs. 5.12 and 5.13, respectively).
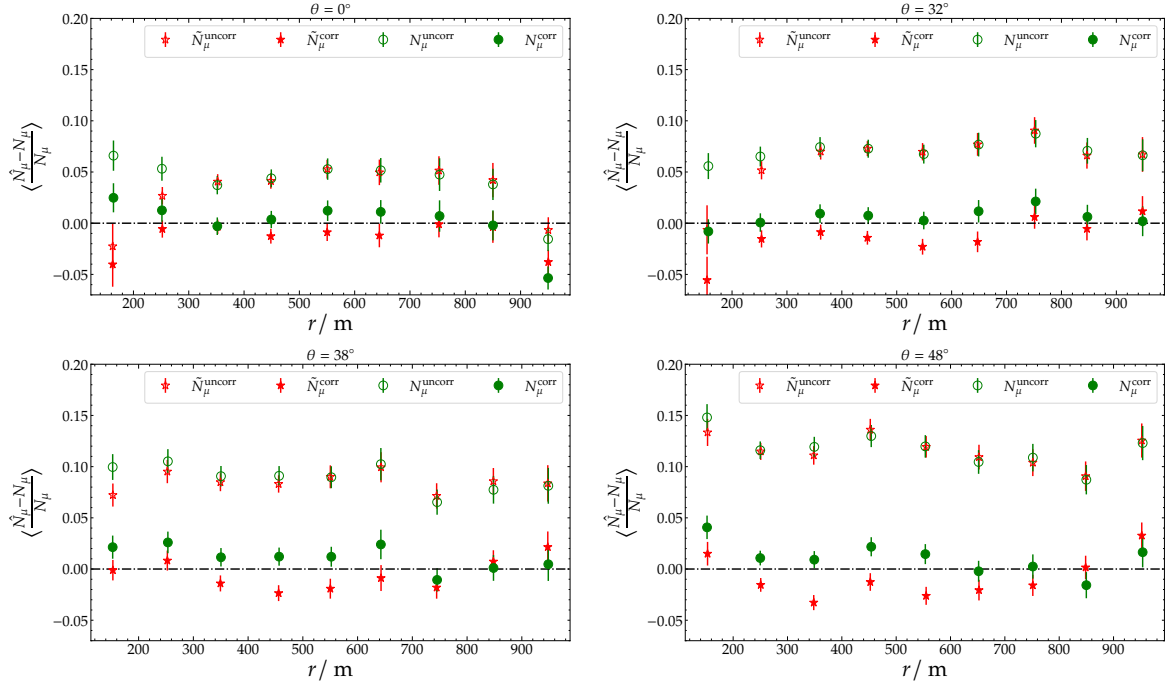

Figure 5.16: Mean relative bias as a function of r of the uncorrected (Eqs. 4.5 and 5.12) and the bias-corrected number of muons (Eqs. 5.11 and 5.13). Upper left (right) panels correspond to $\theta = 0°$ ($\theta = 32°$), whereas lower left (right) correspond to $\theta = 38°$ ($\theta = 48°$)

5.4 Summary

In this chapter, a novel and simple method to estimate the single-muon corner-clipping probability in a data-driven way was presented. In this way, the magnitude of the corner-clipping effect, which until now had to be characterized through simulations, could be quantified for the first time using data.

The method relies on using halves of detectors with either one or two bars showing a muon pattern. For the latter, the absolute difference in the start times of the signals, Δt, allows for estimating the number of corner-clipping muons

Firstly, we used air shower and full detector simulations to validate the method. We have shown that, as a consequence of the corner-clipping muons, the distribution of Δt is fundamentally different in the neighboring and non-neighboring case for small Δt. Indeed, an excess of entries for $\Delta t \lesssim 5$ is present in the neighboring case due to the corner-cliping effect. By quantifying this excess in bins of θ and $\Delta \phi$, $p_{cc}(\theta, \Delta \phi)$ could be estimated. We further confirmed that the estimated p_{cc} increases with θ and $\Delta \phi$, as expected. In addition, we have demonstrated that the estimated and true p_{cc} are compatible.

Secondly, we assessed the bias of the estimator $\hat{N}_\mu$ with and without the corner-clipping correction. When no correction is applied, $\hat{N}_\mu$ increases with θ as a consequence of the corner-clipping muons. In contrast, a flat dependence on θ is obtained when the correction

is applied, indicating that the estimated p_{cc} is succesfully capturing the behaviour of the bias produced by this effect. A zenith- and azimuth-independent residual bias of $\sim 2.5\%$ is corrected for in a final step.

Thirdly, we applied the method to data and confirmed the same qualitative behaviour found in simulations for the Δt distributions and for the estimator of $p_{cc}(\theta, \Delta\phi)$. The estimated p_{cc} is somewhat higher for simulations than to data, which we attributed to simplifications assumed in the detector simulation. This discrepancy, however, has a small impact in the estimator $\hat{N}_\mu$.

Additionally, we compared the bias of the estimator developed in this chapter to the one used in a previous work, which used a different approach to estimate the number of muons and to correct for the bias. We have shown both estimators to be compatible.

Finally, it is relevant to highlight that this method is generally applicable to any kind of segmented detector with time resolution.

Chapter 6

Reconstruction of the muon lateral distribution function

The muon content of an air shower is a mass sensitive observable as heavier primaries produce more secondary muons during the shower development than lighter ones. Typical air shower experiments, consisting of an array of detectors arranged in a grid, only sample a fraction of the surviving muons at the ground. Such is the case of the Pierre Auger Observatory. To overcome this, a muon lateral distribution function (MLDF) is used to fit the muon footprint in the array. Then, the muon density at a reference distance from the shower axis serves as a proxy for the muon content of the shower.

In this chapter, we describe and optimize the procedure to reconstruct the MLDF at the event level. In Section 6.1, we discuss the reasons of not using the time resolution of the detector in the MLDF fit, unlike all the previous analyses involving the UMD. In Section 6.2, we assess the impact in the MLDF fit results of switching from the previous likelihood to the likelihood model proposed in Chapter 4. In addition, a new way of fitting the core during the MLDF fit is introduced. We evaluate the discrimination power of ρ_{450} yielded by the new reconstruction in Section 6.3. Furthermore, we study the impact of leaving the MLDF slope fixed/free on the merit factor of the new recostruction. Finally, we provide a data-driven parameterization of the MLDF slope in Section 6.4.

6.1   On the time information of the detector

In all of the previous analyses of the UMD data, the time resolution of the detector was included. This means that, in contrast to the formality described in Section 4.1, the trace was divided into time windows and a number of muons in each window was estimated. Subsequently, the total number of muons in a detector was obtained by summing over the number of estimated muons in each window.

In the analysis of the PMT data [62], muons were counted in windows of $\sim$22 ns (7 time bins), while in the first analyses of SiPM data [72, 73] a window of $\sim$56 ns (18 bins) was used. The window length in the analyses were selected based on the time response of the different photodetectors and their associated electronics. Later, in Ref. [66], it was shown that dividing the trace in windows, together with a sub-optimal modeling of the dead time of the detector, can lead to biases in the estimators, particularly for large number of muons. Thus, an improved strategy accounting for dead channels was developed. This strategy was used in the analysis of the mean LDF of the UMD SiPM data in Ref. [70].

Due to this precedent, we deem necessary to discuss the reasons behind the choice of not using the time resolution in this work.

The expressions of Eq. (4.4) and Eq. (4.5) (and the subsequent modifications to account for corner-clipping, inefficiency and noise derived in Section 4.1) are built from k, the total number of segments with at least one muon pattern in the entire 6.4 μs-long trace. Consequently, this approach does not utilize the time information of the muon trace: a bar showing multiple patterns throughout its trace is treated the same as a bar showing only one pattern. As a result, all the probability models derived depended solely on the total number of muons irrespective of their arrival time distribution.

Nevertheless, muons arrive at the detector spread in time with a time distribution $d\mu(t)/dt$. The total number of expected muons corresponds to the integral of the distribution over the duration of the trace, $\mu = \int (d\mu/dt)\, dt$. In an effort to use all the available information from the detector, the likelihood of Eq. (4.3) was extended to consider the time resolution of the detector in Ref. [74]. This was achieved by dividing the trace in n_w time windows. In each window, Eq. (4.3) is applied:

$$L(\vec{k}, \vec{\mu}) = \prod_{j=1}^{n_w} \binom{n_s}{k_j} e^{-\mu_j} (e^{\mu_j/n_s} - 1)^{k_j}, \tag{6.1}$$

where k_j and μ_j are the total number of bars with pattern and the number of expected muons in the j-th time window, respectively. μ_j is obtained by integrating the time distribution in the j-th window. It follows that $\mu = \sum_j^{n_w} \mu_j$.

We note that the observable has now changed from a single integer k in Eq. (4.3), to a vector of integers $\vec{k} = (k_1, .., k_{n_w})$ in Eq. (6.1). Thus, contrary to Eq. (4.3), Eq. (6.1) is sensitive to the time distribution of the impinging muons through the k_j. Also, the single parameter μ in Eq. (4.3) is now replaced by the vector of expected muons in each window $\vec{\mu} = (\mu_1, .., \mu_{n_w})$.

As shown in Ref. [66], Eq. (6.1) is sub-optimal as it does not accounts for inhibited channels. When these are considered, the length of the time window can be reduced to a single time bin (i.e., $n_w = 2048$). With these modifications, Eq. (6.1) becomes

$$L(\vec{k}, \vec{\mu}) = \prod_{j=1}^{2048} \binom{n_s - n_j^{\text{inh}}}{k_j} e^{-\mu_j} (e^{\mu_j/(n_s - n_j^{\text{inh}})} - 1)^{k_j}, \tag{6.2}$$

where n_j^{inh} denotes the number of inhibited (dead) channels in the j-th bin. These correspond to the number of bars that presented a muon pattern in an earlier time bin between $j - 12$ and $j - 1$, where 12 bins corresponds to the dead time of the detector (see Section 3.3.4). We notice that the only difference with Eq. (6.1) is the replacement of n_s by $n_s - n_j^{\text{inh}}$. It follows that the effective segmentation of the detector, i.e., the number of available non-inhibited bars, changes in each bin and is given by $n_s - n_j^{\text{inh}}$.

By maximizing the likelihood of Eq. (6.2), the estimator for μ can be obtained:

$$\hat{\mu} = \sum_j^{2048} -(n_s - n_j^{\text{inh}}) \ln(1 - k_j/(n_s - n_j^{\text{inh}})). \tag{6.3}$$

The same reasoning can be used to consider the time resolution in the case of N_μ. For completeness, we write the expressions below:

$$L(\vec{k}, \vec{N_\mu}) = \prod_{j=1}^{2048} \binom{n_s - n_j^{\text{inh}}}{k_j} S(N_{\mu_j}, k_j) \frac{k_j!}{(n_s - n_j^{\text{inh}})^{N_{\mu_j}}}, \tag{6.4}$$

$$\hat{N}_\mu = \sum_j^{2048} \frac{\ln(1 - k_j/(n_s - n_j^{\text{inh}}))}{\ln(1 - 1/(n_s - n_j^{\text{inh}}))}.$$ (6.5)

Following the naming adopted in Ref. [66, 70], we refer to Eq. (6.2) and Eq. (6.4), and its corresponding estimators of Eq. (6.3) and Eq. (6.4), as the one-bin strategy since the muon trace is analyzed in windows of one time bin. In contrast, we refer to Eq. (4.3) and Eq. (4.4) (and to Eq. (4.2) and Eq. (4.5) for N_μ) as the infinite window strategy, since the muon trace is analyzed in a single window equal to the total length of the trace.

Both strategies possess pros and cons. The one-bin strategy is useful for reconstructing the time distribution of muons [66], crucial for timing studies, such as those aiming at reconstructing the muon production depth profile of the shower[1]. However, the arrival times of the muons is irrelevant for the purpose of LDF fitting. Indeed, the relevant parameter for the fit of the LDF is μ (see Eq. (4.1)), while Eq. (6.2) is a function of $\bar{\mu}$. Due to the lack of knowledge of $d\mu/dt$ (and therefore of the μ_j's), the likelihood of Eq. (6.2) can not be computed for a given μ. In Ref. [74], this is overcome by using the profile method treating the μ_j as nuisance parameters. This lead to an approximate likelihood which resulted in a slight improvement in the resolution of the estimator of the muon shower size, particularly at higher energies, and in an increase of unsaturated events. However, in the original publication, the number of time windows was small compared to the total number of bins in the trace since inhibited channels were not taken into account. Applying the profile method to Eq. (6.2) would mean having 2048 nuisance parameters for each of the modules in the event, adding complexity and time to the already computationally expensive process of LDF fitting.

In addition, Eq. (6.2), and thus the estimator of Eq. (6.3), is sensitive to the undershoot present in the fast-shaper signal [66, 75]. Due to this, a signal generated by a late muon can be mounted on top of the undershoot of the signal of an earlier muon in the same bar. As a consequence, the late muon signal, which would have generated a pattern match had the undershoot not existed, could fail to produce a muon pattern, leading to under-counting[2]. This generates a non-trivial bias in the estimator of Eq. (6.3) that depends not only on the total number of impinging muons but also on their time distribution. Although this bias can be removed to certain extent from the estimators of Eq. (6.3) by using air shower and full detector simulations (e.g. via Eq. (5.13) used in Ref. [70]), it is not clear how to include the undershoot effect in the likelihod of Eq. (6.2), necessary for the event-wise MLDF fit. In contrast, Eq. (4.3) and Eq. (4.4) are insensitive to this effect, as it is enough with the earliest muon pattern in the bar to mark it as triggered.

For the previously mentioned reasons, we consider the infinite window strategy the more suitable and conservative approach for the purpose of LDF fitting at the event level. Based on these considerations, it has been adopted by the Observatory as the official strategy in the UMD reconstruction chain in $\overline{\text{Off}\underline{\text{line}}}$.

6.2 Reconstruction optimization

A modified NKG function, like the one used in the Kascade-Grande experiment, was found to provide a good representation of the UMD data. Is thus chosen as the model to fit the MLDF at every event. The function is subsequently evaluated at a reference distance to be

---

[1]In this direction, the study on the time response of the detector shown in Appendix B can be used to estimate the uncertainty in the true arrival time of muons.

[2]The undershoot can extend up to 18 time bins [75]. Thus, increasing the inhibition window from 12 to 30 bins could be benefitial to reduce the impact of the effect, although it would not supress it completely. However, such a large window would make the strategy to effectively perform as the infinite window strategy.

used as a proxy of the total number of muons in the shower. The reference distance, selected to minimize the systematic uncertainty due to the unknown true shape of the LDF, depends almost exclusively on the spacing and shape of the array [38]. For the infill array of the Pierre Auger Observatory, it has been found to be 450 m both for the SD [76] and UMD [63].

The expression for the modified NKG is given by

$$\rho(r) = \rho_{450} \left(\frac{r}{450 \text{ m}} \right)^{-\alpha} \left(\frac{1 + r/r_0}{1 + 450 \text{ m}/r_0} \right)^{-\beta} \left(\frac{1 + (r/10r_0)^2}{1 + (450 \text{ m}/10r_0)^2} \right)^{-\gamma}, \qquad (6.6)$$

where $\alpha = 0.75$, $\gamma = 3$ and $r_0 = 320$ m. These values were found to be optimal to describe the mean LDF observed by the UMD [70]. ρ_{450} is the muon density at the reference distance and β is a shape parameter usually referred as the slope of the LDF. A larger (smaller) value of this parameter translates into a steeper (flatter) LDF.

Like in the SD case, β is only left free if there is enough spacing between the detectors around 450 m to provide a reliable fit. The conditions to fit β are:

- A minimum number of 5 candidates UMD stations. A UMD station is candidate if it has at least one candidate module.

- At least one UMD station in the valid range of $250 \text{ m} \leq r \leq 750 \text{ m}$.

- If there are more than one UMD station in the valid range, the maximum mutual distance has to be larger than 250 m.

- If there are more than two UMD stations in the valid range, the maximum mutual distance has to be larger than 165 m.

- If there are more than three UMD stations in the valid range, the maximum mutual distance has to be larger than 125 m.

If none of the previous conditions are met, β is fixed according to a parameterization depending on the zenith angle and energy of the shower. Said parameterization is obtained using the subset of events in which β was left free as detailed in Section 6.4. Lastly, it is worth to add that the muon LDF is fitted only if there is a minimum of three UMD stations with at least one reconstructed muon each. This condition is necessary to avoid attempting to fit an LDF in events with too few muons.

6.2.1 Event likelihoods

The optimal parameters of the LDF are obtained via a log-likelihood minimization. To this aim, UMD modules in an event are divided into three categories: saturated, silent and candidate. Saturated modules are those in which all the bars in the detector are triggered, silent modules are those that are paired to an untrigered SD tank and candidate detectors correspond to those that are not saturated nor silent. In the following, we describe two methods to combine the information of the detectors into an event likelihood to fit a LDF.

The first method to fit a muon LDF in an event level was proposed in Ref. [65], in which the optimal parameters $\vec{p}$ of the muon LDF were obtained by minimizing $\mathcal{L} = -\ln(L)$, where the event likelihood L was given by

$$L = \prod_i^{N_{\text{sat}}} \frac{1}{2} \left(1 - \text{Erf} \left(\frac{\hat{N}_{\mu_i}^{\text{sat}} - \mu(r_i; \vec{p})}{\sqrt{2\mu(r_i; \vec{p})}} \right) \right) \times$$
$$\prod_i^{N_{\text{cand}}} \frac{\mu(r_i; \vec{p})^{\hat{N}_{\mu_i}} e^{-\mu(r_i; \vec{p})}}{\hat{N}_{\mu_i}!} \times \qquad (6.7)$$
$$\prod_i^{N_{\text{sil}}} e^{-\mu(r_i; \vec{p})} \left(1 + \mu(r_i; \vec{p}) + \frac{\mu(r_i; \vec{p})^2}{2} \right),$$

where the first, second and third term correspond to saturated, candidate and silent modules, respectively. r_i indicates the distance from the shower core of the i−th module, $\mu(r_i; \vec{p})$ is the expected number of muons in the i−th module given by $\mu = \rho(r_i; \vec{p}) A \cos\theta$, where A is the area of the detector, θ is the zenith angle of the shower and $\rho(r_i; \vec{p})$ is the muon density given by Eq. (6.6). In addition, $\hat{N}_{\mu_i}$ denotes the bias-corrected number of estimated muons in the i-th module given by Eq. (5.11)[3]. Lastly, N_{sat}, N_{cand} and N_{sil} correspond to the total number of saturated, candidate and silent modules in the event.

For saturated modules, a point estimation of the number of muons is not possible and only a lower limit can be established. Nevertheless, this information can be used to constrain the LDF at distances close to the core, preventing it from predicting excessively low muon densities near saturated modules. Thus, the formula corresponding to the saturated case in Eq. (6.7) is derived from the approximation of a Poisson distribution with mean μ by a Gaussian distribution with mean μ and standard deviation $\sqrt{\mu}$ when μ is large. Therefore, the probability of the number of muons to be larger than a lower limit $\hat{N}_{\mu_i}^{\text{sat}}$ is

$$P(n > \hat{N}_{\mu_i}^{\text{sat}}) = \frac{1}{\sqrt{2\pi\mu}} \int_{\hat{N}_{\mu_i}^{\text{sat}}}^{\infty} dn \, e^{-\frac{(n-\mu)^2}{2\mu}} = \frac{1}{2} \left[1 - \text{Erf} \left(\frac{\hat{N}_{\mu_i}^{\text{sat}} - \mu}{\sqrt{2\mu}} \right) \right].$$

For silent detectors, there is no measurement available. Still, this constitutes valuable information that can be used to constrain the LDF at large distances, preventing it from predicting excessively high muon densities in regions with silent stations. The term corresponding to the silent detectors corresponds to the probability of the number of muons to be less or equal than two:

$$P(n \leq 2) = \sum_{n=0}^{2} e^{-\mu} \frac{\mu^n}{n!} = e^{-\mu} \left(1 + \mu + \frac{\mu^2}{2} \right).$$

The formula for the candidate modules takes into account that the number of muons impinging a detector fluctuates as a Poisson variable with mean μ. This is not optimal since, as discussed in Section 4.3, it underestimates the fluctutations of $\hat{N}_\mu$, particularly for large number of muons. Additionally, it is worth noting that $\hat{N}_\mu$ is in general a real number, while Poisson statistics requires the measurement to be integer. Although not totally satisfying, this turns out not to be an obstacle since what is actually maximized (minimized) is not L but $-\ln L$. Thus, when the logarithm is taken in the Poisson term, the factorial $\hat{N}_{\mu_i}!$, the only expression that formally needs $\hat{N}_{\mu_i}$ to be integer, can be ignored as it does not depends on the minimization variables $\vec{p}$.

Lastly, we note that the likelihood from Eq. (6.7) was used in the analysis of the UMD PMT data [62] and in the first analyses of UMD SiPM data [72, 73].

The second method was introduced in Ref. [63], in which the distribution of the raw signal in a segmented detector k for a fixed μ, given by Eq. (4.3), was found. This improved

---

[3]At the moment of the publication, a sub-optimal estimator of N_μ that used the time resolution of the detecor was used. See Section 6.1

model naturally accounts for both the Poisson fluctuations in the number of muons and the segmentation of the detector. In Section 4.1 we extended the distribution to account for detector effects, being the corner-clipping muons the most important for the UMD case. The event likelihood is given by

$$
\begin{aligned}
L = {} & \prod_{i}^{N_{\text{cand}}+N_{\text{sat}}} \binom{n_s}{k_i} e^{-\mu(r_i;\vec{p})(1+p_{\text{cc}_i})} \left(e^{\mu(r_i;\vec{p})(1+p_{\text{cc}_i})/n_s} - 1\right)^{k_i} \times \\
& \prod_{i}^{N_{\text{sil}}} e^{-\mu(r_i;\vec{p})} \left(1 + n_s(e^{\mu(r_i;\vec{p})/n_s} - 1) + \frac{n_s(n_s-1)}{2}(e^{\mu(r_i;\vec{p})/n_s} - 1)^2\right),
\end{aligned}
\tag{6.8}
$$

where p_{cc_i} is the corner-clipping probability of the i-th module (see Section 4.1.2). The term corresponding to the silent modules is now obtained by requesting the probability of having k less or equal than two. We note that in this model, candidates and saturated modules have the same likelihood. Also, in contrast to Eq. (6.7), in Eq. (6.8) there is no need to go through the intermediate step of estimating the number of muons in each detector: the raw signal k is used in the candidate and saturated modules.

Since a Poisson likelihood is assumed for candidate modules, we will refer to the (log-)likelihood of Eq. (6.7) as the Poisson likelihood. Correspondingly, we will refer to Eq. (6.8) as the Binomial likelihood. We will assess the perfomance of the two likelihoods in Section 6.2.3.

6.2.2 Core fitting

During the LDF fit of the SD tanks, an estimate $\vec{c}_{\text{SD}} = (x_{\text{SD}}, y_{\text{SD}})$ of the position of the core in the ground plane is obtained. This parameter is highly relevant as it determines the shower plane distances of the detectors. In order to have a reliable estimate of the core, a quality cut, dubbed 6T5, is applied to SD events requesting the station with largest signal to be surrounded by 6 working stations (not necessarily triggered) (see Section 3.1). This ensures that the shower lands inside a working hexagon allowing for a reliable reconstruction of the core position.

A common practice to fit the LDF of subordinate detectors, like the SSD and UMD, is to leave the core position fixed to the one obtained by the SD reconstruction. This approach is not optimal since uncertainty in the core position translates into uncertainty in the shower plane distances of the subordinate detectors and ultimately into the LDF. This effect is particularly relevant for stations close to the core, where the LDF raises very steeply, in which a small offset in the shower plane distance can produce a large shift in the LDF values. Thus, if the core uncertainty is not accounted for, it can bias the fit of the LDFs of subordinate detectors.

Ideally, the core position should be left free in the fit of the LDF of subordinate detectors as well. In this way, the core uncertainty is naturally propagated into the other LDF parameters through the covariance matrix of the fit. However, this would come at the cost of requesting a 6T5 condition to the subordinate detectors too, with the corresponding impact in the number of events. For the UMD array, the dataset of available events for physics analyses would be reduced roughly 90%. It is apparent that an alternative solution is needed.

For the SSD, this is overcome by propagating the core uncertainty into the variance model of the SSD signals [77]. This strategy is not applicable to the UMD since it does not need a variance model: the entire distribution of the signal k is completely determined by the single parameter μ (see Eq. (4.3)). Therefore, we propose a different procedure for the UMD. It consists of leaving the core as a free parameter but adding an extra factor in the likelihood that penalizes core positions that are too far from the SD core. To this aim, we model the distribution of the UMD core (x, y) as a bivariate gaussian whose expected value

corresponds to $\vec{c}_{\mathrm{SD}}$, and whose covariance matrix is given by the covariance matrix of the core coordinates obtained in the SD fit. When taking the logarithm of this factor, a χ^2-like term is obtained.

Therefore, the log-likelihoods corresponding to Eq. (6.7) and Eq. (6.8) now become

$$\mathcal{L}(x, y, \rho_{450}, \beta) = -\sum_{i=1}^{N_{\mathrm{sat}}} \ln L_{\mathrm{sat}_i}(x, y, \rho_{450}, \beta) - \sum_{i=1}^{N_{\mathrm{cand}}} \ln L_{\mathrm{cand}_i}(x, y, \rho_{450}, \beta)$$
$$- \sum_{i=1}^{N_{\mathrm{sil}}} \ln L_{\mathrm{sil}_i}(x, y, \rho_{450}, \beta) + \frac{1}{2}\chi^2(x, y), \tag{6.9}$$

$$\mathcal{L}(x, y, \rho_{450}, \beta) = -\sum_{i=1}^{N_{\mathrm{cand}}+N_{\mathrm{sat}}} \ln L_{\mathrm{cand}_i}(x, y, \rho_{450}, \beta) - \sum_{i=1}^{N_{\mathrm{sil}}} \ln L_{\mathrm{sil}_i}(x, y, \rho_{450}, \beta)$$
$$+ \frac{1}{2}\chi^2(x, y), \tag{6.10}$$

where χ^2 is given by

$$\chi^2(x, y) = \frac{1}{1 - \rho_{\mathrm{SD}}^2} \left[\left(\frac{x - x_{\mathrm{SD}}}{\sigma_{x_{\mathrm{SD}}}} \right)^2 + \left(\frac{y - y_{\mathrm{SD}}}{\sigma_{y_{\mathrm{SD}}}} \right)^2 - 2\frac{\rho_{\mathrm{SD}}}{\sigma_{x_{\mathrm{SD}}}\sigma_{y_{\mathrm{SD}}}}(x - x_{\mathrm{SD}})(y - y_{\mathrm{SD}}) \right],$$

where $\sigma_{x_{\mathrm{SD}}}$, $\sigma_{y_{\mathrm{SD}}}$ are the errors in the SD core position and ρ_{SD} corresponds to the correlation between the SD core coordinates.

Eq. (6.10) and Eq. (6.9) constitute a new way to fit the core position with the UMD. It is thus necessary to evaluate its impact in the LDF fit. For this purpose, in what follows we focus only on Eq. (6.10). We use events with $\lg(E/\mathrm{eV}) > 17.5$ and $\theta < 45°$.

In the upper panel of Fig. 6.1, the LDF fit of a selected event with the core fixed to the SD core is shown. It is apparent that the fit is driven by the UMD modules that are closest to the core, biasing the LDF. The footprint of the event in the UMD array is shown in the middle panel of the same Figure, along with the SD core and its 1-sigma ellipse. The core position obtained when leaving it as a free parameter (with the penalization term) in the UMD fit is also shown. The UMD core remains in the vicinity of the SD core, being separated by a distance of ~ 35 m. Despite being a relatively minor correction in the core position, a clear improvement in the LDF fit can be achieved, as displayed in the lower panel. The ρ_{450} estimate changes from 0.04 m^{-2} to 0.31 m^{-2}, highlighting the importance of fitting the core position.

To illustrate the importance of the penalization term in the log-likelihood, the footprint of event 181064399001 is presented in Fig. 6.2. The core of the shower lands in a hexagon that, at the moment of the event, was only partially filled with UMD modules. This is the case for the vast majority of the events in the UMD dataset. The UMD cores obtained with (triangle) and without (star) the penalization term are shown in the Figure. It is evident that when no penalization term is used, the UMD core is wrongly shifted towards the region filled with UMD detectors.

A histogram with the distance between the SD and UMD core for all the events in the dataset is shown in Fig. 6.6. The mean distance between cores is ~ 16 m and the 95%-quantile is ~ 45 m, which demonstrates that the penalization term is indeed constraining the UMD core close to the SD core.

To evaluate the impact of leaving the core free in the MLDF slope, we use the subset of events with enough information to fit β (see Section 6.2). Each event is reconstructed with

the core free and fixed and the β estimate in each case is compared. In Fig. 6.3, the histogram of the relative difference between the estimate of β with the core free and fixed is shown. It is evident that both cases are compatible.

In Fig. 6.4, the ρ_{450} estimates obtained with a free and a fixed core are compared. For this, β was fixed according to the parameterization described in Section 6.4. For the predominant majority of events, there is no significant difference between the two cases. This is not the case for $\sigma_{\rho_{450}}$, the uncertainty in the ρ_{450} estimate, as displayed in Fig. 6.5. Like with the MLDF slope, the uncertainty is larger when the core is fitted since the uncertainty in the core position is now accounted for and it naturally propagates into $\sigma_{\rho_{450}}$ in the fitting procedure. Therefore, leaving the core free gives an improved and more conservative error estimate of the ρ_{450}.
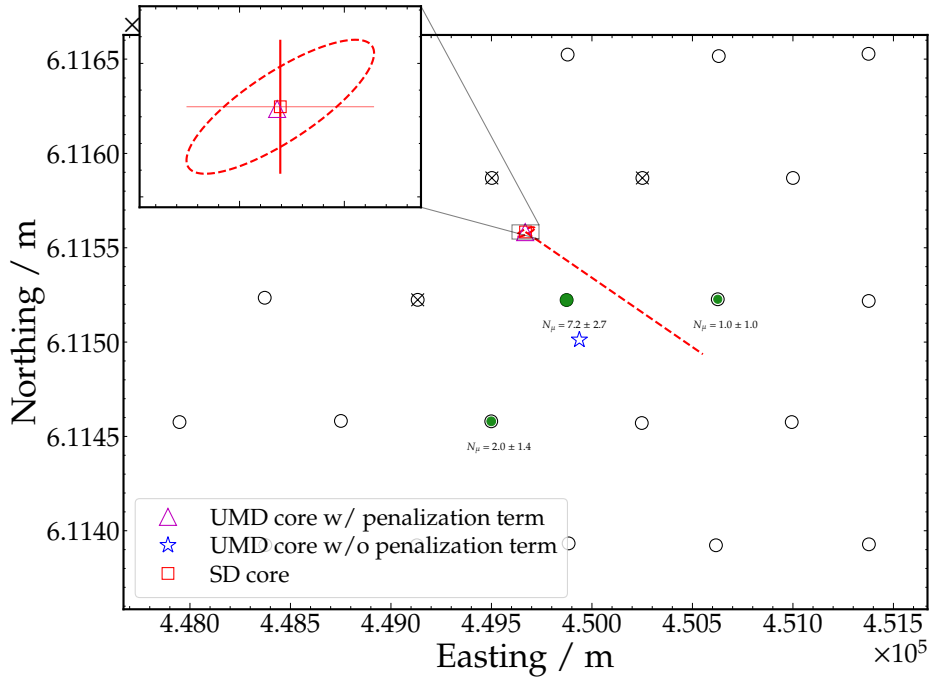
Figure 6.2: Footprint of the event 181061885800 recorded on April 16th of 2018. The size of the marker is proportional to the total number of muons measured by the UMD modules. Black crosses represent stations of the hexagon that did not have a UMD deployed at the moment of the event. Red dashed line represents the axis of the shower. In the inset panel, a zoom in the SD core region can be observed, along with its 1σ ellipse and its errors (vertical and horizontal error bars). The triangle (star) indicates the UMD core obtained with (without) the penalization term in the log-likelihood.
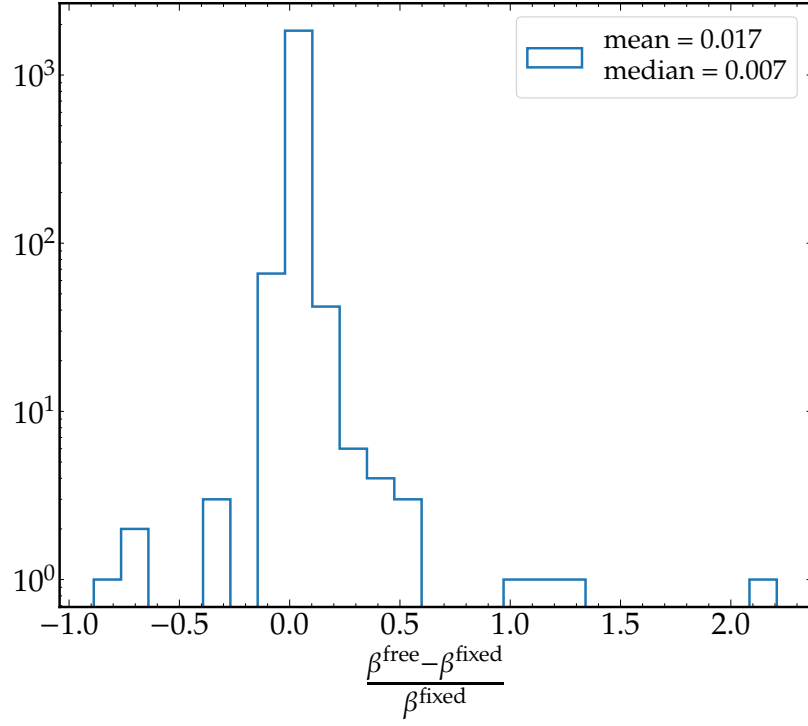
Figure 6.3: Relative difference of the β estimate when the core is free and fixed.
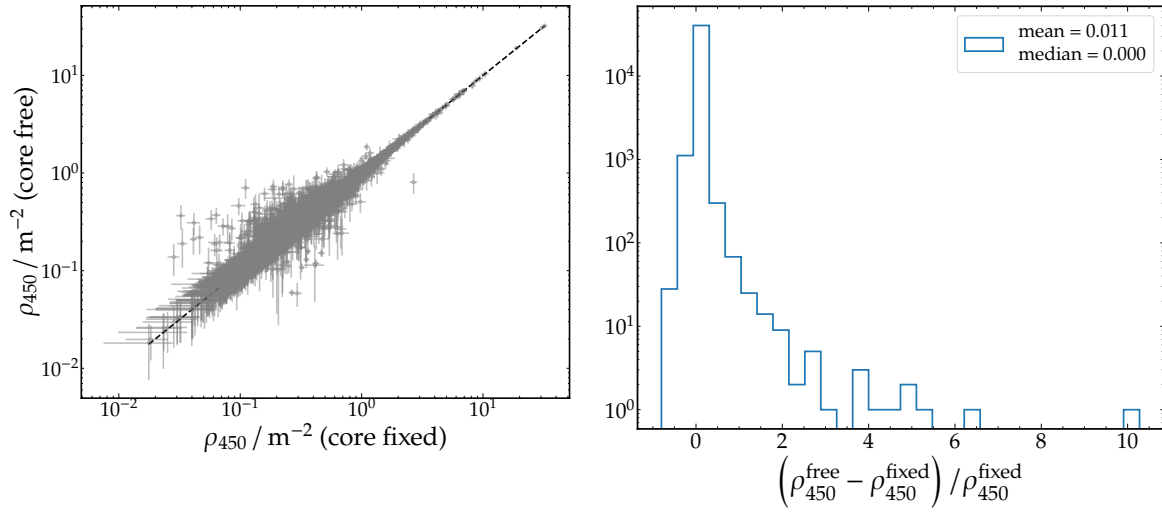

Figure 6.4: Event-level comparison of the ρ_{450} estimate with and without fitting the core. *Left*: Scatter plot. Dashed line indicates the identity. *Right*: Histogram of the relative difference.
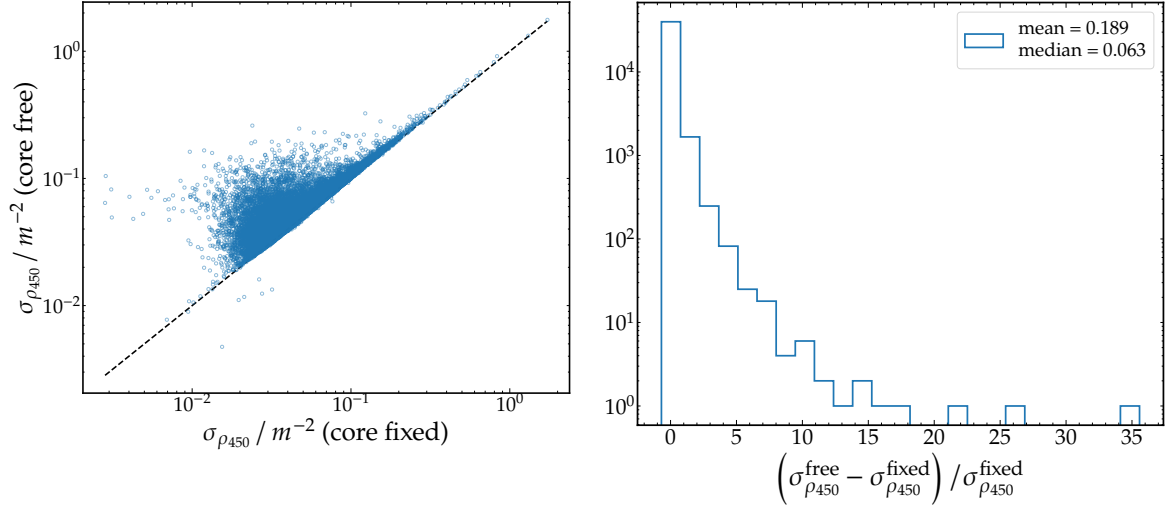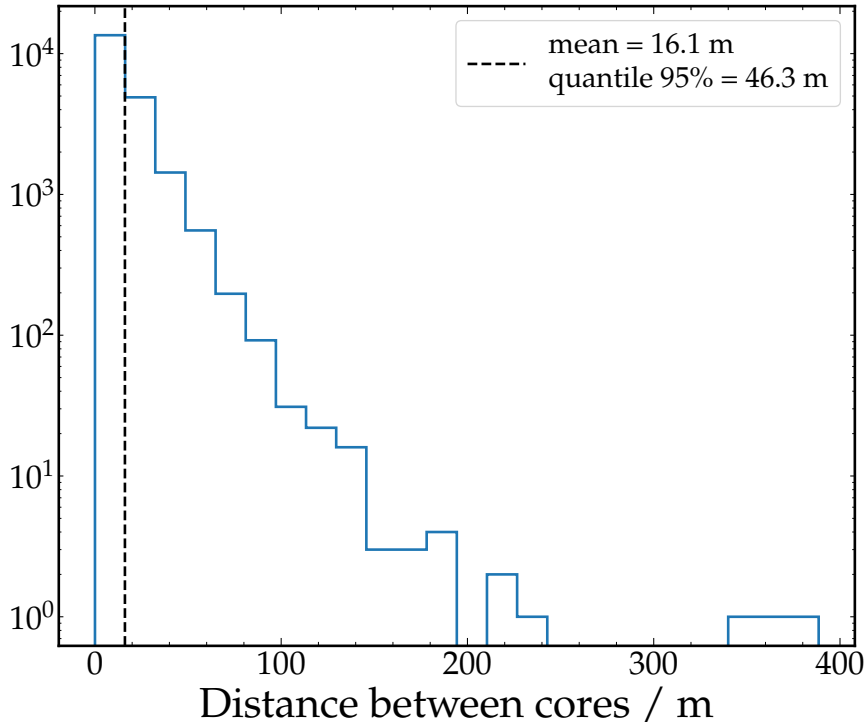
Figure 6.5: Event-level comparison of $\sigma_{\rho_{450}}$, the uncertainty in ρ_{450} estimate, with and without fitting the core. *Left*: Scatter plot. Dashed line indicates the identity. *Right*: Histogram of the relative difference.

Figure 6.6: Histogram of the distance between de SD and UMD cores.

Lastly, we assess the impact in the bias of ρ_{450} of leaving the core free in events whose core lands very close to a station with simulations. To that end, we randomly toss the core in a small tile of 100 m side centered at a station using the set of showers of energy $10^{17.5}$ eV. The bias in ρ_{450} as a function of θ for proton and iron is shown in Fig. 6.7, for the cases with core free (filled markers) and fixed (unfilled markers). When the core is fixed, the bias for proton (iron) can reach up to $\sim$50% ($\sim$20%) for the most vertical zenith angles. In contrast, the bias is significantly lowered when the core is free.
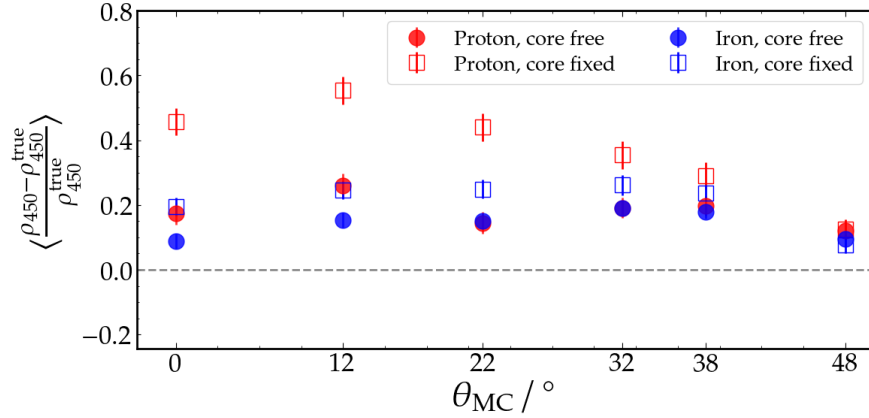
Figure 6.7: Bias in the muon shower size as a function of θ. The case in which the core is left free (fixed) is indicated with filled (unfilled) markers.

6.2.3 Performance of the different likelihoods

As already pointed out, the likelihood of Eq. (6.10) provides a more acccurate modeling of the signal fluctuations (see Section 4.3) since, in addition to the Poissonian fluctuations in the number of muons, it accounts for the fluctuations arising from detector segmentation. It is hence preferred over Eq. (6.9). Consequently, we propose the official reconstruction chain of the UMD data of the Observatory to switch from Eq. (6.9) to Eq. (6.10). In this section, we assess the impact of this change in ρ_{450} and β using the discrete EPOS-LHC simulation library described in Section 7.5.

Each shower was thrown once in the array and the resulting simulated signals were used to fit the LDF of Eq. (6.6) using Eq. (6.9) and Eq. (6.10). The simulation of both the SD and UMD, and the reconstruction procedure was done using $\overline{\text{Offline}}$. The values of p_{cc} found for simulations in Chapter 5 were used.

In each simulated event, a ring of 11 UMD stations placed at 450 meters from the shower core is used to obtain the true muon density at 450 meters, which we denote ρ_{450}. For this, the true muon density in each of the modules in the ring is calcuated by dividing the true number of injected muons by the effective area $A \cos \theta$. Subsequently, ρ_{450} is obtained averaging over the true muon densities of all the modules in the ring. This value can be compared to the estimate $\hat{\rho}_{450}$ retrieved by the LDF fit to assess the bias of the LDF.

Impact on β

For the analysis of the UMD data, β is left fixed during the LDF fit of every event (see Section 6.3). The value of β is obtained from a data-driven parameterization as explained in Section 6.4. Therefore, to replicate the same conditions than the LDF fits in data, it is first necessary to find a parameterization for β optimal for simulations. In what follows, we assess what is the impact of the likelihood model chosen in such parameterization.

The mean β values obtained as function of $\sec \theta$ for the three available energies for proton and iron primaries are shown in Fig. 6.8. These were obtained in events with the right topology to leave the parameter free as explained in Section 6.2. The values obtained with the likelihood of Eq. (6.9) are represented with squares, while the ones yielded by Eq. (6.10) are indicated with triangles. For the smallest energies, the values of β given by both likelihoods are compatible within statistical uncertainties. For the largest energy ($10^{18.5}$ eV), the binomial likelihoods yields slightly larger β values. However, this difference is of

the order of $\lesssim 1\%$ and is negligible for all practical purposes. It is thus evident that the two likelihoods lead to compatible parameterizations of β.

It is worth noting that β decreases with zenith angle, which means that LDF becomes flatter for inclined showers. It is also clear that β increases with energy. Both effects can be understood by the fact that more vertical (and more energetic) showers reach their maximum muon production depth closer to the ground, leaving a steeper footprint in the array. For the same reason, proton showers show slightly larger values of β (i.e. steeper LDFs) than iron showers.

For each energy, the following linear function in $\sec\theta$ was fitted to the β values obtained by the binomial likelihood:

$$\beta = m\left(\sec\theta - 1.2\right) + b. \tag{6.11}$$

The results of such fits are indicated with dashed lines in Fig. 6.8. The dependence of m and b with energy is displayed in Fig. 6.9. The slope m is independent of energy and shows only a slight dependence on the primary particle, being somewhat higher for iron. Therefore, we take the weighted mean over the two primaries and the three energies, yielding $\overline{m} = -1.38$, as indicated by the dashed line in the left panel of the figure. The offset b shows a linear increase with log-energy, and is slightly larger for proton than iron primaries. We combine the values of both primaries to fit a linear model to the dependence of b with $\lg(E/\text{eV})$,

$$b = b_1\left(\lg(E/\text{eV}) - 17.8\right) + b_0, \tag{6.12}$$

yielding $b_0 = 2.86$ and $b_1 = 0.25$. The result is represented with a dashed line in the right panel of the figure. Therefore, the set of values $(\overline{m}, b_0, b_1)$ defines the parameterization to fix the β parameter during the reconstruction in simulations.
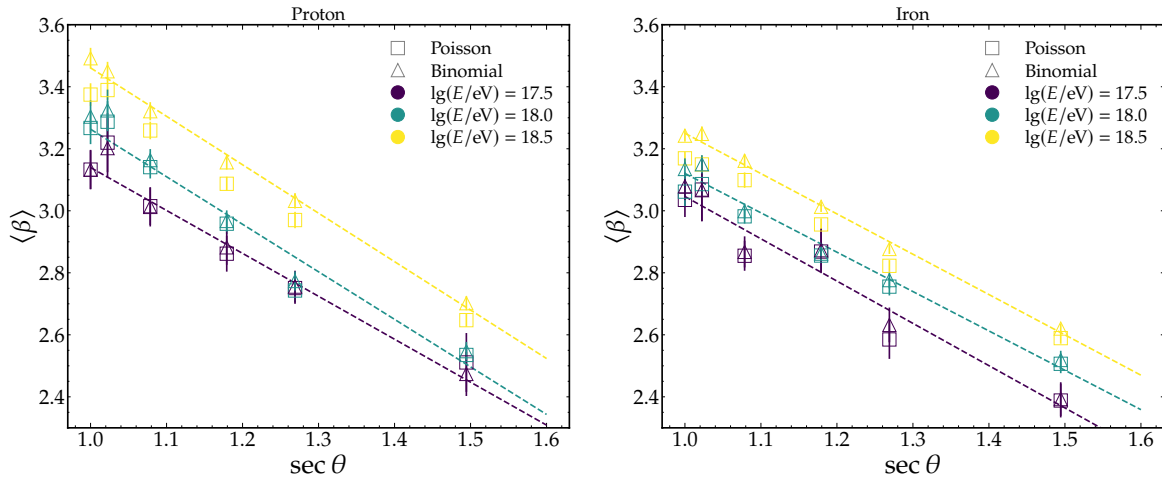

Figure 6.8: Mean β as a function of $\sec\theta$ for different energies using the Poisson (squares) and binomial (triangles) likelihoods. Left (right) panel shows proton (iron) simulations. Dashed lines indicate the results of the fits of Eq. (6.11).
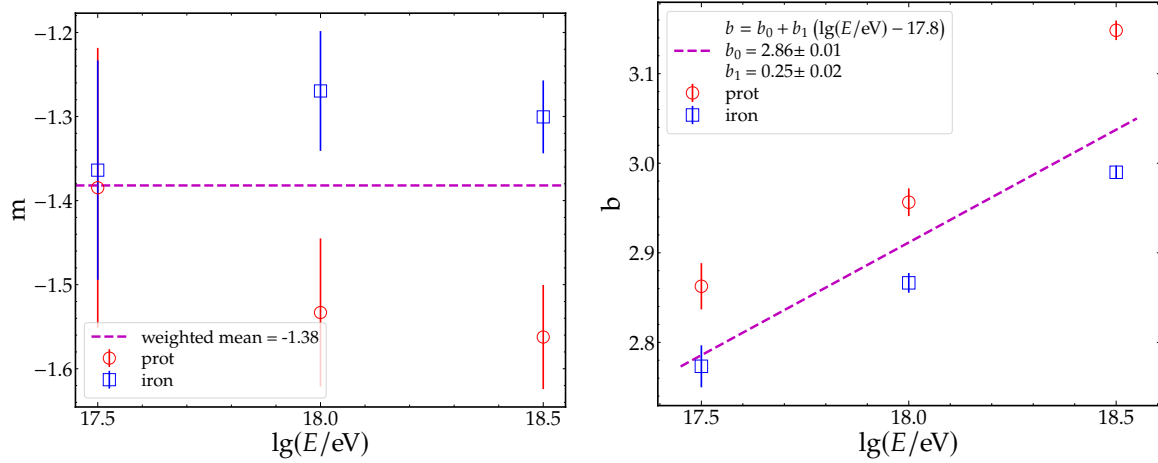
Figure 6.9: Slope (left) and intercept (right) of the model of Eq. (6.11) as function of energy for both primaries.

Impact on ρ_{450}

The histogram of the relative difference between the ρ_{450} estimates given by the two likelihoods for proton (iron) is shown in the left (right) panel of Fig. 6.10. When the event is not saturated, both likelihoods lead to compatible estimates. However, when the event is saturated (i.e., at least one UMD module is saturated), greater dispersion between the two likelihoods is observed, with the presence of several outliers. This is somehow expected as the the likelihoods have different expressions to treat saturated detectors (see Eq. (6.7) and Eq. (6.8)).

An example of a saturated event, corresponding to a proton primary of 10^{18} eV and zenith angle of $22°$, is shown in Fig. 6.11. The relative difference between the ρ_{450} estimates is $\sim 40\%$. The LDF fit using the Poisson (binomial) likelihood is displayed in the upper (lower) panel. The red triangular markers indicate saturated modules, the green square shows the true ρ_{450} obtained with the dense ring of detectors, and the magenta star corresponds to the estimate of the ρ_{450} given by the LDF. It is apparent that the binomial likelihood results in a better fit, yielding a ρ_{450} estimate significantly closer to the true value than the Poisson case.

The bias of the different methods can be assessed using the true ρ_{450} obtained with the ring of detectors at 450 m. The bias and resolution of $\hat{\rho}_{450}$ are displayed as a function of energy for each primary species and likelihood model in the upper and middle panel of Fig. 6.12, respectively. No dependence on the zenith angle was found. The two likelihoods yield compatible biases and resolutions.

During the LDF fit, a 1σ error interval is computed for ρ_{450}. In the lower panel of Fig. 6.12, the coverage of this interval for the Poisson (circles) and binomial (squares) likelihoods, calculated as the fraction of events where the interval includes the true ρ_{450}, is shown. The coverage of the Poisson likelihood decreases with energy, while the binomial likelihood remains stable around 60%. This difference arises because the Poisson model ignores detector segmentation, underestimating signal fluctuations — as already explained — and, thereby, the uncertainty interval. In contrast, the binomial model accounts for segmentation, resulting in larger, more accurate uncertainty intervals and improved coverage. Similar results are obtained using QGSJetII-04 as hadronic model, as shown in Appendix E.
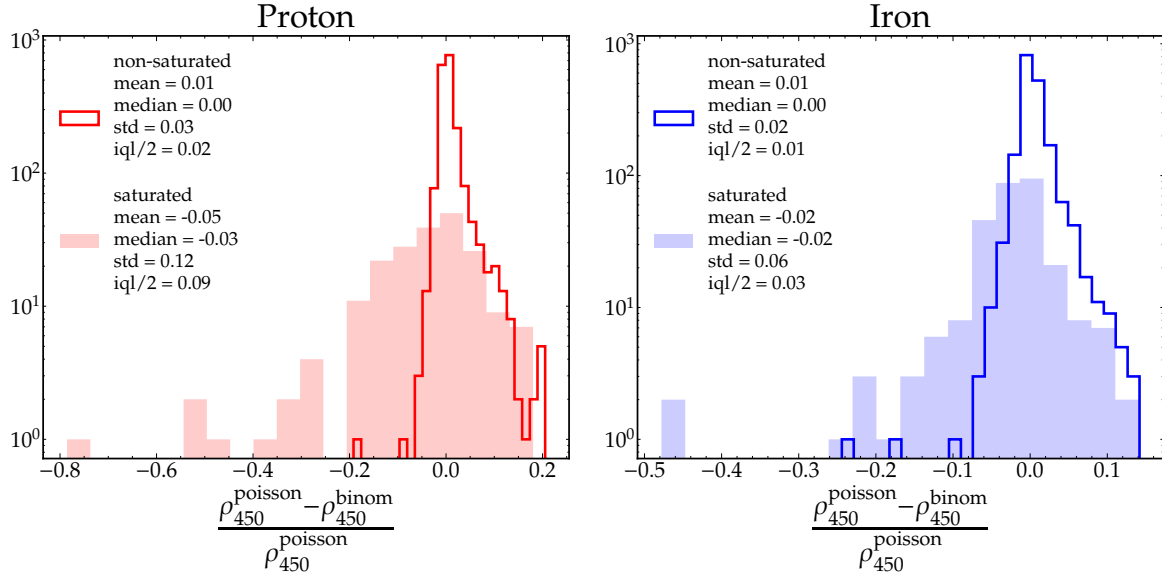
Figure 6.10: Relative difference between the ρ_{450} estimate of the Poisson and binomial likelihood for proton (left) and iron (right) primaries. Unfilled (filled) histogram correspond to non-saturated (saturated) events.
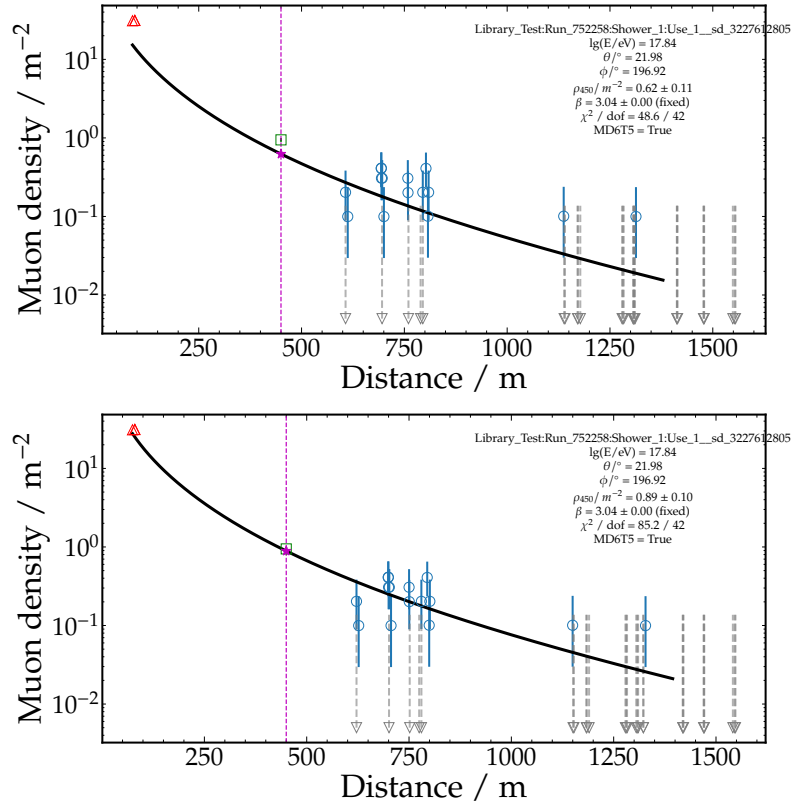

Figure 6.11: LDF fit of a proton shower of 10^{18} eV and zenith angle of $22°$ using the Poisson (upper panel) and the binomial likelihood (lower panel). Empty square indicate the true ρ_{450} obtained with the dense ring.
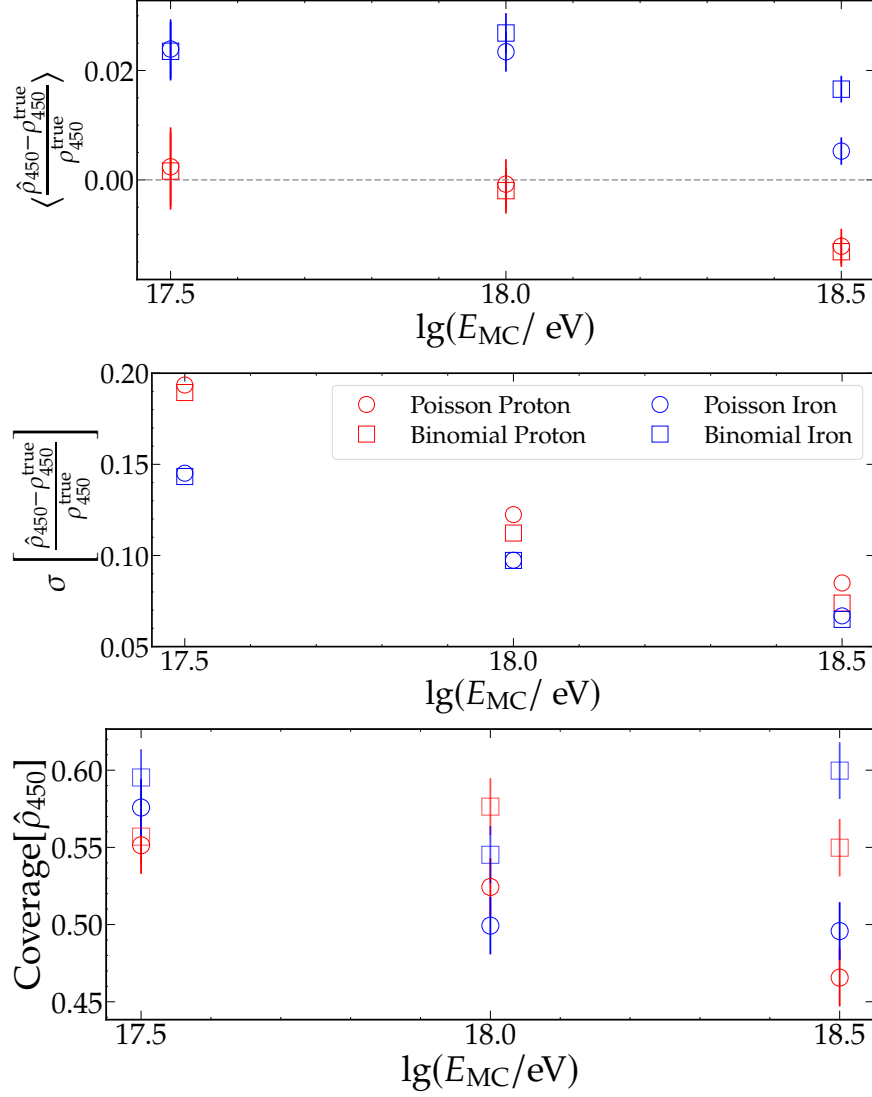
Figure 6.12: Bias (upper panel), resolution (middle panel) and coverage of the 1σ interval (lower panel) of $\hat{\rho}_{450}$ retrieved by the LDF fit for the Poisson (circles) and binomial (squares) likelihoods.

Finally, to further illustrate the difference between the methods in a real event, we show the LDF fit of event 180721359500 in Fig. 6.13. The poor fit yielded by the Poisson case is completely driven by the detectors closer to the core, since these have the largest weight in the likelihood. As a consequence, the UMD core is also shifted towards the position of this station. On the other hand, the binomial likelihood shows an improved fit since, as already mentioned, it correctly accounts for signal fluctuations, reducing the weight of detectors with large signals.
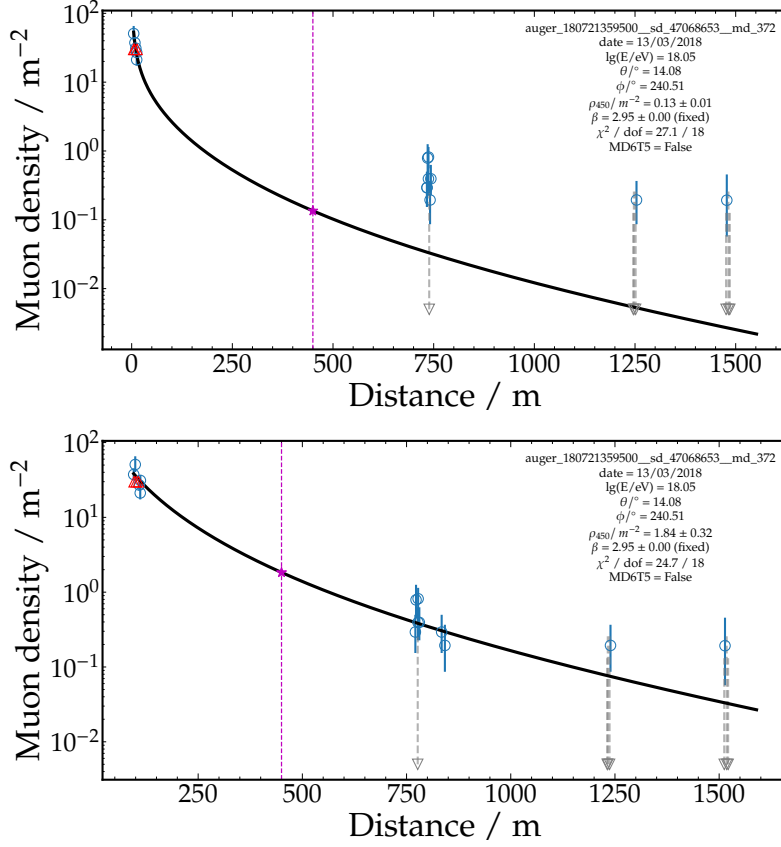
Figure 6.13: LDF fit of event 180721359500 using the Poisson (upper panel) and the binomial likelihood (lower panel).

6.2.4 Corner-clipping correction

In Section 5.1, the bias of the estimator $\hat{N}_\mu$ as function of θ with and without the corner-clipping correction was shown. We demonstrated that when the correction is applied, a flat behaviour with θ is observed, as desired (see Fig. 5.9).

However, $\hat{N}_\mu$ is a module level quantity and is not affected by any additional bias that the MLDF fitting process might be introducing. Thus, it is relevant to study how well the correction performs in the context of MLDF fitting.

For this purpose, we use a subset of simulations of proton and iron primares of 10^{18} eV. Each shower was reconstructed with and without the corner-clipping correction. The latter was accomplished by setting $p_{cc} = 0$ in Eq. (6.10), while the former used the parameterization of $\hat{p}_{cc}$ found for simulations in Chapter 5.

The bias of $\hat{\rho}_{450}$ in each case is shown as function of the zenith angle in Fig. 6.14. For both primaries, when no correction is applied, the bias increases with θ, similarly to what was observed for $\hat{N}_\mu$. In contrast, when the correction is applied, the bias remains constant around $\sim 2.5\%$ for all zenith angles, confirming that the corner-clipping correction is performing as desired.
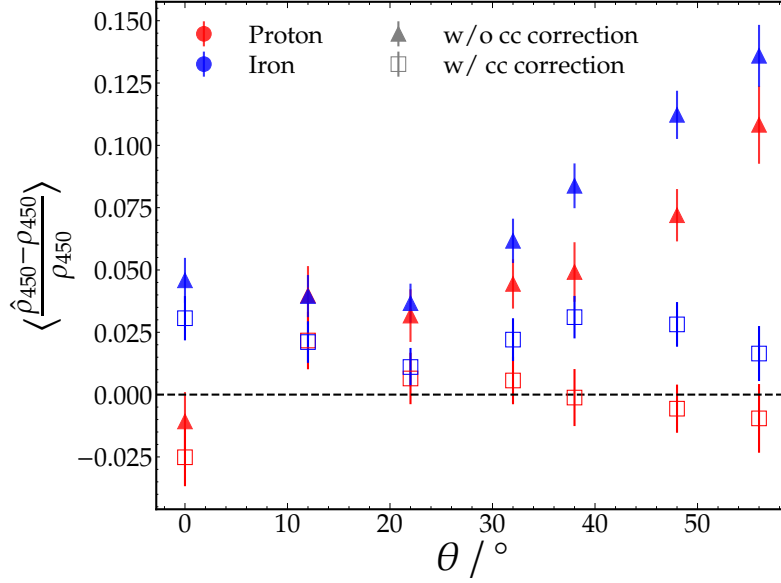
Figure 6.14: Bias of $\hat{\rho}_{450}$ as function of θ with (empty squares) and without (full triangles) the corner-clipping correction developed in Chapter 4 and Chapter 5. Proton (red) and iron (blue) primaries of energy 10^{18} eV with EPOS-LHC as hadronic model were used.

6.3 Discrimination power

The ultimate goal of measuring the muon content of extensive air showers is to discriminate between primary masses. Therefore, it is of our interest to characterize the discrimination power of ρ_{450}, especially after the new adjustments introduced in the reconstruction in the previous chapters and sections. To this aim, we introduce the merit factor

$$f = \frac{\langle \rho_{450} \rangle_{\text{Fe}} - \langle \rho_{450} \rangle_{\text{p}}}{\sqrt{\sigma^2_{\rho_{450_{\text{Fe}}}} + \sigma^2_{\rho_{450_{\text{p}}}}}}, \tag{6.13}$$

where $\langle \ \rangle_{\text{Fe (p)}}$ and $\sigma_{\rho_{450_{\text{Fe (p)}}}}$ indicate the mean and standard deviation over iron (proton) showers, respectively. We note that f measures how separated the mean of the two distributions are relative to their width. Therefore, the larger the value of f, the greater the discrimination power of the method.

For each energy and zenith angle, we computed the merit factor using the ρ_{450} estimate from the LDF fit, denoted as ρ_{450}^{LDF}. In order to have a proxy of the best achievable factor, we additionally compute the merit factor using the true ρ_{450} estimated with the dense ring of detectors at 450 m from the core, referred to as $\rho_{450}^{\text{dense}}$. The corresponding merit factors are denoted as f_{LDF} and f_{dense}, respectively. No dependence of f_{LDF} or f_{dense} on the zenith angle was found. Thus, we take the mean value of the merit factors over all the zenith angles for each energy. The merit factors as function of energy are presented in Fig. 6.15.
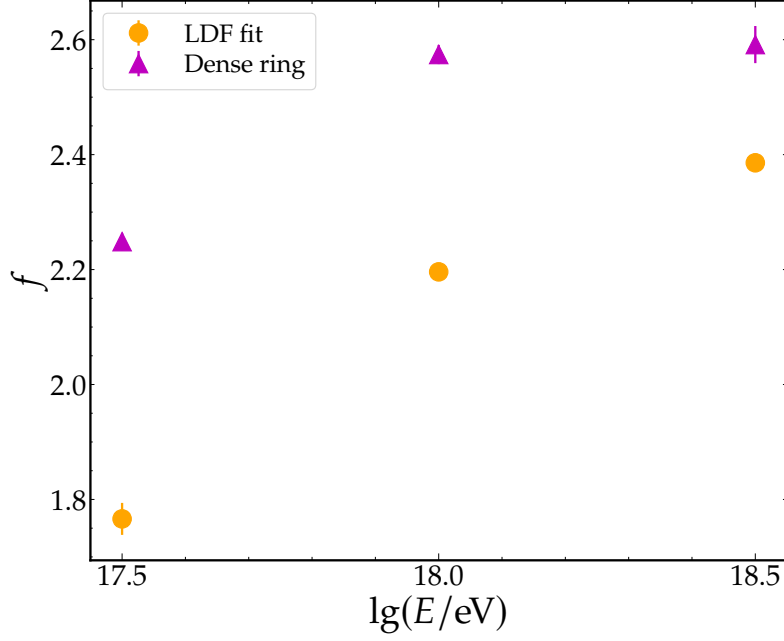
Figure 6.15: Merit factors as function of energy. The errorbars are estimated via the bootstrap method.

Since the relative fluctuations due to shower-to-shower fluctuations decrease with energy, the merit factors using both estimates increase with energy. However, we note that f_{LDF} increases more rapidly, becoming closer to the upper bound f_{dense} as energy increases. This can be explained by the fact that the resolution of ρ_{450}^{LDF} increases with energy. Indeed, more energetic showers possess a larger number of triggered detectors and larger number of muons, minimizing the Poissonian fluctuations in the number of detected particles.

To illustrate this, we show the relative standard deviation of ρ_{450}^{LDF} and $\rho_{450}^{\text{dense}}$ for both primaries as function of energy in the left panel of Fig. 6.16. It is apparent that the fluctuations of both estimates decreases with energy. The fluctuations of ρ_{450}^{LDF} can be thought as having a contribution of both shower-to-shower and reconstruction fluctuations:

$$\left(\frac{\sigma \left[\rho_{450}^{\text{LDF}} \right]}{\langle \rho_{450}^{\text{LDF}} \rangle} \right)^2 = \left(\frac{\sigma \left[\rho_{450} \right]}{\langle \rho_{450} \rangle} \right)^2_{\text{sh-to-sh}} + \left(\frac{\sigma \left[\rho_{450} \right]}{\langle \rho_{450} \rangle} \right)^2_{\text{rec}}. \tag{6.14}$$

Taking the fluctuations of $\rho_{450}^{\text{dense}}$ as a proxy for the shower-to-shower fluctuations, the relative fluctuation due to the reconstruction procedure, $\sigma_{\text{rec}} = \left(\frac{\sigma[\rho_{450}]}{\langle \rho_{450} \rangle} \right)_{\text{rec}}$, can be estimated using Eq. (6.14). The evolution of σ_{rec} as a function of energy for both primaries is presented in the left panel of Fig. 6.16. Despite having relatively large statistical uncertainties, it is clear that there is a decreasing trend with energy. Furthermore, protons have systematically larger reconstruction fluctuations than irons, suggesting that the improvement in the reconstruction resolution is indeed related to having a larger number of muons, decreasing the Poisson fluctuations as a consequence.

Finally, it is relevant to compare the merit factors obtained here with those achieved with X_{max}, the most common observable used for composition analysis. To this aim, we additionally computed the corresponding merit factors by using the true Monte-Carlo X_{max}. We do not account for any reconstruction resolution, so this calculation corresponds to the discrimination power of X_{max} in a best-case scenario. A value of approximately $f_{X_{\text{max}}} = 1.5$ was obtained, independently of energy and zenith angle. The fact that $f_{X_{\text{max}}}$ does not increase

with energy can be explained noting that the difference between the mean X_{max} for proton and iron remains relatively constant around $\sim 100\,\mathrm{g\,cm^{-2}}$. In addition, the $\sigma\,[X_{\mathrm{max}}]$ for both primaries also remains constant for all energies, with a larger value for proton than for irons (see Fig. 4 of Ref. [78]). The merit factors obtained with ρ_{450} displayed in Fig. 6.15 are above 1.8 and present an increasing trend with energy, which highlights the relevance of direct muon measurements for composition studies. However, if the uncertainty in the energy estimate is large enough, the merit factors of the muon measurements can be reduced down to the values of X_{max} [65].
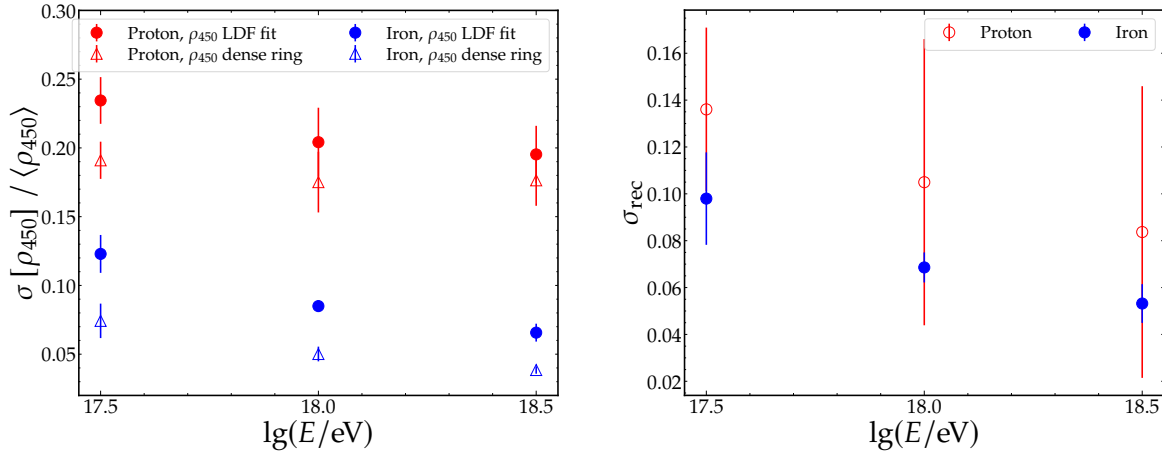

Figure 6.16: *Left*: Relative standard deviations of $\rho_{450}^{\mathrm{LDF}}$ and $\rho_{450}^{\mathrm{dense}}$ as function of energy for proton (red) and iron (blue) primaries. *Right:* Relative fluctuations due to the reconstruction procedure of the LDF fit (see Eq. (6.14)).

6.3.1   Merit factor as function of r

In the analysis of the data obtained with the UMD engineering array, it was found that leaving β free in the LDF fit introduces a dependence of the merit factor on the distance to the core [69]. In contrast, when the parameter is fixed to the parameterized value, the merit factor remains fairly constant for all radial distances. Furthermore, the value of the merit factor with β fixed was in most of the cases equal or larger than the maximum merit factor achieved with β free.

Several changes have occurred since the engineering array, with the most significant being the replacement of PMTs with SiPMs as photodetectors. Additionally, a different parameterization of the LDF Eq. (6.6) was used. Also, the new adjustments in the reconstruction procedure introduced in the previous chapters and sections might also impact this result. Therefore, we repeated the analysis to test if this previous finding still hold.

For each energy and zenith angle, the merit factor at a given distance to the core r was computed by obtaining the mean and standard deviation of $\rho(r)$ over the set of proton and iron showers, where $\rho(r)$ represents the LDF fit evaluated at r. Subsequently, Eq. (6.13) was used replacing ρ_{450} by $\rho(r)$.

In Fig. 6.17, the merit factor as a function of r, with β allowed to vary in the LDF fits, is displayed for different energies and zenith angles. It is evident that f shows a strong dependence on r, with the maximum discrimination power achieved within a distance range of 400 to 700 meters, varying according to energy and zenith angle.

Conversely, when β is fixed, f remains approximately constant across all distances, with its value dependent on energy and zenith angle, as shown in Fig. 6.18. Notably, the value

obtained with a fixed β is generally equal to or greater than the maximum value reached when β is free to vary.

To illustrate this more clearly, Fig. 6.19 presents the ratio between $f(r)$ with β fixed and the maximum f achieved with β free. This ratio exceeds one in most cases, except for the most inclined showers with energies of 10^{18} and $10^{18.5}$ eV.

The results presented here align perfectly with those found in Ref. [69]. We conclude that fixing β during the LDF fit is the most convenient approach.
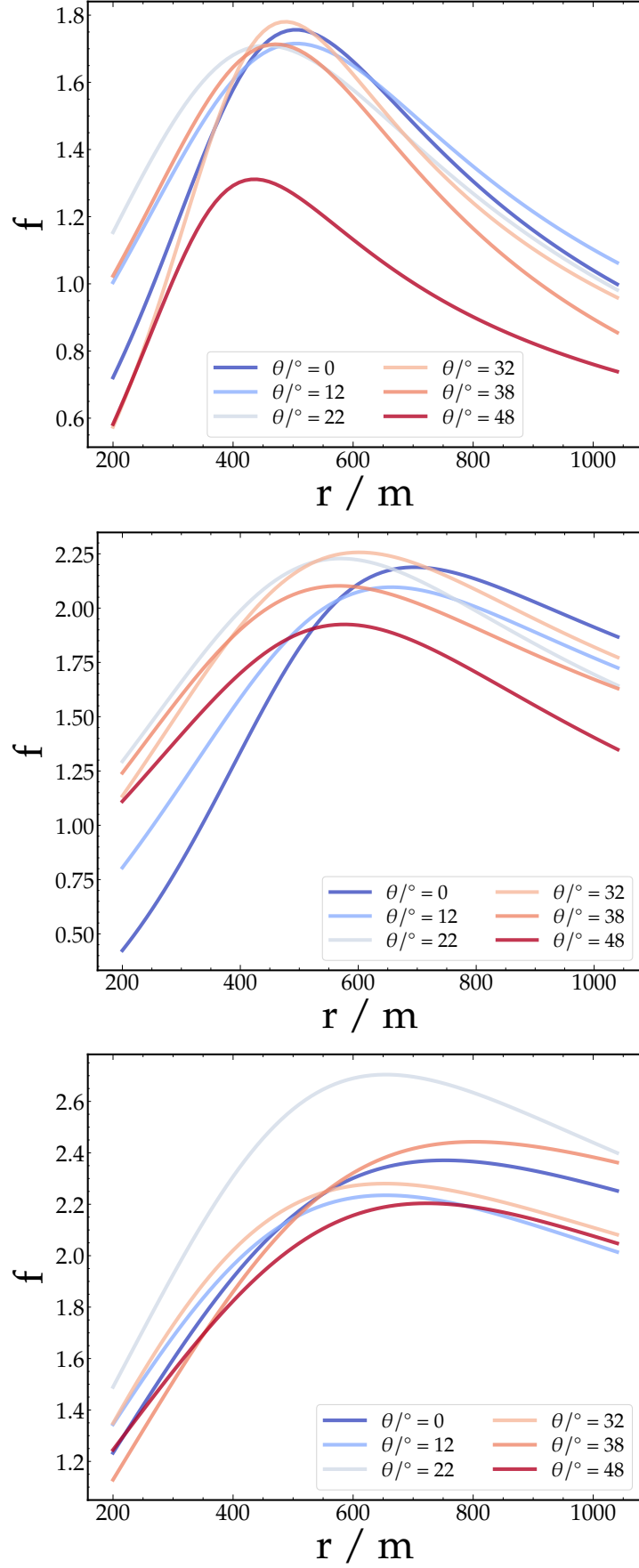
Figure 6.17: Merit factor with β free as function of shower plane distance r for energies of $10^{17.5}$ (upper panel), 10^{18} (middle panel) and $10^{18.5}$ (lower panel).
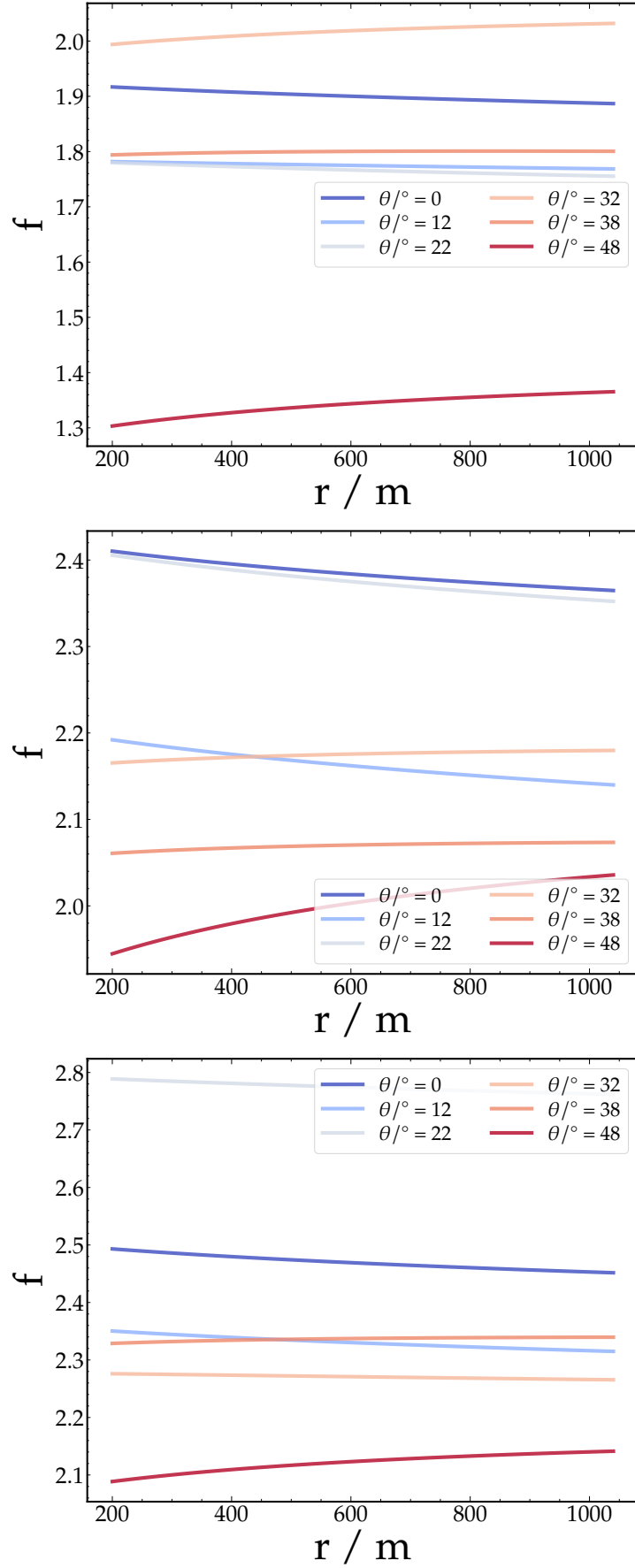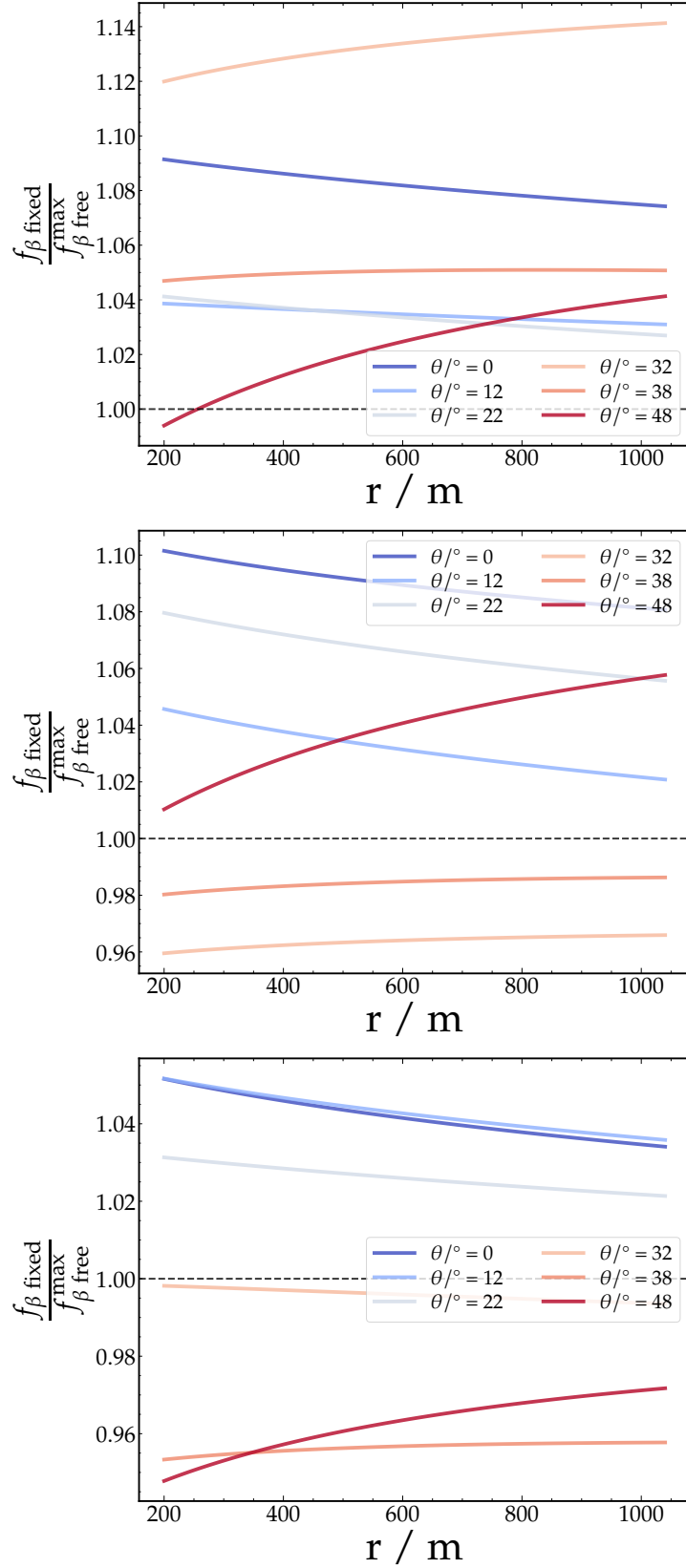
Figure 6.18: Merit factor with β fixed as function of shower plane distance r for energies of $10^{17.5}$ (upper panel), 10^{18} (middle panel) and $10^{18.5}$ (lower panel).

Figure 6.19: Quotient between the merit factor with β fixed and the maximum f achieved with β free as function of shower plane distance r for energies of $10^{17.5}$ (upper panel), 10^{18} (middle panel) and $10^{18.5}$ (lower panel).

6.4 Data-driven parameterization of the MLDF slope

As shown in the previous section, it is advantageous to fix the slope β, leaving only the normalization ρ_{450} as a free parameter. Therefore, a parameterization of β is needed. To this aim, we use the subset of events with enough detector information that allow for a reliable fit of β (see Section 6.2). We additionally request the events to fulfill the standard quality cuts of the SD described in Section 3.1, consisting of fulfilling the fourth- and fifth-level triggers.

In Fig. 6.20, the mean β values as function of $\sec\theta$ for five energy bins are shown. The same behaviour observed for simulations in Section 6.2.3 is found, namely, β decreases with the zenith angle and increases with energy. For each energy bin, we fit the linear model of Eq. (6.11), indicated as dashed lines in the figure.

The dependence of m and b with log-energy is shown in Fig. 6.21. Like in Section 6.2.3, m shows no strong dependence with log-energy, whereas a linear increase is observed for b. Thus, we take the weighted mean of m, $\overline{m}$, and we fit the energy dependence of b with the linear model of Eq. (6.12). In this way, the parameterization of β is defined by the values $(\overline{m}, b_0, b_1) = (-1.21, 2.71, 0.20)$.

To assess how well the parameterization describe the data for different energies, for each event we compute the residuals as the relative difference between the value of β predicted by the parameterization and the one obtained by the fit. The result is displayed in Fig. 6.22, where the relative difference of each event is depicted as a grey circle. The mean and standard deviation of the residuals is computed for each energy bin and are represented as filled and unfilled squares in the figure, respectively. To avoid the influence of a few outliers, the standard deviation is computed as half of the interquantile range between the quantiles 16% and 84%. The mean value of the residuals is centered at zero, indicating that the parameterization is capturing the mean evolution of β with energy.

The standard deviation shows a decreasing trend with energy, being $\sim 25\%$ for $10^{17.5}$ eV and $\sim 8\%$ for $10^{18.5}$ eV. Indeed, low energy events have larger fluctuations as they possess smaller number of muons and less triggered stations. As energy increases, the number of muons and triggered stations increases and, as a consequence, the fit possess more information to constrain the value of β, resulting in smaller fluctuations.

Since β is fixed to fit the MLDF in every event (see Section 6.3), a systematic uncertainty is induced in ρ_{450} due to the uncertainty of the true β. The standard deviation is a measure of how much is expected β to vary, and is therefore valuable to assess this source of systematic. Therefore, we use a second order polynomial to parameterize the standard deviation of the residuals of β as a function of log-energy. The result is represented as a dashed line in Fig. 6.22. We use such parameterization in Section 7.4.4 to study the systematic uncertainty in ρ_{450} induced by fixing β.
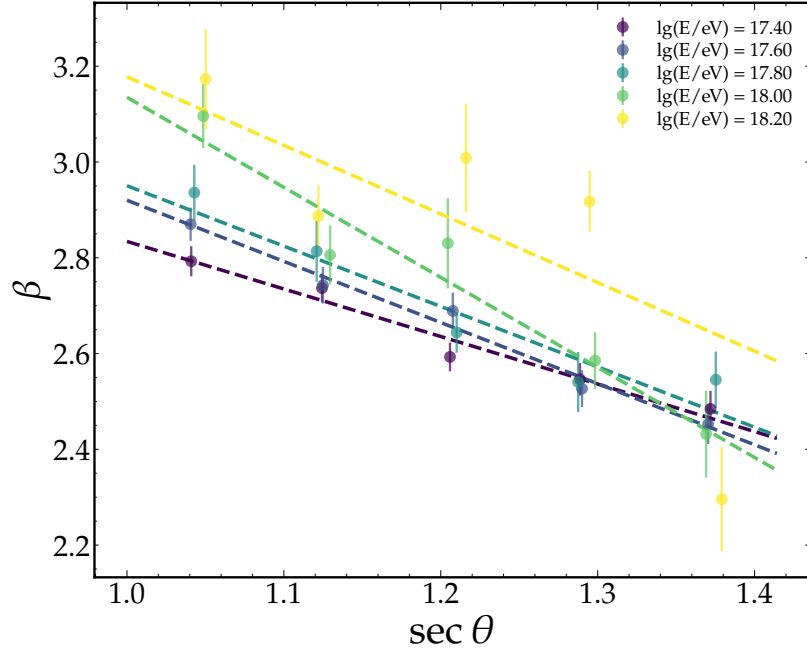
Figure 6.20: Mean β as function of $\sec\theta$ for five energy bins. Dashed lines indicate the fit to Eq. (6.11).
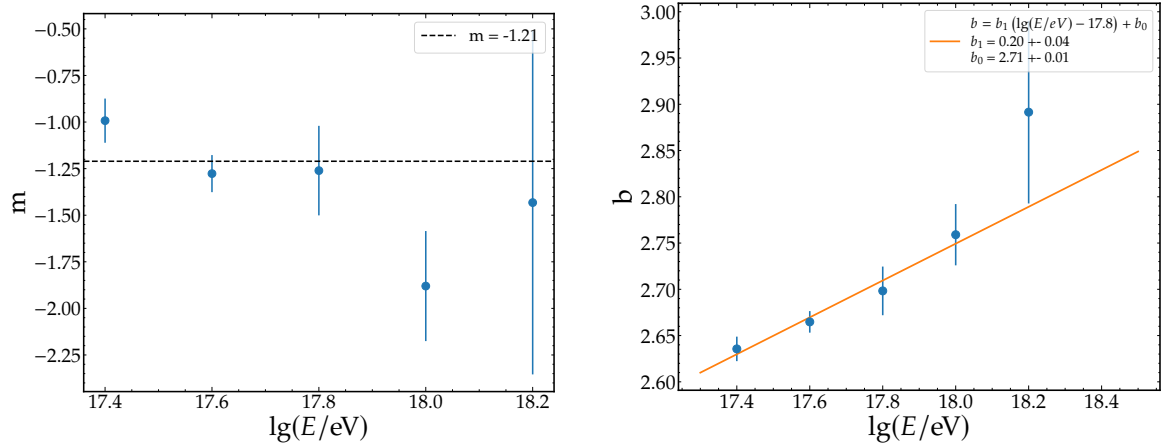

Figure 6.21: Slope (right) and intercept (left) of the linear model of Eq. (6.11) for each energy bin. Dashed line in the left panel indicates the weighted mean whereas the full line in the right panel shows the fit to Eq. (6.12).
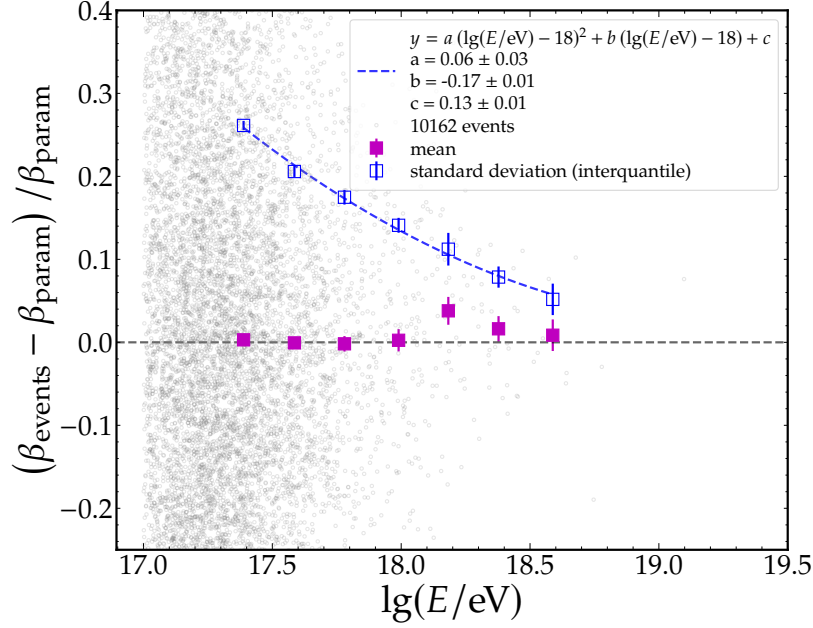
Figure 6.22: Mean (full squares) and standard deviation (unfilled squares) of the residuals of the parameterization of β. Values for each individual event are shown as grey data points. Dashed blue line indicates the parameterization of the standard deviation as a function of log-energy.

6.5 Analysis of the MLDF residuals

The muon density at 450 meters, ρ_{450}, is regarded as a proxy of the total number of muons in the shower and is therefore the main observable used for physics analyses with the UMD. This parameter, obtained by the MLDF fit, depends on the chosen MLDF model (Eq. (6.6)). Thus, to ensure a proper description of the data by the model, it is relevant to assess the residuals of the fits, particularly close to 450 m.

The muon density in a given UMD module is given by

$$\rho_i = \frac{\hat{N}_\mu}{A\cos\theta},$$

where $\hat{N}_\mu$ is the bias-corrected muon estimator of Eq. (5.11), A is the nominal area of the detector and $\cos\theta$ is the cosine of the zenith angle of the shower. The relative residual of the module is then defined as

$$\frac{\rho_i - \mathrm{MLDF}(r_i)}{\mathrm{MLDF}(r_i)},$$

where r_i is the distance of the module from the core, and $\mathrm{MLDF}(r_i)$ is the value of the MLDF model, evaluated at its best-fit parameters, at r_i.

To investigate the behavior of the residuals and its potential dependence on energy and zenith angle, the dataset was divided in two angular bins, $0° < \theta < 30°$ and $30° < \theta < 45°$, and in six log-energy bins, whose bin edges are given by $\lg(E/\mathrm{eV}) = \{17.3, 17.5, 17.7, 17.9, 18.1, 18.3, \infty\}$. All the residuals of the individual-event fits in a given $(\theta, \lg(E))$ bin were accumulated and their mean and median value as function of the distance to the core were obtained. The residuals as a function of the distance for each $(\theta, \lg(E))$ bin is displayed in Fig. 6.23, where each row (column) represents an energy (zenith angle) bin. Filled markers represent the mean, whereas unfilled markers indicate the median in each distance bin. The inset panel

in each plot contains a zoom on the mean residuals in the distance range $400 < r/\text{m} < 500$. The mean residuals are reasonably flat with distance and centered in zero.

The mean and median values tend to coincide near the core, while an increasing discrepancy between the two is observed at larger distances, indicating some asymmetry in the underlying distributions when a small number of muons are sampled. Indeed, in Fig. 6.24 we show the residual distributions for $0° < \theta < 30°$ and $17.3 < \lg(E/\text{eV}) < 17.5$ across three distance ranges: close to the core ($200 < r/\text{m} < 300$), an intermediate range containing 450 m ($400 < r/\text{m} < 500$), and far from the core ($900 < r/\text{m} < 1000$). The three histograms are conveniently normalized to a total of 1000 entries.

For small r, a larger number of muons is sampled and, as a consequence of the central limit theorem, the distribution of $\hat{N}_\mu$ becomes symmetric and bell-shaped. In this limit, $\hat{N}_\mu$ resembles a continuous variable and, as a result, the residuals also exhibit a symmetric, Gaussian-like distribution. An increasing asymmetry in the distributions is observed in the remaining two distance ranges. Indeed, as r increases, the muon counts become scarce and the discrete nature of counting muons becomes apparent as Poissonian fluctuations start to dominate. Specifically, the large peak at -1, visible for the furthest distances, is caused by zero muon measurements.

In the left panel of Fig. 6.25, the mean residual in the relevant distance range of $400 < r/\text{m} < 500$ is shown as a function of energy. It is evident that the mean residuals are compatible with zero for all energies. Some discrepancy seems to arise when dividing the data set in the two angular bins for the energy bin $\lg(E/\text{eV}) \sim 18.2$, the vertical (inclined) bin showing a positive (negative) bias of approximately +8% (-5%). However, both data points show rather large statistical errors and when the whole zenith range is used, this behaviour cancels out. Overall, the residuals are well contained within approximately $\pm 5\%$.

Finally, in the right panel of Fig. 6.25 we show the standard deviation of the residuals as a function of energy. As expected, the fluctuations decrease smoothly with energy as a result of the better quality of the fits with increasing energy.
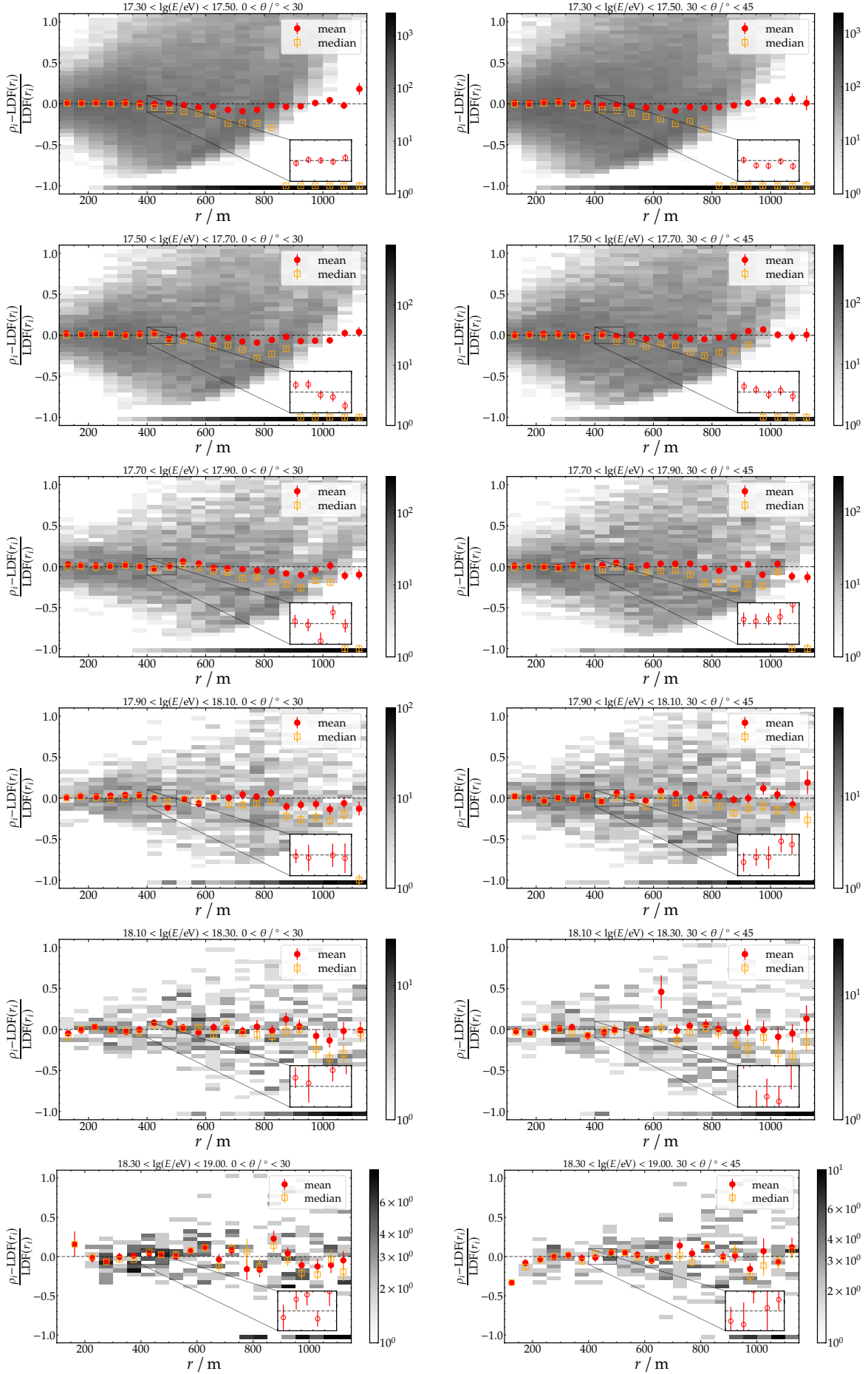
Figure 6.23: Mean and median of the residuals as function of distance to the core for different energies and zenith angle ranges. Each row represents a fixed energy bin. The left (right) column corresponds to the zenith range $0 < \theta/^{\circ} < 30$ ($30 < \theta/^{\circ} < 45$).
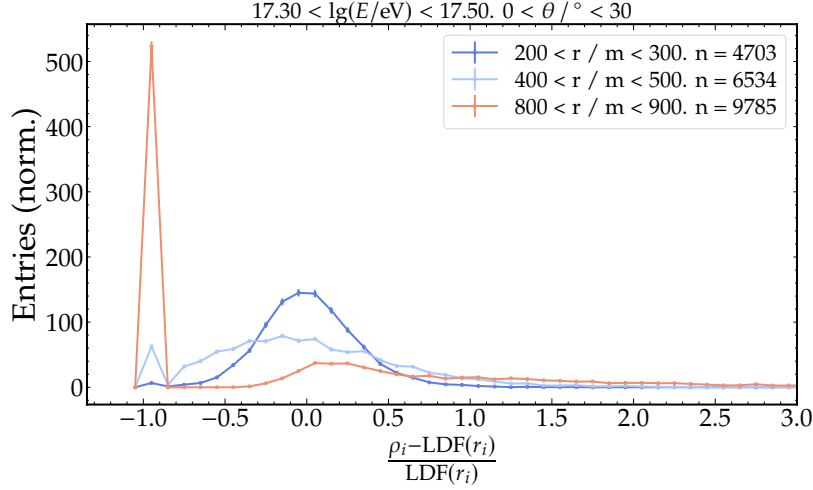
Figure 6.24: Distribution of the residuals for three distance ranges for events with $17.3 < \lg(E/\text{eV}) < 17.5$ and $0 < \theta/° < 30$. Each histogram is normalized to sum 1000 events. The real number of entries in each case is indicated in the legend.
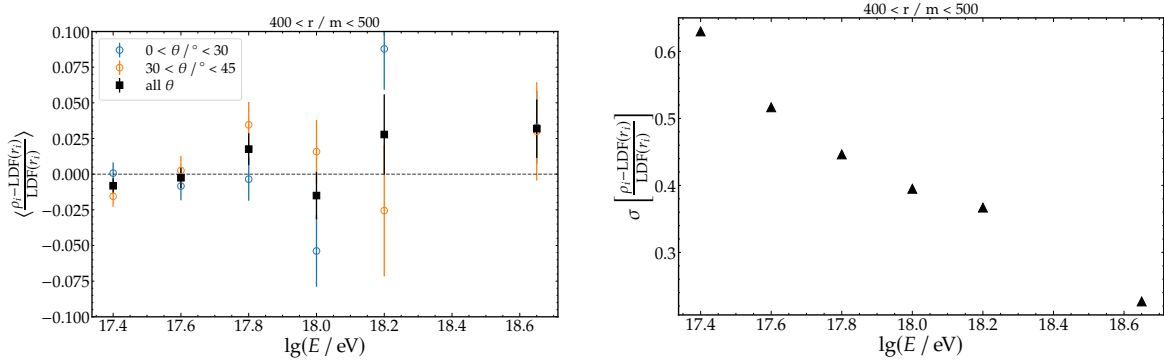

Figure 6.25: Mean value (left) and standard deviation (right) of the residuals at $400 < r/\text{m} < 500$ as a function of energy.

6.6 Summary

In this chapter, we presented several modifications and improvements to the existing reconstruction procedure of the MLDF.

We started by discussing the reasons behind ignoring the time resolution of the detector, which makes this work different from all the previous analyses of UMD data. This decision was motivated by the following reasons: First, when the time resolution of the detector is not considered, the likelihood of a single detector of Eq. (4.3) is exact and depends only on the total number of expected muons μ, irrespective of their time distribution. In contrast, a dependence on the arrival times of the muons in the detector is introduced in the likelihood, which makes its exact analytical calculation not possible, and a computationally expensive method of profiling would need to be implemented by updating the method in Ref. [74] to consider inhibited channels [66]. Second, the undershoot present in the fast shaper signal introduces a bias that depends not only on the total number of impinging muons but also on their time distribution. Air shower simulations followed by full detector simulations can be used to parameterize and correct this bias from the estimators of Eq. (6.3) and Eq. (6.5) [70]. However, it is not clear how to include this effect in the likelihood of Eq. (6.2), necessary to

fit the MLDF at event level. Conversely, when the time resolution is ignored, the likelihood is insensitive to the undershoot.

The next modification involved the core reconstruction and its impact in the MLDF. In the existing reconstruction, the core obtained by the SD reconstruction was fixed to compute the shower plane distances of the UMD detectors, necessary for the MLDF fit. We have shown that for events with UMD detectors close to the core, this can bias the MLDF. A new way of fitting the core with the UMD was developed by adding a penalization term in the event likelihood to constrain the UMD core to the vicinity of the SD core. As a result, previously biased events now show improved MLDF fits. In addition, the core uncertainty is now accounted for and naturally propagates to the ρ_{450}, resulting in a more realistic error estimate.

Another major change introduced in the reconstruction chain was to move from the Poisson to the binomial likelihood, with the modifications introduced in Chapter 4, as the latter involves a more realistic modeling of the signal fluctuations. We showed that the methods yielded compatible bias and resolution of ρ_{450}. However, since the binomial model accounts for detector segmentation, it yields systematically larger and more realistic uncertainty intervals for ρ_{450}, with improved coverage.

We have additionally confirmed that the corner-clipping correction developed in Chapter 4 and Chapter 5 performs correctly. We did so by showing that the bias of $\hat{\rho}_{450}$ increased with θ when no correction is applied. In contrast, the bias remains constant with θ when the correction is used.

The discrimination power of the new reconstruction was assessed. We demonstrated that, since the relative standard deviation of ρ_{450} decreases with energy, the merit factor of ρ_{450} increases with energy. In addition, we have shown that leaving β as a free parameter in the fit introduces a dependence in the merit factor on the distance, confirming the result found in a previous work. In contrast, when β is fixed, the merit factor remains flat with the distance in a value that is, in most cases, equal or larger than the maximum value achieved with β free. Therefore, we concluded that is advantageous to fix β during the MLDF fit.

Also, we presented a data-driven parameterization of β dependent on energy and the zenith angle. By looking at the residuals, we confirmed it provided a good representation of the mean β for all energies. This parameterization is used in the analysis presented in the next chapter to fix β in all the events. In addition, we parameterize the energy dependence of the standard deviation of the residuals of the parameterization of β. This provides an estimate on how much is expected β to vary in each event and is one of the basic ingredients to compute the systematic uncertainty in ρ_{450} produced by fixing β to its mean value, as will be shown in the next chapter.

Finally, we analyzed the residuals of the MLDF for different energies and zenith angle ranges to investigate potential biases in the event-level fits, with particular interest in the crucial range of $400 < r/\text{m} < 500$. We showed that the biases are reasonably centered, compatible to zero within statistical uncertainties and their values contained within $\pm 5\%$.
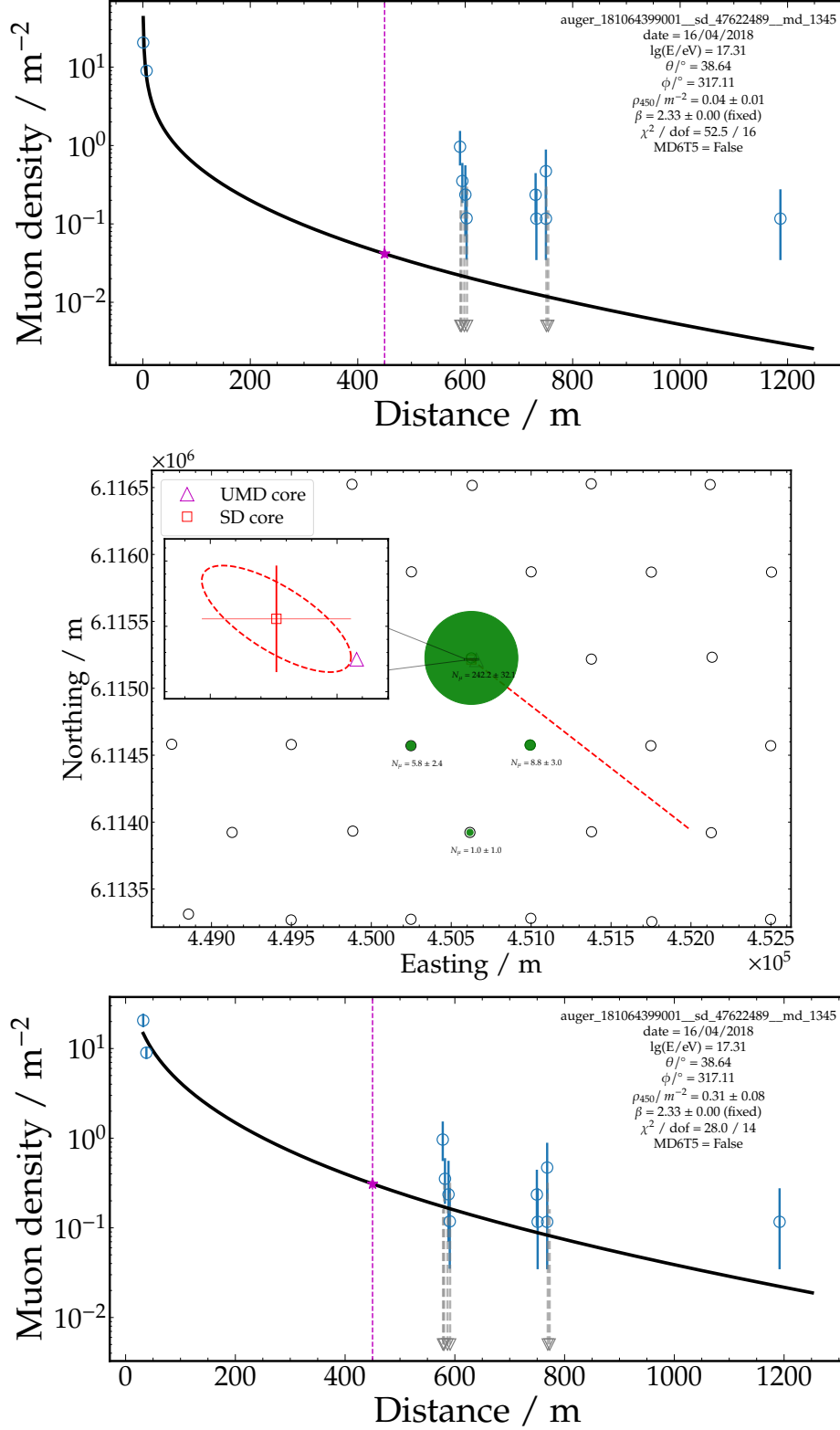
Figure 6.1: Event 181064399001 recorded on April 16th of 2018. Upper-(lower-)most panel corresponds to the UMD LDF fit with the core position fixed (free). Circles represent modules with non-zero signals, while triangles indicate zero-muons measurements. Vertical dashed line indicates the 450 m mark. Middle panel shows the footprint of the event in the UMD array. Unfilled circles indicate SD tanks while filled circles indicate positions in which UMD detectors measured a non-zero signal. The size of the marker is proportional to the total number of muons measured by the UMD modules. Red dashed line represents the axis of the shower. In the inset panel, a zoom in the SD core region can be observed, along with its 1σ ellipse and its errors (vertical and horizontal error bars). Triangular marker indicates the UMD core. The grey dashed lines indicate the Feldman-Cousin interval obtained for modules with zero measured muons, as explained in Section 4.3.

Analysis of the muon content measured by the UMD

In this chapter, we present the measurement of the muon content in air showers using the UMD in the energy range $10^{17.5}$ to $10^{18.9}$ eV and compare the results with predictions from simulations and with other experiments.

In Section 7.1, we describe the dataset and the quality cuts applied to ensure a reliable analysis. The attenuation correction, derived using the Constant Intensity Cut (CIC) method to remove the zenith angle dependence of the muon shower size, is detailed in Section 7.2. The evolution of the attenuation-corrected muon densities is presented in Section 7.3, with systematic uncertainties evaluated in Section 7.4.

The set of simulations used for comparison with the data is described in Section 7.5, while the actual comparison is carried out in Section 7.6, where the mean logarithmic mass is derived and its consistency with the mass inferred from X_{max} is assessed.

The compatibility of these results with previous UMD analyses is discussed in Section 7.7, while Section 7.8 introduces the z-scale to compare our findings with other experiments.

Lastly, since the shape of the lateral distribution of muons is expected to remain largely unchanged with energy and atmospheric depth, Section 7.9 compares the shape of the mean muon LDF observed by the UMD in this work with measurements from the Yakutsk and Akeno observatories, which used the same muon energy threshold.

7.1 Data selection and reconstruction

As explained in Section 3.1, a fiducial cut, known as 6T5, is required to ensure a proper reconstruction of the shower core. This condition consists of requiring the SD station with the largest signal to be surrounded by six working stations, so that the shower core is fully contained in a working hexagon of WCDs. Since the SD energy and geometry reconstruction, on which the UMD reconstruction relies, is still in a preliminary stage with the new electronics, we restrict the analysis to the period in which the WCDs were operating with the old electronics. Thus, an additional condition is imposed: only SD stations operating with the old electronics are accepted for the SD reconstruction. Consequently, the 6T5 hexagon needs to be formed by stations operating with old electronics.

In Fig. 7.1, the monthly number of events from 2018 to 2025 is shown. Up to January 2021, we observe an average of approximately 100 events per month, with some drops due to periods of poor data acquisition or detector malfunctions. From January 2021 to December 2021, an increase in the number of events is observed as a consequence of the expansion of

the UMD array with the deployment of new positions, reaching an average of roughly 250 events per month. From December 2021 to February 2023, when the transition between the old and new electronics of the WCDs in the SD-750 array occurred, there are no SD hexagons with the same kind of electronics. Consequently, no event fulfill the 6T5 and the usage of old electronics simultaneously. After that, when the entire array was equipped with the new electronics, we fully entered Phase 2[1]. Thus, the time period for the data considered in this analysis spans from January 1st, 2018, to December 31st, 2021.

Furthermore, we apply all the standard quality cuts used for the official SD data production for ICRC2023, which include a physical T4 trigger (see Section 3.1), a successful fit of the SD LDF, and the rejection of known bad data acquisition periods or lighting issues. In addition to the standard SD quality cuts, the UMD requires additional conditions for the events; these include the requirement that the SD station with the largest signal in the event has a non-rejected UMD detector and a successful fit of the muon LDF. We remind the reader that the LDF model used for the UMD is that of Eq. (6.6). The binomial log-likelihood from Eq. (6.10) is applied, with ρ_{450} and the core coordinates (x, y) treated as free parameters. The slope β is fixed to the energy- and zenith-dependent parameterization presented in Section 6.4, and the corner-clipping probability parameterization derived from data (Section 5.2) is used. Finally, we restrict the analysis to events with $\theta < 45°$ in order to minimize the loss of the detector's effective area.
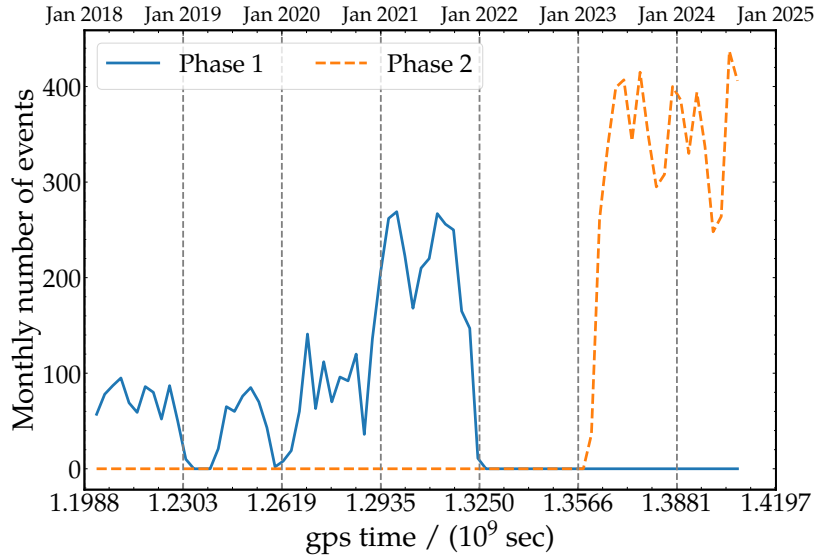

Figure 7.1: Monthly number of events as a function of GPS time. Only Phase 1 events are considered for this work.

7.1.1   Energy cut

To define an energy range for the physics analysis, it is necessary to ensure that the set of cuts applied to the events—both from the SD and UMD—still define the fully efficient regime. In other words, we need to assess wether the cuts imposed to the dataset are not biasing the selection towards a prefered zenith angle range. This regime can be determined by identifying the minimum energy E_{th} above which the distribution of $\sin^2 \theta$ is uniform. To achieve this, we perform a scan over the energy threshold E_{cut}. For each E_{cut}, we conduct a

---

[1]We remind the reader that the operation of WCDs with old electronics is referred to as Phase 1, whereas the current operation with new electronics is known as Phase 2 (see Section 3.3.2).

χ^2 test to assess the uniformity of the $\sin^2 \theta$ distribution for events with energy above E_{cut}. In this way, we define E_{th} as the lowest E_{cut} for which the p-value of the test exceeds 5%.

In Fig. 7.2, the χ^2 values and corresponding p-values as a function of $\lg(E_{cut}/eV)$ are displayed. A threshold energy of $10^{17.55}$ eV was obtained, which we round to $E_{th} = 10^{17.5}$ eV. Thus, we restrict our analysis to events with $\lg(E/eV) > 17.5$. For visualization purposes only, we retain one energy bin below E_{th}.

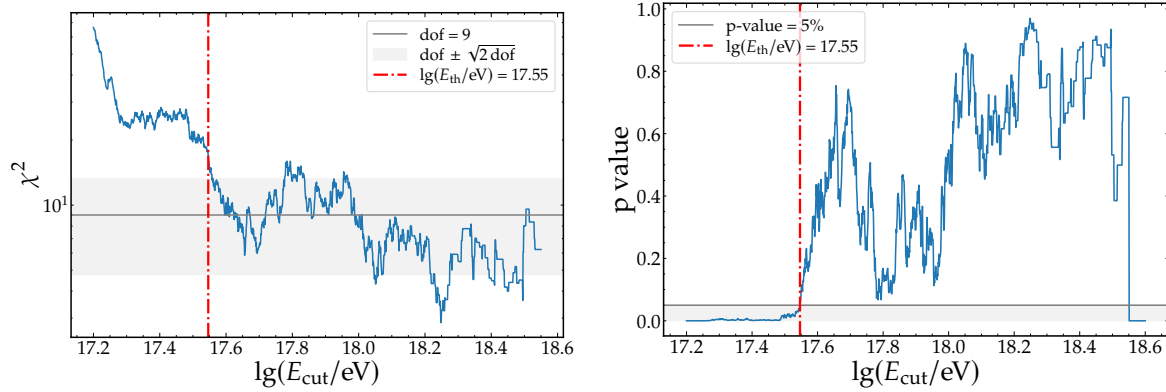After all these cuts are applied, we obtain a total of 4838 events (13255 if we consider $\lg(E/eV) > 17.3$).

Figure 7.2: Observed χ^2 (left) and p-value (right) of the uniformity test as a function of E_{cut}. The vertical dashed line indicates the minimum energy above which the p-value exceeds 5%.

7.2 Attenuation correction (CIC)

In this section, we aim to remove the zenith dependence of the muon shower size ρ_{450}.

Inclined showers must traverse a greater thickness of the atmosphere before reaching the ground. As a consequence, less particles survive to reach the detectors thus leaving a weaker footprint in the array compared to a more vertical shower generated by the same primary with the same energy. Although this effect is predominant for electromagnetic particles, high-energy muons, like those detected by the UMD, also suffer from attenuation as they have to additionally travel longer distances through the soil before reaching the underground detector as the zenith angle of the shower increases. Thus, the muon shower size ρ_{450} depends not only on the energy, but also on the zenith angle of the shower[2]. We can factorize these dependencies as

$$\rho_{450}(E, \theta) = \rho_{ref}(E) f_{att}(\theta), \tag{7.1}$$

where ρ_{ref} is the zenith-independent muon shower size estimator and is interpreted as the ρ_{450} the shower would have produced had it arrived at the reference zenith angle θ_{ref}. On the other hand, $f_{att}(\theta)$ captures the zenith angle dependence of the shower size due to attenuation and is given by

$$f_{att}(\theta) = 1 + a\,x + b\,x^2, \tag{7.2}$$

where $x = \sin^2 \theta - \sin^2 \theta_{ref}$.

Therefore, with the knowledge of $f_{att}(\theta)$, ρ_{450} can be converted to the zenith-independent quantity ρ_{ref} via Eq. (7.1).

---

[2]The number of muons also depends on the primary particle. In this way, Eq. (7.1) is averaged over the underlying mass distribution of the primary beam.

For the analysis of data, the reference angle is typically chosen to be the median of the zenith angle distribution, such that most of the events have a minor correction (i.e., $f_{att}(\theta)$ close to 1). For the UMD-750, the reference angle is chosen to be $35°$. We note that this corresponds to the median of the zenith angle distribution when $0 < \theta/° < 55$, slightly differing from $30°$, the median obtained for the zenith range used in this work ($0 < \theta/° < 45$). This sub-optimal reference zenith angle has only a small impact in the total systematic uncertainty budget (see Section 7.4.1) and has been used in previous UMD analyses ([62, 69, 73]). Therefore, we chose to remain with $\theta_{ref} = 35°$ for a straightforward comparison to the previous UMD results.

To obtain the attenuation function $f_{att}(\theta)$, we employ the Constant Intensity Cut (CIC) procedure [39]. This method, vastly used to characterize the attenuation of the SD signals, relies on the assumption that the cosmic ray flux is isotropic and, as a consequence, the number of events dN above an energy threshold E_0 in the full efficiency region must follow

$$dN \propto \sin\theta \cos\theta d\theta = \frac{1}{2}d(\sin^2\theta).$$

Therefore,

$$\frac{dN}{d\sin^2\theta} = \text{constant}. \tag{7.3}$$

Since there is a one-to-one mapping between energy and shower size, from Eq. (7.3) it follows that the number of events above a given ρ_{450}^{cut}, onwards defined as intensity $n(\rho_{450} > \rho_{450}^{cut})$, must be constant in equally-spaced bins of $\sin^2\theta$. In the left panel of Fig. 7.3, we show $n(\rho_{450} > \rho_{450}^{cut})$ as a function of ρ_{450}^{cut} for five equally-spaced $\sin^2\theta$ bins, ranging from $\sin^2\theta = 0$ to $\sin^2\theta = 0.62$ ($\theta \sim 52°$) in steps of 0.125. Only the first four bins, spanning our working range of $0 < \theta/° < 45$, are taken into account for the analysis. The remaining, most inclined bin ($0.5 < \sin^2\theta < 0.62$) is preserved for visualization only.

If no attenuation effects were present, a horizontal cut at fixed n_{cut} values should yield compatible values in the ρ_{450}^{cut} for the different angular bins. Therefore, any deviation of ρ_{450}^{cut} from a constant is attributed to attenuation alone, allowing to obtain f_{att}.

To illustrate the procedure, we show three horizontal cuts, corresponding to $n_{cut} = 300, 500, 700$, marked as horizontal dashed lines in the left panel of Fig. 7.3. For each n_{cut}, the corresponding ρ_{450}^{cut} values for each zenith bin are displayed in the right panel of the figure. The errorbars were computed via bootstrap as described in Ref. [79]. To obtain ρ_{35}, a and b, the resulting ρ_{450}^{cut} values for each n_{cut} are fitted to Eq. (7.1), as displayed by full lines.
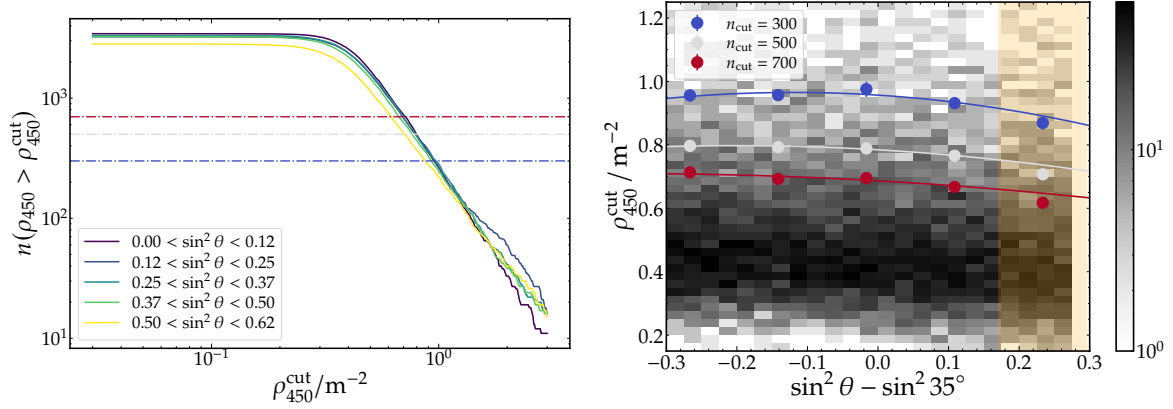
Figure 7.3: *Left*: Number of events with $\rho_{450} > \rho_{450}^{\text{cut}}$ as a function of ρ_{450}^{cut} for different equally-spaced $\sin^2\theta$ bins. Horizontal dashed lines indicate constant intensities of 300, 500 and 700. *Right*: ρ_{450}^{cut} as function of $x = \sin^\theta - \sin^2 35°$ for intensities of 300, 500 and 700. Full lines represent the fits to Eq. (7.1). The 2D histogram shows the underlying distribution of events in the (x, ρ_{450}) space. The orange shaded band indicates the most inclined bin $0.5 < \sin^2\theta < 0.62$ ($45 < \theta/° \lesssim 52$), which is not considered for the fit and preserved for visualization only.

The parameters of f_{att}, a and b, depend on the arbitrarily chosen value of n_{cut}. In turn, we note that n_{cut} is related to the energy cut, as displayed in Fig. 7.4: a smaller (larger) n_{cut} implies a larger (smaller) energy cut.
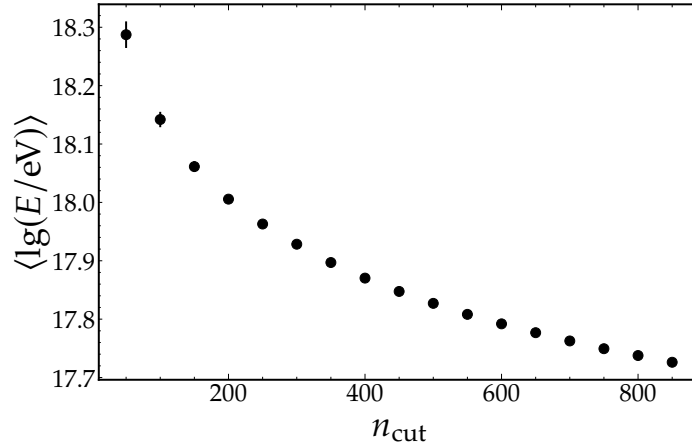

Figure 7.4: Mean energy of events (over the entire zenith range) as function of n_{cut}.

Therefore, the procedure is repeated for several values of n_{cut} to investigate the dependence of a and b on this parameter, as shown in Fig. 7.5. Both a and b remain relatively flat with respect to n_{cut}. The ultimate values of a and b, chosen as a weighted mean over the entire n_{cut} scan, are indicated as dashed horizontal lines in the left panel of Fig. 7.5. The corresponding f_{att} is shown as a black full line in the right panel of the Figure.
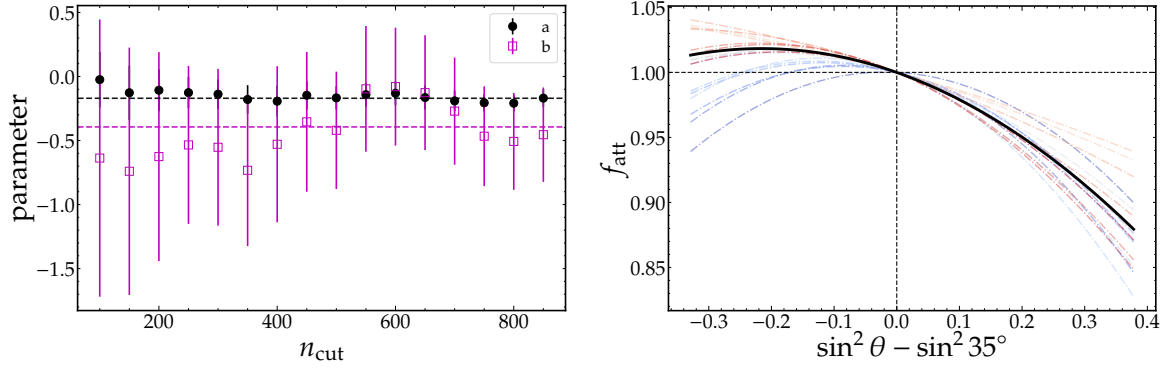
Figure 7.5: *Left*: a and b of the attenuation function (Eq. (7.2)) as a function of n_{cut}. Horizontal dashed line indicate the weighted mean of a and b. *Right*: Dashed lines represent plots of f_{att} for different n_{cut}. Black full line shows the final function, obtained by using the weighted mean of a and b.

An uncertainty for f_{att} is needed for a proper propagation to the muon estimator ρ_{35}. To that end, we obtain the covariance matrix of a and b using the values displayed in the left panel of Fig. 7.5. We summarize all the information related to a and b in Table 7.1. The uncertainty of f_{att} is thus obtained by usual Gaussian error propagation:

$$\sigma_{f(x)}^2 = \left(\frac{\partial f}{\partial a}\right)^2 \sigma_a^2 + \left(\frac{\partial f}{\partial b}\right)^2 \sigma_b^2 + 2\frac{\partial f}{\partial a}\frac{\partial f}{\partial b}\text{Cov}(a,b), \tag{7.4}$$

where $\frac{\partial f}{\partial a} = x$, $\frac{\partial f}{\partial b} = x^2$, and the remaining quantities can be found in Table 7.1. The definitive f_{att} and its 1σ uncertainty band is shown in Fig. 7.6. The uncertainty is null when $\theta = 35°$ and increases as the zenith angle deviates from this value, which explains why the reference angle should be chosen as the median or mode of the zenith angle distribution.

a	σ_a^2	b	σ_b^2	$\text{Cov}(a,b)$
-0.170	0.0021	-0.394	0.0444	-0.0018

Table 7.1: Optimal values and their uncertainties of the attenuation function f_{att}.
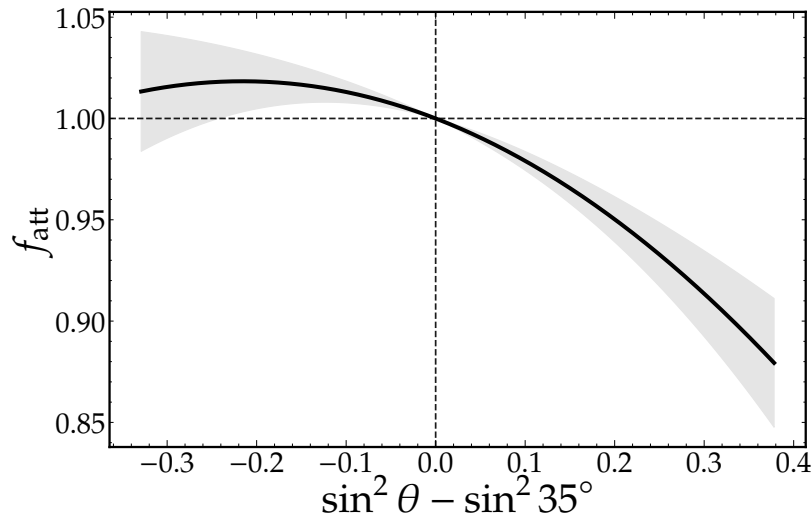

Figure 7.6: Attenuation function and its 1σ uncertainty band.

To verify that the derived attenuation function is working properly, the mean of the normalized density $\rho_{450}/(E/10^{18}\ \text{eV})^{0.9}$ as a function of log-energy for three angular bands is shown in the left panel of Fig. 7.7. Full circles indicate the mean over the entire range $0 < \theta/° < 45$, whereas unfilled triangles (squares) indicate the mean over a vertical (inclined) range of $0 < \theta/° < 30$ ($30 < \theta/° < 45$). Although not highly significant, a clear split is visible between the vertical and inclined sets, the latter showing systematically smaller muon densities as a consequence of muon attenuation. In the right panel of the Figure, the same analysis is displayed for the attenuation-corrected quantity ρ_{35}. It is evident that the zenith dependence has been removed and no significant differences between the angular bands is observed. To furhter illustrate this, in Fig. 7.8 we show the ratio between the means of the vertical and inclined datasets as a function of energy. For the uncorrected values, the vertical dataset show $\sim 3\%$ greater values, while the ratio is compatible to unity for the corrected values.
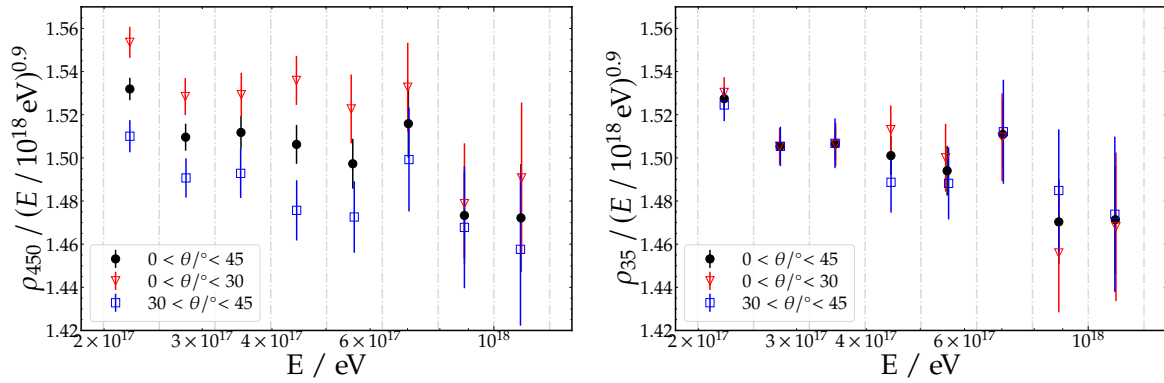

Figure 7.7: Normalized muon shower size for different angular bands as a function of energy. The left panel corresponds to the uncorrected case, whereas the right panel shows the attenuation-corrected values.
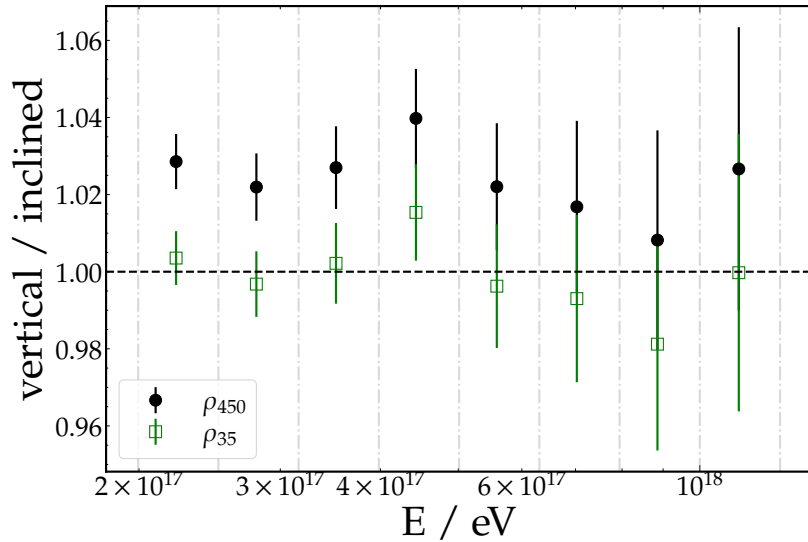

Figure 7.8: Ratio between the vertical ($0 < \theta/° < 30$) and inclined ($30 < \theta/° < 45$) dataset as a function of energy. Full (emptys) markers correspond to the uncorrected (corrrected) case.

7.3 Evolution of the muon content with energy

In Fig. 7.9, we present the energy evolution of the normalized density $\rho_{35} / (E/10^{18}\text{eV})^{0.9}$. This normalization with energy is applied to reduce the energy dependence and facilitate visualization. Since the number of muons increases roughly as $E^{0.9}$, a constant composition within a given energy range would correspond to a horizontal line when using the normalized density. In the upper panel of the figure, we show both the full unbinned dataset along with the mean (full circles) and median (empty triangles) of the distributions in each energy bin. To better visualize the evolution, the lower panel displays only the mean and median. The lowermost log-energy bin corresponds to $\lg(E/\text{eV}) = 17.3$ (one energy bin below full efficiency of the array, see Section 7.1.1), increasing in steps of $\Delta\lg(E/\text{eV}) = 0.2$ up to $\lg(E/\text{eV}) = 18.9$. Events with energies greater than $10^{18.9}$ eV are grouped into the same bin, which contains only three events. In both panels, the lower and upper brackets indicate the systematic uncertainty of the mean normalized density. We delay the details of how systematic uncertainties are calculated to Section 7.4.

The muon content seems to decrease smoothly with energy up to $\sim 10^{18.4}$ eV, where a break is observed towards larger densities. This feature is visible both for the mean and the median of the distributions, indicating that is not likely to be caused by outliers. The interpretation of this result in terms of mass composition will be discussed in Section 7.6.
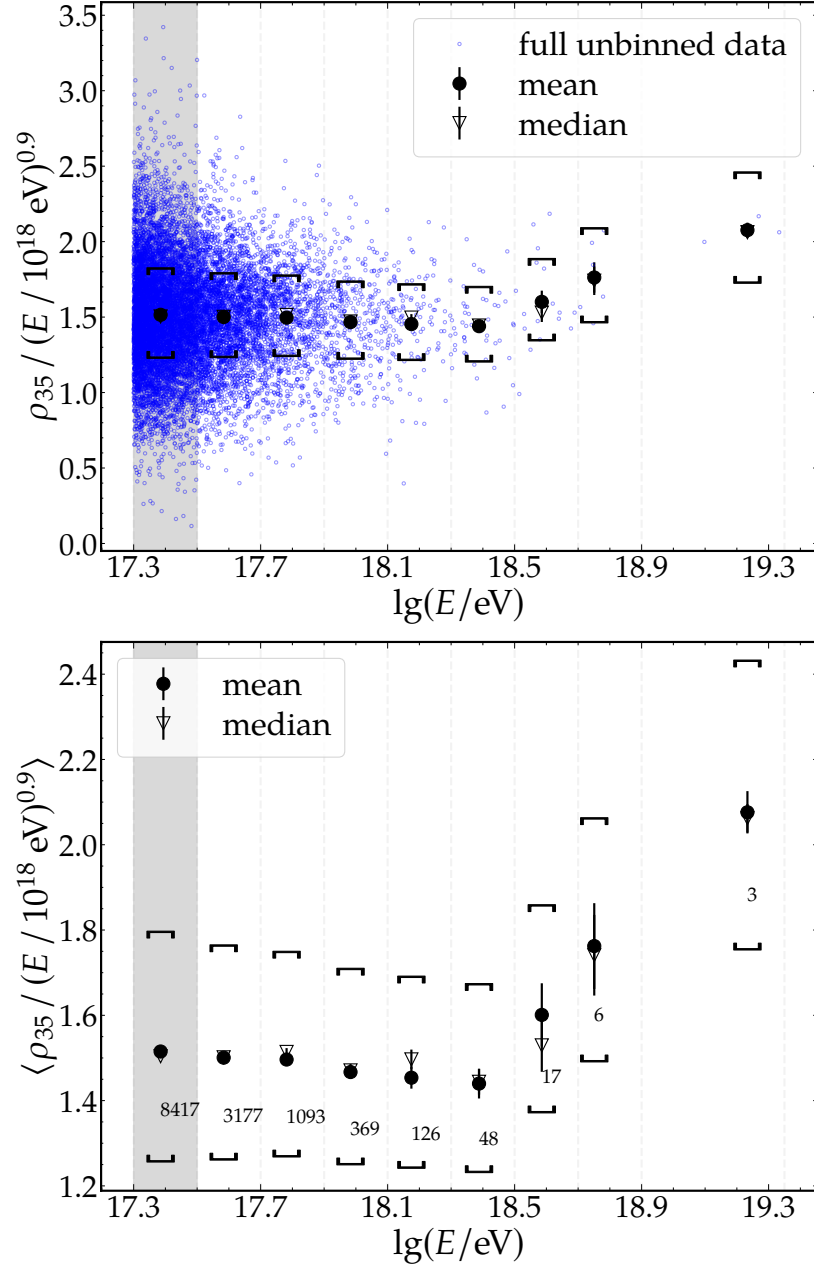
Figure 7.9: Normalized ρ_{35} as a function of energy. The upper panel shows the underlying un-binned dataset together with the binned data, whereas the lower panel only shows the binned data. Error bars indicate the standard deviation of the mean, while brackets correspond to the systematic uncertainty calculated in Section 7.4. The horizontal position of the data points corresponds to the mean energy in the bin. The number of events in each energy bin is stated in the lower panel. The shaded grey area indicates $\lg(E/\text{eV}) < 17.5$, corresponding to the region below full efficiency as explained in Section 7.1.1.

7.4 Systematic uncertainties

In this section, we detail the calculation of the systematic uncertainties for ρ_{35}. As explained in Section 7.2, ρ_{35} is obtained via Eq. (7.1). Therefore, we compute the systematic uncertainty with the following formula:

$$\left(\frac{\sigma_{\rho_{35}}}{\rho_{35}}\right)^2 = \left(\frac{\sigma_{\rho_{450}}}{\rho_{450}}\right)^2 + \left(\frac{\sigma_{f_{att}}}{f_{att}}\right)^2 + \left(\frac{\sigma_{\rho_{35}}^{\text{energy scale}}}{\rho_{35}}\right)^2, \qquad (7.5)$$

where $\sigma_{\rho_{450}}$ encapsulates all the uncertainty due to the UMD measurement only (i.e., without considering the uncertainty in the energy), $\sigma_{f_{att}}$ corresponds to the uncertainty in the attenuation function given by Eq. (7.4) described in Section 7.2, and $\sigma_{\rho_{35}}^{\text{energy scale}}$ indicates the uncertainty in ρ_{35} induced by the uncertainty in the energy scale. In turn, we write $\sigma_{\rho_{450}}$ as a contribution of three sources:

$$\sigma_{\rho_{450}}^2 = \sigma_{\text{LDF}}^2(E) + \sigma_{p_{cc}}^2 + \sigma_{\text{rec}}(E)^2 + \sigma_{\text{pattern}}^2, \qquad (7.6)$$

where σ_{LDF} is the uncertainty due to the unknown true shape of the muon LDF, $\sigma_{p_{cc}}$ is the contribution due to the corner-clipping correction developed in Chapter 5, σ_{rec} corresponds to the contribution of the reconstruction procedures, and σ_{pattern} indicates the systematic introduced by the choice of the muon pattern. We note that σ_{LDF} and σ_{rec} can potentially depend on energy.

In what follows, we explain the procedure to compute each of the contributions in Eq. (7.5) and Eq. (7.6).

7.4.1   Attenuation correction

For an event with a zenith angle θ, the uncertainty in f_{att} is determined by evaluating Eq. (7.4) at θ. In Fig. 7.10, we present the evolution of σ_f / f_{att} as a function of $\sin^2 \theta - \sin^2 35°$. It is evident that the relative uncertainty increases as θ deviates from the reference angle of $35°$, reaching a maximum of approximately 3% for $\theta = 0°$ and $\theta = 45°$. By construction, the uncertainty is zero for $\theta = 35°$.

To quantify the uncertainty of f_{att}, we take the mean value of σ_f / f_{att} over the events, which follow an underlying $\sin \theta \cos \theta$ distribution. In Fig. 7.11, we show $\langle \sigma_f / f_{att} \rangle$ as a function of $\lg(E/\text{eV})$. As expected, no energy dependence is observed. A value of $\sigma_f / f_{att} \sim$ 1% is found for all energy bins. Consequently, we adopt this value as the estimate of the systematic uncertainty.
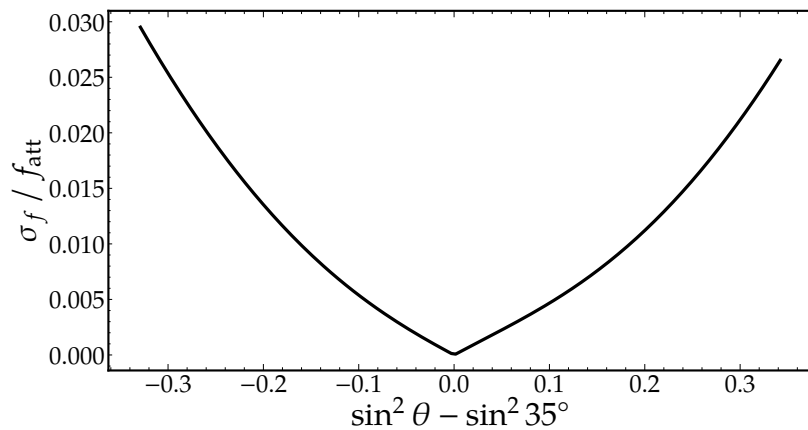

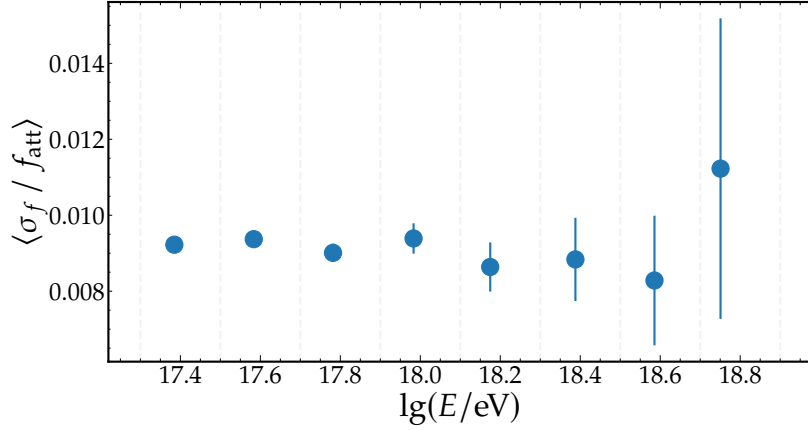**Figure 7.10:** Relative uncertainty of the attenuation function as a function of $\sin^2 \theta - \sin^2 35°$.

Figure 7.11: Mean relative uncertainty of the attenuation function as a function of log-energy.

7.4.2   Corner-clipping correction

The uncertainty in the corner-clipping correction developed in Chapter 5, parameterized in Eq. (5.9) and Eq. (5.10), needs to be accounted for to estimate a systematic effect. To this end, we obtain an uncertainty in p_{cc} by usual Guassian propagation:

$$\sigma_p^2 = \left(\frac{\partial p}{\partial m}\right)^2 \sigma_m^2 + \left(\frac{\partial p}{\partial b}\right)^2 \sigma_b^2, \tag{7.7}$$

where we neglect the correlation between m and b and the partial derivatives are given by

$$\frac{\partial p}{\partial m} = \sin \Delta\phi - 1/2,$$
$$\frac{\partial p}{\partial b} = 1. \tag{7.8}$$

In turn, σ_m and σ_b depend on θ and are obtained by propagating the uncertainty in Eq. (5.10):

$$\sigma_m^2 = \left(\frac{\partial m}{\partial m_0}\right)^2 \sigma_{m_0}^2 + \left(\frac{\partial m}{\partial m_1}\right)^2 \sigma_{m_1}^2 + 2\mathrm{cov}(m_0, m_1)\frac{\partial m}{\partial m_0}\frac{\partial m}{\partial m_1},$$
$$\sigma_b^2 = \left(\frac{\partial b}{\partial b_0}\right)^2 \sigma_{b_0}^2 + \left(\frac{\partial b}{\partial b_1}\right)^2 \sigma_{b_1}^2 + 2\mathrm{cov}(b_0, b_1)\frac{\partial b}{\partial b_0}\frac{\partial b}{\partial b_1}, \tag{7.9}$$

where

$$\frac{\partial m}{\partial m_0} = \frac{\partial b}{\partial b_0} = 1,$$
$$\frac{\partial m}{\partial m_1} = \frac{\partial b}{\partial b_1} = \sec\theta - 1.2, \tag{7.10}$$

and $m_0 = 0.03$, $\sigma_{m_0} = 0.002$, $m_1 = 0.14$, $\sigma_{m_1} = 0.01$, $b_0 = 0.035$, $\sigma_{b_0} = 0.001$, $b_1 = 0.076$ and $\sigma_{b_1} = 0.004$. The covariances are $\mathrm{cov}(m_0, m_1) = 8.9 \times 10^{-6}$ and $\mathrm{cov}(b_0, b_1) = 7.6 \times 10^{-7}$. All these values were obtained by the covariance matrix of the fits shown in Fig. 5.13.

In Fig. 7.12, the parameterizations of m and b (Eq. (5.10)) together with the 1σ band given by Eq. (7.9) are displayed. The 1σ and 2σ bands (via Eq. (7.7)) of p_{cc} as a function of $|\sin \Delta\phi|$ for four different zenith angles are shown in Fig. 7.13.
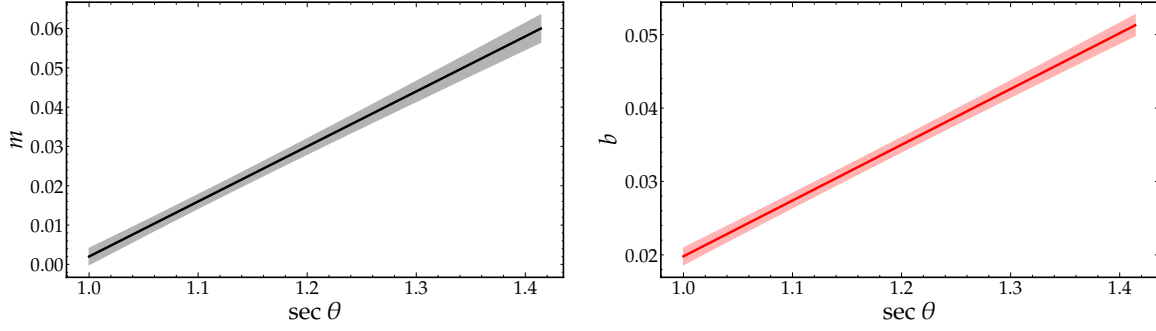
Figure 7.12: Solid lines indicate the parameterziations of Eq. (5.10), whereas the shaded areas correspond to the 1σ bands in m and b given by Eq. (7.9).
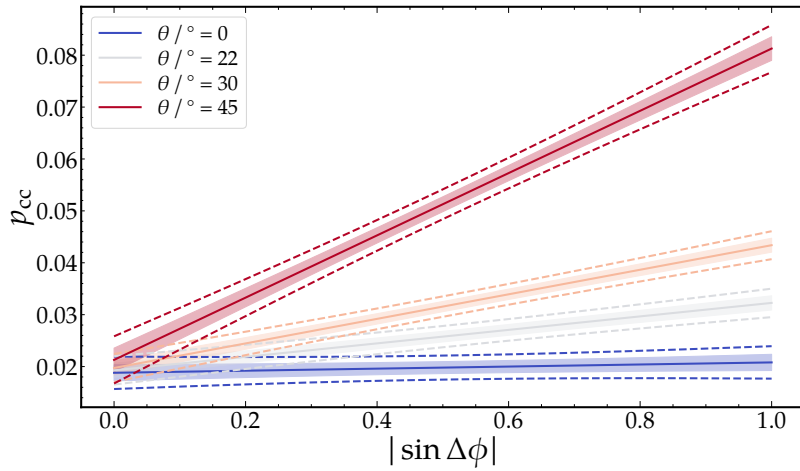

Figure 7.13: p_{cc} parameterization of Eq. (5.9) for four different zenith angles, together with the corresponding 1σ (shaded bands) and 2σ (dashed lines) intervals.

To assess a systematic uncertainty, the standard reconstruction of data was repeated with shifted probabilities $p_{cc}(\theta, \Delta\phi)^{\pm} = p_{cc}(\theta, \Delta\phi) \pm 2\sigma(\theta, \Delta\phi)$, leaving all the remaining reconstruction parameters unchanged[3]. Furthermore, an additional reconstruction was performed but using the corner-clipping correction found for simulations (see Fig. 5.6). As discussed in Section 5.2, the parameterization of p_{cc} for simulations shows some zenith-dependent discrepancy with the one obtained for data. Although we showed that such discrepancy is not significant as it produces at most a 3% difference in the maximum likelihood estimators, this test serves to evaluate the impact of using the two parameterizations in the end-to-end result.

The evolution of $\rho_{35} / (E/10^{18} \text{ eV})^{0.9}$ with energy obtained with the different parameterizations of p_{cc} is shown in the left panel of Fig. 7.14. All the markers lie almost on top of each other and is visually difficult to see a significant impact. In the left panel of the figure, the ratio between the mean muon density obtained for each alternative p_{cc} and the standard p_{cc} in each energy bin is displayed. When p_{cc}^{-} is used, a smaller corner-clipping correction is applied and therefore the ρ_{450} are systematically higher than those obtained with the standard p_{cc}. In contrast, a larger correction is applied when utilizing p_{cc}^{+}, shifting ρ_{450} downwards. Finally, the values of p_{cc} for simulations are systematically higher than those for data and, consequently, the muon shower sizes are systematically smaller.

---

[3]In particular, we did not repeat the CIC each time.

It is evident that using different corrections produces only small impact, being at most 0.6% when using the simulation parameterization. Consequently, we use this value as an estimate of the systematic uncertainty due to different corner-clipping corrections.

Finally, to illustrate the reason for the minimal impact of the correction on the muon shower size, we present in Fig. 7.15 the log-likelihood (logarithm of Eq. (4.14)) for a single module with $k = 5$ and $k = 50$ for different p_{cc}. In addition to reaching their minima at very similar μ values, regardless of the value of p_{cc}, the shape and curvature of the log-likelihood curves are nearly identical. In other words, the log-likelihood curves exhibit similar behavior for all μ, particularly near the minima. This is most clearly observed for small k ($k = 5$ in the figure), where the likelihoods are very broad for being dominated by Poisson fluctuations. As a consequence, the event likelihood, defined as the sum of the log-likelihoods of the individual module likelihoods, is only marginally affected by differences in the value of p_{cc}, reaching its minimum at a nearby ρ_{450}.
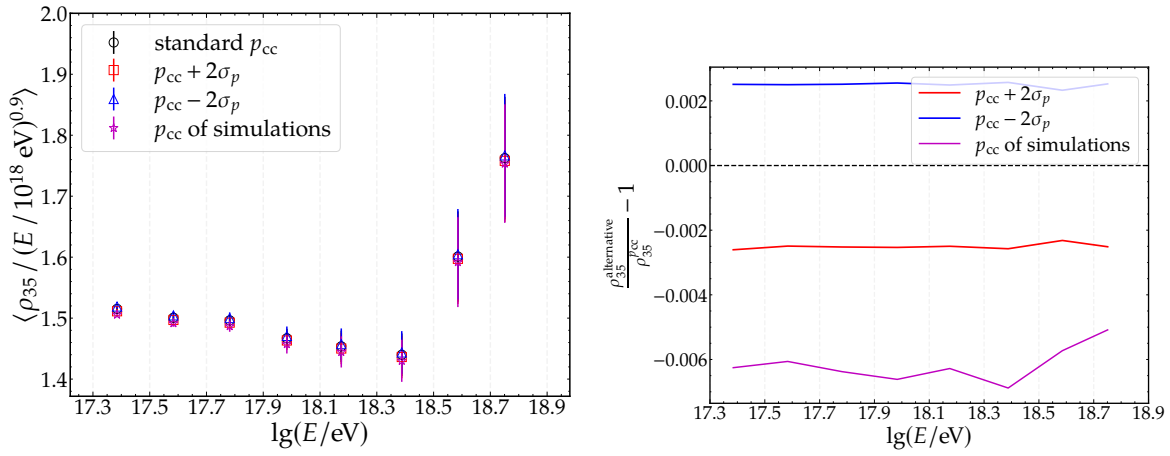

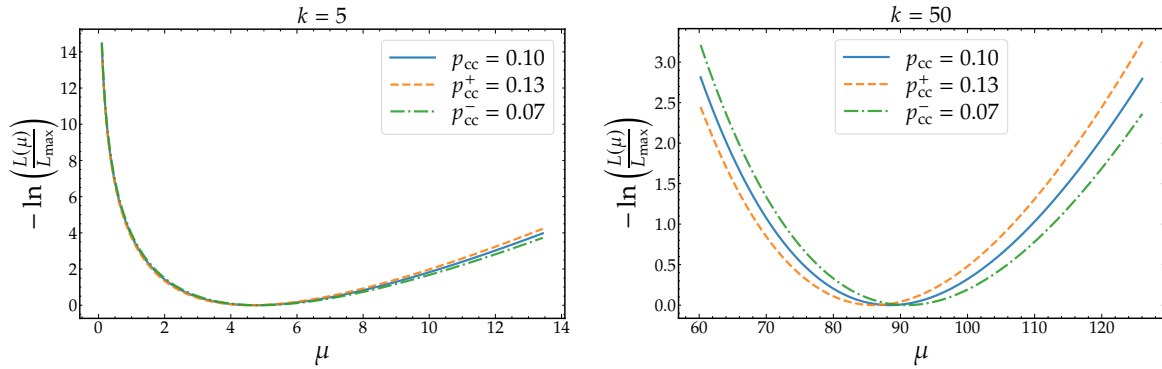**Figure 7.14:** Impact in the final result of using different corner-clipping corrections.

Figure 7.15: Log-likelihoods (logarithm of Eq. (4.14), normalized by its maximum) for a module with $k = 5$ (left) and $k = 50$ (right) for different values of p_{cc}.

7.4.3 Muon pattern

The typical width of a muon signal is approximately $\sim 7 - 8$ "1s". The condition for identifying a muon signal in a bar is the presence of at least one sequence of four consecutive "1s" in its binary trace (see Section 3.3.4). This criterion was chosen to maximize the signal-to-noise ratio, preventing noise signals—composed predominantly of sequences with three or fewer

"1s" in the trace—from being misidentified as muons, while ensuring high efficiency for muon detection [59].

However, differences in the UMD modules (SiPM gain, scintillators, fibers, electronics) throughout the array can result in some detectors systematically producing wider signals than others (see Appendix I), making them slightly more efficient or noisier. Aging effects, although shown not to be highly significant, can also play a minor role, as UMD modules output 0.7% fewer "1s" per year (see Appendix I).

To assess the impact of selecting four consecutive "1s" as the muon pattern, we repeated the reconstruction procedure using patterns of three and five consecutive "1s", keeping all other configuration parameters unchanged. When a shorter pattern is used, a higher muon efficiency is expected at the cost of also increasing false positives due to noise. Conversely, a decrease in the efficiency is awaited when using a wider pattern[4]. Thus, this test ultimately provides the possibility to explore the impact of varying the detector efficiency. Although we acknowledge that this approach may overestimate the uncertainty, we consider it a coarse but conservative estimation.

In the left panel of Fig. 7.16, the normalized muon density as a function of energy is shown for both the standard and alternative pattern definitions. When three "1s" are required, it is more likely for detectors to trigger on more bars, either due to noise signals that were previously rejected or weak muon signals that failed to produce four "1s". Consequently, the muon measurement is pushed toward higher values. In contrast, when a pattern of five "1s" is used, short signals previously accepted are now ignored, resulting in fewer triggered bars. As a result, the detector becomes less efficient, shifting the measurement toward lower values. In the right panel of the figure, the ratio between the results obtained with the alternative patterns and the standard pattern of four "1s" is displayed as a function of energy. The shorter pattern results in a shift of $+5\%$ while the wider pattern results in a shift of -7%. Therefore, we take these values as systematic uncertainties.
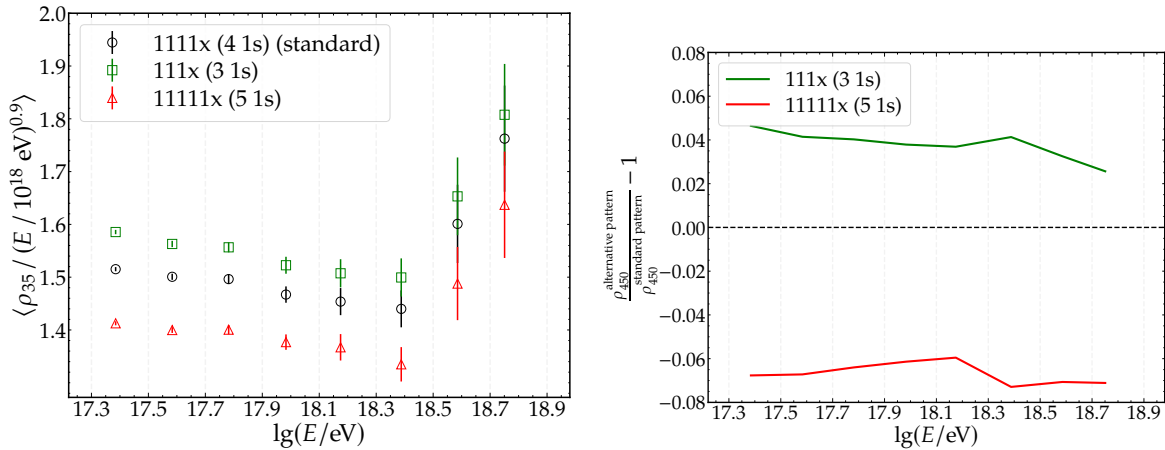

Figure 7.16: Impact of using different muon patterns in the end result.

7.4.4 Systematic uncertainty in ρ_{450} due to unknown MLDF shape and optimal distance

Fixing β to a parameterized value fixes the MLDF shape during the fit. However, the true value of β varies for each event. Therefore, fixing the slope can induce a bias in ρ_{450}.

---

[4]We note that different muon patterns would also affect the corner-clipping correction developed in the Chapter 5: a shorter (wider) pattern would produce more (less) overcounting due to corner-clipping.

To investigate this, using the events in which β can be left free, we computed the ratio between the ρ_{450} obtained with β fixed and free. The mean and median ratio as function of energy are shown in Fig. 7.17. The two statistics are slightly different due to the presence of some outliers, mainly saturated events, in the lower energy bins. The mean difference between the ρ_{450} with fixed and free slope is at most $\sim 3\%$ for the lowest energy bin, and decreases with energy. If we take the median as a reference, the difference is further reduced below 1% for all energies. Thus, for the events in which β can be left free, we can conclude that fixing the slope does not significantly changes the result of ρ_{450}.
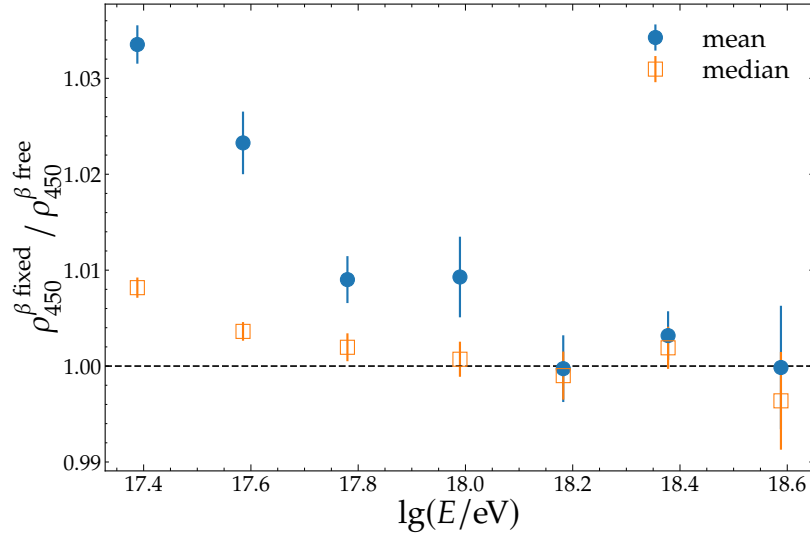

Figure 7.17: Comparison of ρ_{450} obtained with β free and fixed.

However, the vast majority of events does not allow for a free β, as already discussed. To assess the systematic uncertainty in ρ_{450} induced by fixing β, we use a similar approach to the one used by the SD. The method consists in, for each event, repeating the fit but fixing the slope to a shifted value $\beta_{\pm} = \beta_0 \times (1 \pm \sigma_\beta(E))$, where β_0 is given by the parameterization described in the previous section and the magnitude of the shift $\sigma_\beta(E)$ depends on the energy of the event and is given by the quadratic parameterization shown in Fig. 6.22. If we name $\rho_{450}^{\pm}$ the ρ_{450} value obtained with the slope fixed to $\beta_{\pm}$, a systematic uncertainty can be defined as

$$\sigma_{\rho_{450}}^{\text{sys}} = \frac{|\rho_{450}^+ - \rho_{450}^-|}{2}. \tag{7.11}$$

This excercise also allows to obtain r_{opt} for each event, the optimal distance at which the MLDF is independent of β. This is defined as the distance at which the MLDFs with shifted β coincide. A selected event is shown as an example to illustrate the method to obtain r_{opt} and $\sigma_{\rho_{450}}^{\text{sys}}$ in Fig. 7.18.
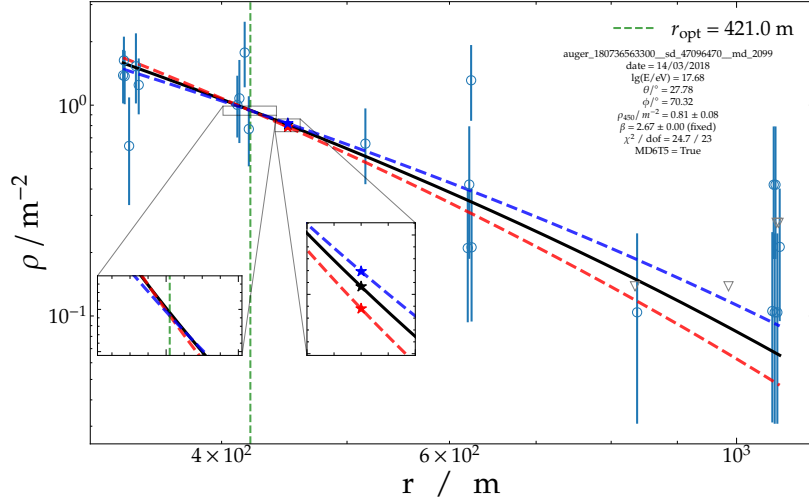
Figure 7.18: Method to obtain r_{opt} and $\sigma_{\rho_{450}}^{\mathrm{sys}}$ for an event. Black line indicates the LDF with β fixed to the parameterized value, while red (blue) dashed line represents the LDF with beta fixed to β_+ (β_-). The stars indicate the value of ρ_{450} in each case. Vertical green line represents r_{opt}.

It is worth noting that r_{opt} and $\sigma_{\rho_{450}}^{\mathrm{sys}}$ are intimately related, as shown in Fig. 7.19. When r_{opt} is below (above) 450 meters, ρ_{450}^- is greater (smaller) than ρ_{450}^+, and therefore the difference $\rho_{450}^+ - \rho_{450}^-$ is negative (positive). Naturally, when $r_{\mathrm{opt}} = 450$ m, the systematic uncertainty is null. The further r_{opt} deviates from 450 m, the larger (in absolute value) the difference between ρ_{450}^+ and ρ_{450}^-.

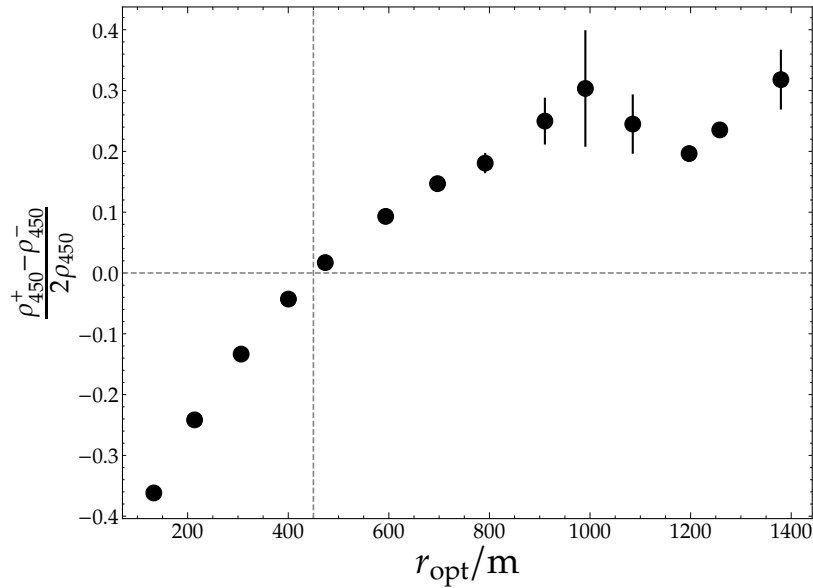**Figure 7.19:** Mean value of $\frac{\rho_{450}^+ - \rho_{450}^-}{2\rho_{450}}$ as a function of r_{opt}. The vertical dashed line indicates 450 meters, whereas the horizontal line marks the null value.

In the left panel of Fig. 7.20, we show the mean relative systematic error as a function of energy. We also show the energy evolution of the mean relative statistical error. The statistical error is provided by the MLDF fit procedure in each event, and is mainly driven by the number of triggered stations and the total number of muons. For the two types of uncertainties, it is necessary to disinguish between events with and without saturation.

Saturated detectors do not fully constrain the MLDF close to the core, and as a consequence, the fit loses leverage, resulting in larger uncertainties, both statistical and systematic.

Systematic and statistical uncertainties decrease with energy, regardless of the saturation status. This is a consequence of the increasing number of triggered stations, which results in a better constrain to the MLDF fit. Additionally, a larger number of muons is measured in each detector, which decreases the sampling fluctuations.

The zenith dependence of the errors is displayed in the right panel of Fig. 7.20. For unsaturated events, the statistical and systematic errors show no dependence on the zenith angle. In contrast, the uncertainties for saturated events become smaller for more inclined showers. This is a result of a geometrical effect. Vertical saturated events have a saturated detector close to the core, while the bulk of unsaturated detectors, corresponding to the first crown surrounding the saturated position, are at a similar shower plane distance, determined by the array spacing (750 m for the UMD). As a result, the MLDF is weakly constrained, leading to larger uncertainties. For inclined events, the first crown of unsaturated detectors spans a wider range of distances to the core, providing better constrains for the fit.

The mean relative systematic uncertainty using all the events (i.e., both saturated and non-saturated) as a function of energy is displayed with triangular empty markers in Fig. 7.21. For lower energies, where saturation is unlikely, the uncertainty is dominated by non-saturated events. As the energy increases, the fraction of saturated events rises, and the uncertainty of saturated events begin to dominate, causing a slight increase in the systematic uncertainty in the higher energy bins. To capture this behaviour, a quadratic function was used to fit the energy dependence of the systematic uncertainty, shown as a dashed line in the figure. This parameterization allows us to obtain an estimate of the systematic error to an arbitrary value of energy.
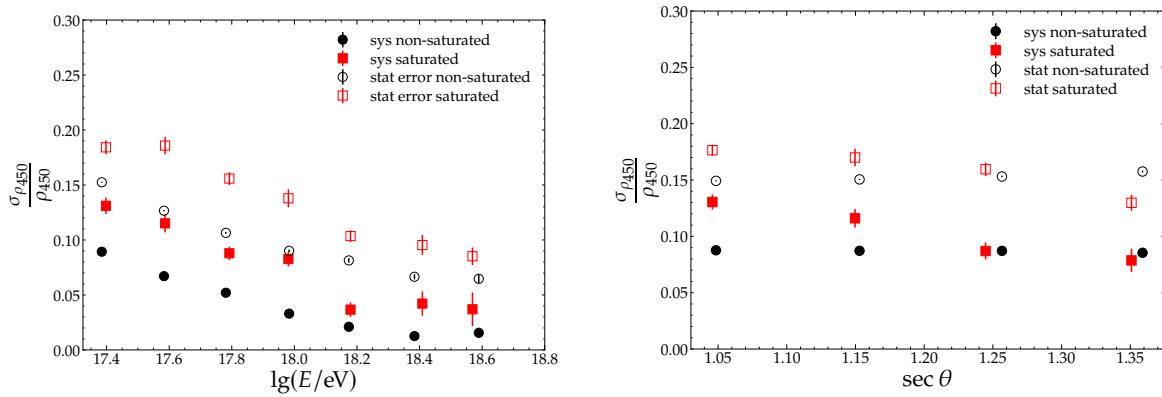

Figure 7.20: Statistical and systematic uncertaintes of ρ_{450} as function of energy (left) and $\sec\theta$ (right). Saturated and non-saturated events are treated separately.
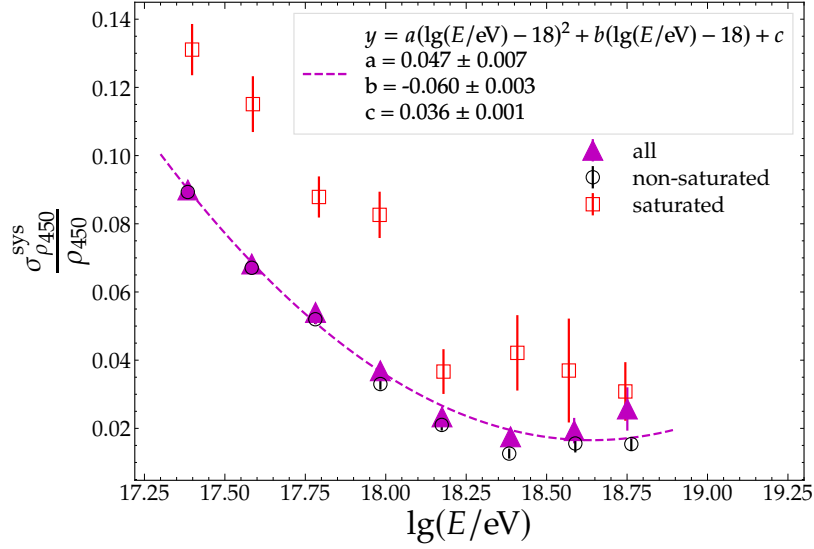
Figure 7.21: Mean relative systematic uncertainty of ρ_{450} due to fixing β as a function of energy including both saturated and non-saturated events.

The optimal distance r_{opt} as a function of energy (left panel) and zenith angle (right panel) is shown in Fig. 7.22. Due to the aforementioned feature of the saturated events, the optimal distance is systematically larger for them. Higher energy events produce bigger footprints on the ground and therefore possess more triggered detectors further from the shower core. As a result, a smooth increase of the optimal distance with energy is observed. On the other hand, only a weak dependence is found with the zenith angle.
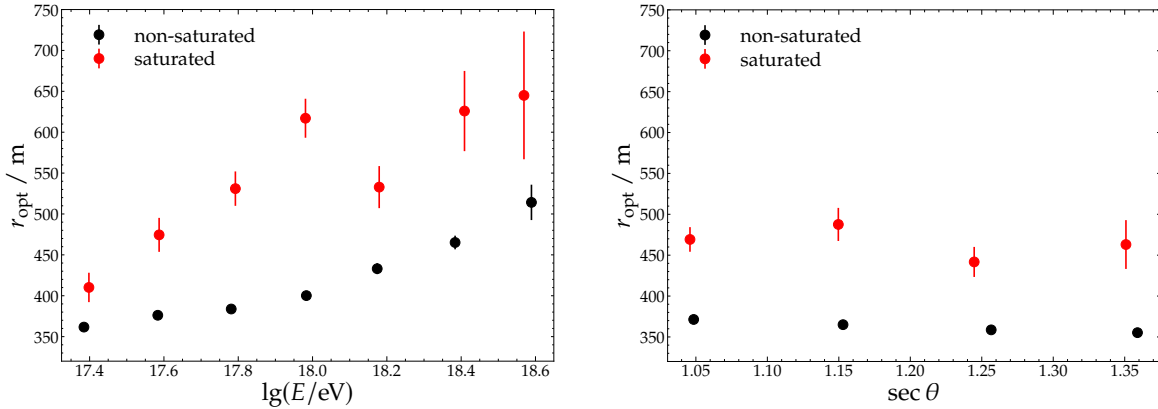

Figure 7.22: Mean optimal distance as function of energy (left) and $\sec\theta$ (right). Saturated and non-saturated events are treated separately.

7.4.5   Reconstruction procedure

As explained in Chapter 6, the standard reconstruction of the UMD now leaves the UMD core free while leaving the LDF slope β fixed to a parameterized value (see Section 6.4). We try two additional configurations, namely, with the core and β fixed and with the core fixed with β free in every event. Freeing both the core and the slope in every event is not feasible. The maximum difference of $\langle\rho_{35}\rangle$ between the reconstructions in each energy bin serves as a measure of the systematic uncertainty due to the reconstruction configuration. In the left panel of Fig. 7.23, the evolution of ρ_{35}—normalized to reduce the energy dependence—for

the different configurations is displayed. The ratio between the standard and alternative reconstruction configurations is observed in the right panel of the figure. Fixing both the core and β produces a negligible impact, below 1% in all energy bins. When β is free, the difference with the standard configuration is well contained within $\pm 2\%$, with the exception of the highest energy bin ($10^{18.7} < E / \text{eV} < 10^{18.9}$), for which a difference of $\sim 6\%$ is observed, although only 6 events are present in this bin and the statistical error of the two points overlap. Therefore, we take a contribution of 3% for all energies, as a compromise between the 2% and 6% observed for lower and higher energy bins, respectively.
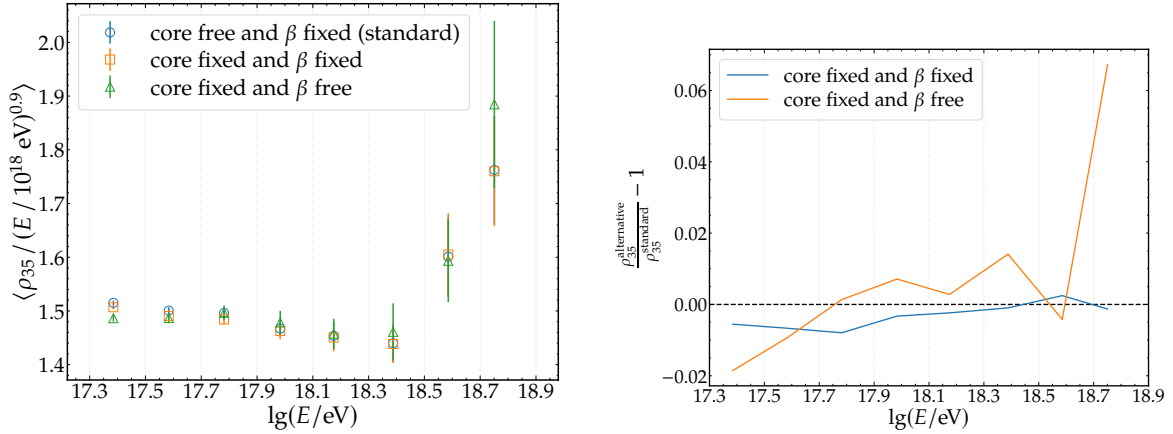

Figure 7.23: Impact of using different reconstruction configurations.

7.4.6 Long-term stability

To evaluate the stability of the result over time, we divided our dataset into two periods with the same number of events. The division time between the datasets was set to GPS time 1295698963 s, corresponding to January 26, 2021. Thus, Period 1 spans from January 1st, 2018 to January 26, 2021 whereas Period 2 spans from January 26, 2021 to December 21, 2021. Both periods contain 6627 events above $10^{17.3}$ eV each. Since the UMD array was deployed at varying rates, with deployment still ongoing, the first period spans almost three years, whereas the second covers less than one year (see Fig. 7.1).

In the left panel of Fig. 7.24, we show the mean normalized muon density as a function of energy for each period, as well as for the full period. A split is visible between the two periods, with Period 1 showing slightly larger values than Period 2. In the right panel of the figure, the ratio between the mean for one period and that of the full period is displayed for each energy bin. The effect is less than 2%, as observed at the lower energies where statistical uncertainties do no dominate. This may likely be the result of Period 1 being dominated by a small set of detectors as the UMD array was not very large (see Fig. 7.1). Therefore, we conservatively take a $\pm 2\%$ contribution to the systematic uncertainty budget.
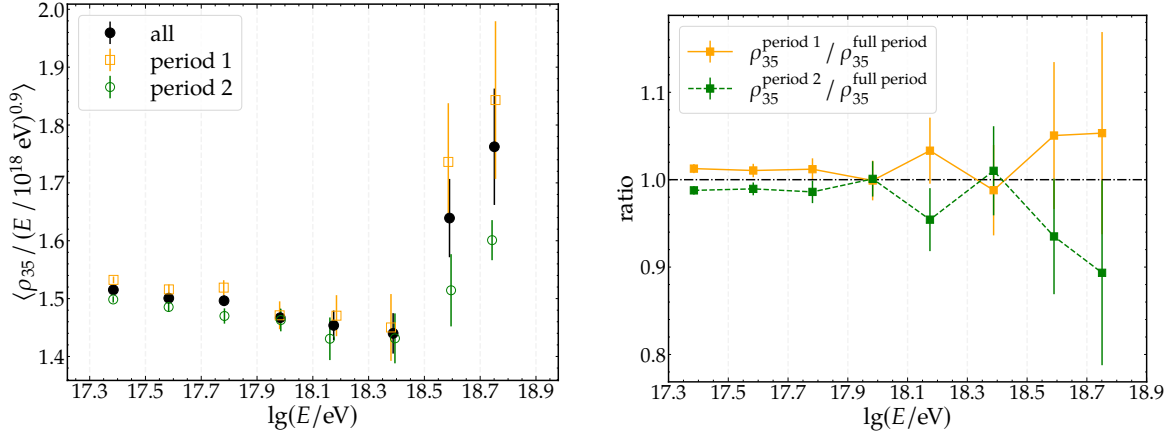
Figure 7.24: *Left*: Mean normalized muon density for different time periods. *Right*: Ratio between the mean ρ_{35} obtained in a selected period and the full period for each energy bin.

7.4.7   Energy scale

The number of muons increases almost linearly with energy (see Eq. (2.13)). Therefore, a positive (negative) shift in the energy scale would produce an apparent decrease (increase) in the muon number when averaged in an energy bin. To estimate the systematic induced in the muon measurement due to this effect, we shift the energy of each event $\pm 14\%$, which corresponds to the systematic uncertainty in the SD energy estimate [11]. Then, we proceed to compute the mean of the muon density in each energy bin using the same binning. The relative difference of the mean muon density in each bin, with and without shifts in the energies, serves as an estimate of the systematic uncertainty. As shown in Fig. 7.25, a $+14\%$ increase in energy results in a -11% shift in the muon density (red upward-pointing triangles), while a -14% decrease in energy produces a $+14\%$ shift in the muon density (blue downward-pointing triangles). Thus, we take these as systematic.
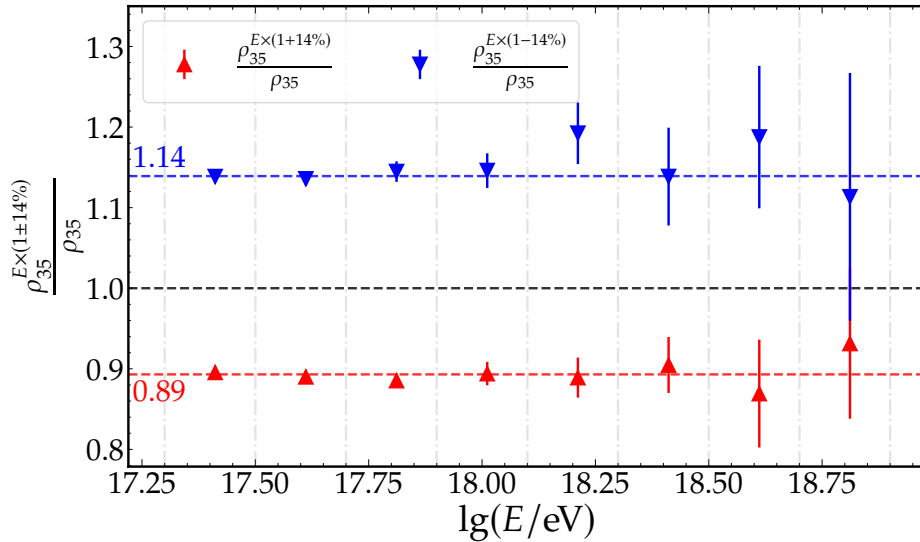

Figure 7.25: Systematic uncertainty in ρ_{35} due to shifts in the energy scale.

7.4.8 Total systematic uncertainties

In Table 7.2, we summarize the contributions of all sources of systematic uncertainties. The largest contribution arises from the uncertainty in the energy scale. In Fig. 7.26, the different contributions to the systematic uncertainty as a function of energy are depicted with dashed lines. The total systematic uncertainty, calculated as the sum in quadrature of all the uncertainties, is represented by a solid olive line. The solid grey line indicates the total uncertainty when considering only the UMD measurement, i.e., excluding the contribution of the energy scale.

Source	Relative uncertainty
Attenuation correction (CIC)	1%
Corner-clipping	0.6%
LDF shape	from 10% to 2%
Muon pattern	$+5\%$ -7%
Reconstruction	3%
Long-term	2%
Energy scale	$+14\%$ -11%

Table 7.2: Table summarizing the contributions to the systematic uncertainty
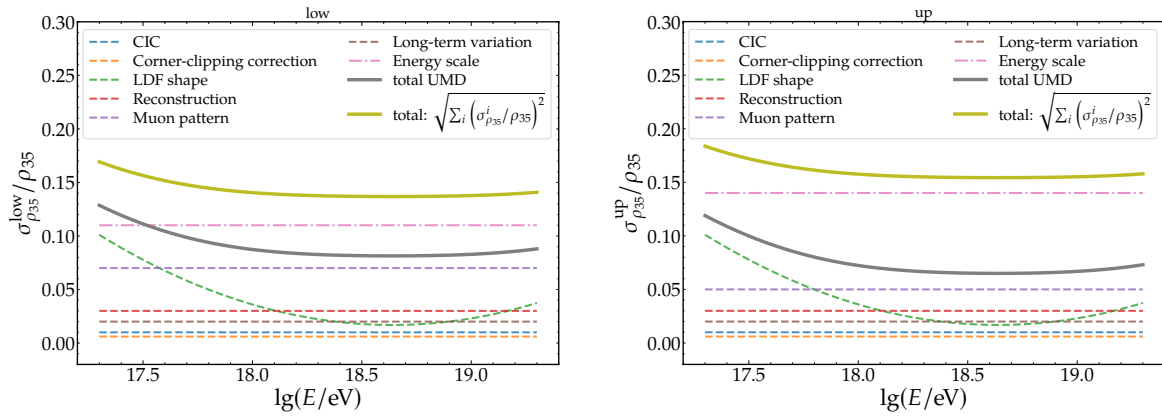

Figure 7.26: Systematic uncertainties as a function of energy. Lower (upper) error is shown in the left (right) panel. The total systematic uncertainty, indicated with solid olive line, is computed as the sum in quadrature of all the contributions (Eq. (7.5)). The solid grey line shows the total uncertainty without considering the contribution of the energy scale.

7.5 Simulations

7.5.1 Library

For the interpretation of the muon measurements, it is necessary to obtain the expected outcome of the muon content for fixed primaries using air-shower and full detector simulations. In this section, we describe the set of simulations used to that end.

We have used a library of pre existent simulated showers generated with the COsmic Ray Simulations for KAscade (CORSIKA) framework [24] available in the KIT cluster. The library comprised proton and iron primaries, EPOS-LHC [27, 28] and QGSJetII-04 [29] as high-energy hadronic interaction models, and contained the discrete energies $10^{17.5}$ eV, 10^{18} and $10^{18.5}$, and zenith angles $\theta/° = \{0, 12, 22, 32, 38, 48\}$. Each primary, hadronic model,

energy and zenith angle combination had 120 showers, leading to a total of $N_{\mathrm{E}} \times N_\theta \times N_{\mathrm{prim}} \times N_{\mathrm{model}} \times N_{\mathrm{sh}} = 3 \times 6 \times 2 \times 2 \times 120 = 8640$ showers. The azimuth angle of each shower is uniformly distributed between $0°$ and $360°$.

Each shower was thrown once to the simulated SD-UMD-750 array. The impact point of the shower was uniformly sampled from a distribution centered on a central WCD tile, as shown in Fig. 7.27. Both the response of the SD and UMD, as well as the posterior reconstruction of their simulated signals, were performed using $\overline{\mathrm{Offline}}$. The reconstruction chain for the simulated signals is identical to that used for the data, yielding for each simulated shower a reconstructed ρ_{450} by means of the MLDF fit to the detector signals. The corner-clipping correction is the one obtained for simulations in Section 5.1.
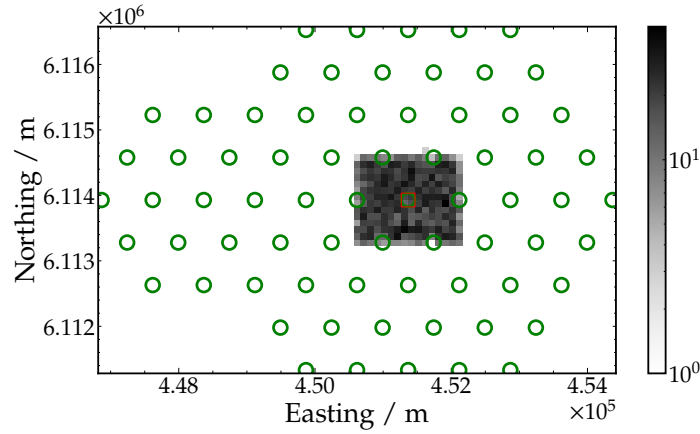

Figure 7.27: Distribution of simulated core positions.

7.5.2   Energy evolution of the muon content in simulations

To take into account attenuation in data, the muon shower size ρ_{450} produced by a shower with an arbitrary zenith angle θ is converted to ρ_{35}, interpreted as the ρ_{450} the shower would have produced had it arrived at a reference zenith angle $\theta_{\mathrm{ref}} = 35°$, as explained in Section 7.2. In this way, the zenith angle dependence of the muon shower size is removed, allowing to focus the analysis in the energy evolution of the estimator. Therefore, it would be convenient to have a set of showers with $\theta_{\mathrm{MC}} = 35°$ to be compared to data.

However, the library possess six zenith angles and none of them equals $35°$. Thus, to obtain the expected $\rho_{35}(E)$ we proceed as follows. For a fixed energy, primary and hadronic model, we obtain the mean ρ_{450} for each zenith angle. Then, we fit the evolution of $\langle \rho_{450} \rangle$ with $x = \sin^2 \theta_{\mathrm{MC}} - \sin^2 35°$ with Eq. (7.1), obtaining ρ_{35}, a and b as a result of the fit. An example of this procedure applied to EPOS-LHC proton showers of $10^{17.5}$ eV is shown in Fig. 7.28.
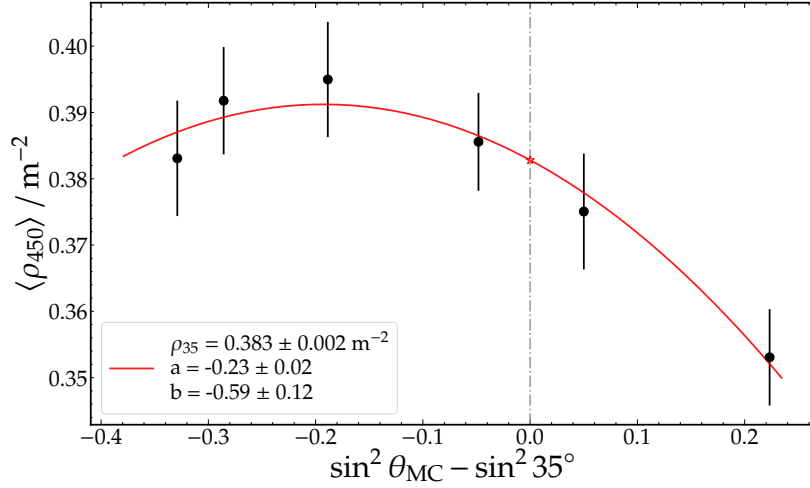
Figure 7.28: Procedure to obtain ρ_{35} for EPOS-LHC proton showers of $10^{17.5}$ eV. Each point corresponds to the mean ρ_{450} for each zenith, whereas the error bars indicate the standard deviation of the mean.

In this way, a set of three ρ_{35} values is obtained, one for each of the energies in the library. To be able to evaluate ρ_{35} at arbitrary energies, and not only to the ones available in the library, the evolution of ρ_{35} with the Monte-Carlo energy is fitted with a power law, as expected within the framework of the Heitler-Mathews model descrbed in Section 2.3 (see Eq. (2.16)),

$$\rho_{35}(E_{\text{MC}}) = a \left(\frac{E_{\text{MC}}}{10^{18} \text{ eV}} \right)^b , \qquad (7.12)$$

where a, the muon density at 10^{18} eV, and b, the logarithmic gain, are free parameters.

The resulting fits are shown in the top panel of Fig. 7.29 for the two primaries and hadronic models. To ease visualization and weaken the energy dependence, we normalize ρ_{35} by a factor $\left(E_{\text{MC}}/10^{18} \text{ eV} \right)^{0.9}$, as displayed in the bottom panel of the Figure.

The ratio of the muon density at 10^{18} eV between primares for a fixed model, and between models for a fixed primary, can be obtained to quantify the different muon contents expected. Both hadronic models predict ~ 50 % more muons for iron than proton, being the ratios $\left(\frac{a_{\text{Fe}}}{a_{\text{P}}} \right)_{\text{EPOS-LHC}} = 1.512 \pm 0.007$ and $\left(\frac{a_{\text{Fe}}}{a_{\text{P}}} \right)_{\text{QGSJetII-04}} = 1.504 \pm 0.012$. The ratio between models are $\left(\frac{a_{\text{EPOS-LHC}}}{a_{\text{QGSJetII-04}}} \right)_{\text{P}} = 1.045 \pm 0.008$ and $\left(\frac{a_{\text{EPOS-LHC}}}{a_{\text{QGSJetII-04}}} \right)_{\text{Fe}} = 1.051 \pm 0.005$, indicating that EPOS-LHC predicts ~ 5 % more muons than QGSJetII-04, regardless of the primary.
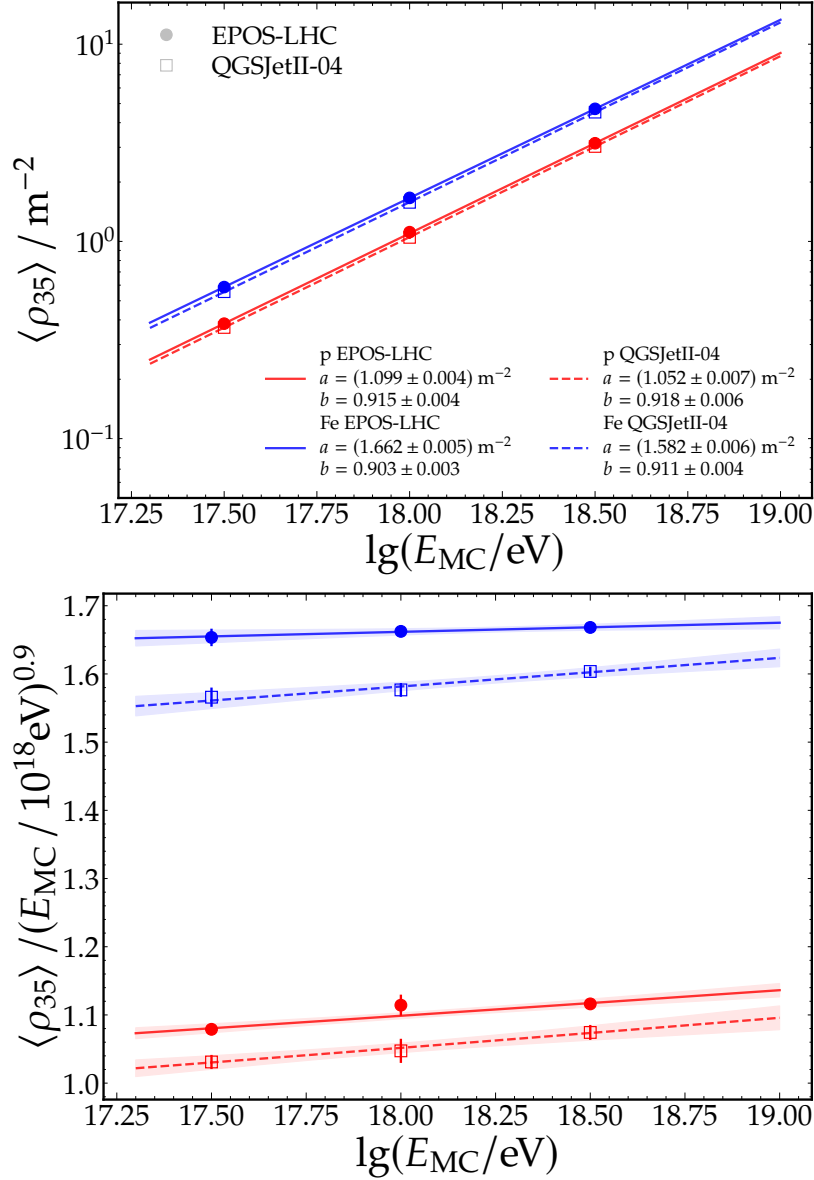
Figure 7.29: *Top*: Fit of the ρ_{35} values obtained in simulations to Eq. (7.12). The optimal parameters are stated in the lower right corner. *Bottom*: Same as in upper panel but normalized by $\left(E/10^{18}\ \mathrm{eV}\right)^{0.9}$ to weaken the energy dependence. The shaded bands indicate the 1σ uncertainties of the fits. The Monte-Carlo energy is used.

Another relevant quantity needed for the analysis is the energy evolution of the mean of the natural logarithm of ρ_{35}, $\langle\ln(\rho_{35}/\mathrm{m}^{-2})\rangle$. To obtain this, for each energy, primary particle, and hadronic model in the library, the reconstructed ρ_{450} of each shower is converted into ρ_{35} using Eq. (7.1). The attenuation function f_{att} used was the one previously obtained by fitting $\langle\rho_{450}\rangle$ as a function of $x = \sin^2\theta_{\mathrm{MC}} - \sin^2 35°$. For instance, for EPOS-LHC proton showers with $10^{17.5}$ eV, the attenuation function derived from the fit in Fig. 7.28 was utilized.

As an example, the mean $\ln(\rho_{35}/\mathrm{m}^{-2})$ as a function of x is shown in Fig. 7.30 for this set of showers. As expected, any zenith angle dependence is removed by f_{att}. The mean value of $\ln(\rho_{35}/\mathrm{m}^{-2})$ across all showers is indicated as a dashed horizontal line. In this way, a set of three values of $\langle\ln(\rho_{35}/\mathrm{m}^{-2})\rangle$ was obtained for each primary particle and hadronic model (one value for each energy). These values are shown in Fig. 7.30.

The dependence of the mean logarithmic muon density on energy was fitted with a linear function of log-energy:

$$\langle \ln(\rho_{35} \, / \, \mathrm{m}^{-2}) \rangle = m \left(\lg(E_{\mathrm{MC}}/\mathrm{eV}) - 18 \right) + c. \tag{7.13}$$

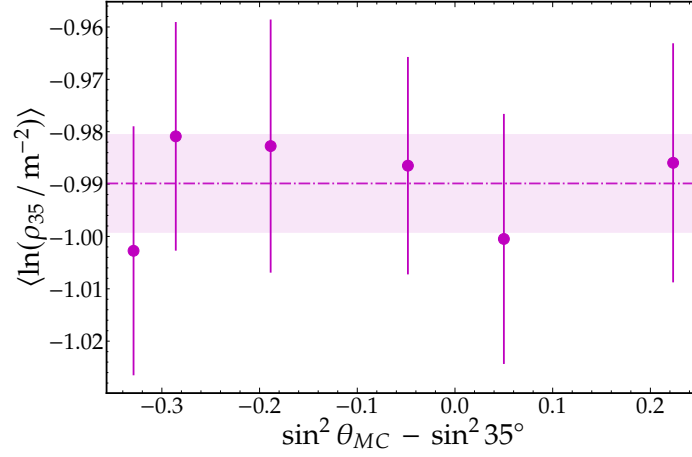The results of these fits are also shown in Fig. 7.30.

Figure 7.30: Mean of $\ln(\rho_{35}/\mathrm{m}^{-2})$ as a function of $\sin^2 \theta_{\mathrm{MC}} - \sin^2 35°$ for EPOS-LHC proton showers of $10^{17.5}$ eV. The mean over all the showers is indicated as a dashed horizontal line. The shaded area corresponds to the mean $\pm$ one standard deviation of the mean.
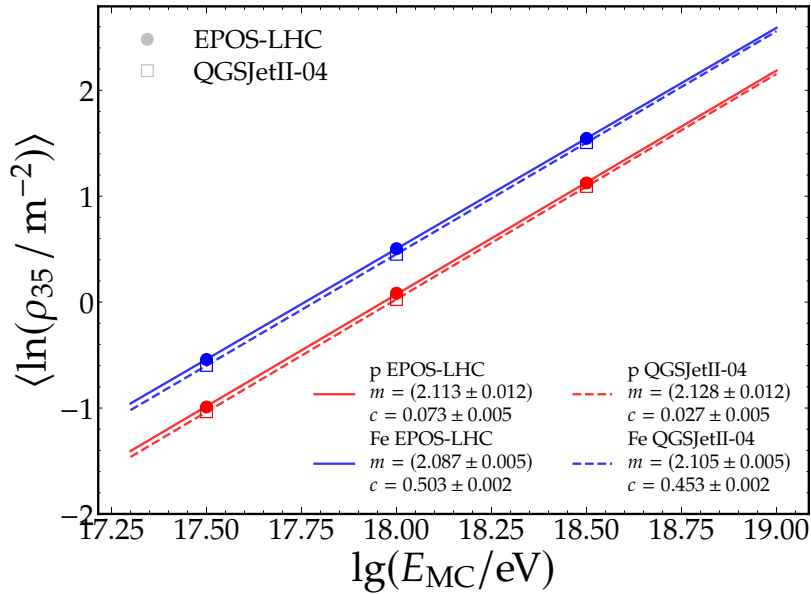
Figure 7.31: Evolution of $\langle \ln(\rho_{35} \, / \, \mathrm{m}^{-2}) \rangle$ with Monte-Carlo energy. Lines indicate fits to Eq. (7.13).

Impact of the energy reconstruction

The vertical axis in Fig. 7.29 corresponds to the reconstructed ρ_{35}, obtained via the muon LDF fit to the simulated signals, following the same procedure as applied to the data. Thus, the effects of the muon detector and its reconstruction procedure are taken into account.

However, the horizontal axis represents the true Monte Carlo energy, E_{MC} (which also impacts the vertical axis of the lower panel). In data, the reconstructed energy by the SD, E, is used instead, and the muon density is obtained as a function of this estimate. Because the number of muons increases rapidly with E_{MC} (approximately $E_{MC}^{0.9}$), reconstruction effects in the energy must be accounted for before comparing data and simulations, even if E is an unbiased estimator of E_{MC} [80]. In order to take into account energy reconstruction effects, we follow the procedure adopted in Refs. [70, 81]. The mean muon density ρ_{35} in a reconstructed energy bin $E^- < E < E^+$, with a bin center E^c, divided by E^α, is obtained by

$$\left\langle \frac{\rho_{35}}{(E/10^{18}\text{eV})^\alpha} \right\rangle (E^c) = \frac{\int_{E^-}^{E^+} \int_0^\infty \frac{\rho_{35}^{\text{sim}}(E_{MC})}{(E/10^{18}\text{eV})^\alpha} J(E_{MC}) G(E|E_{MC}) \epsilon(E_{MC}) dE_{MC} dE}{\int_{E^-}^{E^+} \int_0^\infty J(E_{MC}) G(E|E_{MC}) \epsilon(E_{MC}) dE_{MC} dE}, \tag{7.14}$$

where

- $\rho_{35}^{\text{sim}}(E_{MC})$ is the reconstructed mean muon density ρ_{35} as a function of the Monte-Carlo energy given by Eq. (7.12) shown in Fig. 7.29.

- $J(E_{MC})$ is the cosmic ray flux observed by the Pierre Auger Observatory taken from Ref. [82] given by

$$J(E_{MC}) = J_0 \left(\frac{E_{MC}}{10^{18.5} \text{ eV}} \right)^{-\gamma_1} \prod_{i=1}^3 \left[1 + \left(\frac{E_{MC}}{E_{ij}} \right)^{1/\omega_{ij}} \right]^{(\gamma_i - \gamma_j)\omega_{ij}}, \tag{7.15}$$

  where $j = i + 1$, $J_0 = 1.315 \times 10^{-18} \text{km}^{-2}\text{sr}^{-1}\text{yr}^{-1}\text{eV}^{-1}$, $E_{12} = 5 \times 10^{18}$ eV, $E_{23} = 13 \times 10^{18}$ eV, $E_{34} = 46 \times 10^{18}$ eV, $\gamma_1 = 3.29$, $\gamma_2 = 2.51$, $\gamma_3 = 3.05$, $\gamma_4 = 5.1$, and $\omega_{ij} = 0.05$.

- $G(E|E_{MC})$ is the resolution function of the SD energy. It corresponds to the conditional probability of reconstructing a shower with true energy E_{MC} to a reconstructed energy E. Following Ref. [83], we adopt a Gaussian distribution centered in E_{MC} (i.e., unbiased) and a standard deviation given by

$$\sigma(E_{MC}) = E_{MC} \left(0.06 + 0.05 \times (E_{MC}/10^{18} \text{ eV})^{-1/2} \right). \tag{7.16}$$

- $\epsilon(E_{MC})$ corresponds to the trigger efficiency function of the SD-750 taken from Ref. [70]. Its formula reads

$$\epsilon(E_{MC}) = \frac{1}{2} + \frac{1}{2}\text{erf}\left[3.71 \lg \left(\frac{E_{MC}}{10^{16.93}\text{eV}} \right) \left(1 + 0.187 \lg \left(\frac{E_{MC}}{10^{16.93}\text{eV}} \right) \right) \right]. \tag{7.17}$$

The cosmic ray flux $J(E_{MC})$ (Eq. (7.15)), resolution function $G(E|E_{MC})$ and trigger probability (Eq. (7.17)) are displayed in Fig. 7.32.
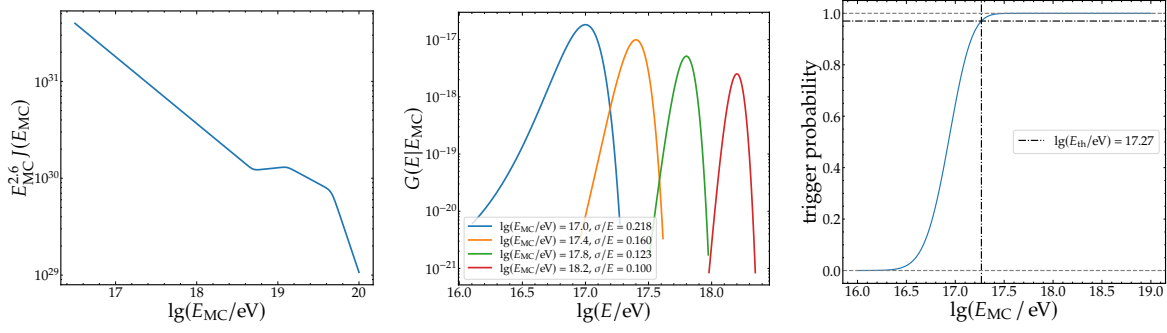
Figure 7.32: Functions used to account for energy reconstruction effects in the muon measurement via the convolution of Eq. (7.14). *Left*: Cosmic ray flux (Eq. (7.15)). *Middle*: Resolution function of the SD energy estimate for four Monte-Carlo energies. The apparent assymetry in the Gaussian distribution is due to the logarithmic scale of the x-axis. The standard deviation for each energy given by Eq. (7.16) is stated in the legend. *Right*: Trigger probability of the SD-750 (Eq. (7.17)). Horizontal grey lines indicate the null and unity values, while the vertical black line marks the threshold energy where the trigger probability equals 97%.

It is worth noting that the energy threshold—the energy above which the array triggers with a probability greater than 97%—derived from Eq. (7.17) is $10^{17.3}$ eV, which is lower than the value obtained using the uniformity χ^2 test with data in Section 7.1.1. This discrepancy is most likely due to the additional conditions imposed on UMD events, which were not considered in Eq. (7.17).

In the upper panel of Fig. 7.33, the curves of $\langle \rho_{35}^{\text{sim}} / (E_{\text{MC}} /, 10^{18} \text{ eV})^\alpha \rangle$ as a function of the true Monte Carlo energy E_{MC} (as shown in the bottom panel of Fig. 7.29) and $\langle \rho_{35} / (E / 10^{18} \text{ eV})^\alpha \rangle$ as a function of the reconstructed energy E, with $\alpha = 0.9$, are shown for EPOS-LHC. For the latter, we take the same bin edges used for data, the lower-most edge corresponding to $\lg(E/\text{eV}) = 17.3$ (on energy bin below full efficiency for data, see Section 7.1.1) increasing with a step of $\Delta \lg(E/\text{eV}) = 0.2$. The two curves are very similar. In the lower panel of the figure, the ratio between the two curves is displayed, showing that the difference between them is at most $\sim 5\%$ near $10^{17.3}$ eV, the energy threshold implied by Eq. (7.17).

It is interesting to note that, for energies above 10^{17} eV, the convolved muon density ρ_{35} retrieved by Eq. (7.14) is smaller than ρ_{35}^{sim}. In contrast, for energies below this value, ρ_{35} is larger than ρ_{35}^{sim}. This behavior can be explained by examining the integrand of Eq. (7.14). For a fixed E, the inner integral corresponds to the integral of $\rho_{35}^{\text{sim}}(E_{\text{MC}})$ weighted by the function $w(E_{\text{MC}}) = G(E|E_{\text{MC}}) J(E_{\text{MC}}) \epsilon(E_{\text{MC}})$. In Fig. 7.34, w (conveniently normalized to be 1 at its maximum) is displayed for different reconstructed energies E, indicated as vertical dashed lines.

Above $10^{17.3}$ eV, the threshold defined by Eq. (7.17), $\epsilon \sim 1$, so the weighting function is defined by the product $G(E|E_{\text{MC}}) J(E_{\text{MC}})$. The resolution function $G(E|E_{\text{MC}})$ is symmetric, but the flux $J(E_{\text{MC}})$ is highly asymmetric, steeply falling with energy. Therefore, w is also asymmetric, giving more weight to smaller energies[5]. Indeed, as observed in Fig. 7.34, the weight function w for those reconstructed energies E above $10^{17.3}$ eV (in the figure, this is $\lg(E/\text{eV}) = \{17.5, 18\}$) gives more weight to MC energies $E_{\text{MC}} < E$, as deduced from the fact that the maximum of w is reached below E. Since $\rho_{35}^{\text{sim}}(E_{\text{MC}})$ increases with energy (see Eq. (7.12)), the muon density values at smaller energies, which have more weight in the integral, dominate, resulting in $\rho_{35}(E) < \rho_{35}^{\text{sim}}(E_{\text{MC}} = E)$.

The same effect is observed for energies close to but slightly below the threshold (in the figure, $\lg(E/\text{eV}) = 17$). Although formally ϵ cannot be approximated by unity, the drop in

---

[5]In other words, an event with a reconstructed energy E is more likely to originate from a shower with true energy $E_{\text{MC}} < E$.

the trigger probability (see right panel of Fig. 7.32) is still not large enough to compensate the steeply falling energy spectrum in this case.

For energy far below the threshold, the trigger probability ϵ becomes dominant. In this case, a reconstructed energy E is more likely to come from a true energy $E_{\mathrm{MC}} > E$. Indeed, as observed in the plot of w for $\lg(E/\mathrm{eV}) = 16$ in Fig. 7.34, the maximum of w is achieved above E, resulting in larger weights to Monte-Carlo energies above E. However, we stress that the analysis of this work is restricted to energies $\lg(E/\mathrm{eV}) > 17.5$, as explained in Section 7.1.1. Therefore, the convolved densities below this value (shaded area in Fig. 7.33) are not used.

Finally, it is also worth noting that w becomes narrower for larger energies, which illustrates the fact that the resolution improves with energy (see Eq. (7.16)).
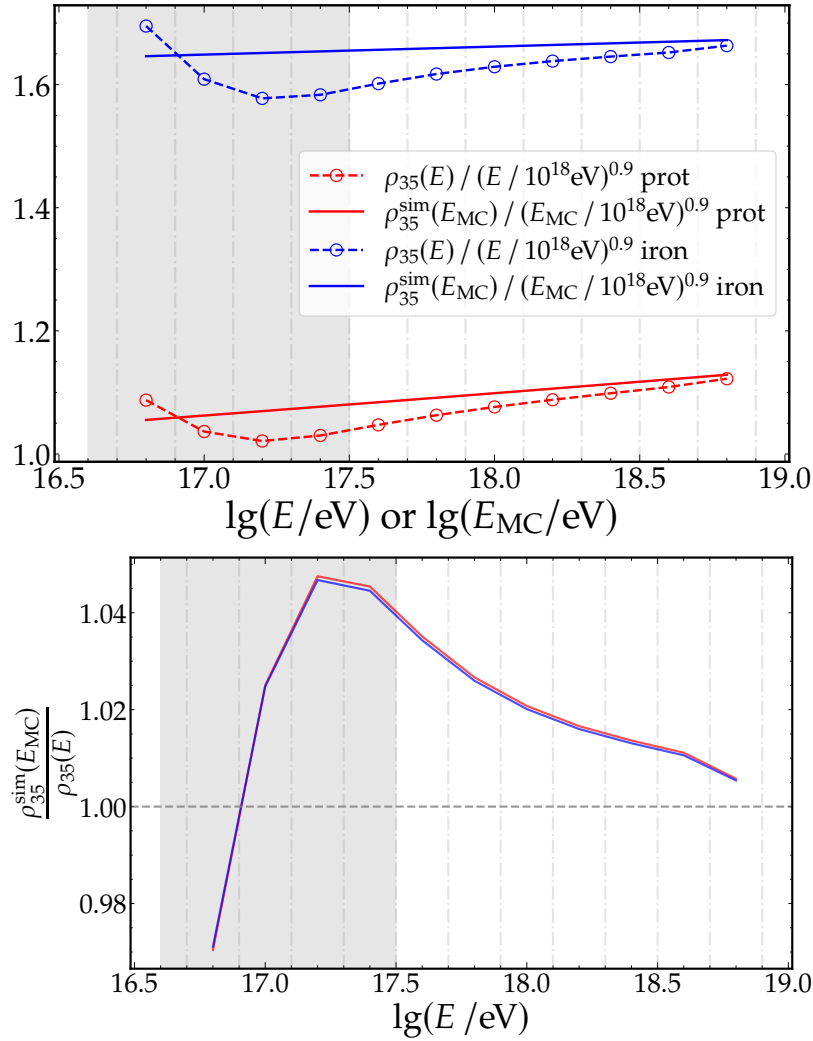

Figure 7.33: Effect of the convolution of Eq. (7.14) for EPOS-LHC showers. Shaded grey bands indicates the region below full efficiency that will not be used for the analysis, as explained in Section 7.1.1 ($\lg(E/\mathrm{eV}) < 17.5$). Vertical dashed lines marks the log-energy bin edges. *Upper panel*: Comparison between the ρ_{35} curves for iron (blue) and proton (red), with (dots joined by dashed lines) and without (solid lines) accounting for energy reconstruction effects. *Lower panel*: Ratio between the curves with and without accounting for energy reconstruction effects for proton (red) and iron (blue).
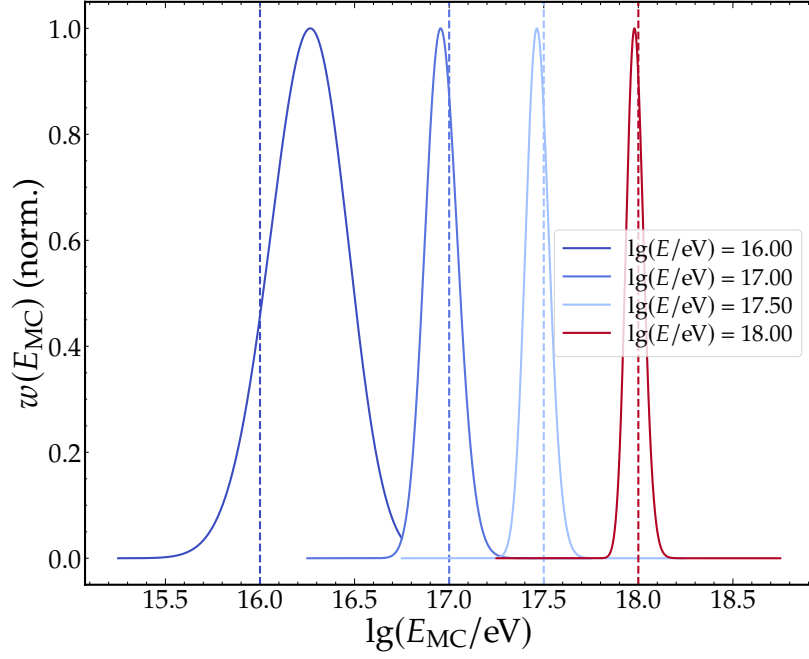
Figure 7.34: Weight function $w(E_{\mathrm{MC}}) = G(E|E_{\mathrm{MC}}) \, J(E_{\mathrm{MC}}) \, \epsilon(E_{\mathrm{MC}})$ as a function of $\lg(E_{\mathrm{MC}}/\mathrm{eV})$ for different reconstructed log-energies $\lg(E/\mathrm{eV})$, indicated by vertical dashed lines. For $\lg(E/\mathrm{eV}) = \{17, 17.5, 18\}$, the maximum of w is reached below E, indicating that w gives more weight to $E_{\mathrm{MC}} < E$. In contrast, for $\lg(E/\mathrm{eV}) = 16$, the maximum is reached above E, showing that energies $E_{\mathrm{MC}} > E$ have more weight.

The evolution of the mean logarithmic muon density with Monte Carlo energy must also be convolved with Eq. (7.14) before being compared to data. To that end, we substitute $\left\langle \frac{\rho_{35}}{(E/10^{18}\mathrm{eV})^\alpha} \right\rangle$ with $\langle \ln \rho_{35} \rangle$ on the left-hand side and $\frac{\rho_{35}^{\mathrm{sim}}}{(E/10^{18}\mathrm{eV})^\alpha}$ with $\langle \ln \rho_{35} \rangle_{\mathrm{sim}}$ on the right-hand side of Eq. (7.14). Here, $\langle \ln \rho_{35} \rangle_{\mathrm{sim}}$ corresponds to the linear model in Eq. (7.13), which describes the evolution of the mean logarithmic density with Monte Carlo energy, as shown in Fig. 7.31. The result of the convolution in the logarithmic density is shown in Fig. 7.35.
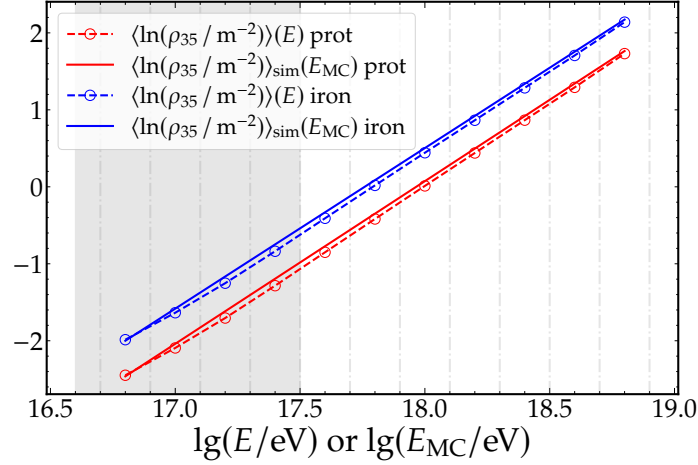
Figure 7.35: Effect of the convolution of Eq. (7.14) for the mean logarithmic density for EPOS-LHC showers. Shaded grey bands indicates the region below full efficiency that will not be used for the analysis, as explained in Section 7.1.1 ($\lg(E/\mathrm{eV}) < 17.5$). Vertical dashed lines marks the log-energy bin edges. Comparison between the $\langle \ln \rho_{35} \rangle$ curves for iron (blue) and proton (red), with (dots joined by dashed lines) and without (solid lines) accounting for energy reconstruction effects.

7.6 Comparison of data and simulations

The normalized muon density as a function of log-energy, along with the expected results for protons and iron using EPOS-LHC and QGSJetII-04, is shown in Fig. 7.36. Within systematic uncertainties, the measurements are compatible with iron primaries, except for the highest energy bin, which suggests a composition heavier than iron. However, this last bin ($\lg(E/\mathrm{eV}) > 18.9$) is wide and contains only three events. For this reason, we exclude it from the following analysis.
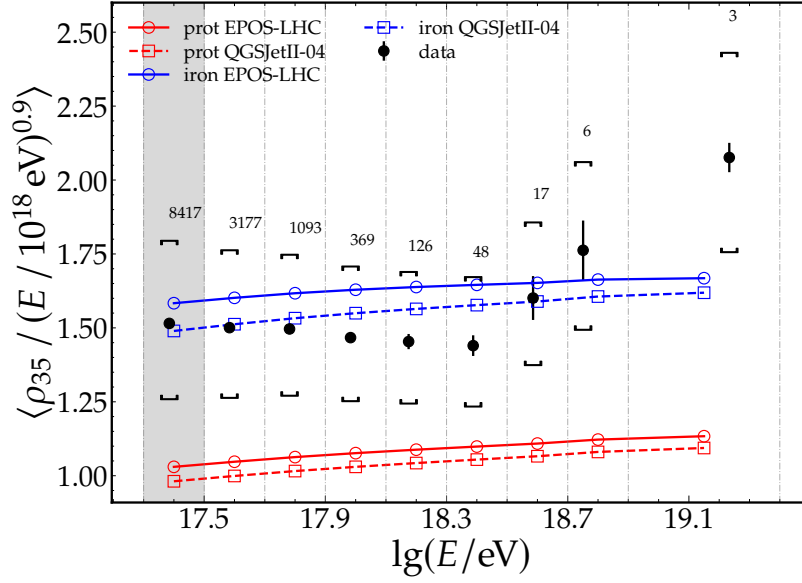
Figure 7.36: Normalized muon density as a function of energy. Error bars indicate statistical uncertainties, whereas brackets denote systematic uncertainties. Simulation results for protons and iron, obtained using the integral convolution as explained in Section 7.5.2, are shown as red and blue markers, respectively, joined by lines. The shaded grey area indicates $\lg(E/\text{eV}) < 17.5$, corresponding to the region below full efficiency as explained in Section 7.1.1.

For a given hadronic model, the mean logarithmic mass in each energy bin can be obtained as (see Eq. (2.18))

$$\langle \ln A \rangle = \ln 56 \frac{\langle \ln \rho_{35} \rangle_{\text{data}} - \langle \ln \rho_{35} \rangle_{\text{p}}}{\langle \ln \rho_{35} \rangle_{\text{Fe}} - \langle \ln \rho_{35} \rangle_{\text{p}}}, \tag{7.18}$$

where $\langle \ln \rho_{35} \rangle_{\text{p, Fe}}$ indicates the expected value of $\ln(\rho_{35})$ for proton and iron primaries, respectively, obtained as explained in Section 7.5.2. The mean logarithmic mass for each hadronic model is displayed in Fig. 7.37, along with the logarithmic mass inferred from $X_{\max}$ measurements of the Pierre Auger Observatory taken from Ref. [84]. The mass inferred from UMD measurements follows a similar energy-dependent trend to that of $X_{\max}$, suggesting a transition from heavier to lighter elements up to $10^{18.4}$ eV, after which a shift toward heavier masses is observed. However, the mass predicted by the UMD is systematically heavier than that predicted from $X_{\max}$, providing evidence that the two observables—the muon content and $X_{\max}$—are not consistently reproduced by any of the hadronic models. Assuming that $X_{\max}$ is sufficiently well reproduced in simulations, this discrepancy suggests a muon deficit in the simulations.
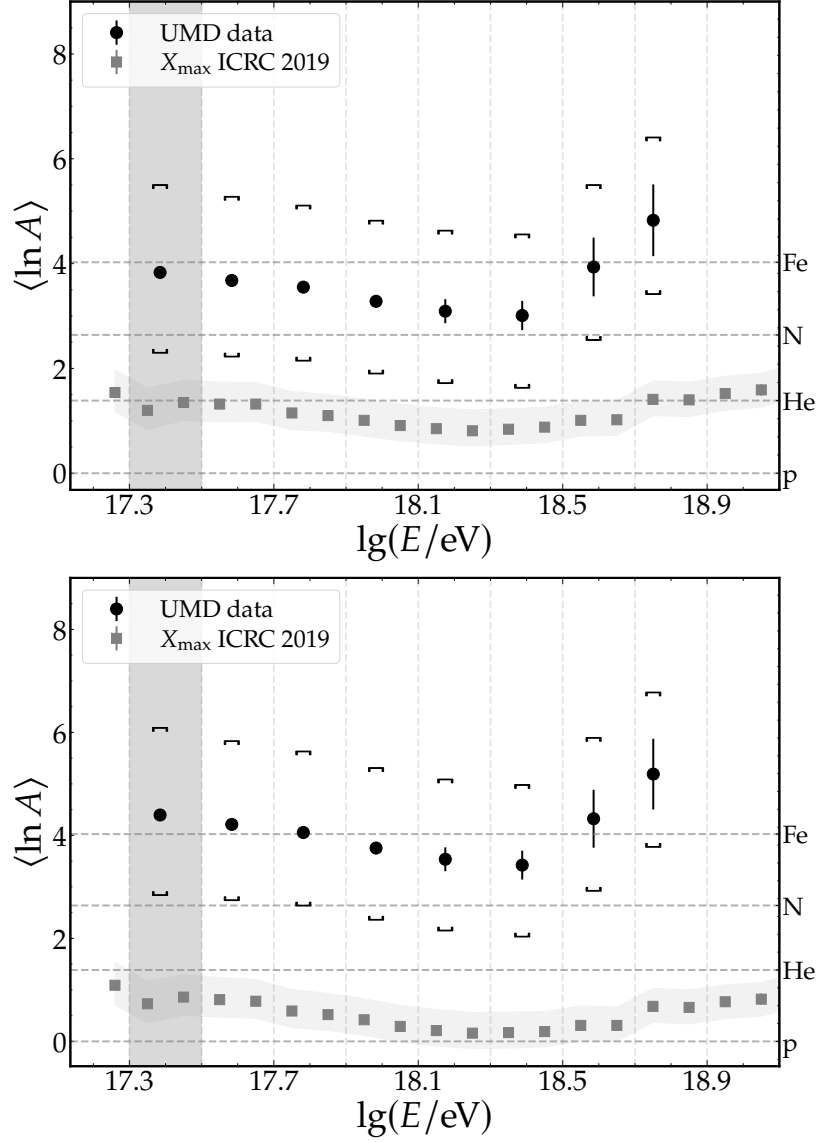
Figure 7.37: Mean logarithmic mass as a function of energy for EPOS-LHC (upper panel) and QGSJetII-04 (lower panel). Error bars indicate statistical uncertainty, whereas brackets correspond to systematic uncertainties. Grey markers indicate the logarithmic mass inferred from X_{max} measurements [84]. The shaded grey area indicates the energy bin below full efficiency (see Section 7.1.1), preserved for visualization only.

In order to quantify the muon deficit, $\langle \ln \rho_{35} \rangle$ and $\langle X_{\text{max}} \rangle$ must be related via $\langle \ln A \rangle$. The logarithmic mass inferred from $\langle X_{\text{max}} \rangle$ in an energy bin is given by (see Eq. (2.19))

$$\langle \ln A \rangle = \ln 56 \frac{\langle X_{\text{max}} \rangle_{\text{data}} - \langle X_{\text{max}} \rangle_{\text{p}}}{\langle X_{\text{max}} \rangle_{\text{Fe}} - \langle X_{\text{max}} \rangle_{\text{p}}}, \tag{7.19}$$

where $\langle X_{\text{max}} \rangle_{\text{p, Fe}}$ denotes the expected value of X_{max} for proton and iron primaries, respectively. If X_{max} and ρ_{35} were consistently described by a hadronic model, the logarithmic mass predicted by them should be the same. Thus, if we set Eq. (7.19) equal to Eq. (7.18), we obtain

$$\langle \ln \rho_{35} \rangle = m \langle X_{\text{max}} \rangle + b, \tag{7.20}$$

where

$$m = \frac{\langle \ln \rho_{35} \rangle_{\text{Fe}} - \langle \ln \rho_{35} \rangle_{\text{p}}}{\langle X_{\max} \rangle_{\text{Fe}} - \langle X_{\max} \rangle_{\text{p}}},$$

$$b = \langle \ln \rho_{35} \rangle_{\text{p}} - m \langle X_{\max} \rangle_{\text{p}}.$$

Therefore, by comparing data and simulations in the $(X_{\max}, \ln \rho_{35})$ plane, the discrepancy between them can be studied.

In Fig. 7.38, the mean $X_{\max}$ and $\ln \rho_{35}$ are shown for $17.5 < \lg(E/\text{eV}) < 17.7$. The expected values for protons and iron, as predicted by EPOS and QGSJetII-04, are also displayed. The line connecting the proton and iron expectations for each hadronic model corresponds to Eq. (7.20). Assuming that $X_{\max}$ is well described by the models, the discrepancy must stem from the muon number. Thus, the disagreement between the muon content in data and simulations can be assessed by comparing the distance between the measured and expected $\langle \ln \rho_{35} \rangle$, assuming the models accurately describe both observables. The latter is obtained by evaluating Eq. (7.20) at the mean $X_{\max}$ observed in data. To this end, we define the factor

$$f = \exp \left(\langle \ln \rho_{35} \rangle_{\text{data}} - \langle \ln \rho_{35} \rangle_{\text{sim}} \right), \tag{7.21}$$

where $\langle \ln \rho_{35} \rangle_{\text{data}}$ and $\langle \ln \rho_{35} \rangle_{\text{sim}}$ correspond to the measured and expected values of $\langle \ln \rho_{35} \rangle$, respectively. The exponential function is applied to account for the fact that these are logarithmic quantities. Thus, a value of f greater (smaller) than one corresponds to a muon deficit (surplus) in the simulations with respect to the data. For the example of Fig. 7.38, a value of $f_{\text{EPOS-LHC}} = 1.273 \pm 0.005 \, (\text{stat.})^{+0.23}_{-0.17} \, (\text{sys.})$ and $f_{\text{QGSJetII-04}} = 1.411 \pm 0.006 \, (\text{stat.})^{+0.25}_{-0.20} \, (\text{sys.})$ is obtained for EPOS-LHC and QGSJetII-04, respectively, which implies that the muon content would need to be increased by 27% for EPOS-LHC and 41% for QGSJetII-04 for them to consistently describe $X_{\max}$ and $\ln \rho_{35}$.
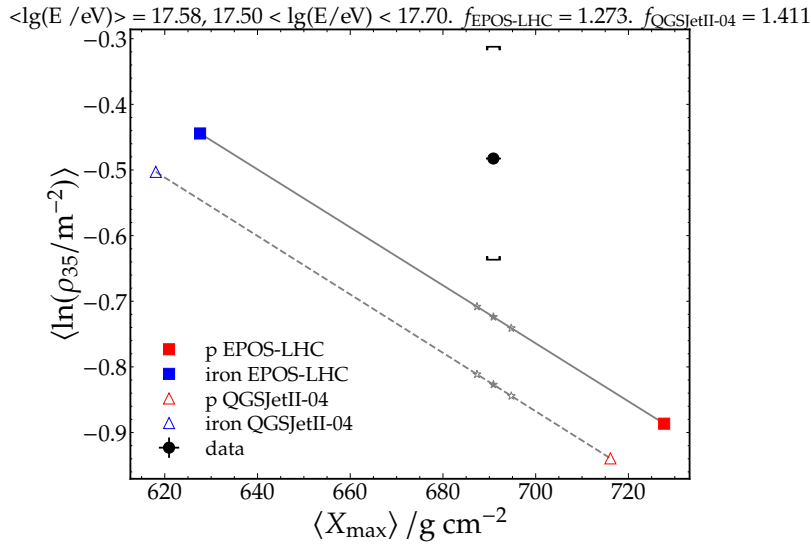

Figure 7.38: Comparison between data and simulations in the $(X_{\max}, \ln \rho_{35})$ plane for $17.5 < \lg(E/\text{eV}) < 17.7$.

Applying this procedure in each energy bin, the discrepancy between data and simulations can be studied as a function of energy. In Fig. 7.39, the f factor is shown as a function of energy for EPOS-LHC (upper panel) and QGSJetII-04 (lower panel). Both models yield factors greater than unity, indicating a disagreement between the muon content in data and simulations within the considered energy range. QGSJetII-04 systematically shows larger values than EPOS-LHC, exhibiting a more pronounced disagreement with simulations. To

assess the significance of the discrepancy, the distance of the measured f from one, expressed in units of σ, is indicated in each energy bin. Here, σ corresponds to the total uncertainty, calculated as the quadrature sum of the statistical and systematic errors.

Regardless of the absolute value of f, both models exhibit a similar trend with energy, characterized by a relatively flat behavior up to $10^{18.4}$ eV, beyond which a break is observed, leading to increasing values of f. This suggests that the magnitude of the muon deficit in simulations becomes more pronounced around that energy. Indeed, below $10^{18.4}$ eV, the significance of the muon deficit is approximately 1.6σ (2.15σ) for EPOS-LHC (QGSJetII-04), whereas above the break it increases up to 1.95σ (2.46σ). Nevertheless, it is important to highlight that only 23 events are available in the energy bins above $10^{18.5}$ eV; therefore, more statistics are needed before definitive conclusions can be drawn.

Lastly, it is worth to mention that the impact of energy binning and the comparison between using the convolved and uncolvolved muon densities for the simulations can be found in Appendix F.
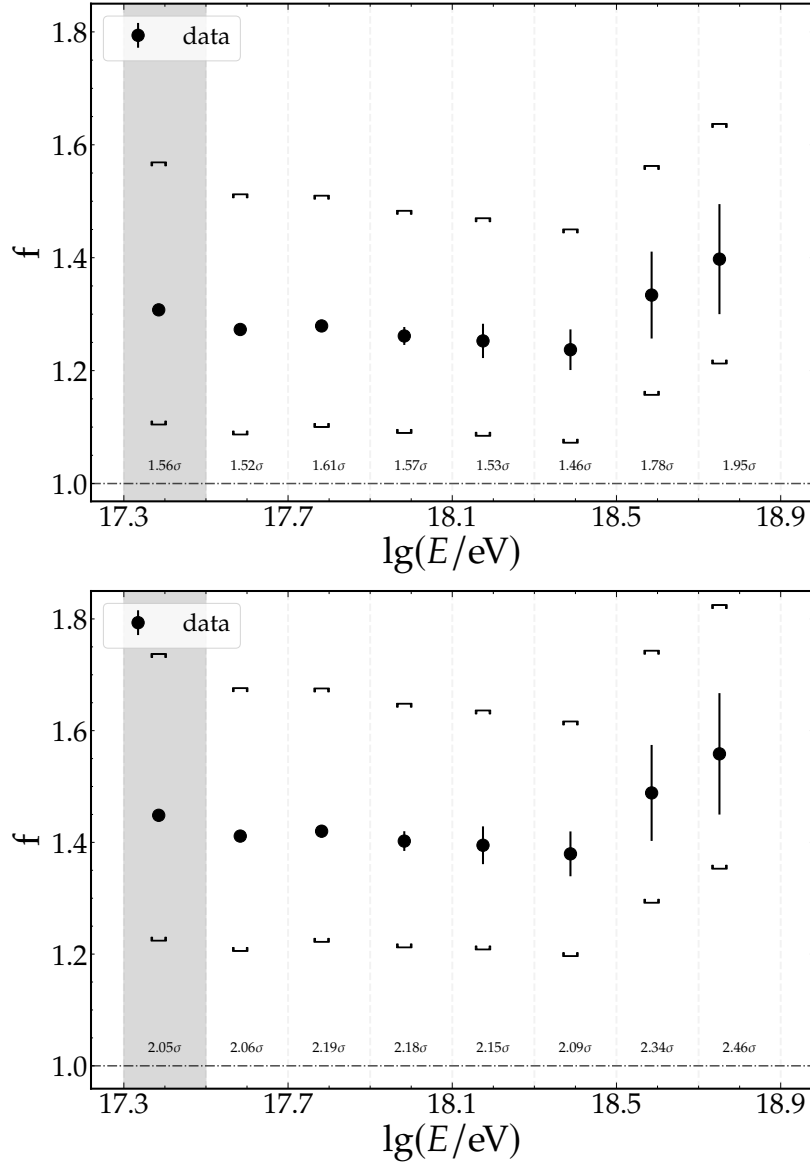
Figure 7.39: Factor comparing the agreement between the muon content in data and simulations (Eq. (7.21)) as a function of energy for EPOS-LHC (upper panel) and QGSJetII-04 (lower panel). Error bars indicate statistical error whereas brackets correspond to systematic uncertainties. The horizontal dashed line indicates unity. The shaded grey area indicates the energy bin below full efficiency (see Section 7.1.1), preserved for visualization only. The distance to unity in units of σ is indicated in each bin, where σ corresponds to the total uncertainty.

7.7 Comparison to previous UMD results

Figure 7.40 shows a comparison between the results obtained in this work and previous results obtained with the UMD operating in its final design with SiPMs, as in this work.

The dashed line corresponds to Ref. [73] and was obtained by performing event-wise fits, as in this work, although there were some differences in the reconstruction procedure, such as a different corner-clipping correction, inhibition windows, and β parameterization. The solid line, from Ref. [70], was obtained from a study on the mean muon LDF in bins of energy and zenith angle. A slight difference appears to be present between these results and those obtained in this work (black data points). However, a different SD energy estimate

was used in this work compared to the one used in those studies. The SD-FD calibration curve described in Section 3.1 (see Fig. 3.5) is regularly updated, and slight differences in the SD energy estimate can arise in studies conducted at different times. This is particularly relevant for muon analyses, as they are highly sensitive to energy. When the same SD energy estimate as in Refs. [70, 73] is used, the unfilled red markers are obtained, showing excellent agreement between all the measurements. Thus, we conclude that all measurements obtained with the UMD operating with SiPMs are consistent with each other.

In Fig. 7.41, we compare the results obtained in this work with those from the engineering array phase of the UMD, reported in Refs. [62, 69], in which prototypes of the detector operating with PMTs were used. In the right panel of the figure, we show the ratio between the results for each energy bin, indicating that the densities obtained with the engineering array are approximately 20% higher than those found in this work and in previous SiPM analyses. Figure 7.42 provides a more detailed comparison between the two results for each energy bin, indicating the systematic uncertainty intervals in each case. It is important to note that the systematic uncertainty considered for this comparison does not include the uncertainty in the energy scale, as this is the same in both analyses. For the engineering array, the uncertainty in the ρ_{35} scale was reported to be 14.3% [62, 69], whereas in this work, it corresponds to the grey curve in Fig. 7.26.

The uncertainty intervals of both analyses overlap. Indeed, when considering the systematic uncertainties of the two analyses, the ratios between the results shown in the right panel of Fig. 7.41 are at the edge of consistency, being compatible with unity in most of the energy bins. However, despite this apparent compatibility, it is noteworthy that such a difference between the central values can have a significant impact on the interpretation of the measurement, such as in the case of the muon puzzle. For example, the muon deficit reported by the engineering array analysis was also quantified through Eq. (7.21), but using the unconvolved densities as a reference. The magnitude of the deficit reported there was $38\%^{+21\%}_{-18\%}$ and $50\%^{+23\%}_{-20\%}$ for EPOS-LHC and QGSJetII-04, respectively. If we use the unconvolved densities for our calculation, we obtain $\sim 20\%^{+20\%}_{-20\%}$ and $\sim 30\%^{+20\%}_{-20\%}$, respectively (see Fig. F.4).
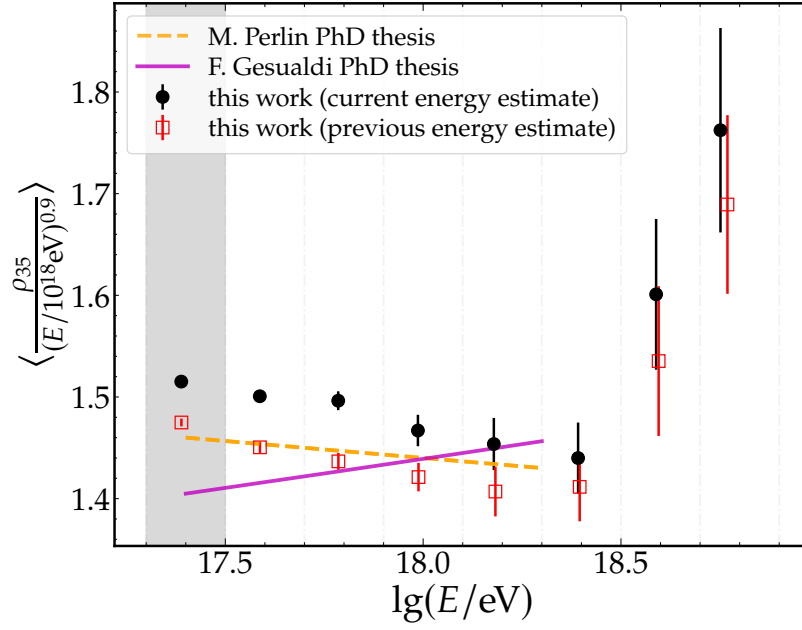
Figure 7.40: Comparison of the results obtained in this work with others obtained with the UMD operating in its final design with SiPMs. Dashed line corresponds to Ref. [73], full line to Ref. [70]. The unfilled square markers correspond to the results obtained when using the same energy estimate as in Refs. [70, 73].
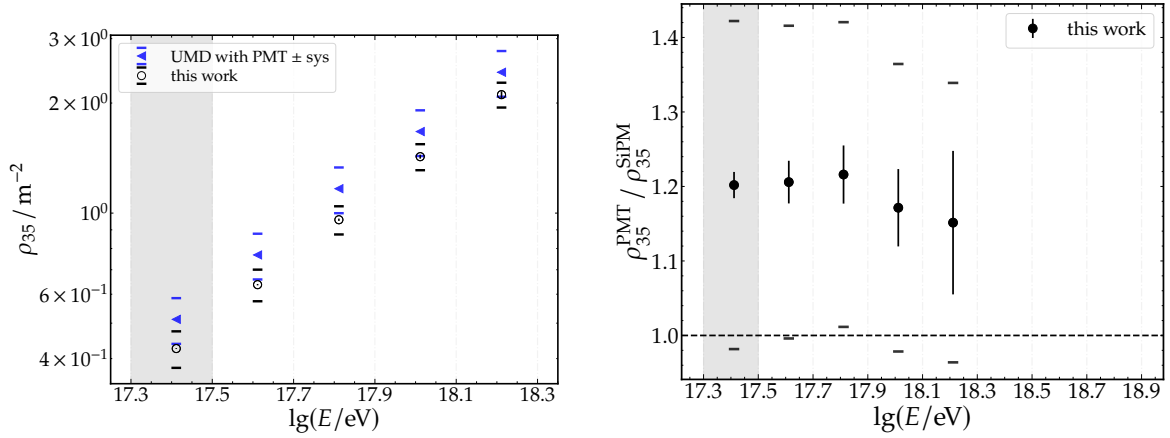

Figure 7.41: Comparison of the muon density obtained with the engineering array (Refs. [62, 69]) and this work. In the left panel, the mean ρ_{35} as a function of energy is displayed, whereas in the right panel the ratio of the two results in each energy bin is shown. Error bars indicate statistical uncertainties, whereas brackets show the systematic uncertainties.
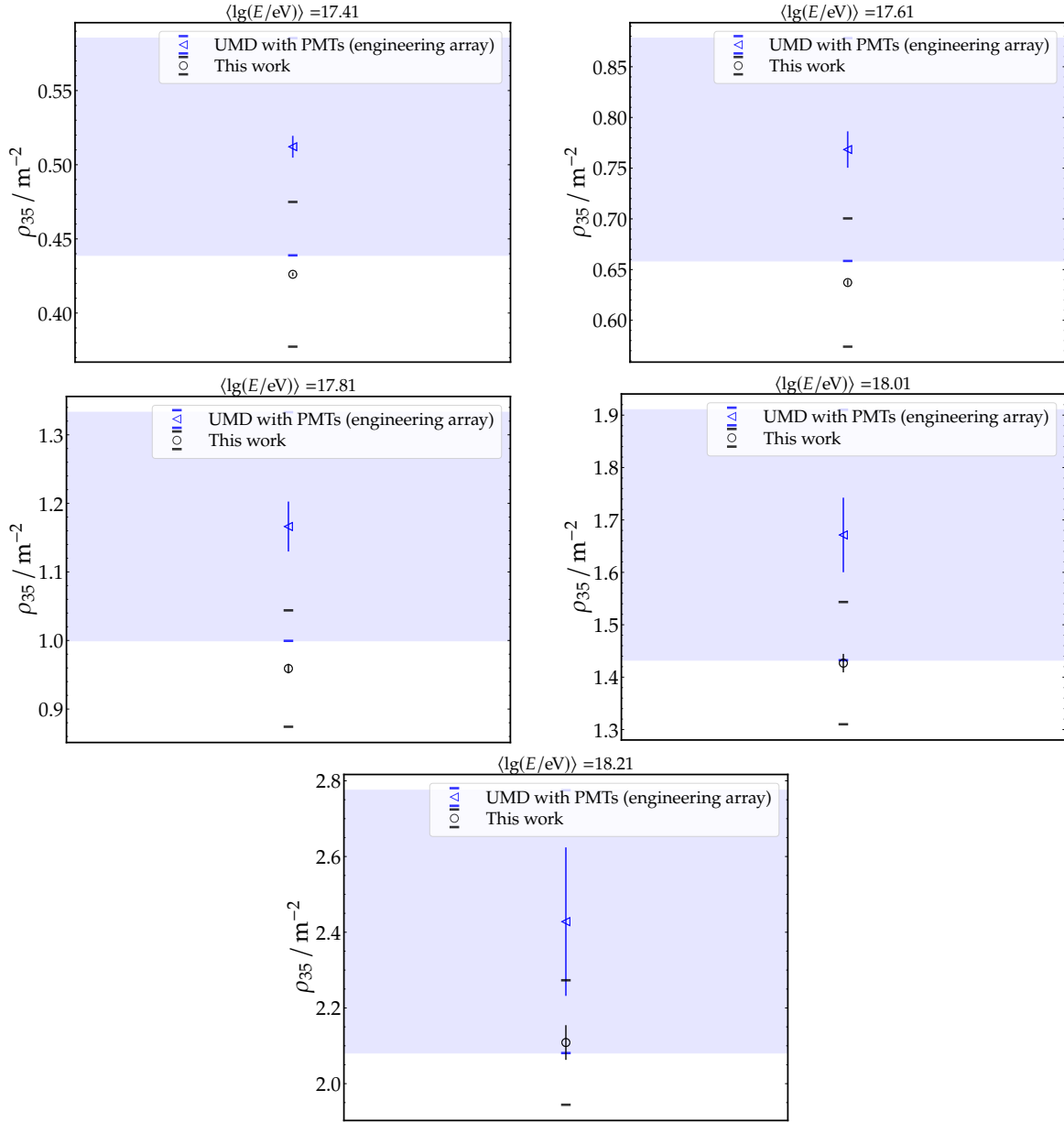
Figure 7.42: Comparison of the muon density obtained with the engineering array (Refs [62, 69]) and this work for each energy bin. The shaded blue are corresponds to the systematic uncertainty interval for the engineering array's analysis.

7.8   Comparison of the muon content to other experiments

Comparing muon measurements conducted in different air-shower experiments is challenging and not straightforward. The proxy for the muon content of air showers used in different observatories is affected by the unique characteristics of each observatory, such as the type of detector, atmospheric depth, the distance to the shower core at which the muons are sampled, zenith angle range, energy threshold for muons, and so on. Big efforts have been carried out in recent years by the Working Group for Hadronic Interactions and Shower Physics (WHISP) to categorize and order a wide variety of muon measurements obtained under different experimental conditions. Since its foundation, progress on this meta-analysis of muon data has been regularly reported in dedicated international conferences [4, 85, 86].

In order to compare measurements obtained under different experimental conditions, the z factor was introduced by the WHISP, given by

$$z = \frac{\ln\langle\rho_{35}\rangle - \ln\langle\rho_{35}\rangle_{\mathrm{p}}^{\mathrm{det}}}{\ln\langle\rho_{35}\rangle_{\mathrm{Fe}}^{\mathrm{det}} - \ln\langle\rho_{35}\rangle_{\mathrm{p}}^{\mathrm{det}}}, \tag{7.22}$$

where $\langle\rho_{35}\rangle_{\mathrm{p,\,Fe}}^{\mathrm{det}}$ represents the mean ρ_{35} obtained over a set of simulated proton and iron showers, respectively, accounting for detector simulations and applying the same reconstruction procedure as in data. In this way, the different experimental conditions of each observatory are accounted for, allowing different measurements to be compared.

Equation (7.22) has relevant properties that are desirable. The energy dependence of the muon content is removed (with a remaining dependence only through the mass composition), with the expected value being 0 for proton showers and 1 for iron showers, provided simulations reproduce the data well. Additionally, biases of the form $\ln\rho_{35}^{\mathrm{meas}} = A + B\ln\rho_{35}^{\mathrm{true}}$, where $\rho_{35}^{\mathrm{meas}}$ and $\rho_{35}^{\mathrm{true}}$ are the measured and true muon densities, respectively, cancel out in z. Further details and discussion on the z-scale and its properties can be found in Refs. [85, 87].

Offsets between the energy scales of different observatories further complicate comparisons, as the number of muons increases rapidly with energy. For instance, two identical experiments with a 20% energy offset would show an 18% difference in their muon data-to-Monte Carlo ratio because their muon measurements would be compared to simulations at different apparent energies [85]. To mitigate this effect, a cross-calibration between the energy scales between observatories is introduced by the WHISP, ensuring that all measurements are expressed on a common energy scale.

Since the flux of cosmic rays is highly isotropic up to $10^{19.2}$ eV, it serves as a universal reference to match the energy scales of different experiments. A relative shift of 10.4% was found by the *Spectrum Working Group* between the flux measured by the Pierre Auger and Telescope Array collaborations [88]. Therefore, the reference energy scale E_{ref} was defined as the midpoint between the scales of the two experiments. The cross-calibration involves finding a scaling factor $E_{\mathrm{ref}}/E_{\mathrm{data}}$ for each experiment, such that its energy spectrum, measured on the E_{data} scale, coincides with the reference one. By construction, the factor needed to convert the Auger scale to the reference scale is $f_{\mathrm{Auger}} = E_{\mathrm{ref}}/E_{\mathrm{data}} = 1.052$. It is necessary to highlight that the cross-calibration accounts for relative offsets between different experiments, but does not remove a potential global offset between the experimental and true energy. Thus, an uncertainty of at least 10% is expected in the reference energy scale.

By using Eq. (2.16), the z values reported in a given experiment can be converted to the reference scale by [85]

$$z_{\mathrm{ref}} = z_{\mathrm{data}} + \beta\frac{\ln(E_{\mathrm{data}}/E_{\mathrm{ref}})}{\ln\langle\rho_{35}\rangle_{\mathrm{Fe}}^{\mathrm{det}} - \ln\langle\rho_{35}\rangle_{\mathrm{p}}^{\mathrm{det}}}, \tag{7.23}$$

where $\beta \sim 0.9$, and z_{data} and z_{ref} are the z values reported in the experiment and reference energy scale, respectively.

To serve as a reference and to account for the effect of an energy-dependent mass composition on z, an expected value for z can be derived assuming a given $\langle\ln A\rangle$. By means of Eq. (2.19), we obtain

$$z_{\mathrm{mass}} = \frac{\langle\ln A\rangle}{\ln 56}. \tag{7.24}$$

In our case, we use the mean logarithmic mass inferred from the Global Spline Fit (GSF) as reference [89]. If the z values obtained from muon measurements agree with z_{mass}, then

there is no muon deficit in the simulations. Therefore, a measure of the muon deficit in simulations is defined as

$$\Delta z = z - z_{\text{mass}}. \tag{7.25}$$

A positive (negative) value of Δz indicates a muon deficit (surplus) in the simulations. A value compatible to zero implies agreement between data and simulations.

In Fig. 7.43, the z values for EPOS-LHC and QGSJetII-04 as a function of energy, obtained in this work, are presented. Both the values in the Auger scale, calculated using Eq. (7.22), and the values expressed in the reference scale, obtained via the conversion in Eq. (7.23), are shown. We note that the x-axis differs between the two cases: in the Auger scale, it is expressed as a function of the Auger energy, while in the reference scale, it is expressed as a function of the reference energy. The positive shift in the Auger scale required to match the reference energy scale makes the muon measurement more compatible with lighter masses, shifting the z value in the reference scale toward a more proton-like value. The dashed line and grey band indicate z_{mass}—computed via Eq. (7.24)—as expected from the GSF model and the X_{max} measurement at the Pierre Auger Observatory, respectively.
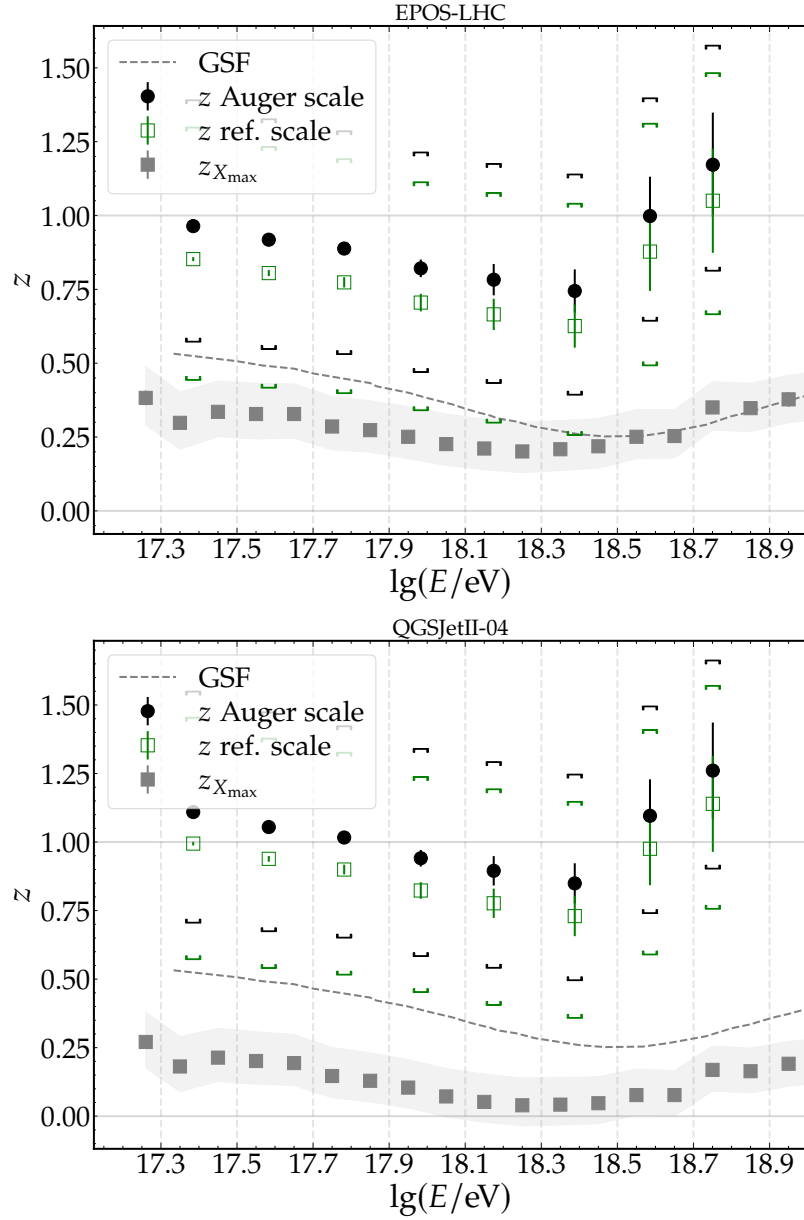
Figure 7.43: Comparison of the z values obtained in this work using the Auger energy scale (Eq. (7.22)) and the reference energy scale, obtained converting the values in the Auger scale via Eq. (7.23). The upper panel corresponds to EPOS-LHC whereas the lower panel to QGSJetII-04. The grey band and dashed line corresponds to the z values expected from X_{max} measurements at the Pierre Auger Observatory [84] and the GSF composition model [89] via Eq. (7.24), respectively. Grey horizontal lines marks $z = 0$ and $z = 1$, the expected values for a pure proton and pure iron compositions, respectively.

In Fig. 7.44, the z values obtained in this work are compared to those from other experiments, all expressed in the reference energy scale. The error bars are calculated as the quadrature sum of the systematic and statistical uncertainties. The values from the other experiments were extracted from Figure 3 of Ref. [4]. We note that the z values are lower than those previously reported by the engineering array with PMTs as photodetectors, driven by the lower number of muons measured with the current design operating with SiPMs, as discussed in Section 7.7. At the highest energy bins (above $10^{18.4}$ eV), the values obtained in this work are compatible with those obtained by inclined hybrid events at the Pierre Auger

Observatory [1] and AGASA [81], as opposed to those from Yakutsk, which are compatible with the expectations of the GSF model.

Lastly, to remove the mass composition dependence, we show the Δz values from this work and other experiments in Fig. 7.45. As discussed in Section 7.6, the results obtained in this work indicate a relatively constant muon deficit up to $10^{18.4}$ eV, being compatible with GSF for EPOS-LHC but not compatible with QGSJetII-04. An increase in the magnitude of the deficit is observed above that energy, suggesting that whatever process is originating the muon discrepancy might be enhanced around that energy. However, we highlight again that only 23 events are available in the energy bins above $10^{18.5}$ eV; therefore, more statistics are needed before stronger statements can be done about the energy-dependent trend of the muon deficit above $10^{18.4}$ eV with the UMD.
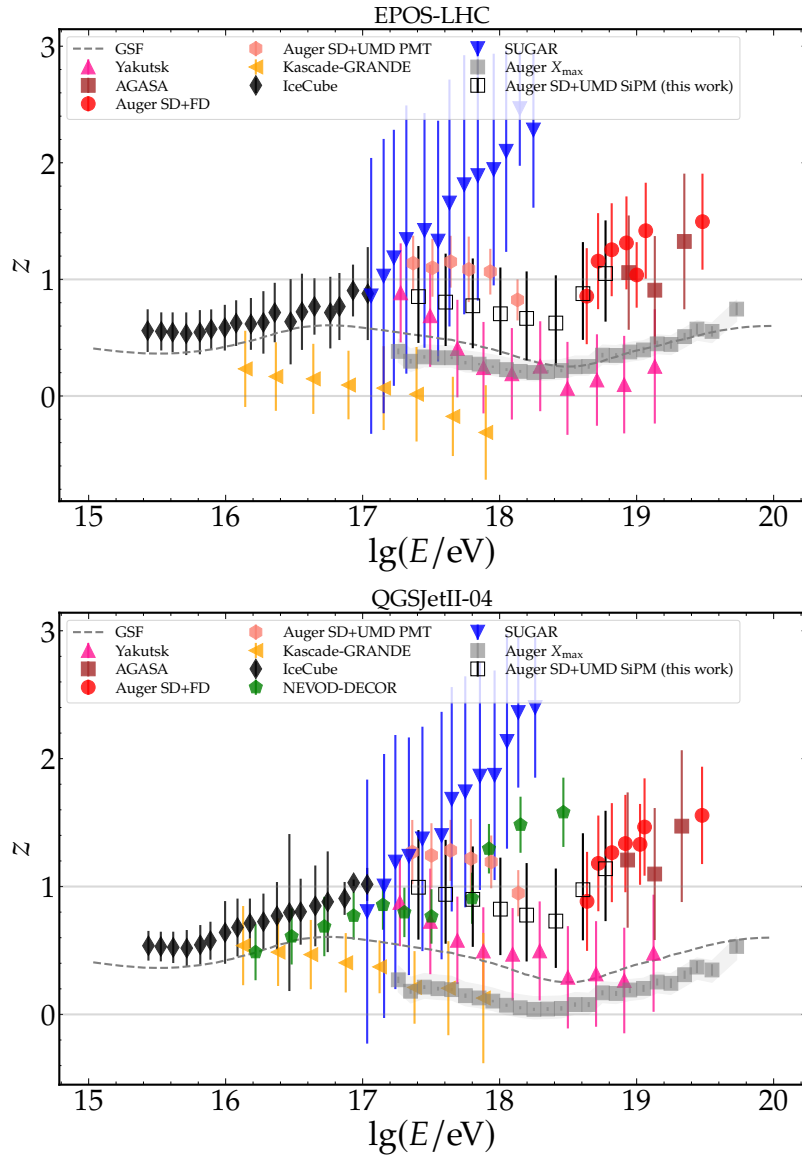

Figure 7.44: Comparison of the z values obtained in this work with other experiments, extracted from Fig. 3 of Ref. [4]. All the values are in the reference energy scale. The upper panel corresponds to EPOS-LHC whereas the lower panel to QGSJetII-04. The grey band and dashed line corresponds to the z values expected from $X_{\max}$ measurements at the Pierre Auger Observatory [84] and the GSF composition model [89] via Eq. (7.24), respectively. Grey horizontal lines marks $z = 0$ and $z = 1$, the expected values for a pure proton and pure iron compositions, respectively.
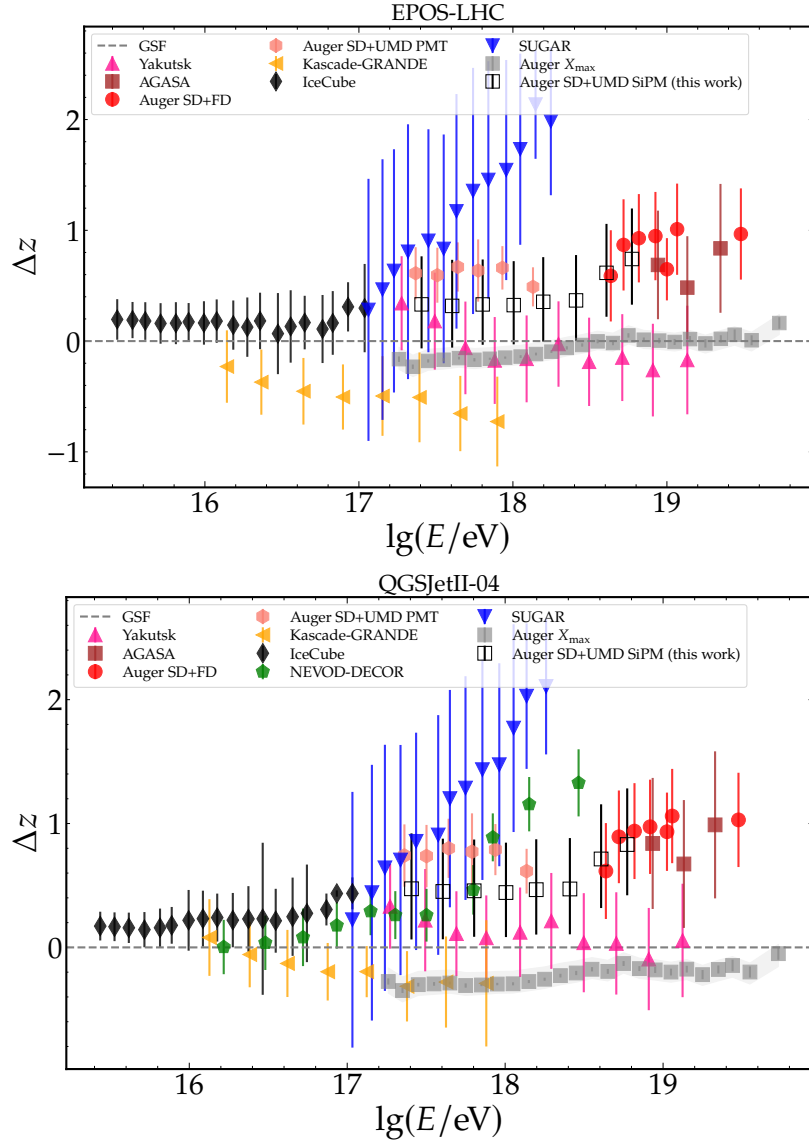
Figure 7.45: Comparison of the Δz values obtained in this work with other experiments via Eq. (7.25). All the values are in the reference energy scale. The upper panel corresponds to EPOS-LHC whereas the lower panel to QGSJetII-04. The grey band and dashed line corresponds to the z values expected from X_{max} measurements at the Pierre Auger Observatory [84] and the GSF composition model [89] via Eq. (7.24), respectively. Grey horizontal dashed line marks $\Delta z = 0$, the expected value for no muon deficit in the simulations.

7.9   Comparison of mean MLDF with other experiments

In addition to making a fit in each individual event, the MLDF can be studied in mean values. To do so, muon density measurements ρ_i of events within an energy and zenith angle range are grouped together. Since the muon number increases as $\sim E^{0.9}$, the densities measured in an event with energy E are normalized by the factor (E_{bin}/E), where E_{bin} is the center of the energy bin. The data is further binned in shower plane distances r and the mean value of the normalized densities is obtained for each r bin. This binned data is finally fitted to a suitable MLDF model, allowing to study the evolution of the mean MLDF with energy and zenith angle. This approach was used to analyze the mean MLDF recorded by the UMD in Ref. [70].

Studies of the mean MLDF of muons with $E_\mu > 1$ GeV were also conducted in other UHECR observatories, such as the ones located at Akeno, Japan [90] (corresponding to an atmospheric depth of 920 gcm^{-2}) and Yakutsk, Russia [91] (located at a depth of 1020 gcm^{-2}).

To cover a large energy range, muon measurements at Akeno were carried out with three arrays with different spacing and areas, namely A1, A20 and A100, covering 1, 20 and 100 km^2 respectively. A100 is also known as AGASA, which stands for Akeno Giant Air Shower Array. We will focus on the results of the A1 and A20 arrays as they overlap with the energy range accesible by the UMD. In both arrays, the core, arrival direction and energy of the showers was determined by surface scintillator detectors. The muon measurements were obtained by eight 25 m^2 stations, each of which was comprised of 50 rectangular proportional counters containing P10 gas and shielded by 2 m of concrete.

In the case of Yakutsk, the muon detectors consists of underground scintillator shielded by 2.3-3 m of soil. In Ref. [91], data taken from the muon detectors over 1974 and 1992 was used. Over that period, different configurations of detectors were utilized: a single 8 m^2 detector with a threshold of 0.7 GeV was operative since 1974 to 1986; three 36 m^2 detectors with a threshold of 1 GeV were used since 1978 and five detectors with an area of 20 m^2 and a threshold of 1 GeV were available since 1986. Like in the case of Akeno, arrival direction, core and energy of the showers were obtained independently by ground-based detectors.

Akeno, Yakutsk and Auger have different depths and very likely systematic differences between their energy estimates. The latter is particularly relevant, since the number of muons increases nearly proportional to the energy of the primary particle. For these reasons, comparing the absolute scale of the mean MLDF (i.e., the absolute number of muons) measured by different observatories is not straightforward and must be done by the abstract z-scale, as disccused in Section 7.8.

Nevertheless, the shape of the MLDF is not expected to change dramatically with atmospheric depth nor with primary energy[6]. Furthermore, as shown in the next section, these two variables can be, to some degree, accounted for when comparing shapes of MLDFs measured at different depths and energies. This provides a good opportunity to compare the shape of the mean MLDF obtained by the UMD with that obtained by Akeno and Yakutsk.

7.9.1   On the dependence of the MLDF shape with depth and energy

To study the dependence of the MLDF shape on atmospheric depth and energy, we perform a simple exercise using the parameterization of the UMD LDF slope β shown in Section 6.4. With this, we aim to estimate how much the shape of the UMD LDF is expected to change with these variables. We remind the reader that the remaining shape parameters in Eq. (6.6), (α, r_0, γ), are fixed, so the shape of the LDF is completely determined by β alone.

We begin by expressing the parameterization in terms of the atmospheric depth X replacing $\sec \theta = X/X_{\text{Auger}}$, where $X_{\text{Auger}} = 870$g cm^2. We can further write $X = X_0 \sec \theta$, where X_0 represents the vertical atmospheric overburden of a given observatory. The expression now reads

$$\beta = -1.21 \left(\frac{X_0 \sec \theta}{X_{\text{Auger}}} - 1.2 \right) + 0.2(\lg(E/\text{eV}) - 17.8) + 2.71. \tag{7.26}$$

With this simple change, we can extrapolate the value of β if the UMD had been located in an observatory with an arbitrary X_0. Thus, to estimate how much we expect the shape of the UMD LDF to change at Akeno and Yakutsk, we only need to replace $X_0 = X_{\text{Akeno}} = 920$g cm^2 and $X_0 = X_{\text{Yakutsk}} = 1020$g cm^2, respectively.

---

[6]Indeed, as shown in Fig. 6.20 and Fig. 6.21, the slope of the MLDF increases logarithmically with energy.

The LDFs with the β values corresponding to the atmospheric depths of Auger, Akeno and Yakutsk are shown in the left panel of Fig. 7.46. All the functions are normalized to an arbitrary ρ_{450} and plotted for $r < 800$ m. The steepest LDF corresponds to the Auger case, as it is the shallower observatory, whereas the flattest is that of Yakutsk, located near sea level. Akeno, being at an intermediate depth, has an expected LDF that lies between the Auger and Yakutsk functions.

In the right panel of the figure, the quotient between the Auger LDF and Akeno's (solid line) and Yakutsk (dashed line) is shown. From the figure, we conclude that a difference of $\sim 5\%$ between Auger and Akeno and of $\sim 10\%$ between Auger and Yakutsk LDFs is expected. We stress that this difference is expected only due to the observatories being at different atmospheric depths.

In addition to having different atmospheric depths, the observatories also present systematic differences in their energy scales. As is apparent from Eq. (7.26), the MLDF shape also depends on the energy. Since the dependence is logarithmic, its impact is usually small. However, if the offset between the energy scales of the experiments is large enough, it is a priori not clear if this can result in a non-negligible effect. Therefore, differences in the MLDF shape measured at different observatories can arise due to relatively large offsets between their energy scales.

As explained in Section 7.8, the so-called reference energy scale, defined as the midpoint between the scales of the Pierre Auger and Telescope Array collaboratins, is used to compare muon measurements between different observatories. The energy measured at a given observatory E_{data} needs to be multiplied by a factor $f_{\text{data}} = E_{\text{ref}}/E_{\text{data}}$ to be transformed to the reference scale. By construction, we have $f_{\text{Auger}} = 1.052$. From Ref. [92], we obtain $f_{\text{Yakutsk}} = 0.8^7$, while the corresponding factor for AGASA is $f_{\text{AGASA}} = 0.68$ [81]. Since A20 was a prototype of AGASA, we assume $f_{\text{AGASA}} = f_{\text{A20}}$. The ratio between the energy scale of A20 and A1 was found to be $E_{\text{A20}}/E_{\text{A1}} = 1.1$ [93]. With these factors, we can estimate the relative offset between the energy scales of Auger with A1, A20 and Yakutsk: $E_{\text{Auger}}/E_{\text{A1}} = f_{\text{A20}} \times 1.1/f_{\text{Auger}} = 0.71$, $E_{\text{Auger}}/E_{\text{A20}} = f_{\text{A20}}/f_{\text{Auger}} = 0.65$ and $E_{\text{Auger}}/E_{\text{Yakutsk}} = f_{\text{Yakutsk}}/f_{\text{Auger}} = 0.76$.

We note that in order to convert Auger scale to both Akeno or Yakutsk's energy scales a positive shift is needed. This means that if the same shower is measured at the three observatories, Auger would assign it an energy of $\lg(E_{\text{Auger}})$, while Akeno and Yakutsk would report $\lg(E_{\text{A1}}) = \lg(E_{\text{Auger}}) + 0.15$, $\lg(E_{\text{A20}}) = \lg(E_{\text{Auger}}) + 0.19$ and $\lg(E_{\text{Yakutsk}}) = \lg(E_{\text{Auger}}) + 0.12$, respectively. This means that the energy of the events of Auger used to compare with Akeno and Yakutsk measurements can be shifted to account for this effect. For example, the measurements of A1 reported for a given energy bin $\lg E_1 < \lg E_{A1} < \lg E_2$ should be compared to Auger events with energies $\lg E_1 - 0.15 < \lg E_{\text{Auger}} < \lg E_2 - 0.15$.

7.9.2 Distance cuts for the mean MLDF of the UMD

As already discussed, a muon density estimate can not be obtained for saturated detectors. These are likely to occur closer to the core, where the particle density becomes increasingly large. However, non-saturated detectors can also be found close to the core. The muon density estimates with these detectors are biased as they are sampling a downward fluctuation of the underlying muon density distribution. To avoid considering such detectors in the analysis, a minimum distance cut r_{min} must be applied.

In addition, measurements obtained too far from the core, where the trigger probability of the SD tank decreases, should be avoided. These measurements consistute a biased sample

---

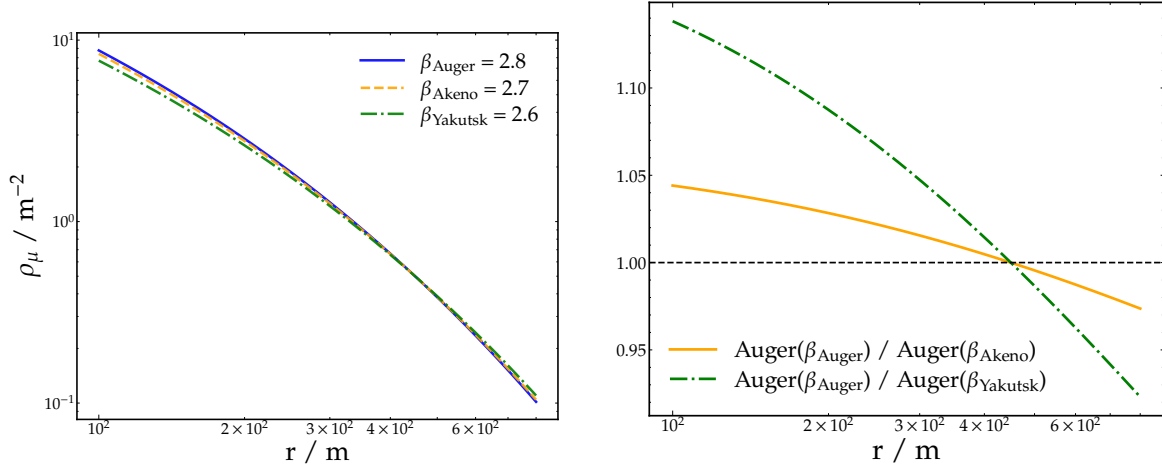[7]From table 1 of the reference, we get $f_{\text{Yakutsk}} = 1/1.24$.

Figure 7.46: *Left*: Expected LDFs at Auger, Akeno and Yakutsk atmospheric depths, obtained by Eq. (6.6) varying β according to Eq. (7.26). They are normalized at 450 m. *Right*: Expecetd quotient between Auger and Akeno's LDF (solid line) and Auger and Yakutsk (dashed-dotted line).

as they are an upward fluctuation of the triggering process of the SD tank. Thus, a maximum distance cut $r_{\max}$ is needed.

In Ref. [70], $r_{\min}$ was defined as the distance in which the saturation probability is 1%, denoted as r_{sat}, following the criteria explained in Section 4.1.1. Furthermore, $r_{\max}$ was defined as the distance in which the trigger probability of the tank reaches 90%, represented as $r_{90\%}$. In this way, a value of r_{sat} and $r_{90\%}$ (and hence of $r_{\min}$ and $r_{\max}$) was obtained in each energy and zenith angle bin.

The values of r_{sat} and $r_{90\%}$ as function of energy for different zenith angle bins are shown in Fig. 7.47[8]. To be able to extrapolate them to an arbitrary energy and zenith, we fitted a linear function $y = m(\lg(E/\text{eV}) - 17.6) + b$ to the curves of each zenith bin, shown as dashed lines in the figure. The slope m and b were further parameterized as quadratic functions of $\sin^2 \theta$, as shown in Appendix G.

The maximum difference between the linear model and the values of r_{sat}, presented in the left panel of Fig. 7.47, is of 25 m. This difference is of the same order than the typical r_{sat} values. Thus, we conservatively adopt $r_{\min} = r_{\text{sat}} + 25$ m. No such offset is needed for $r_{90\%}$ and therefore we take $r_{\max} = r_{90\%}$.

7.9.3   Comparison with muon densities measured with A1

The mean MLDF of showers within the energy range of $10^{16.5}$-$10^{18.5}$ eV was studied with the A1 array at Akeno [90]. Only vertical showers with $\sec\theta < 1.1$ ($\theta \lesssim 25°$) were selected, and a step of $\Delta \lg(E/\text{eV}) \sim 0.2$ was used for the energy binning[9]. Due to the size of the array, only measurements up to 800 m from the shower core were possible. A good description of their data was obtained with a slight modification of the formula proposed by Greisen derived for showers with lower energies [94]:

$$\rho_{\text{Greisen}}(r) = \rho_0 \frac{1}{r_0^2} \left(\frac{r}{r_0} \right)^{-\alpha} \left(1 + \frac{r}{r_0} \right)^{-\beta}, \tag{7.27}$$

---

[8]We thank Flavia Gesualdi for providing these data points.

[9]The binning is actually done in the number of electrons N_e, the measure used for determining the shower size. We convert N_e to energy using Eq. 1 of Ref. [90].
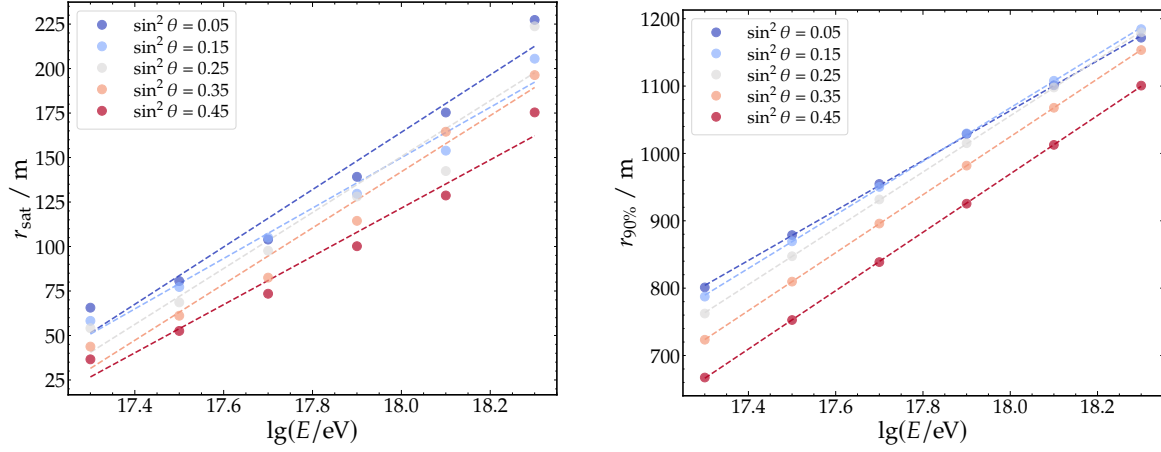
Figure 7.47: Minimum (left) and maximum (right) distances for each energy and zenith angle bin. The data points correspond to the ones found in Figs. 6.12 and 6.14 of Ref. [70]. Dashed lines indicate fits to a linear model.

where ρ_0 is a scaling factor and $\alpha = 0.75$. The shape of the MLDF is determined by the parameters β and r_0. It is worth noting that these are correlated and increasing (decreasing) β (r_0) leads to steeper LDFs. The reported optimal values for A1 data were $r_0 = (266 \pm 33)$ m and $\beta = 2.52 \pm 0.04$, and no significant dependence neither on energy nor zenith angle was found [90].

To compare the mean MLDF measured by the UMD under conditions as close as possible to those of Akeno's, we perform the same binning in energy and the same cut in zenith angle as those used for the A1 analysis. The log-energy bin edges of the A1 dataset that overlap with the accesible energies for the UMD are $\lg(E/\text{eV}) = \{17.39, 17.61, 17.84, 18.07, 18.29\}$. Furthermore, we perform the same binning in the r variable, taking care of excluding any bin in the UMD set for which $r < r_{\min}$ or $r > r_{\max}$, where $r_{\min}$ and $r_{\max}$ are determined as explained in the previous section.

The A1 data was extracted from figure 2 of Ref. [90]. Due to the difficulty of extracting error bars from the figure, an error of 5% is assumed in each data point. The raw data set is displayed in the left panel of Fig. 7.48. In the right panel of the figure, all the MLDFs are normalized to match an arbitrary value in the radial bin that contains 450 m. For energies below $10^{17.62}$ eV, all the MLDFs seem to follow a common shape. This is not the case for the three highest energy bins, for which a strong deviation from the overall trend is visible for distances closer to the core. For these energies, the measurements seem to reach a plateau when decreasing the distace to the core, suggesting possible detector saturation. This is relevant to assess, as they correspond to the energy region of the measurements of the UMD.

To further investigate the hypothesis of saturation, let us consider the highest energy bin (open triangles). From the right panel, the measurement that is at $\lg(r/\text{m}) \sim 2.46$ is the first measurement deviating from the common LDF shape observed at lower energies. If we take the absolute value of this measurement $\rho^{\text{sat}} \sim 6 \text{ m}^{-2}$ as an estimate of the saturation limit (the area $\rho > \rho^{\text{sat}}$ is enclosed by grey in the left panel), we see that the measurements of the lower energy bins, taken at distances closer to the core, that are above this value (i.e., inside the grey area in the left panel) coincide with the measurements that deviate from the universal LDF shape on the right panel.

We understand this as an indication that those measurements might be affected by detector saturation. Most of these measurements are at core distances for which no UMD measurement is available due to the minimum distance cut descibed in the previous section.
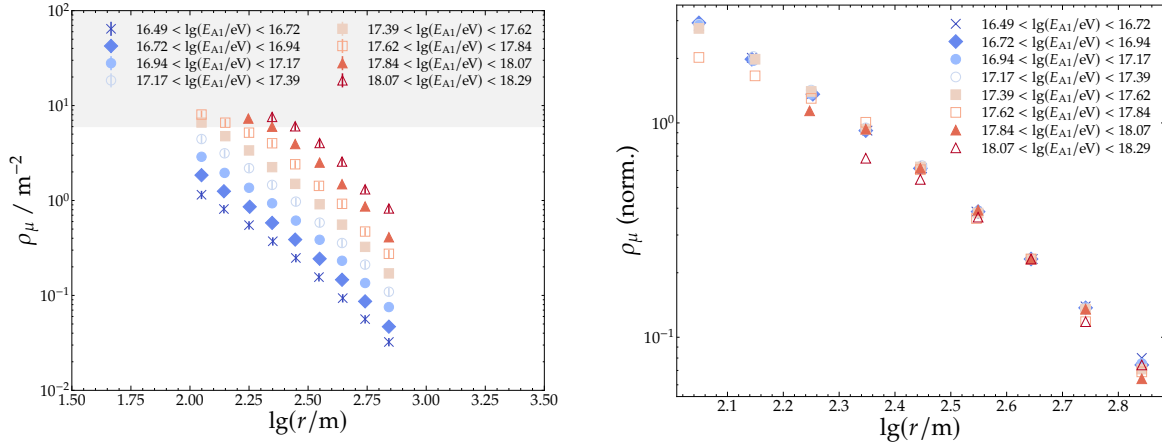
Figure 7.48: *Left*: Raw dataset of the A1 array, taken from Fig. 2 of Ref. [90]. The grey area indicates the region in which detector saturation is suspected (see text for details). *Right*: Normalized data to match an arbitrary value at ∼450 m.

Thus, we do not exclude this data points from the analysis, but we use a different marker to highlight them in the following plots.

To fit both the UMD and A1 data, the function of Eq. (7.27) was normalized such that the scaling factor ρ_0 represents ρ_{450}, the muon density at 450 meters, the reference distance of the UMD array. In the left panel of Fig. 7.49, the UMD and A1 data of the lowest-energy bin, along with their fits to Eq. (7.27), are shown. The agreement between the two measurements is quite remarkable, even in absolute values. It is also evident that the model of Eq. (7.27) properly describes the data of the two observatories within this distance range. The equivalent figures corresponding to the remaining energy bins can be found in Appendix H.

To focus only on the shape of the LDFs, the A1 data is scaled with a factor $\rho_{450}^{\mathrm{UMD}}/\rho_{450}^{\mathrm{A1}}$, where $\rho_{450}^{\mathrm{UMD}}$ (ρ_{450}^{A1}) is the muon density at 450 meters of the UMD (A1) data obtained by the fit. The scaled data is jointly plot with the UMD points in the right panel of Fig. 7.49. This procedure is repeated in each energy bin so that the UMD data can be compared to the scaled A1 data. The maximum scaling factor was found to be 1.06 for the energy bin $17.61 < \lg(E/\mathrm{eV}) < 17.84$, indicating an overall agreement in the absolute muon densities of the two experiments.

The comparison between the UMD and the (scaled) A1 data is shown for each energy in Fig. 7.50. Each row in the figure represents a single energy bin. The left column displays the two sets of data (equivalently to the right panel of Fig. 7.49). To visualize more clearly the differences in the LDF shape between the two set of measurements, the ratio between the UMD and the A1 data for each radial bin is shown in the right panel of each row.

For all energies, the ratio $\rho_{\mathrm{UMD}}/\rho_{\mathrm{A1}}$ is typically within $\pm 10\%$ and decreases with distance, indicating that the LDFs measured by the UMD are steeper than those found by A1. Indeed, Akeno is located at a lower altitude (larger atmospheric depth) and therefore a flatter LDF is expected as explained in Section 7.9.1.

In addition, the shift in the energy scales between the experiments would also make the Auger LDFs steeper when compared to the A1 data, as discussed in Section 7.9.1. To further study the impact of the energy, instead of using the same nominal log-energy bin edges than those used at Akeno, we bin the UMD dataset in shifted log-energy bins considering the expected shift of $\lg(E_{\mathrm{Auger}}/\mathrm{eV}) - 0.15 = \lg(E_{\mathrm{A1}}/\mathrm{eV})$ between the energy estimates of the observatories. For example, the A1 data corresponding to the bin $17.39 < \lg(E_{\mathrm{A1}}/\mathrm{eV}) < 17.61$ is now compared to the Auger data belonging to the bin $17.24 < \lg(E_{\mathrm{Auger}}/\mathrm{eV}) < 17.37$.
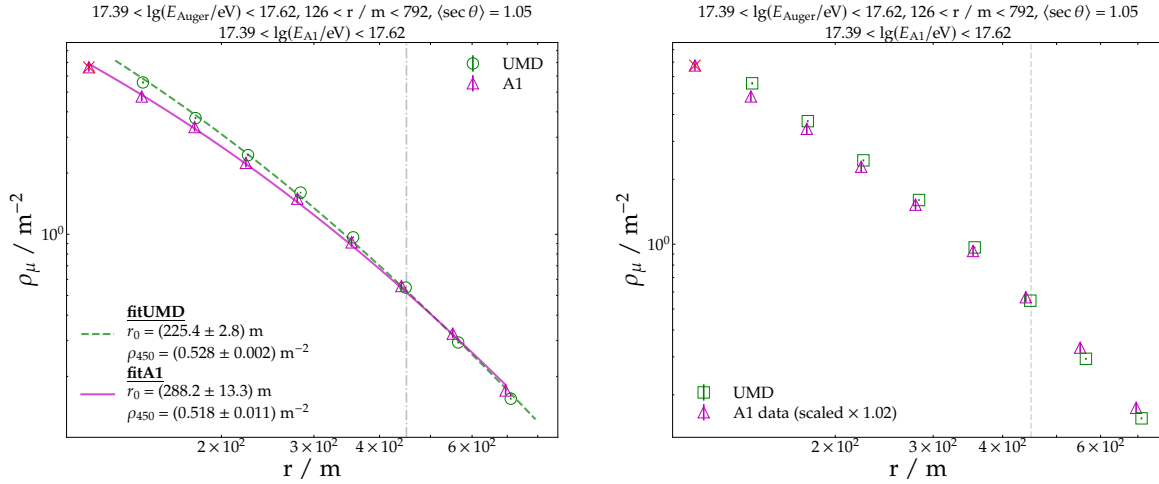
Figure 7.49: Comparison between the UMD and A1 mean MLDF in the energy range $10^{17.39} < E/\text{eV} < 10^{17.61}$ and for $\sec \theta < 1.1$. The vertical dashed line indicates 450 m. Red crosses represent A1 measurements suspected of saturation (see text for details). *Left*: Raw UMD and A1 data and its fits to Eq. (7.27). *Right*: UMD and scaled A1 data. The scaling factor is stated in the figure.

For each energy bin, we show the ratio of the UMD and the A1 scaled data comparing the case with (unfilled squares) and without (filled circles) energy shift in Fig. 7.51. Since the Auger events have lower energies for the energy-shifted case, it is possible to add new radial bins closer to the core. When this happens, the UMD measurements are now compared to the data points of the A1 dataset that are suspected of saturation (red crosses in the figure), causing an increase in the ratio. With the exception of these data points, it is evident that shifting the energy estimate does not significantly change the results.

With the energy shift accounted for, we note that now the difference in the shape can only be attributed to the different depths of the observatories. Thus, we also plot the expected ratio between the two LDFs obtained in Section 7.9.1 by extrapolating the Auger LDF slope to the Akeno observation level (full line in Fig. 7.46). While most of the data points overlap with the curve within their uncertainties, it is also clear that the ratio observed in data is slightly larger than the expected one. This suggests that the extrapolation described in Section 7.9.1 is not capturing the full dependence of the LDF shape with the atmospheric depth. A possible explanation is that the LDF slope β alone is not enough to describe the evolution of the LDF shape with depth, and that some other shape parameter (r_0, α, or γ) in the Auger LDF function (Eq. (6.6)) is sensitive to depth. Another possibility is that the values of some of the aforementioned shape parameters, which are currently fixed, should be slightly adjusted. Nevertheless, considering the systematics that are very likely involved, the agreement between the expected and measured ratio is reasonably good.

Lastly, as already mentioned, when no energy shift is applied, the scaling factor needed to match the ρ_{450} estimates of both datasets is at most 1.06, which indicates that the absolute values of the measurements of the two observatories are in relatively good agreement. In contrast, when the energy of the Auger events is shifted, the muon densities of the UMD measurements is reduced such that the scaling factors are now approximately 0.75. If no large systematic uncertainties in the measurements of the muon densites in the two experiments are expected, this would suggest a relatively small shift in the energy scales, smaller than the one expected according to what was discussed in Section 7.9.1.

7.9.4   Comparison with muon densities measured with A20

Mean MLDFs were also obtained at Akeno with the 20 km^2 array, A20. This bigger array allowed to measure muon densities at distances further than 800 m from the core. In this case, the muon densities were obtained for $\sec \theta < 1.2$ ($\theta \lesssim 33°$) and two relatively wide energy bins, namely, $10^{17.5} < E/\text{eV} < 10^{18}$ and $10^{18.5} < E/\text{eV} < 10^{19}$. The former is chosen for the comparison as it belongs to the energy region accesible by the UMD.

In order to capture the behaviour of the LDF at distances larger than 800 m obtained with A20, Eq. (7.27) had to be modified to

$$\rho_{\text{A20}}(r) = \rho_0 \frac{1}{r_0^2} \left(\frac{r}{r_0} \right)^{-\alpha} \left(1 + \frac{r}{r_0} \right)^{-\beta} \left(1 + \left(\frac{r}{800 \text{ m}} \right)^3 \right)^{-\delta}, \qquad (7.28)$$

where $\delta \sim 0.6$, ρ_0 is a scaling factor, and the shape parameters r_0 and β had the same values than the ones of A1. Like we did with Eq. (7.27) for the comparison with A1 data, we rearrange Eq. (7.28) such that the scaling factor represents ρ_{450}, the muon density at 450 m.

The value of δ is reported in the reference with an approximate symbol instead of an uncertainty, which makes us pressume that the uncertainty of this parameter was rather large. Therefore, we still use Eq. (7.28) to fit the UMD and A20 data, but leaving r_0 as a free parameter. In any case, this fit is only used to find a scaling factor between the datasets, like it was done in the previous section with Eq. (7.27).

The same cuts in energy and zenith angle applied to the A20 dataset were applied to the UMD data. Furthermore, we also use the same binning in r, discarding any bin for which $r < r_{\text{min}}$ or $r > r_{\text{max}}$. In the left panel of Fig. 7.52 we show the A20 measurements, extracted from Fig. 5 of [90], together with the UMD data points. Full and dashed lines indicate the fits of both datasets to Eq. (7.28).

Again, to focus solely on the shape of the LDFs, the A20 data is scaled with a factor $\rho_{450}^{\text{UMD}}/\rho_{450}^{\text{A20}}$, where ρ_{450}^{UMD} and ρ_{450}^{A20} are the muon densities at 450 m obtained by the fits to the UMD and A20 data, respectively. Unlike with A1 data, the absolute densities of the two datasets are somewhat dissimilar, the scaling factor being 1.26. As mentioned earlier, this suggests that the expected shift between the A1 and A20 energy scales derived in Section 7.9.1 might need to be adjusted.

The scaled A20 data is plot jointly to the UMD points in the right panel of Fig. 7.52. The agreement in the shape of the two LDFs is remarkable. Indeed, as presented with full circles in Fig. 7.54, the ratio between the UMD and the (scaled) A20 data is consistent to 1 within uncertainties, and is $\sim 5\%$ at most.

To account for the expected shift in the energy scales discussed in Section 7.9.1, the log-energy of the UMD dataset is shifted -0.19. The raw UMD and A20 data are displayed in the left panel of Fig. 7.53. Since the energy of the UMD events is lower, their absolute muon density also decreases, such that the scaling factor to match the two datasets is now 0.85. This factor is smaller (in absolute value) than the 1.25 needed for the case with no energy shift, which indicates that the shift in the scales is in the right direction. The scaled A20 data is presented in the right panel of Fig. 7.53, where it is apparent that the excellent agreement in the shape of the two sets still holds. The ratio is displayed with unfilled squares in Fig. 7.54, where no significant difference with the case without energy shift is observed.

We conclude that the shape of the mean muon LDFs measured at A1 and A20 are in good agreement with that of the UMD.

7.9.5 Comparison with Yakutsk measurements

Mean MLDFs in the energy range $17.3 < \lg(E/\text{eV}) < 19.3$ with $\sec\theta < 1.11$, measured at the Yakutsk array, were reported in Figure 1 of Ref. [91]. In particular, we focus on the log-energies $\{17.3, 17.7, 18.1, 18.5\}$ as they coincide with energies accesible with the UMD.

Their data is fitted by the model

$$\rho_{\text{Yakutsk}}(r) = \rho_0 \frac{1}{r_0^2} \left(\frac{r}{r_0}\right)^{-\alpha} \left(1 + \frac{r}{r_0}\right)^{0.75-\beta} \left(1 + \left(\frac{r}{2000\ \text{m}}\right)\right)^{-1}, \qquad (7.29)$$

where ρ_0 is a scaling factor, $r_0 = 280$ m and β is a shape paremeter that is left free. Like before, we rearrange the equation such that ρ_0 becomes ρ_{450}.

Like in the previous comparisons, we use the same energy, zenith angle and distance binning for the UMD data. Also, for each energy, we use Eq. (7.29) to fit both the Yakutsk and UMD data to obtain a scaling factor between the two datasets. As an example, we show the fit results for the log-energy bin $17.2 < \lg(E/\text{eV}) < 17.4$ in the left panel of Fig. 7.55. The scaled Yakutsk data and the UMD data is displayed in the right panel of the Figure.

The comparison between the UMD and the scaled Yakutsk data is shown for each energy in Fig. 7.56. Each row in the figure represents a single energy bin. The left column displays the two sets of data. To visualize more clearly the differences in the LDF shape between the two set of measurements, the ratio between the UMD and the Yakutsk data for each radial bin is shown in the right panel of each row.

It is apparent that the MLDFs of Yakutsk are steeper than those of the UMD. This is in contradiction to what is expected according to the discussion given in Section 7.9.1. Since Yakutsk is located at a lower altitude than Auger (and Akeno), a flatter LDF is expected.

To compute the muon densities at Yakutsk, it is assumed that the energy threshold for muons is of $1 \times \sec\theta$ GeV, and that, on average, muons deposit $10.5 \sec\theta$ MeV in the underground scintillators. In Ref. [95], a detailed study of the transmission of particles through the soil and their energy deposit in the scintillators was conducted using GEANT4. There, it is shown that the conventional threshold of 1 GeV for vertical muons is not entirely optimal, as vertical muons with energies down to 0.65 GeV can reach the detectors. Furthermore, the reference energy deposit of 10.5 MeV for vertical muons, assumed to interpret the experimental data of the muon detectors, can be significantly exceeded by a factor of 1.5. As a consequence, the obtained signals can be up to 30 % larger, leading to an overestimation of the number of muons. In addition, it was determined that gamma particles can reach the underground scintillators and significantly contribute to the detector signal, especially closer to the shower axis. Thus, a possible explanation for the discrepancy between the UMD and the Yakutsk LDFs can be found in an overestimation of the muonic signal in the Yakutsk detectors, especially considering that the Yakutsk data used in this thesis were extracted from Ref. [91], published almost 15 years before the study conducted in Ref. [95]. This, however, is only a possibility and no definitive answer can be given at this point to explain this discrepancy.

To study the potential impact of the different energy scales, the log-energy of the Auger events used for the analysis is shifted by -0.12 (see Section 7.9.1). In Fig. 7.57, we show the ratio between the UMD and Yakutsk measurements with (unfilled squares) and without (filled circles) energy shift. In addition, the expected ratio due to the difference in the altitude of the observatories, estimated in Section 7.9.1, is shown as a full line. Like in the comparison to the Akeno data, it is evident that the shift in the energy scale does not change the result.

7.10   Summary

In this chapter, we presented the measurement of the muon content of air showers obtained with the UMD in the energy range $10^{17.5} < E/\mathrm{eV} < 10^{18.9}$.

In Section 7.1, we described the quality cuts applied to the dataset. Due to the preliminary stage of the SD reconstruction with the new electronics, we considered only the period in which the WCDs operated with the old electronics, spanning from January 1st, 2018, to December 21st, 2021. In addition, we showed that $10^{17.5}$ eV is an adequate energy threshold for the analysis. A total of 4,838 events remained after applying all the cuts.

The attenuation correction was presented in Section 7.2, where we demonstrated that the zenith angle dependence of the muon shower size, although not large, was effectively removed after the correction.

The evolution of the attenuation-corrected muon shower size with energy was presented in Section 7.3. An assessment of the systematic uncertainties was provided in Section 7.4, where contributions from the attenuation correction, unknown true LDF shape, reconstruction procedure, muon pattern definition, long-term stability, and energy scale were studied. The largest contribution arises from the energy scale uncertainty (14%), followed by the limited knowledge of the true LDF shape, which can account for up to 10% at lower energies, and the muon pattern definition, reaching up to 7%. The reconstruction procedure and long-term variation contribute 3% and 2%, respectively, whereas the attenuation and corner-clipping corrections are subdominant, with contributions of 1% and 0.6%, respectively.

In Section 7.5, we described the analysis performed on simulated showers to obtain the expected values for pure proton and iron compositions, which are necessary for interpreting the measurements previously presented in Section 7.3. A discrete library consisting of proton and iron primaries with energies $10^{17.5}$, 10^{18}, $10^{18.5}$ eV, and zenith angles 0, 12, 22, 32, 38, and 48 degrees was utilized. EPOS-LHC and QGSJetII-04 were used as hadronic models. The analysis involved fitting the evolution of the mean ρ_{35} and $\ln \rho_{35}$ as a function of the Monte-Carlo energy for each primary and hadronic model. The effects of energy reconstruction and binning, neccesary to compare the simulations to data, were accounted for in a later step using an analytical approach.

Measurements and simulations were compared in Section 7.6. The mean logarithmic mass inferred from this work, shown in Fig. 7.37, shows a trend towards light massess up to approximately $10^{18.4}$ eV, where a break occurs and a trend towards heavier composition is observed. This result is consistent to what is expected from the energy-dependent trend of the mass composition inferred from $X_{\max}$ measurements. The mass inferred here, however, is systematically heavier than that derived from $X_{\max}$, indicating that both observables are not consistently described by the hadronic models used in this work, being this discrepancy more pronounced for QGSJetII-04. Assuming $X_{\max}$ is sufficiently well described by the simulations, this results provides further evidence of a muon deficit in the simulations. To quantify the deficit, measurements of mean $\ln \rho_{35}$ and $X_{\max}$ were compared, and a deficit factor f was defined in Eq. (7.21) such that f compatible to 1 indicates agreement between muon and $X_{\max}$ measurements. For both hadronic models, we have $f > 1$ with significances of approximately 1.5σ and 2.2σ for EPOS-LHC and QGSJetII-04 below $10^{18.4}$ eV, respectively. An increase in the significance of the muon deficit is observed beyond $10^{18.4}$ eV, with 1.95σ and 2.46σ for EPOS-LHC and QGSJetII-04, respectively. Although this suggests an increase in the magnitude of the deficit above $10^{18.4}$ eV, it is necessary to stress that only 23 events are available in the subsequent energy bins (17 events in $10^{18.5} < E/\mathrm{eV} < 10^{18.7}$ and 6 in $10^{18.7} < E/\mathrm{eV} < 10^{18.9}$), and therefore more statistics are needed before stronger statements can be done on the energy-dependent trend of the muon deficit at the highest energies with the UMD.

A comparison with previous muon densities obtained with the UMD, both with the prototype detector operating with PMTs and with the final design using SiPMs, was presented in Section 7.7. The results obtained here are in agreement with those previously obtained with the final design of the UMD and are at the edge of consistency with those reported in the engineering array analysis, with the muon densities being approximately 20% smaller in this work. This difference affects the significance of the reported muon deficit.

The muon content obtained in this work was compared to those reported by other experiments in Section 7.8 by introducing the z-scale and working within the reference energy scale established by the WHISP. The quantity $\Delta z = z - z_{\mathrm{mass}}$ removes the effect of the energy-dependent composition on z, providing a measure of the muon deficit in the simulations. The obtained Δz are somewhat similar to the factor f and, indeed, the two quantities exhibit a similar behaviour with energy, indicating a relatively flat muon deficit below $10^{18.4}$ eV, with an increase above that value. In particular, the Δz (and naturally also z) values at the highest energy bins ($10^{18.4}$ to $10^{18.9}$ eV) are compatible with those from the analysis of hybrid inclined events at the Pierre Auger Observatory and AGASA. However, the same caveat on the limited statistics in these bins, as previously mentioned, also applies here.

Lastly, in Section 7.9, the shape of the mean muon LDF observed in this work was compared to that reported by the observatories at Yakutsk, Russia, and Akeno, Japan, which measured muons with the same energy threshold. This comparison was motivated by the fact that, unlike the absolute number of muons, the shape of the muon LDF is not expected to change drastically with energy or atmospheric depth. Our results show good agreement with Akeno, whereas tension is observed when compared to Yakutsk's measurements. The mean LDFs measured at Yakutsk are steeper than those reported at Akeno and in this work, whereas a flatter LDF is expected due to Yakutsk being closer to sea level.
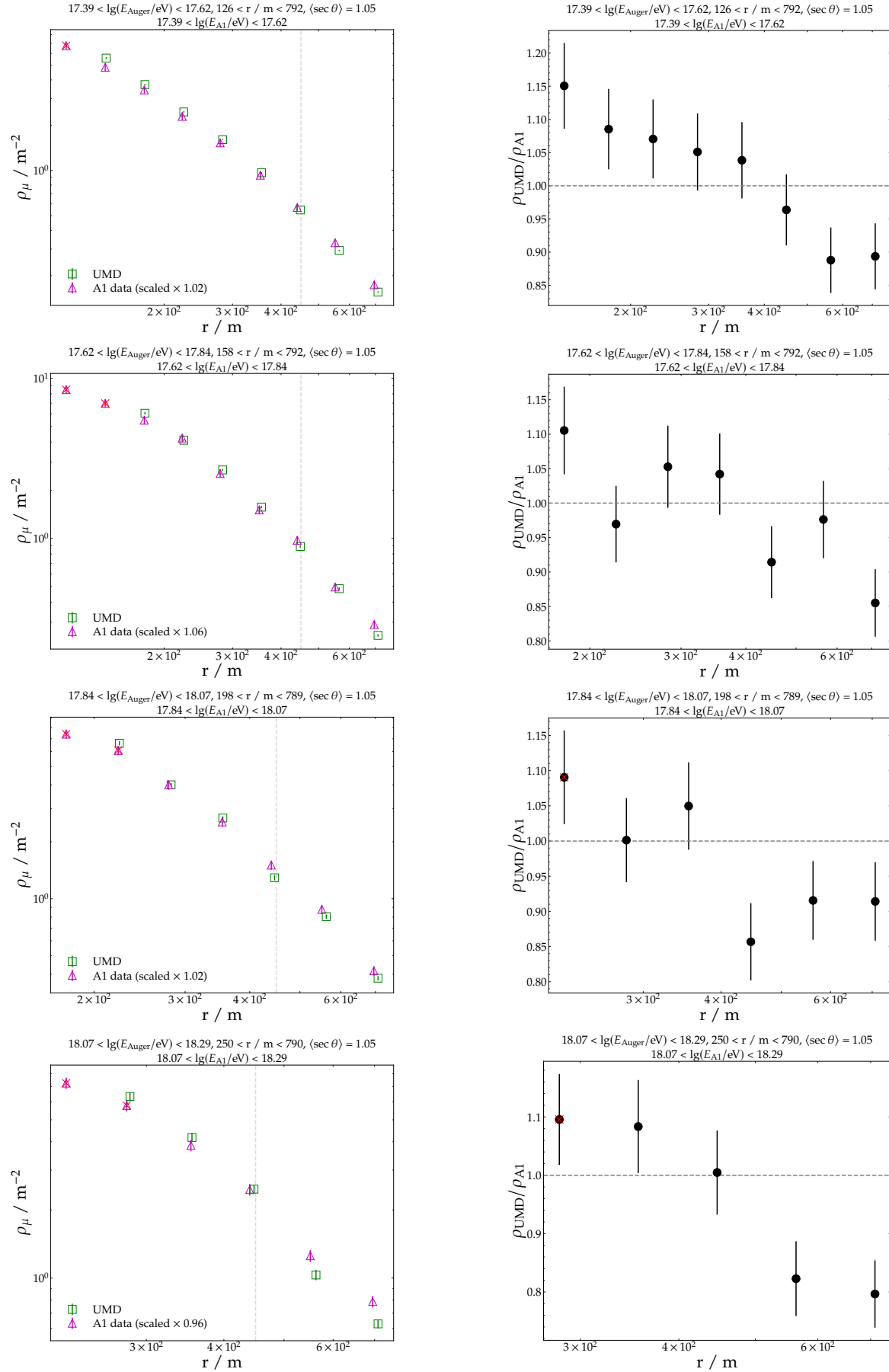
Figure 7.50: Comparison between the UMD and the scaled A1 data (the scaling factor is stated in each figure). Each row represents a single energy bin. For each energy, the left panel displays the two sets of data, while the right shows the ratio between the UMD and A1 scaled measurements for each radial bin. Red crosses represent A1 measurements suspected of saturation (see text for details).
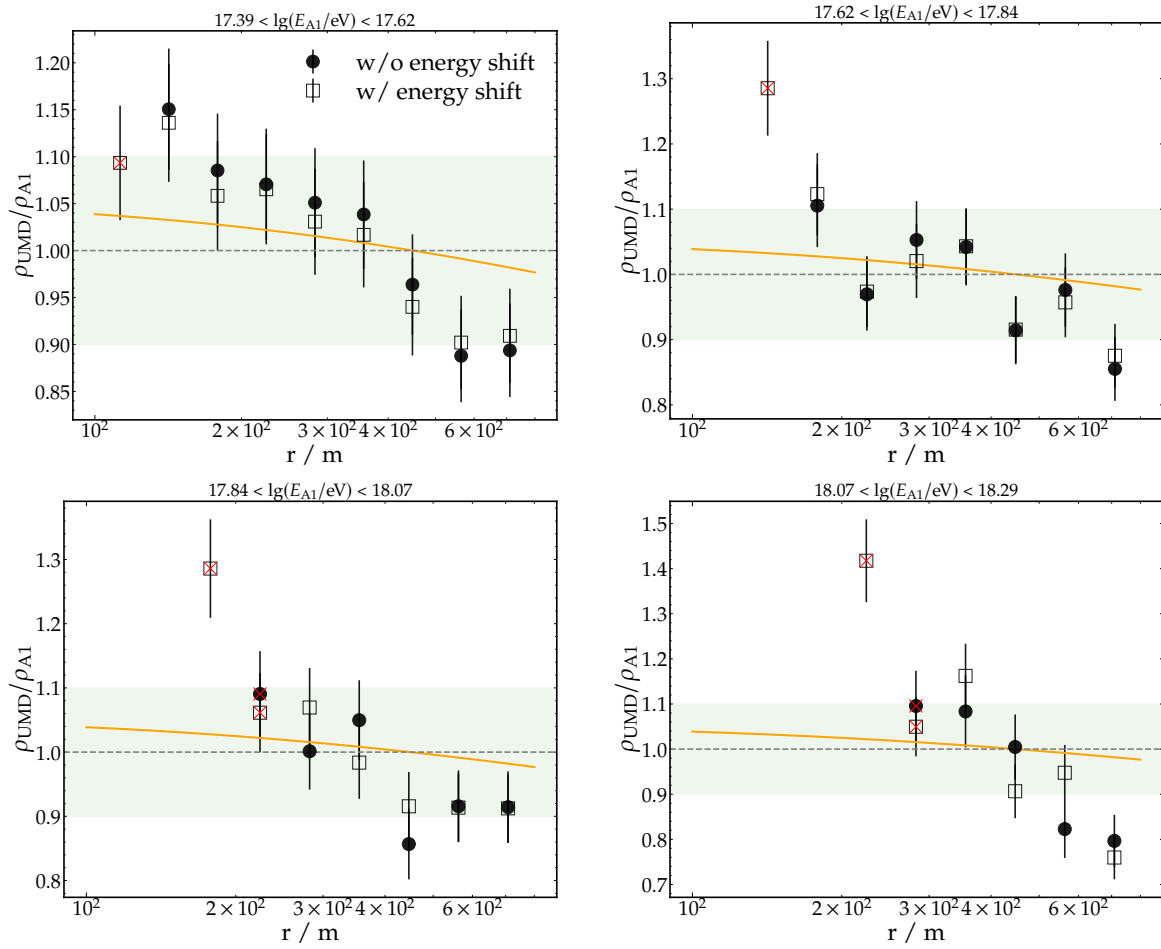
Figure 7.51: Ratio between the UMD and A1 scaled measurements for each radial bin with (unfilled squares) and without (full circles) energy shift in the Auger data. Red crosses represent A1 measurements suspected of saturation (see text for details). Shaded area indicates the $\pm 10\%$ region. The full line indicates the expected ratio calculated in Section 7.9.1 varying the UMD LDF slope β to the observation level of Akeno.
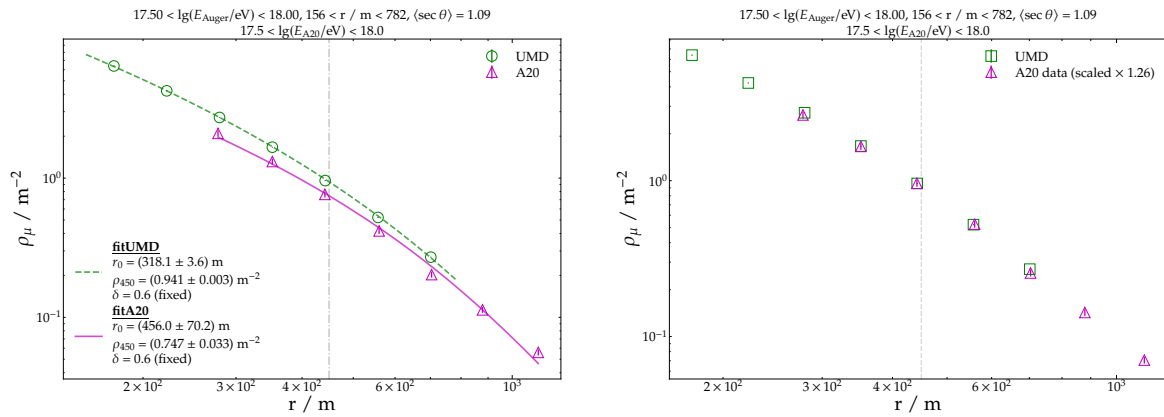
Figure 7.52: Comparison between the UMD and A20 mean MLDF in the energy range $10^{17.5} < E/\text{eV} < 10^{18}$ and for $\sec\theta < 1.2$. The vertical dashed line indicates 450 m. *Left*: Raw UMD and A20 data (taken from Fig. 5 of Ref. [90]) and its fits to Eq. (7.28). *Right*: UMD and scaled A20 data. The scaling factor is stated in the figure.
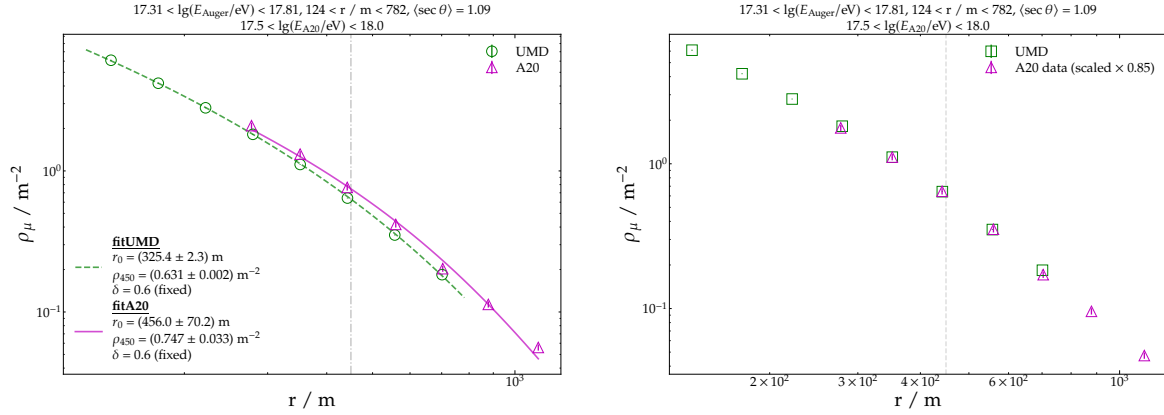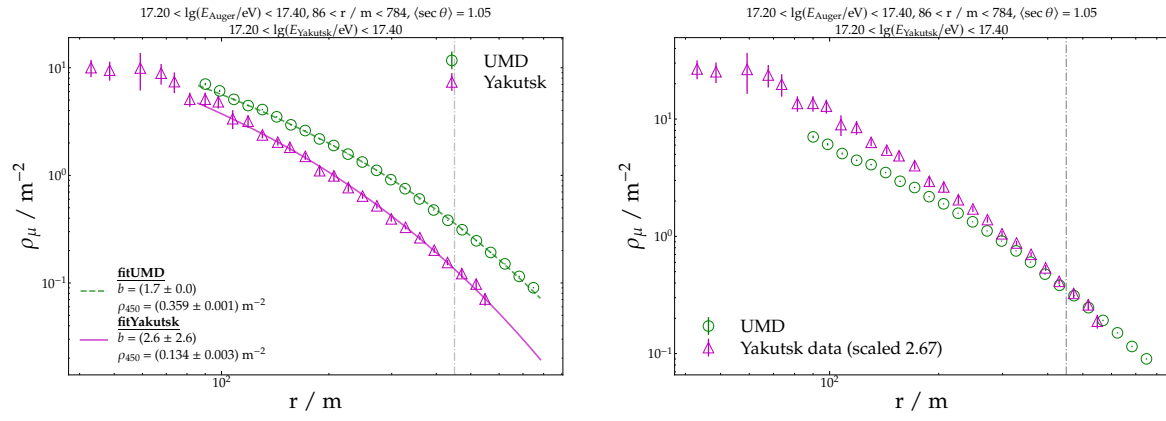
Figure 7.53: Comparison between the UMD and A20 mean MLDF for $\sec\theta < 1.2$. The A20 energies are in the range $10^{17.5} < E_{\mathrm{A20}}/\mathrm{eV} < 10^{18}$ whereas the Auger energies are within $10^{17.21} < E_{\mathrm{Auger}}/\mathrm{eV} < 10^{17.81}$ to account for the expected shift in the energy scale. The vertical dashed line indicates 450 m. *Left*: Raw UMD and A20 data (taken from Fig. 5 of Ref. [90]) and its fits to Eq. (7.28). *Right*: UMD and scaled A20 data. The scaling factor is stated in the figure.
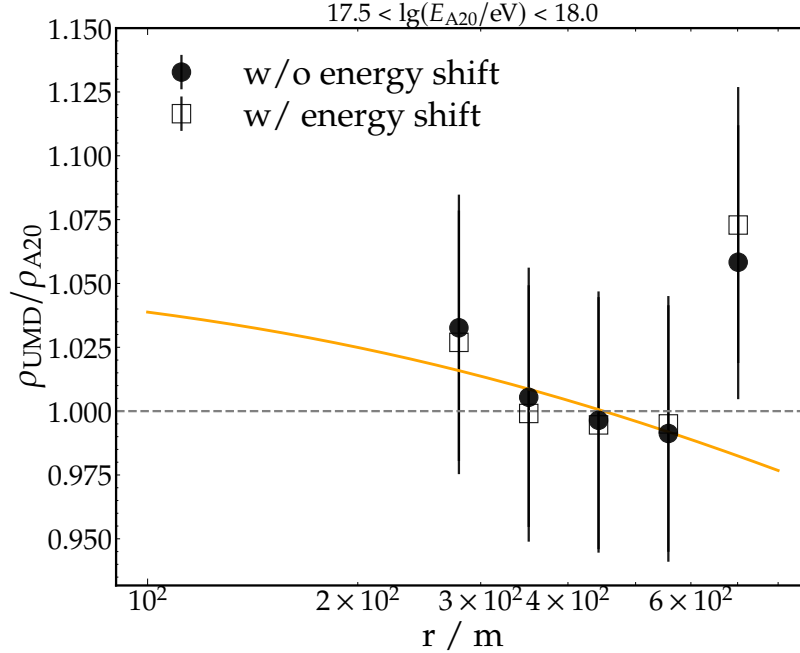
Figure 7.54: Ratio between the UMD and A20 scaled measurements for each radial bin with (unfilled squares) and without (full circles) energy shift in the Auger data. The full line indicates the expected ratio calculated in Section 7.9.1 varying the UMD LDF slope β to the observation level of Akeno.

Figure 7.55: Comparison between the UMD and Yakutsk mean MLDF for $\sec\theta < 1.11$. The vertical dashed line indicates 450 m. *Left*: Raw UMD and Yakutsk data (taken from Fig. 1 of [91]) and its fits to Eq. (7.29). *Right*: UMD and scaled Yakutsk data. The scaling factor is stated in the figure.
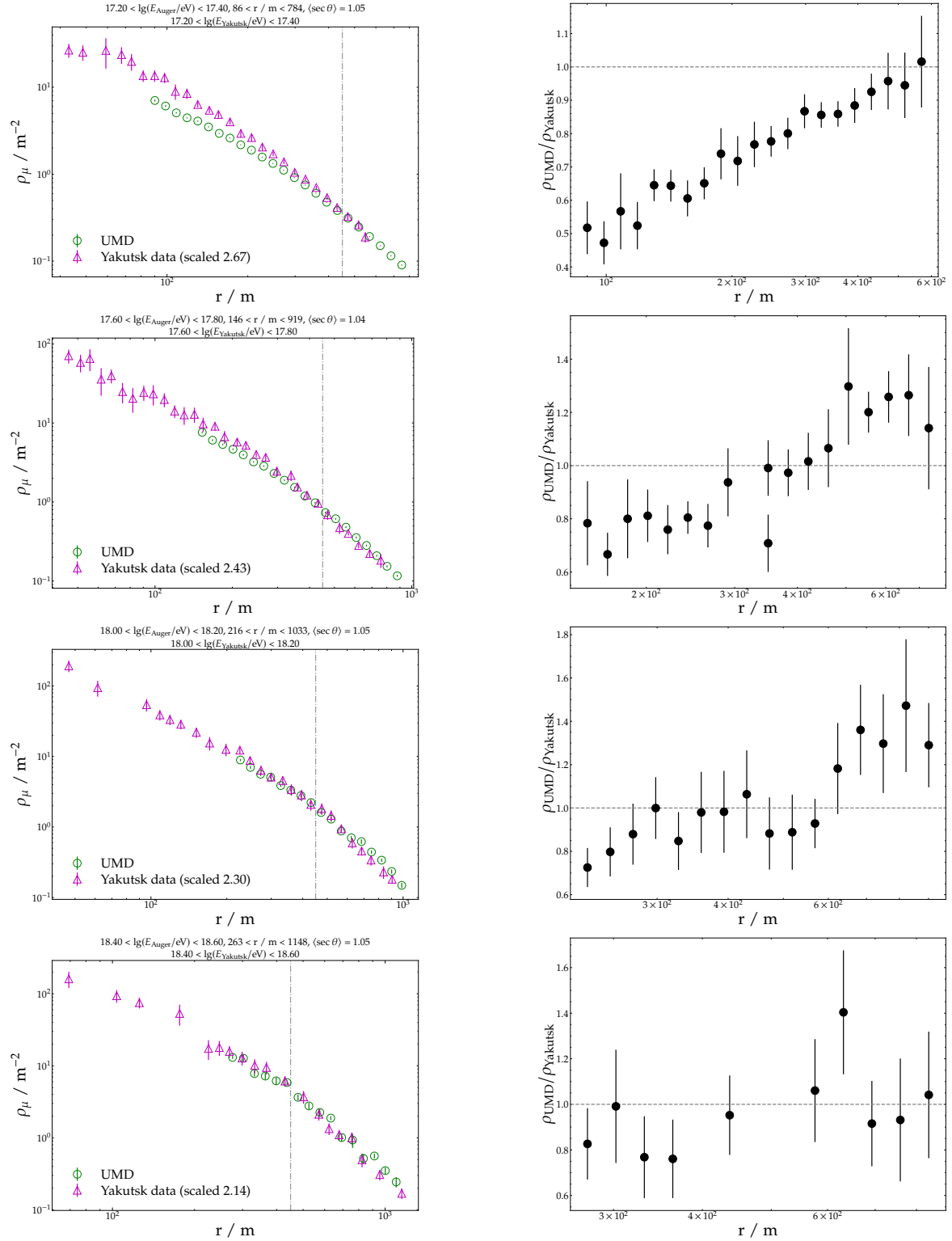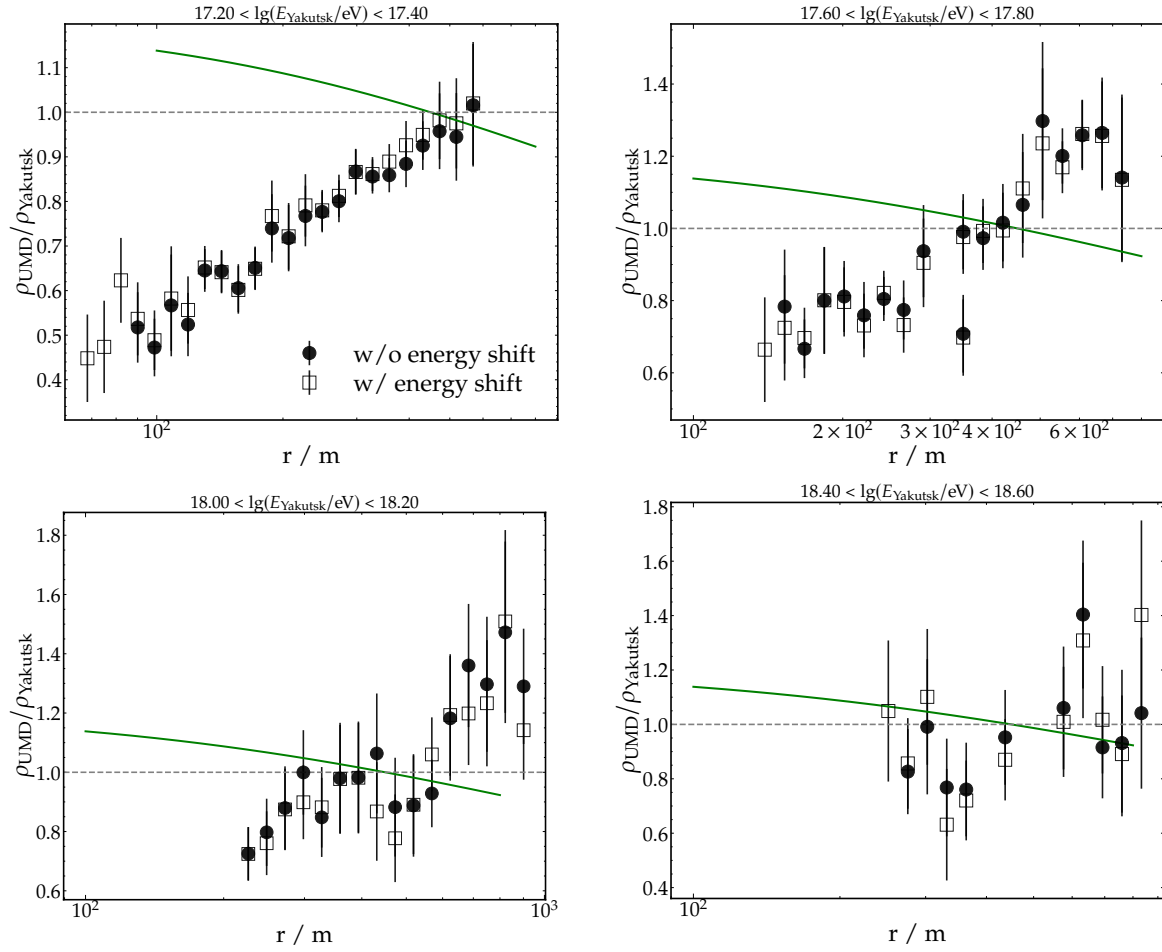
Figure 7.56: Comparison between the UMD and the scaled Yakutsk data (the scaling factor is stated in each figure). Each row represents a single energy bin. For each energy, the left panel displays the two sets of data, while the right shows the ratio between the UMD and Yakutsk scaled measurements for each radial bin.

Figure 7.57: Ratio between the UMD and the Yakutsk scaled measurements for each radial bin with (unfilled squares) and without (full circles) energy shift in the Auger data. The full line indicates the expected ratio calculated in Section 7.9.1 varying the UMD LDF slope β to the observation level of Yakutsk.

Chapter 8

Summary and Conclusions

The measurement of the muon content of air showers produced by ultra-high-energy cosmic rays (UHECRs) is of critical importance for the field. On one hand, the number of muons is a mass-sensitive observable and, unlike $X_{\max}$, it can be sampled with high statistics using arrays of ground-based muon detectors that operate with nearly 100% duty cycle. The determination of the mass composition of UHECRs is essential to break the degeneracy between different astrophysical scenarios that aim to explain the long-standing questions surrounding the origin and acceleration mechanisms of UHECRs. On the other hand, the discrepancy between the inferred mass from $X_{\max}$ and muon measurements suggests that current hadronic models do not reproduce these observables consistently. This discrepancy, known as the *muon puzzle*, indicates that some aspect of hadronic physics at the highest energies -beyond those achiveable by human-made accelerators- is not yet understood. Thus, muon measurements also provide a unique opportunity to test the internal consistency of current high-energy hadronic models, helping to shed light on hadronic physics at the highest energies, and providing essential input for model builders to better tune their models. Both the trend of the inferred mass of the cosmic-ray beam and a quantification of the muon deficit were addressed in this work. In what follows, we summarize the main results of this thesis.

The basic aspects and current knowledge of UHECRs was presented in Chapter 2, whereas a broad description of the Pierre Auger Observatory and its main components, with particular focus on the Undeground Muon Detector (UMD), was provided in Chapter 3.

In Chapter 4, the likelihoods of an ideal segmented detector developed in Ref. [64] for a fixed number of muons N_μ, and in Ref. [63] for a fixed number of expected muons μ, were extended to account for detector noise, inefficiency and corner-clipping muons. The case of fixed μ is particularly relevant, as it considers Poisson fluctuations and can be straighforwardly used in the fit of the lateral distribution function (LDF) of muons at the individual event level, as we do later in this thesis. The extension of the likelihoods was achieved by proposing easily interpretable probabilistic models, where the key parameters are the detector noise probability p_n, the single-muon detector inefficiency p_I, and the single-muon corner-clipping probability p_{cc}, all of which can potentially be measured in the laboratory using standard instrumentation. The framework developed is generally applicable to any type of segmented detector. For the particular case of the UMD, the values of p_n and p_I inferred from previous laboratory measurements are small and can be neglected for practical purposes.

In Chapter 5, we presented a data-driven method to estimate p_{cc}, and validated its self-consistency with simulations. We compared the estimated and true p_{cc}, confirming that the method yields an unbiased estimate of p_{cc}. We also demonstrated that p_{cc} successfully captures the behavior of the bias in $\hat{N}_\mu$ induced by the corner-clipping effect. In this way, the framewok developed in Chapter 4, together with the estimated corner-clipping probability, were validated with full detector simulations. We then proceeded to apply the method to data. The estimated p_{cc} obtained in data shows a qualitatively similar behaviour with respect to θ and ϕ as found in simulations, although it shows systematically lower values. The difference increases with zenith angle and might indicate that corner-clipping is somewhat overestimated in simulations. This, however, has only a small impact on the estimator $\hat{N}_\mu$ and, overall, on the LDF reconstruction, as discussed later in Section 7.4.2. We highlight that this approach enabled the first quantification of the corner-clipping effect using data, an effect previously addressed solely through simulations. Moreover, this method is generally applicable to any type of segmented detector with time resolution.

Within the framework developed in the previous chapters, in Chapter 6 we optimize the procedure to fit a muon LDF at the event level. Based on the findings of Ref. [66], we begin by discussing why we ignore the detector resolution, in contrast to all previous analysis involving the UMD. Then, we extended the event log-likelihood to allow fitting the core position during the LDF fit, even in events with a small number of triggered detectors or whose core is not surrounded by a working UMD hexagon. This significantly improves the quality of the fit in events where the core lies very close to a station, and also improves the error estimation on ρ_{450}, as the core uncertainty is naturally propagated to the uncertainty of the remaining parameters during the fit. Since the existing reconstruction was based on a Poisson likelihood, we assessed the impact of switching to the binomial likelihood developed in Chapter 4. No significant differences were found for the bias or resolution of ρ_{450}, whereas an improved error estimation, leading to a greater coverage of the 1σ interval, was observed for the binomial likelihood, as expected, since the latter is a more realistic model for a segmented detector. Using the subset of events in which β can be reliably fit, we obtained a data-driven parameterization dependent on the zenith angle and energy, which is subsequently used to fix the parameter during the fits to the events. Lastly, we showed that the residuals of the LDF around 450 m from the core are reasonably well centered in zero within approximately $\pm 5\%$.

In Chapter 7, using the optimized reconstruction developed in the previous chapters, the muon measurement of air showers within energies $10^{17.5}$ to $10^{18.9}$ eV was presented. The results were compared to simulations, other experiments, and previous UMD results. When compared to previous analyses with the UMD, we observe compatibility with those obtained with the final design of the detector, which employs silicon photomultipliers as photodetectors, as is the case in this work. The results reported by the UMD engineering array, which was operated with photomultiplier tubes, are at the edge of consistency with our results, showing muon densities $\sim 20\%$ larger than those found here. As a result, the muon deficit reported here is of smaller magnitude.

Regarding the mass composition, our findings, displayed in Fig. 8.1, show that the energy-dependent trend of the inferred mean logarithmic mass is consistent with expectations from X_{max} measurements, indicating a transition from heavy lo light elements from $10^{17.5}$ up to $\sim 10^{18.4}$ eV, where a break towards heavier elements is observed. Thus, this result confirms the trend in the composition of the cosmic ray beam inferred from X_{max}.

The inferred mass, however, is systematically heavier than that predicted from X_{max}. Under the assumption that X_{max} is well described by the hadronic models, the results of this work provide further evidence of a muon deficit in the simulations. To quantify the deficit and its energy dependence, two quantities were utilized, namely f (Eq. (7.21)) and Δz

(Eq. (7.25)) both exhibiting similar behavior—a relatively flat trend up to $10^{18.4}$ eV, followed by increasing values at higher energies. The energy evolution of f is displayed in Fig. 8.2. Although statistics are still scarce for energies above $10^{18.4}$ eV, this trend suggests that the muon deficit becomes more pronounced around this energy.

Motivated by the fact that the shape of the muon LDF is not expected to change drastically with energy or atmospheric depth, we compared the shape of the mean muon LDF to that reported by the observatories at Yakutsk, Russia, and Akeno, Japan, which measured muons with the same energy threshold of 1 GeV. Our results show good agreement with Akeno, whereas tension is observed when compared to Yakutsk's measurements. The mean LDFs measured at Yakutsk are steeper than those reported at Akeno and in this work, despite a flatter LDF being expected due to Yakutsk's lower altitude, closer to sea level.

This work focused on UMD data from Phase 1 of the Observatory's operation. The reconstruction methods developed here and the analyses applied to the data can be straight-forwardly applied to the expanding dataset of Phase 2 of the Observatory's operation. This dataset is already larger than the one used in this work and can therefore be used to analyze mass composition and test hadronic models at the highest energies with greater statistical significance.
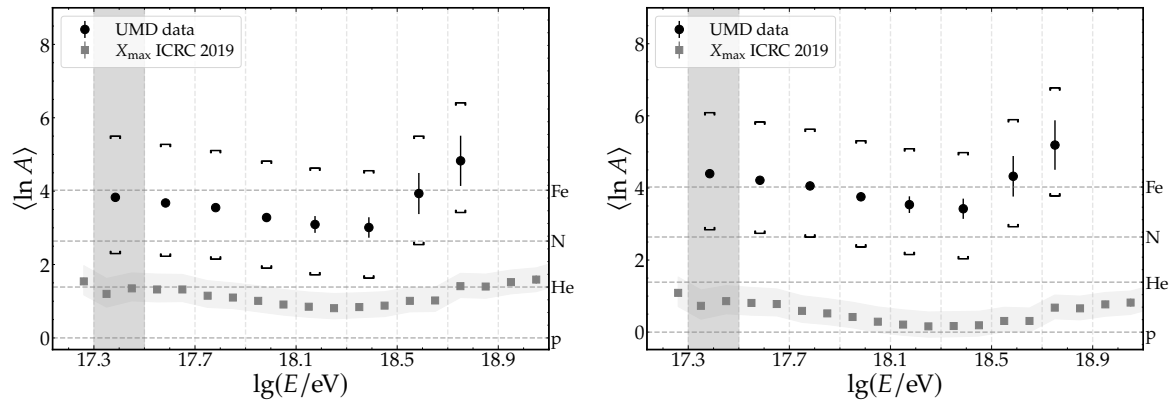

Figure 8.1: Mean logarithmic mass as a function of energy for EPOS-LHC (left) and QGSJetII-04 (right panel). Error bars indicate statistical uncertainty, whereas brackets correspond to systematic uncertainties. Grey markers indicate the logarithmic mass inferred from $X_{\max}$ measurements [84]. The shaded grey area indicates the energy bin below full efficiency (see Section 7.1.1), preserved for visualization only.
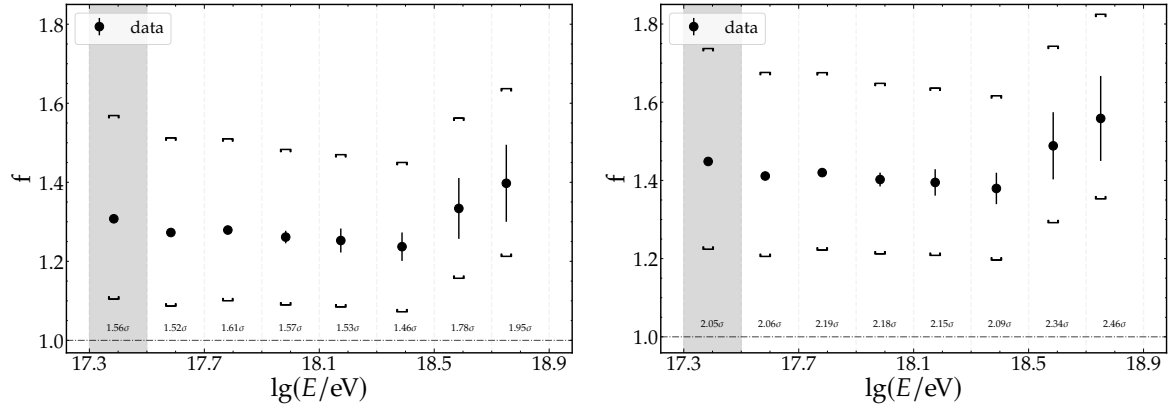
Figure 8.2: Factor comparing the agreement between the muon content in data and simulations (Eq. (7.21)) as a function of energy for EPOS-LHC (left panel) and QGSJetII-04 (right panel). Error bars indicate statistical error whereas brackets correspond to systematic uncertainties. The horizontal dashed line indicates unity. The shaded grey area indicates the energy bin below full efficiency (see Section 7.1.1), preserved for visualization only. The distance to unity in units of σ is indicated in each bin, where σ corresponds to the total uncertainty.

Appendix A

On the probability distribution $P(k|\mu)$

In Section 4.1 the detector inefficiency and the corner-clipping effect were included in the single-module likelihood proposing a multinomial process (Eq. (4.18)). The key idea was to think in terms of effective number of particles N_{eff}; the inefficiency would decrease this number while corner-clipping muons would increase it.

In the derivation of the distribution $P(k|\mu)$ in Ref. [63], it is shown that if $N_\mu \sim \text{Poiss}(\mu)$, then $P(k|\mu)$ is given by Eq. (4.3). Therefore, in order to be able to assure that the modified $P(k|\mu)$ given in Eq. (4.20) is the true distribution of k, one needs to prove that $N_{\text{eff}} \sim \text{Poiss}(\mu_{\text{eff}})$. It is instructive to generalize our problem: let $N \sim \text{Poiss}(\mu)$ and $K \sim \text{Binom}(N, p)$. Lets define $M_- = N - K$ and $M_+ = N + K$.

For M_- we have:

$$P(M_- = m) = \sum_{N=0}^{\infty} P(K = N - m|N, p)P(N|\mu) = \sum_{N=0}^{\infty} \frac{N!}{(N-m)!m!}p^{N-m}(1-p)^m \frac{\mu^N e^{-\mu}}{N!},$$

Conveniently multiplying by $\mu^m \mu^{-m} e^{-\mu p} e^{\mu p}$ we obtain

$$P(M_- = m) = [\mu(1-p)]^m \frac{e^{-\mu(1-p)}}{m!} \sum_{N=0}^{\infty} (\mu p)^{N-m} \frac{e^{-\mu p}}{(N-m)!}$$

$$= \text{Poiss}(m|\mu(1-p)) \sum_{N=0}^{\infty} (\mu p)^{N-m} \frac{e^{-\mu p}}{(N-m)!}.$$

Finally, we note that since $m \leq N$, the term with the sum actually goes from $N = m$ to ∞. Therefore, $\sum_{N=m}^{\infty} (\mu p)^{N-m} \frac{e^{-\mu p}}{(N-m)!} = \sum_{j=0}^{\infty} (\mu p)^j \frac{e^{-\mu p}}{(j)!} = 1$. Thus,

$$P(M_- = m) = \text{Poiss}(m|\mu(1-p)).$$

We conclude that M_- follows a Poisson distribution with mean $\mu(1-p)$.

A similar excercise with M_+ does not lead to a Poisson or any known closed distribution to our knowledge.

By making the substitution $N = N_\mu$ and $K = n_I$ we obseve that M_- is N_{eff} when $p_{cc} = 0$. Thus, when $p_{cc} = 0$, Eq. (4.20) is exact. This corresponds to what is observed in the upper panels of Figs. 4.8 and 4.9.

If we substitute $N = N_\mu$ and $K = n_{cc}$ we have that M_+ is N_{eff} when $p_I = 0$. Therefore, when $p_I = 0$ (and $p_{cc} \neq 0$), Eq. (4.20) is approximate.

We can generalize and conclude that $N_{\text{eff}} \sim \text{Poiss}(\mu_{\text{eff}})$ only if $p_{cc} = 0$.
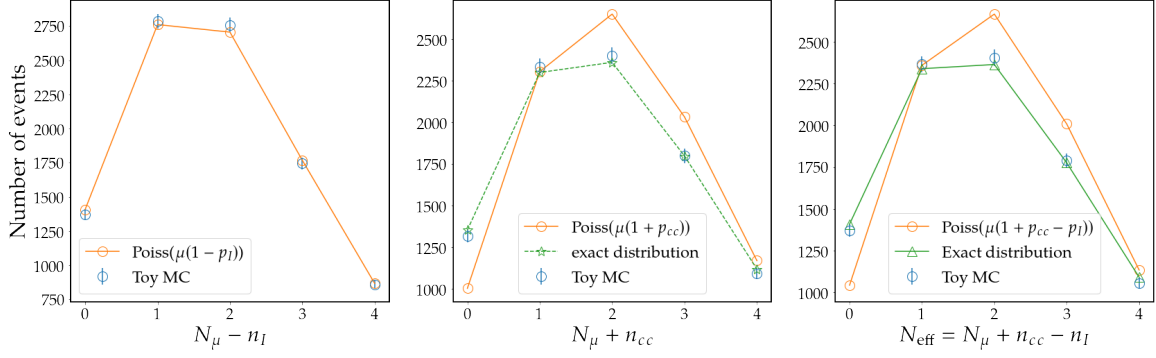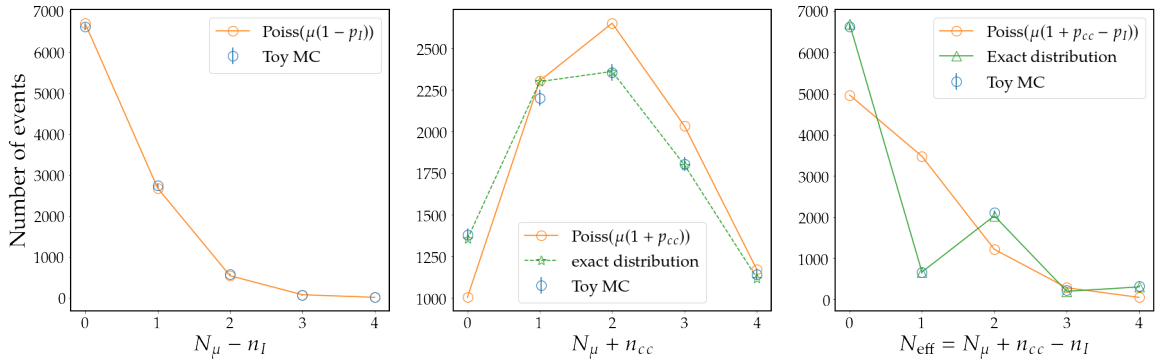
Figure A.1: Results of the Monte-Carlo simulation described in Section 4.1.3 for $\mu = 2$, $p_I = 2\%$ and $p_{cc} = 15\%$. *Left:* Distribution of $N_\mu - n_I$. *Center*: Distribution of $N_\mu + n_{cc}$. *Right:* Distribution of N_{eff}.

Figure A.2: Results of the Monte-Carlo simulation described in Section 4.1.3 for $\mu = 2$, $p_I = 80\%$ and $p_{cc} = 15\%$. *Left:* Distribution of $N_\mu - n_I$. *Center*: Distribution of $N_\mu + n_{cc}$. *Right:* Distribution of N_{eff}.

Finally, we show in Figs. A.1 and A.2 the distributions of $N_\mu - n_I$, $N_\mu + n_{cc}$ and $N_{\text{eff}} = N_\mu + n_{cc} - n_I$ for $\mu = 2$ obtained in the Monte-Carlo simulation described in Section 4.1.3 along with the Poisson expectations and the true distribution. Indeed, we confirm that $N_\mu - n_I$ (i.e. M_-) follows a Poisson distributions with mean $\mu(1 - p_I)$ and $N_\mu + n_{cc}$ (i.e. M_+) and N_{eff} do not follow Poisson distributions with means $\mu(1 + p_{cc})$ and $\mu(1 + p_{cc} - p_I)$, respectively. However, we note that for $p_I = 2\%$, the Poisson approximation is sufficiently good. The true distribution of N_{eff}, represented with green lines, comes from computing

$$P(N_{\text{eff}}|\mu) = \sum_{N_\mu=0}^{\infty} \left[\sum_{n_I=0}^{n_I=N_\mu} P(n_I, n_{cc} = N_{\text{eff}} - N_\mu + n_I | N_\mu) P(N_\mu|\mu) \right],$$

where $P(N_\mu|\mu)$ is a Poisson distribution with mean μ and $P(n_I, n_{cc}|N_\mu)$ is given by Eq. (4.18).

Appendix **B**

Study on the time response of the detector using corner-clipping muons

The corner-clipping muons provide a unique opportunity to conduct a study on the time response of the detector. The start time t of a muon pattern produced by a muon hitting a bar at a distance l from the SiPM at time t_0 can be conveniently written as

$$t = t_0 + l/c + t_r, \tag{B.1}$$

where c is the speed of light in the fiber and t_r corresponds to the delay due to the response of the detector. This is a random variable which encapsulates both the decay of the scintillator-fiber system and the electronics response.

As already discussed, the signature of a corner-clipping muon is to produce two muon patterns with very small time difference in adjacent bars. If we write the start time of the two bars involved using Eq. (B.1) and substract them, we have

$$\Delta t = \Delta t_0 + \Delta l/c + \Delta t_r.$$

Since the same muon is responsible for the two signals, we can approximate $\Delta t_0 = 0$ and $\Delta l = 0$. Thus, for corner-clipping muons, we have

$$\Delta t = \Delta t_r. \tag{B.2}$$

Therefore, assuming a probability distribution for t_r, a model for Δt_r, our observable, can be derived and fit to data.

To propose a model for t_r it is convenient to plot the data displayed in Fig. 5.10 using the Δt preserving the sign instead of its absolute value. We arbitrarily compute Δt as the difference between the start times of the strip with the larger ID and the strip with the smaller ID. The result is shown in Fig. B.1. As expected, a symmetrical peak around zero can be observed. The shape of the Δt peak resembles a triangular distribution, which in turn corresponds to the expected distribution of the difference between two uniform random variables. Thus, we propose a uniform distribution for t_r between 0 and $t_{\max}$, which we denote $U(0, t_{\max})$.

The uniform distribution is defined in a continuous time variable. However, our time measurements are in discrete time bins due to the sampling of the electronics. Therefore, the discretization has to be taken into account. The probability of the start time to be in the n time bin is
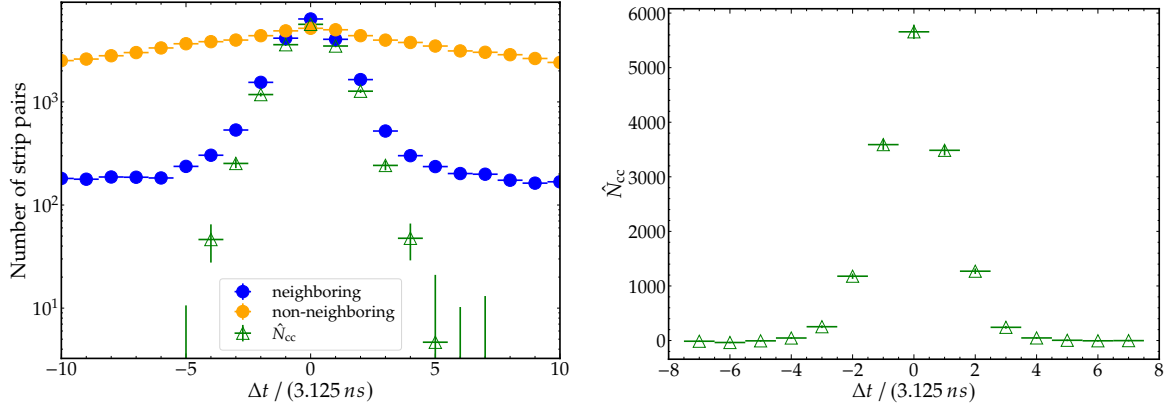
Figure B.1: *Left:* Same as in Fig. 5.10 but preserving the sign in Δt. *Right:* $\hat{N}_{cc}$ in linear scale. The shape of the peak resembles a triangular distribution.

$$P(t_{bin} = n|t_{max}) = \int_{n\,3.125\,ns}^{(n+1)\,3.125\,ns} U(0, t_{max})dt, \tag{B.3}$$

where $3.125\,ns$ corresponds to the sampling time of the electronics.

Thus, the probability of $\Delta t = k$ is

$$P(\Delta t = k|t_{max}) = \begin{cases} \sum_{j=0}^{\infty} P(t_{bin} = k+j)P(t_{bin} = j) \text{ if } k > 0 \\ \sum_{j=0}^{\infty} P(t_{bin} = j-k)P(t_{bin} = j) \text{ if } k < 0 \\ \sum_{j=0}^{\infty} P(t_{bin} = j)P(t_{bin} = j) \text{ if } k = 0. \end{cases} \tag{B.4}$$

The fit of the model of Eq. (B.4) to data and simulations is shown in Fig. B.2. The $\hat{N}_{cc}(\Delta t)$ values were previously normalized to represent a probability. It is apparent that the timing distribution of data is wider than the one found in simulations. Indeed, the t_{max} value found for data ($7.8\,ns$) is larger than the one for simulations ($4.5\,ns$), although the discrepancy is not significant as it is of the order of the sampling time of the detector. This difference, not relevant for the purpose of our analysis as the time resolution of the detector is not used (see Section 6.1), is not surprising and can be explained by the fact that data is affected by detector-to-detector fluctuations between the different modules deployed in the field.

The timing model proposed in this section can be used for simplified toy Monte-Carlo simulations of the detector and to estimate uncertainties in future studies involving timing information of the detector.
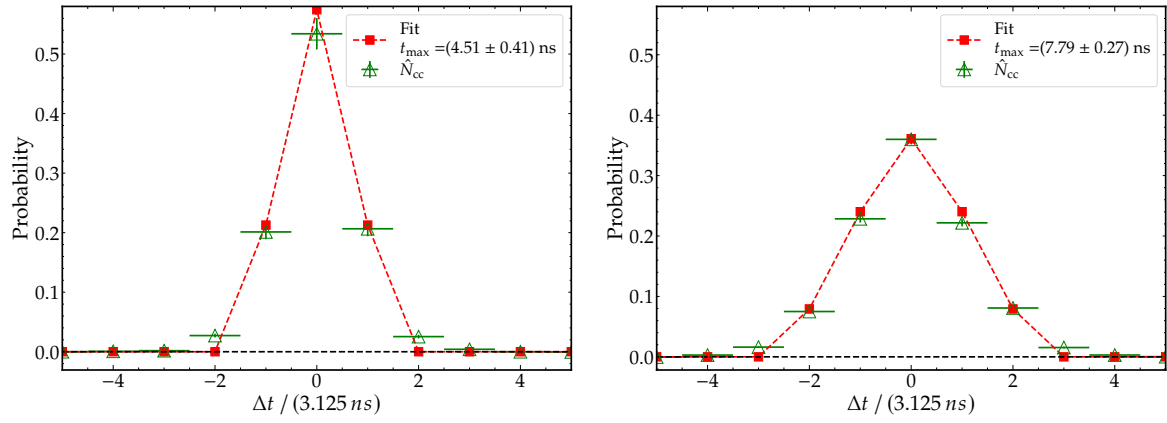
Figure B.2: Fit of the model of Eq. (B.4) (red squares with dashed lines) to the measured probabilites (green markers) as obtained with simulations (left) and data (right). The measured probability in a given Δt was obtained by $\hat{N}_{cc}(\Delta t)/(\sum_{\Delta t} \hat{N}_{cc}(\Delta t))$, and it represents the probability of a corner-clipping muon to produce a Δt time difference between the signals start times.

C

Feldman-Cousins interval calculation

Following the Feldman-Cousins (FC) procedure [68], the $1 - \alpha = 68.2\%$ interval is constructed as follows:

- For fixed μ, the values (k_1, k_2) such that $P(k_1 \leq k \leq k_2 | \mu) \geq 1 - \alpha$ are found. The interval $k_1 \leq k \leq k_2$ is referred to as acceptance region. The k values are included in the acceptance region in decreasing order of the ratio $P(k|\mu) / P(k|\hat{\mu})$ until the sum of $P(k|\mu)$ meets or exceeds the value $1 - \alpha$. k_1 and k_2 are then the minimum and maximum values of k in the acceptance region, respectively. Performing a scan over values of μ, two bands $k_1(\mu)$ and $k_2(\mu)$ are obtained (blue lines in the left panel of Fig. C.1).

- A given observed k defines a horizontal line in Fig. C.1 (e.g. $k = 0$ dashed green line) which interesects the constructed bands. The corresponding μ interval is obtained by the lower- and upper-most edge of the intersection (green markers).

- For each possible observed k, the interval (μ_1, μ_2) is constructed.

When constructing the bands shown in the left panel of Fig. C.1, the actual coverage of the interval can be computed. This coverage can be compared to the one obtained in Monte-Carlo experiments as a sanity check. The results of these toy experiments is compared to the analytical coverage in the right panel Fig. C.1, in which a very good agreement can be observed.
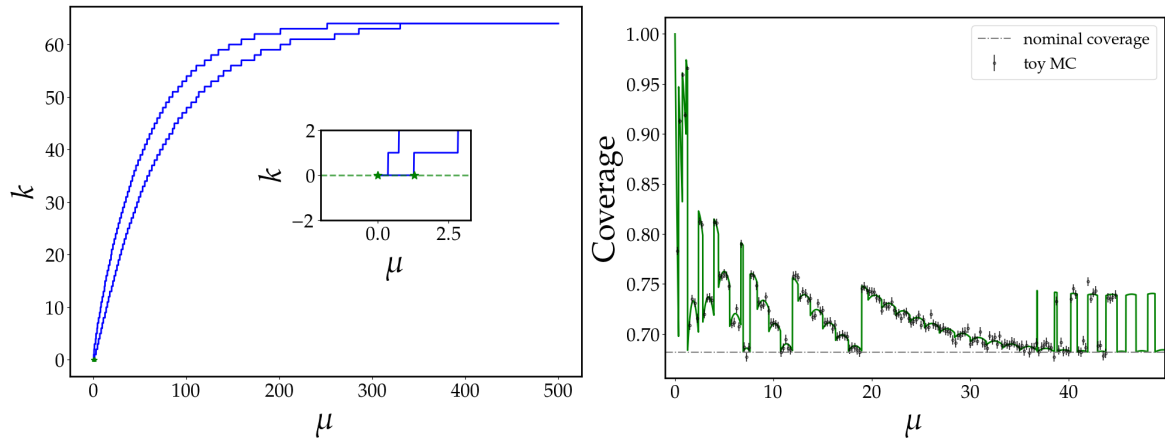
Figure C.1: *Left:* Confidence belt constructed with the Feldman-Cousins procedure. As an example, the interval for $k = 0$ is represented with green markers. *Right:* Analytical coverage calculated during the Feldman-Cousins procedure as a function of μ is represented with a green line. The coverages obtained with toy MC experiments is denoted with black unfilled circles. Horizontal dashed line marks the 68.2% value.

Appendix D

Performance of the corner-clipping correction on QGSJetII-04

In Fig. 5.9, we showed that the estimated corner-clipping probability successfully captures the zenith-dependent bias introduced in $\hat{N}_\mu$ by the corner-clipping muons using air showers simulated with EPOS-LHC. In Fig. D.1, we show the same but applied to simulations performed with QGSJetII-04 as hadronic model. It is apparent that the parameterization of the estimated corner-clipping probability obtained in Fig. 5.6, derived from EPOS-LHC showers, performs equally well on showers simulated with QGSJetII-04. Indeed, muons are highly collimated, regardless of the model, and thus no significant impact in the corner-clipping effect is expected between different hadronic models.
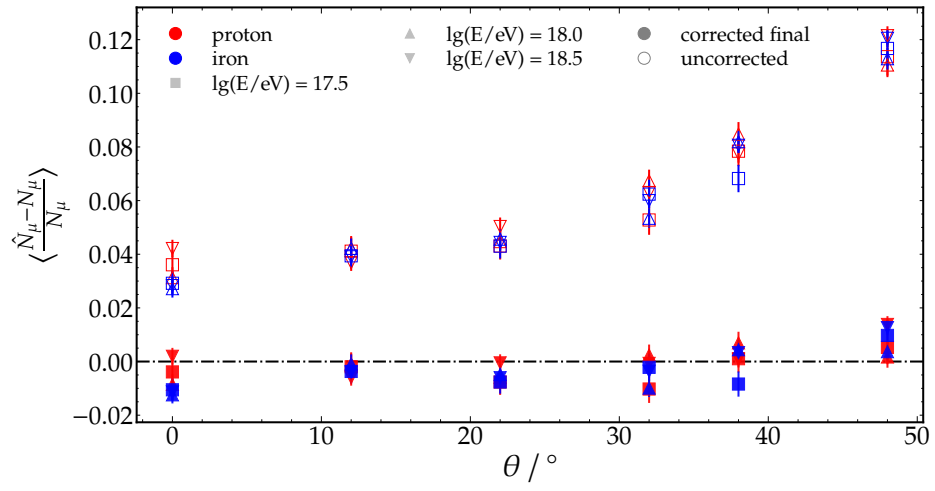
Figure D.1: Same as in Fig. 5.9 but using QGSJetII-04 as hadronic model.

Performance of the muon LDF reconstruction on QGSJetII-04

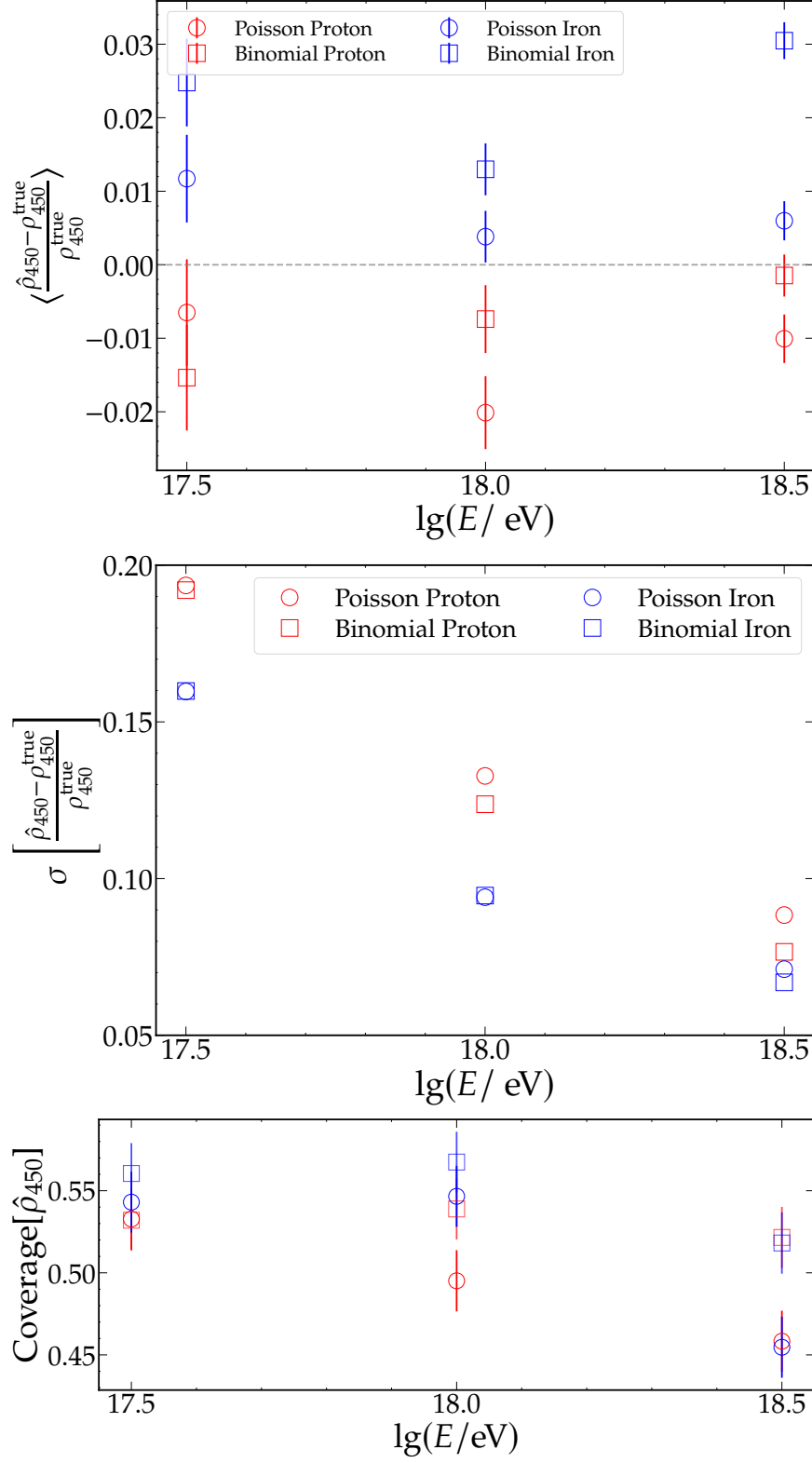In Fig. E.1, we show the same as in Fig. 6.12 but using QGSJetII-04 as hadronic interaction model.

Figure E.1: Bias (upper panel), resolution (middle panel) and coverage of the 1σ interval (lower panel) of $\hat{\rho}_{450}$ retrieved by the LDF fit for the Poisson (circles) and binomial (squares) likelihoods.

Additional plots of the comparison of the muon content between data and simulations

F.1 Impact of using convolved or uncolvolved densities in the final results

The comparison between data and simulations in the $(X_{\max}, \ln\rho_{35})$ plane for all the energy bins is shown in Fig. F.1 for EPOS-LHC and in Fig. F.2 for QGSJetII-04. The case in which the uncolvolved simulations are used is also displayed.

The mean logarithmic mass and the deficit factor (Eq. (7.21)) obtained with the convolved and uncolvolved densities are displayed in Fig. F.3 and Fig. F.4, respectively.

F.2 Alternative energy binning
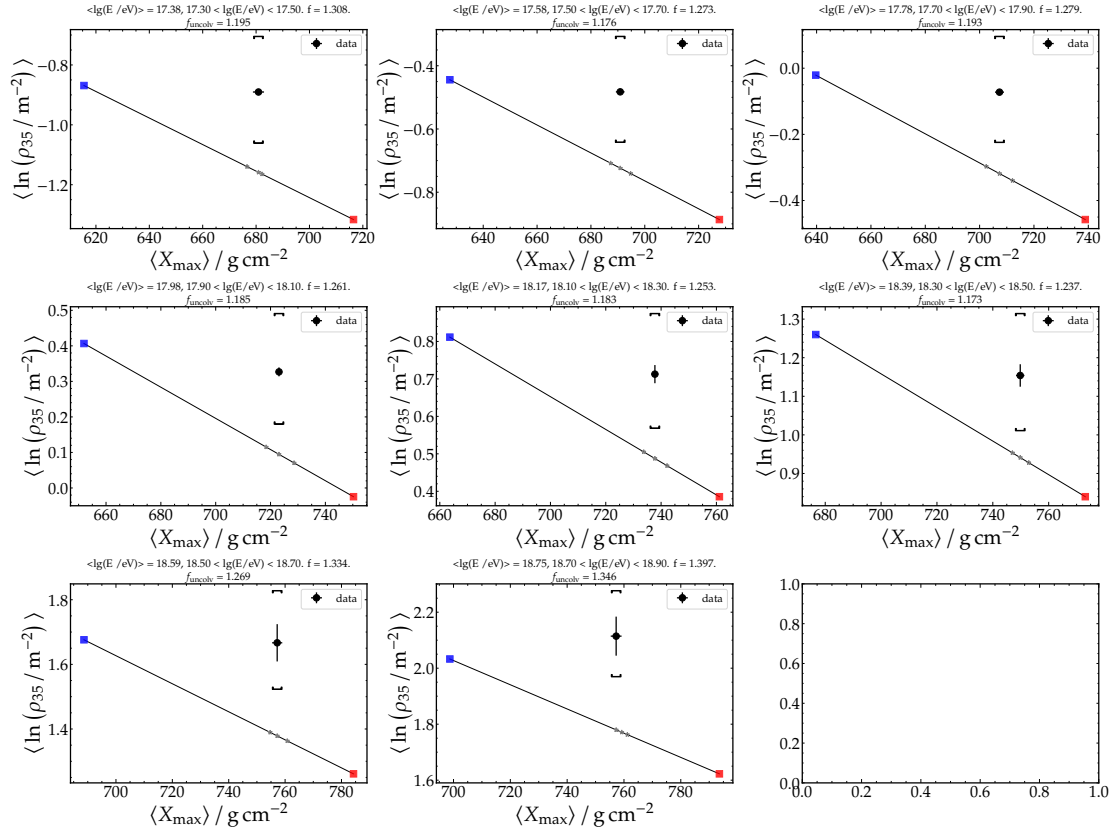
Figure F.1: Comparison between data and simulations of EPOS-LHC. The filled markers joined by a full line correspond to the convolved values obtained via Eq. (7.14). The unfilled markers joined by dashed line corespond to the uncolvolved values shown in Fig. 7.31.
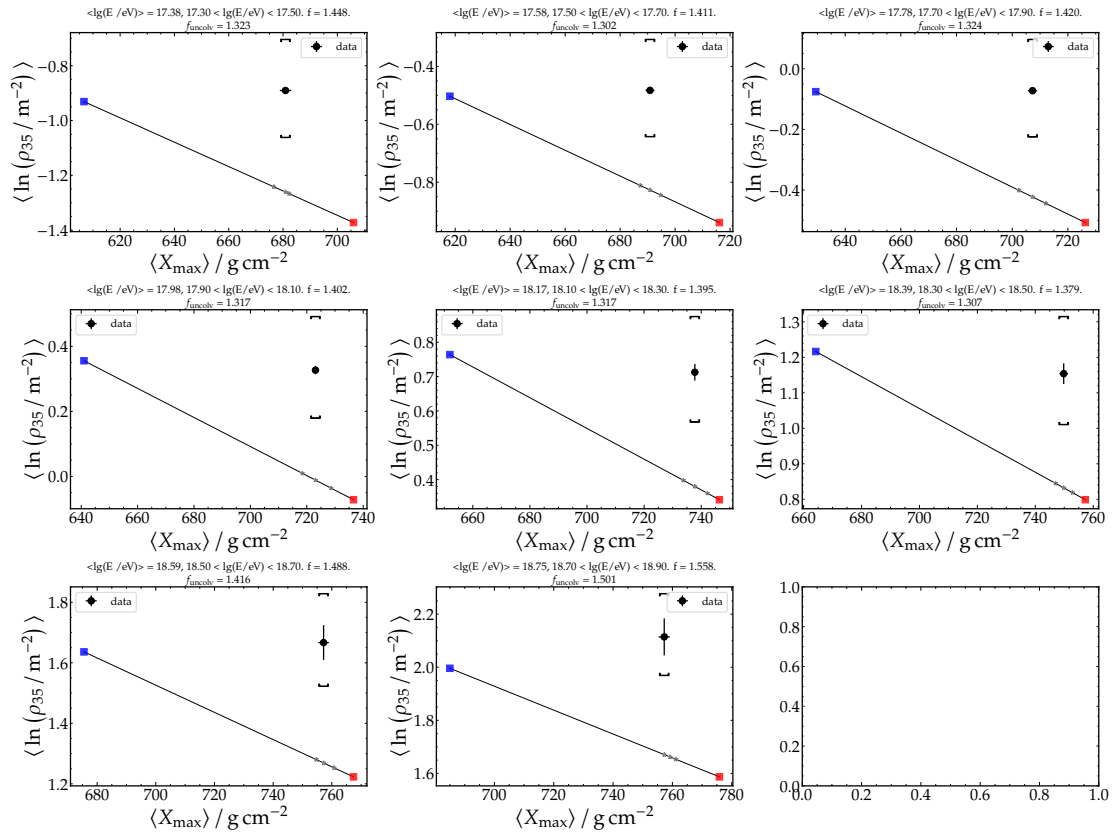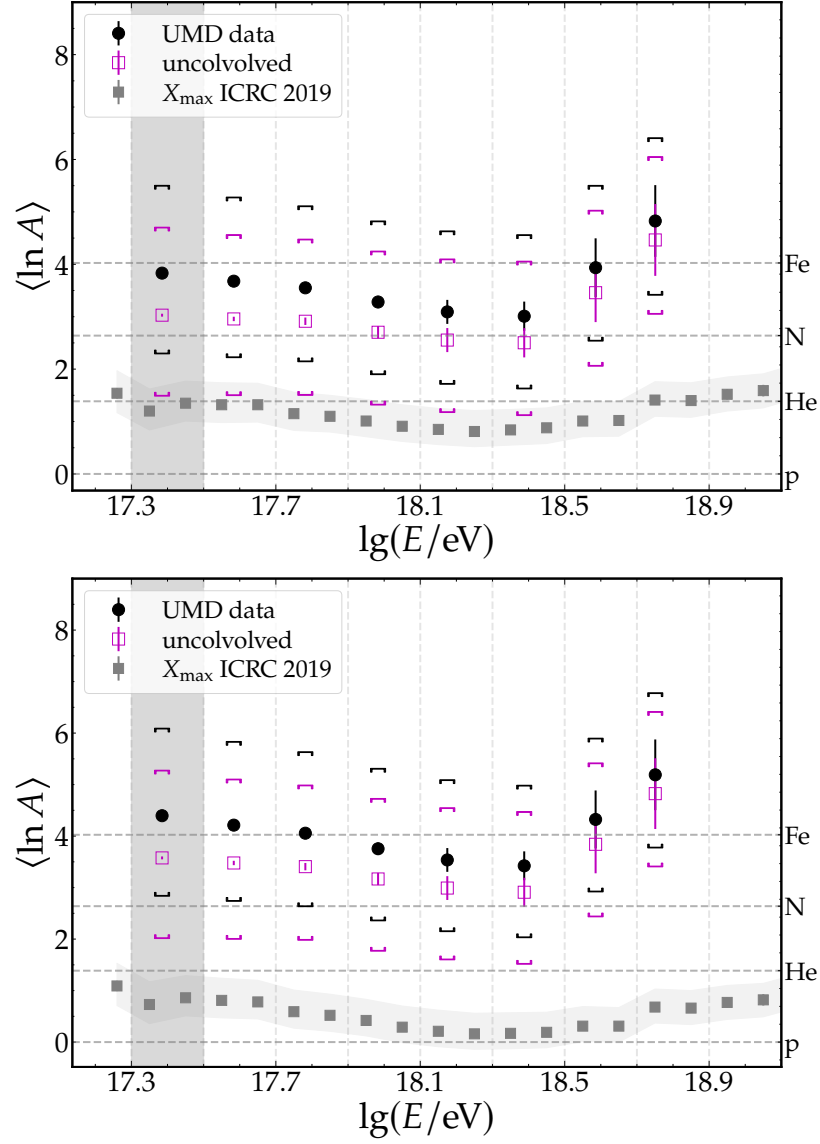
Figure F.2: Comparison between data and simulations of QGSJetII-04. The filled markers joined by a full line correspond to the convolved values obtained via Eq. (7.14). The unfilled markers joined by dashed line corespond to the uncolvolved values shown in Fig. 7.31.

Figure F.3: Mean logarithmic mass as a function of energy for EPOS-LHC (upper panel) and QGSJetII-04 (lower panel). Error bars indicate statistical uncertainty, whereas brackets correspond to systematic uncertainties. Grey markers indicate the logarithmic mass inferred from X_{max} measurements [84]. The shaded grey area indicates the energy bin below full efficiency (see Section 7.1.1), preserved for visualization only. The magenta markers indicate the masses inferred with the uncolvolved densities shown in Fig. 7.31.
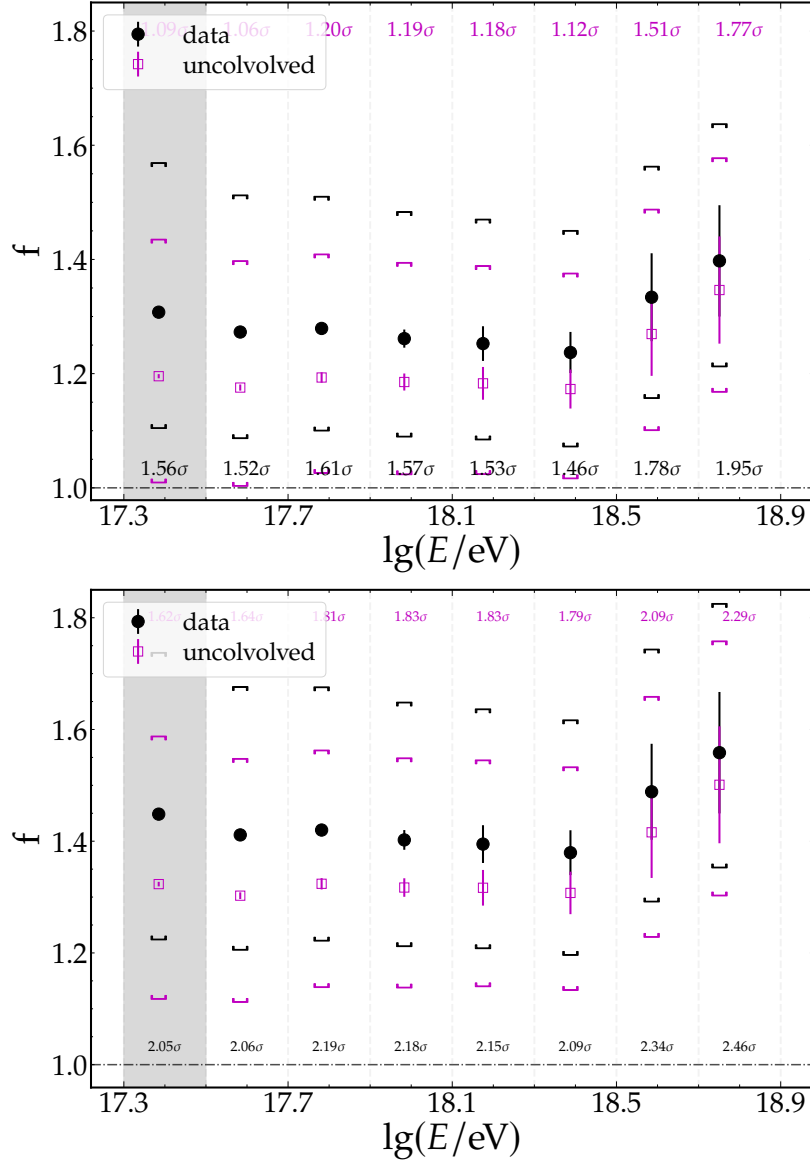
Figure F.4: Factor comparing the agreement between the muon content in data and simulations (Eq. (7.21)) as a function of energy for EPOS-LHC (upper panel) and QGSJetII-04 (lower panel). Error bars indicate statistical error whereas brackets correspond to systematic uncertainties. The horizontal dashed line indicates unity. The shaded grey area indicates the energy bin below full efficiency (see Section 7.1.1), preserved for visualization only. The distance to unity in units of σ is indicated in each bin, where σ corresponds to the total uncertainty. The magenta markers indicate the values inferred with the uncolvolved densities shown in Fig. 7.31. Their significance is displayed at the top of each bin in magenta font.
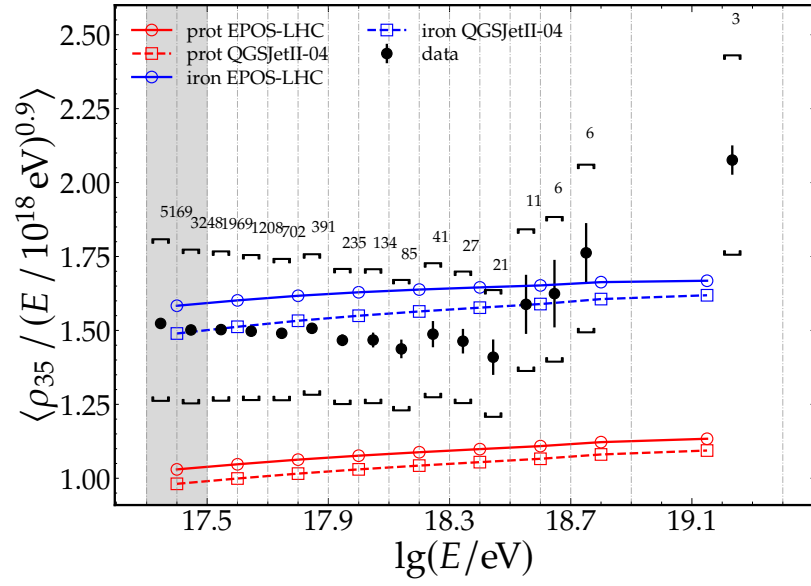
Figure F.5: Same as in Fig. 7.36 but with alternative binning in energy with step of $\Delta \lg(E/\text{eV}) = 0.1$.
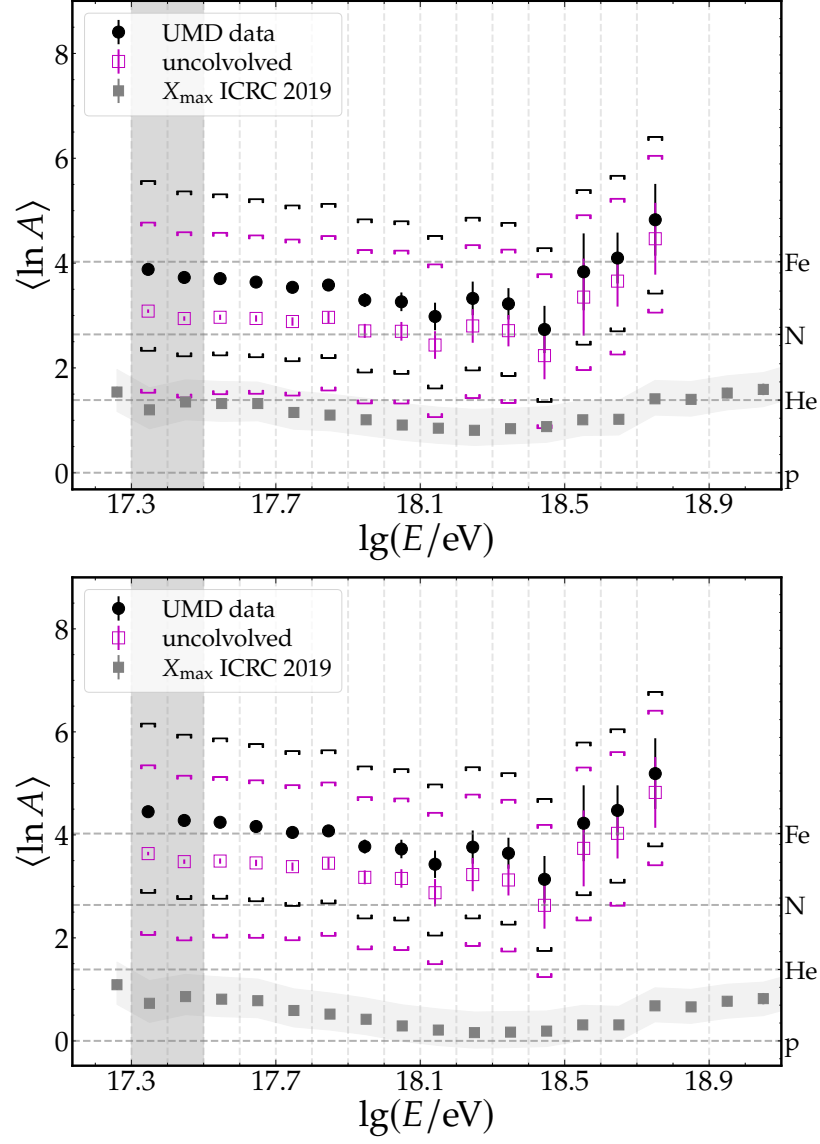
Figure F.6: Same as in Fig. F.3 but with alternative binning in energy with step of $\Delta \lg(E/\text{eV}) = 0.1$. Upper (lower) panel corresponds to EPOS-LHC (QGSJetII-04).

Figure F.7: Same as in Fig. F.4 but with alternative binning in energy with step of $\Delta \lg(E/\text{eV}) = 0.1$. Upper (lower) panel corresponds to EPOS-LHC (QGSJetII-04).
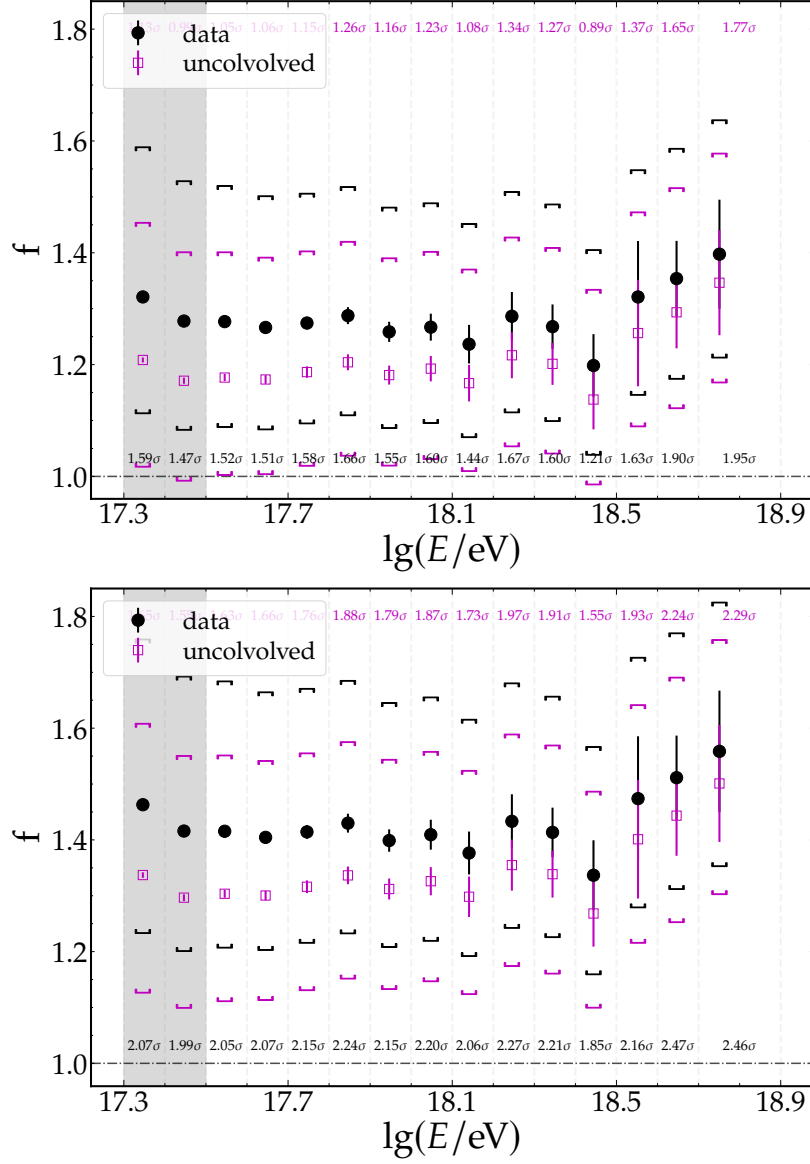
Parameterization of distance cuts for the mean MLDF analysis

As shown in Section 7.9.2, the evolution of r_{sat} and $r_{90\%}$ with energy for different zenith bins was model as a linear function $y = m(\lg(E/\text{eV}) - 17.6) + b$. The dependence with $\sin^2 \theta$ of m and b was further parameterized as a quadratic polynomial in $\sin^2 \theta$, with the exception of m for r_{sat}, for which no clear dependence was observed. For this case, the weighted mean was taken. Such parameterizations are shown in Fig. G.1 and Fig. G.2 for r_{sat} and $r_{90\%}$, respectively.
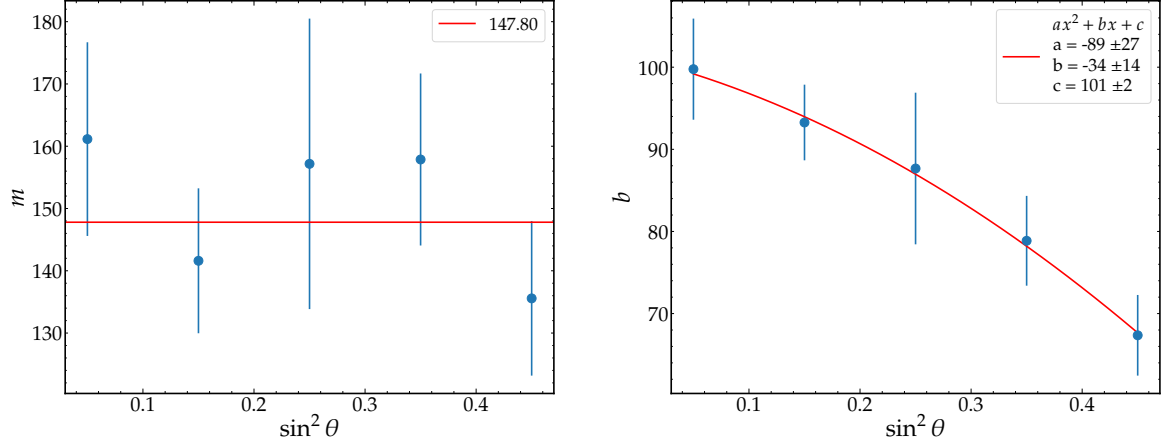
Figure G.1: Slope (left) and intercept (right) of the linear fits of r_{sat} as function of $\sin^2 \theta$. Since the slope does not show a dependence in $\sin^2 \theta$, the weighted mean was used. For the intercept, a quadratic model was used to fit its $\sin^2 \theta$ dependence.
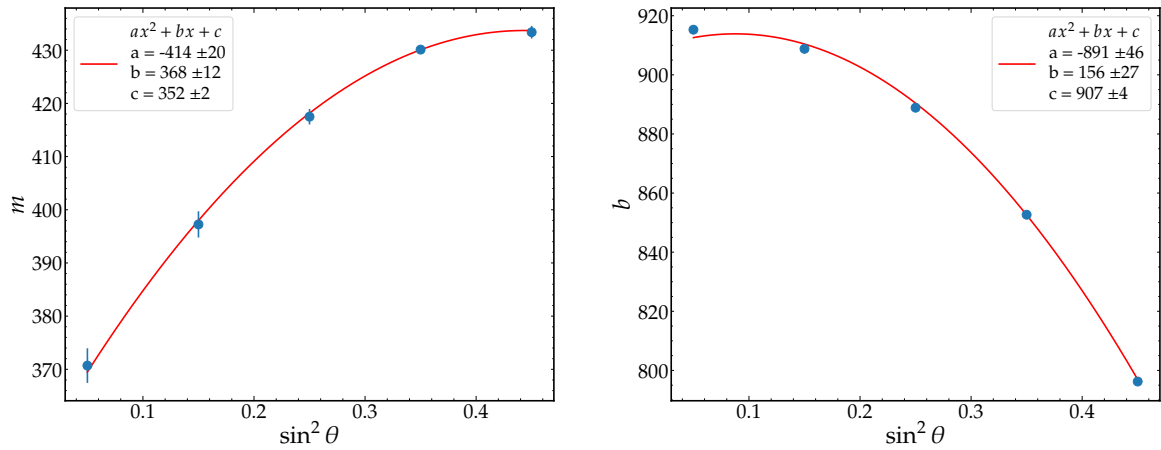

Figure G.2: Slope (left) and intercept (right) of the linear fits of $r_{90\%}$ as function of $\sin^2 \theta$. A quadratic model was used to fit their $\sin^2 \theta$ dependence.

Additional plots in the comparison of the LDF shape with Akeno and Yakutsk

In the left panel of Fig. 7.49, the comparison between the raw A1 data and the UMD points was shown for the lowest energy bin. In Fig. H.1, we show the same for the remaining energy bins. In addition, in Fig. H.2 we show the corresponding plots when the Auger energy is shifted.
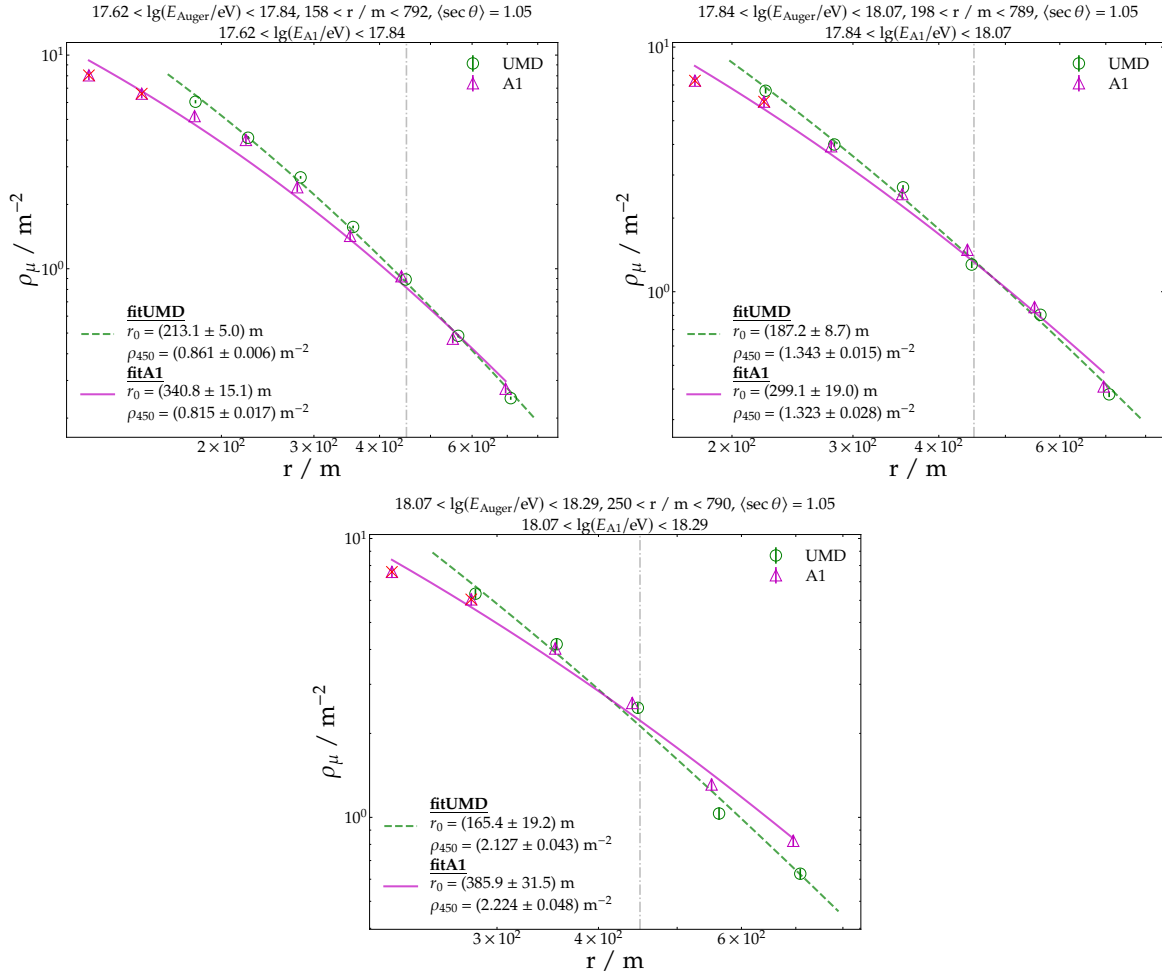
Figure H.1: Comparison between the UMD and raw A1 mean MLDF for $\sec\theta < 1.1$ in the energy bins $10^{17.62} < E/\text{eV} < 10^{17.84}$ (upper left), $10^{17.84} < E/\text{eV} < 10^{18.07}$ (upper right) and $10^{18.04} < E/\text{eV} < 10^{18.29}$ (lower panel). The vertical dashed line indicates 450 m. Red crosses represent A1 measurements suspected of saturation (see text for details). Full and dashed lines indicate the fits to Eq. (7.27).

Figure H.2: Comparison between the UMD and raw A1 mean MLDF for $\sec\theta < 1.1$. The log-energy of Auger is shifted -0.15, according to the expected shift in the energy scale of the experiments. The vertical dashed line indicates 450 m. Red crosses represent A1 measurements suspected of saturation (see text for details). Full and dashed lines indicate the fits to Eq. (7.27).
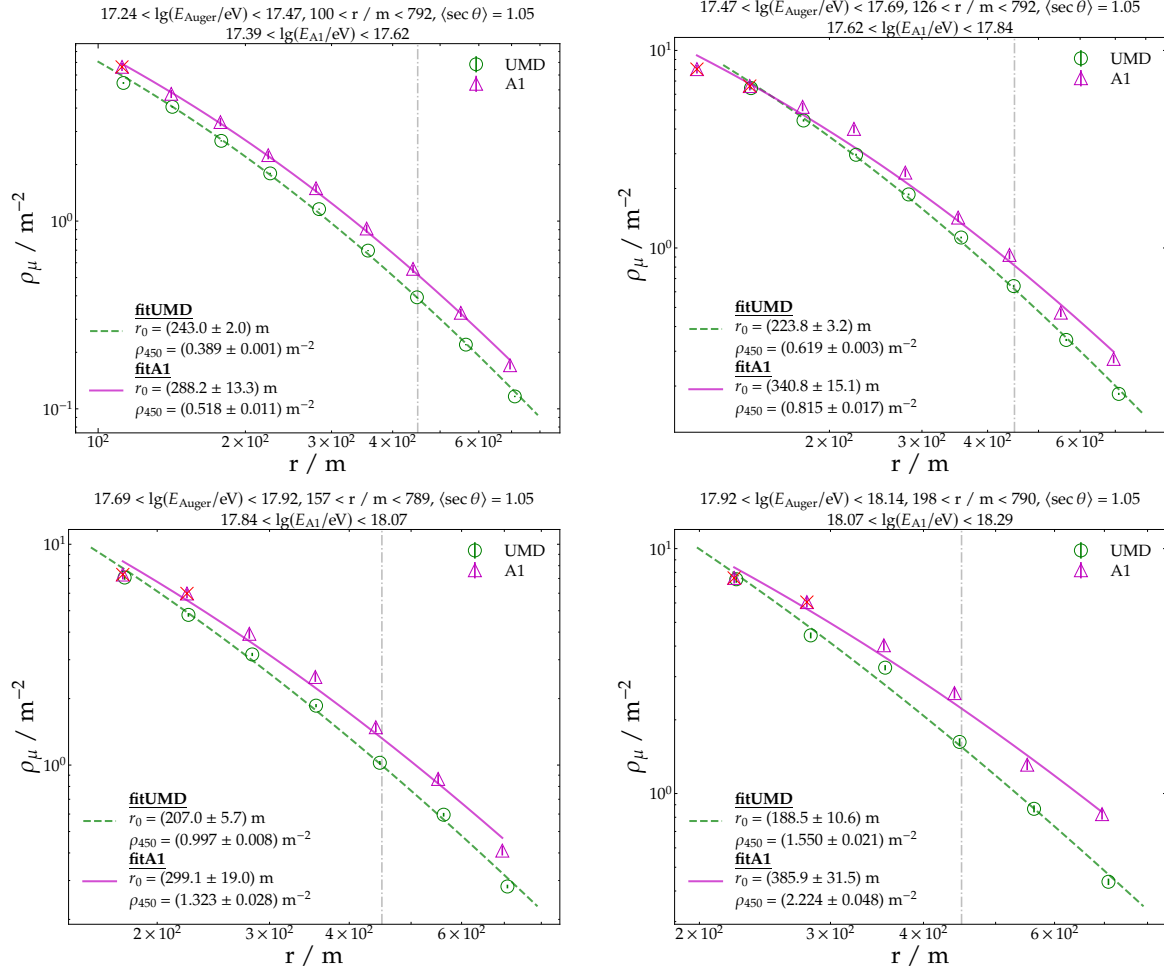
Detector characterization and long-term performance

In this section, we evaluate the stability of the data-taking period and validate the expected features of the detector signals in the field; in particular, the impact of fiber attenuation in the detector signals. This ensures a proper understanding of the detector's behavior and its performance over time.

In Appendix I.1, we present a study on optical fiber attenuation based on field data. While previous analyses have been conducted in laboratory settings, here we assess the fiber attenuation using real operational conditions.

In Appendix I.2, we examine the long-term performance of the detector signals.

In the two analysis, we considered both binary and ADC acquisition modes of the detector. Although only the former is used in this thesis for physics analysis, analyzing the ADC mode provides additional insights both in the fiber attenuation effect and into the time-dependent behavior of the detector.

I.1   Fiber attenuation

Fiber attenuation plays a major role in signal fluctuations as a muon hitting the closest to the SiPM can yield almost twice the number of photon-equivalents than one hitting the furthest. This translates into having a larger number of 1s (charge) in the binary (ADC) trace when muons hit the strip closer to the SiPM. This effect was characterized under controlled conditions in the laboratory [60].

A study like that conducted in the laboratory is not feasible with deployed modules as the impact point of the muon in the strip is unknown during an air-shower event. However, the attenuation of photons in the fiber can be assessed using the fact that strips in the UMD modules have different fiber lengths. Since the dome with the SiPM array is in the center of the detector, the length of the fiber between the end of a strip and the SiPM array, referred to as manifold length, is different for each strip, see Fig. I.1. Due to the symmetry of the module, this leads to 16 groups each composed by 4 strips with the same fiber length. Consequently, we expect both the mean number of 1s and charge produced by a single muon to be lower in strips with longer fibers.
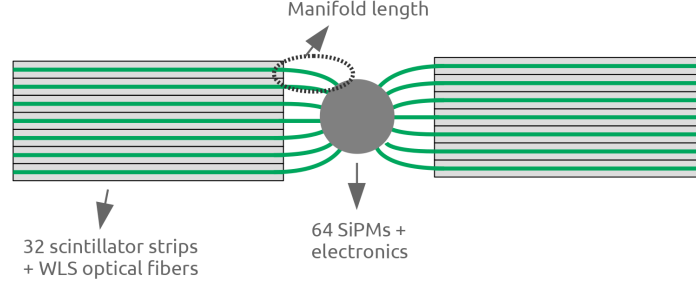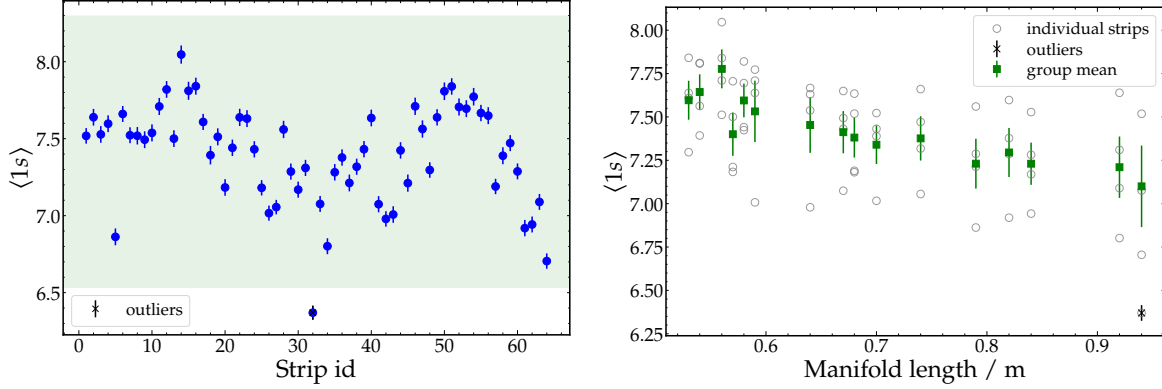
Figure I.1: Sketch of a UMD module.

Figure I.2: *Left*: Average number of 1s of each scintillator of module 101 of UMD station 1761. The green area indicates the region enclosed by $\langle \#1s \rangle_{\text{module}} \pm 3s_{\text{module}}$, outside which strips are tagged as outliers and rejected for subsequent analysis. *Right*: Same as in the right panel but as a function of the manifold length. The green squares indicate the mean over strips with the same fiber length.

I.1.1 Binary channel

To inspect for a fiber effect in the data, the average number of 1s, $\langle \#1s \rangle$, in all the strips of every module was calculated using three years of air-shower events. In a module-by-module analysis, we excluded any scintillator suspected of malfunctioning by identifying scintillators with extreme values of $\langle \#1s \rangle$. This was achieved through an iterative procedure. The mean value $\langle \#1s \rangle_{\text{module}}$ and the standard deviation s_{module} over the 64 scintillators in each module were computed. Any bars outside the region defined by $\langle \#1s \rangle_{\text{module}} \pm 3s_{\text{module}}$ were considered outliers and excluded. This procedure was repeated using the subset of scintillators that were not excluded, until no new outliers were found. As an example, this procedure is displayed for a selected module in Fig. I.2. Out of 5439 strips in the field considered for this analysis, 70 (1%) were tagged as outliers and excluded.

The fiber attenuation is already visible —using only one detector— in the right panel of Fig. I.2, where an anti-correlation between $\langle \#1s \rangle$ and the fiber length can be observed. In order to characterize the attenuation in a global way, we show in Fig. I.3 the values of $\langle \#1s \rangle$ of all the strips as a function of the fiber length (grey-unfilled circles), where the green squares indicate the mean over group of strips with the same fiber length. In the right panel of the figure, only the green squares are shown for better visualization. The fiber effect is quite clear as there is an anti-correlation between the manifold length and $\langle \#1s \rangle$, which translates into a difference of $\sim 5\%$ in the number of 1s between the shortest and longest fiber. We fitted a linear model, yielding a decrease in the mean number of 1s of $-0.7/\text{m}$.

As explained in Section 3.3.4, typical muon signals generate between seven and eight consecutive 1s, whereas a condition of at least four consecutive 1s in the binary trace is
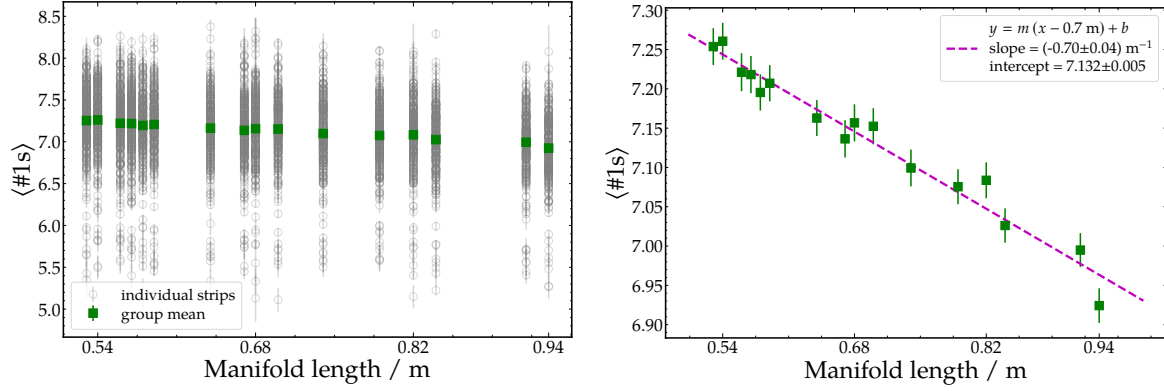
Figure I.3: Average number of 1s as a function of the manifold length using all the strips. The mean number of 1s for individual strips is denoted by gray-unfilled markers. The green squares indicate the mean over strips with the same fiber length. In the right panel, only the latter is shown, together with the fit to a linear model.
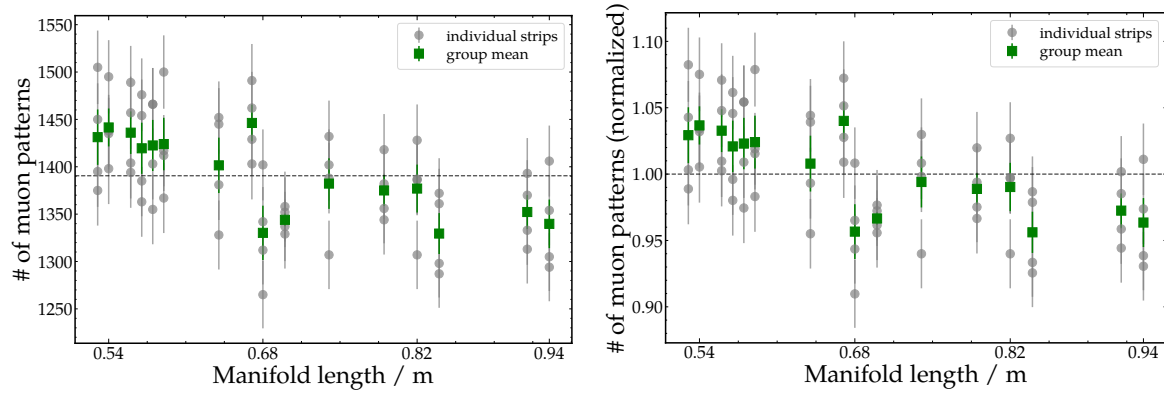

Figure I.4: *Left*: Number of muon patterns as a function of manifold length for module 103 of UMD station 1760. The green squares indicate the mean over strips with the same fiber length. Horizontal dashed line indicates the median of the number of muon patterns. *Right*: Same as in left panel but normalized by the median.

required for a bar to be considered hit by a muon, a condition referred to as the muon pattern. As demonstrated in Fig. I.3, strips with longer fibers generate, on average, fewer 1s. Thus, it is relevant to assess whether fiber attenuation has an impact on the efficiency of muon detection in the bars; that is, how often strips with longer fibers generate a muon pattern compared with strips with shorter fibers. To this end, for each strip of every module, the number of air-shower events in which it had a muon pattern was obtained. Since modules have been operating in the field for different periods due to being deployed at different times, modules deployed earlier participate in more events. To compare modules deployed at different times, we compute the median of the strip-level number of events for each module. Then, the number of events for each strip is normalized by this quantity. An example of this procedure is shown in Fig. I.4 for a selected module.

The normalized number of events for all strips is displayed as a function of manifold length in Fig. I.5. Again, we only show the mean over strips with the same fiber length in the right panel to ease visualization. The influence of fiber attenuation is also visible here, showing that strips with longer fibers are slightly more inefficient, having on average less number of muon patterns, leading to a difference of $\sim 2.5\%$ between the shortest and longest fiber.
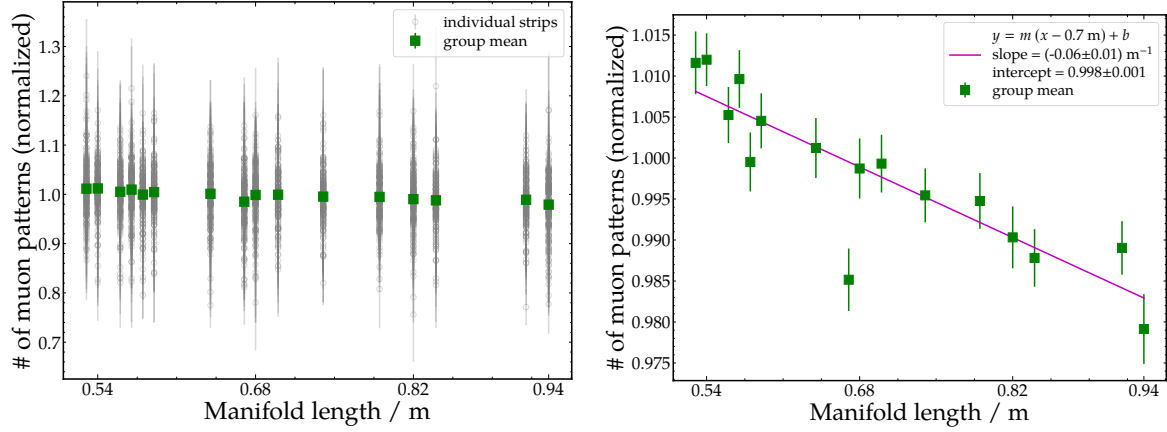
Figure I.5: *Left*: Normalized number of muon patterns as a function of manifold length using all the strips. The green squares indicate the mean over strips with the same fiber length. In the right panel, only the latter is shown along with a linear fit.

I.1.2 ADC channel

The fiber effect was additionally studied with the ADC channel following a similar procedure. For this purpose, modules with only a single strip with a single muon pattern in its binary trace were selected to guarantee that only one muon hits the detector. Subsequently, the ADC trace was integrated to obtain its charge.

To have a clean dataset and minimize the impact of noise, we demand some quality checks on the traces of the UMD modules. First, we ask that the start time of the binary channel t_{binary}, defined as the time bin with the first "1" in the trace, is inside the region 375 ADC samples $< t_{\text{binary}} < 750$ ADC samples (green shaded area in right panel of Fig. I.6). This is a rather coarse condition and it is based on the region of the binary trace where positive samples are more likely to occur as a consequence of the delays of the T2-TH and T2-ToT triggers in the WCD, see left panel of Fig. I.6. In this way, we aim to avoid muon patterns starting too early or too late in the trace, which may be likely due to noise. Then, we demand for a causal connection between the binary and the ADC. Both modes have different delays since they are built with different electronics. The binary channel is faster than the integrator, meaning that the muon signal starts earlier in the binary trace than in the ADC. For this reason, we only take into account traces in which 32 ADC samples $< t_{\text{max}} - t_{\text{binary}} < 56$ ADC samples, where t_{max} is the time of maximum amplitude in the ADC trace. The whole procedure is visible for a selected module in Fig. I.6.

The mean single-muon charge of all the strips sharing the same manifold length was obtained, as displayed in the left panel of Fig. I.7. Like in the binary channel, the fiber attenuation is quite clear as strips with longer fibers have lower single-muon charge values, which yields a difference of $\sim 10\%$ between the shortest and the longest fiber. This confirms and validates the expected behaviour of the detector in terms of fiber attenuation.

I.2 Long-term performance

Since the environmental conditions, such as temperature, in which the detector operates cannot be controlled, it is crucial to monitor the long-term behaviour of the signals. This is necessary to account for any seasonal effect in any subsequent higher-level physics analysis. In this section, we study the long-term evolution of the signals of the binary and ADC mode.
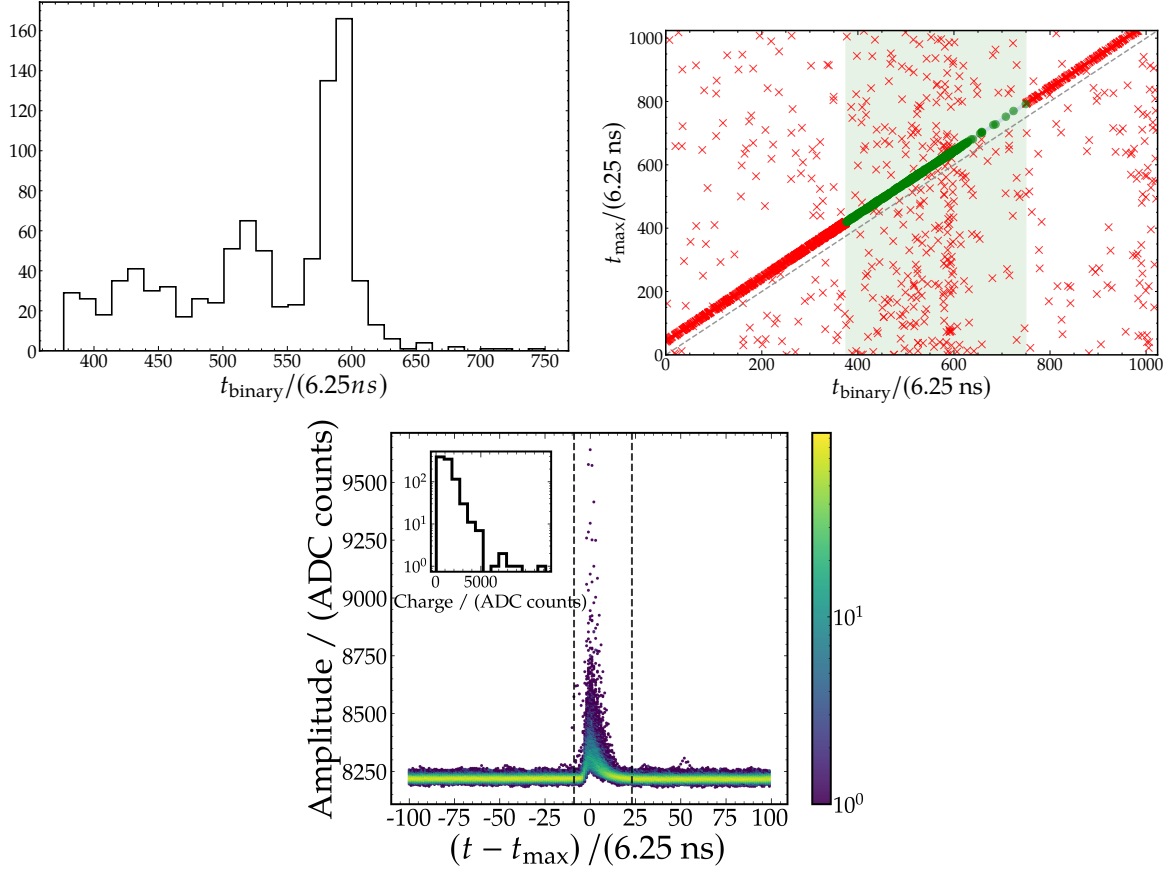
Figure I.6: Example of the cleaning procedure for module 101 of the UMD station 1760. *Upper left*: Distribution of start times of muon patterns in events with only one activated bar. Each peak corresponds to one of the WCD triggers, whose algorithms have different delays. *Upper right*: Scatter plot of t_{binary} and t_{max}. The green shaded area correponds to 375 ADC samples $< t_{\text{binary}}$ < 750 ADC samples. The green circles indicate the accepted traces for the analysis, whereas the red crosses show traces that do not fulfill the criteria to be accepted (see text for details). *Lower panel*: Single-muon ADC traces accepted for the analysis. The vertical dashed lines show the integration window, whereas the inset panel shows the charge distribution.

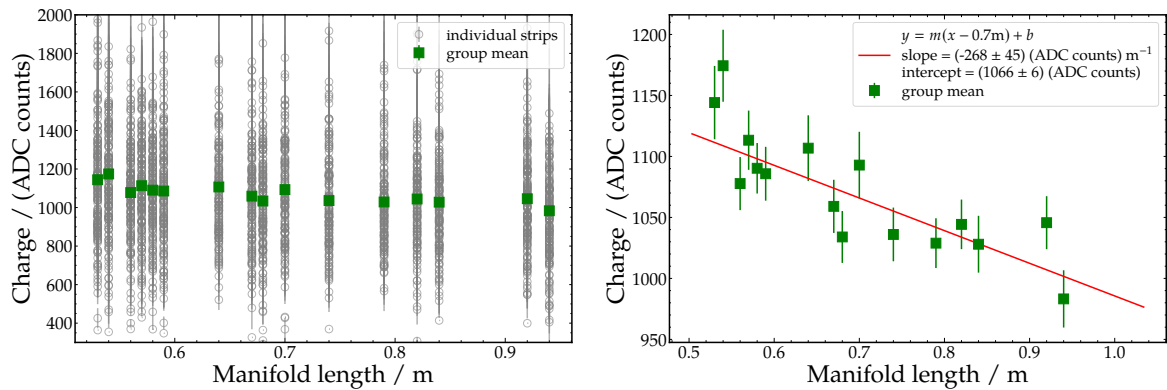**Figure I.7:** Single-muon charge as a function of the manifold length using all the strips. The green squares indicate the mean over strips with the same fiber length. In the right panel, only the latter is shown along with a linear fit.

For every local station trigger, an algorithm running in parallel to acquisition scans over the 64 binary traces; if only one muon pattern is found in the whole module, the charge
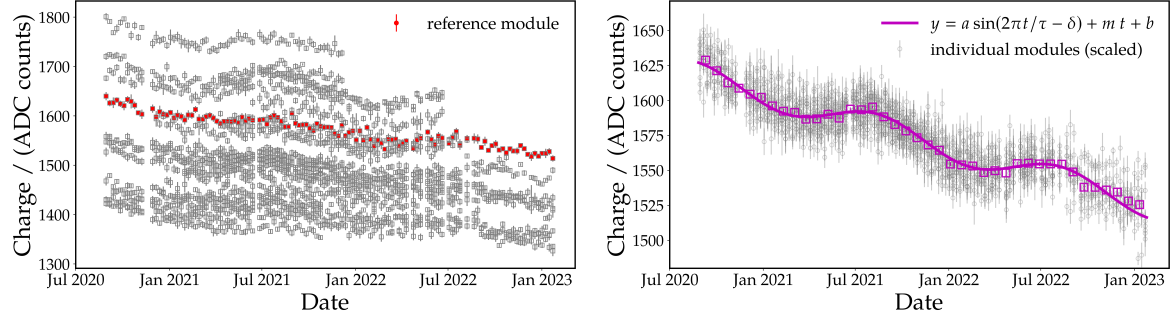
Figure I.8: *Left:* Raw time series of the online single-muon charge estimate. Some modules have not measurements during the whole period due to malfunctioning or bad data taking periods. Module-to-module variations can be seen due to SiPM gain differences between the modules. Red markers show the time series of the reference module to which all the modules are scaled. *Right:* Scaled time series. Unfilled magenta markers shows the profile over the whole set of modules. The magenta line corresponds to the fit of a sinus (seasonal fluctuations) plus a linear term (aging).

of the ADC trace is computed and streamed [59]. We will refer to the single-muon charge estimated this way as *online* charge. In the left panel of Fig. I.8, the weekly mean of the online charge is shown for a set of modules deployed over 2019, for which enough data is available for a long-term analysis. Module-to-module differences can be observed due to different SiPM gains between the modules. Thus, the time serie of an arbitrary module was chosen as a reference (red markers in left panel of Fig. I.8) and a scaling factor for each module was fitted to match this reference. The result of this is displayed on the right panel of Fig. I.8. It is evident that a universal behaviour arises which includes a seasonal fluctuation and a long-term drift related to the aging of the detector. In a phenomenological approach, we fit a model that incorporated a sinusoidal component to capture the seasonal oscillations, along with a linear component to represent the aging effect. The fluctuations correspond to $\pm 1\%$ whereas the aging rate (slope of the linear term) is of $-2.5\%/\text{yr}$.

The biweekly mean of the #1s using air-shower events was obtained for each module in the same time period. The raw time series are shown in the left panel of Fig. I.9. The same module as previously chosen was selected as a reference for scaling the remaining modules. The scaled time series along with the profile over all the detectors and a fit to the same model is shown in the right panel of Fig. I.9. The same qualitative behaviour seen in Fig. I.8 is found. In this case, a seasonal fluctuation of $\pm 1\%$ along with an aging rate of $-0.7\%/\text{yr}$ is observed. The difference in aging rate between the ADC and binary modes is attributed to the fact that the ADC mode is sensitive to the signal charge, whereas the binary mode relies on an amplitude threshold, thus being sensitive to the signal amplitude.

In addition, the long-term behaviour of the SiPM gains was assessed. It is known that the SiPM gain decreases with temperature. For that reason, a temperature compensation mechanism is implemented in the high-voltage source of the electronics [59]. Still, there may be some minor residual temperature dependence remaining. It is thus important to verify that this residual dependence remains within acceptable limits. Measurements of the SiPM gain were periodically performed for over a year in a single module following the procedure detailed in Ref. [58][1]. The gain for each SiPM was determined in each measurement and the average value over the 64 channels was obtained. The relative fluctuations of the average gain is shown in red markers in Fig. I.10. A fluctuation of $\pm 1\%$ is observed, being as expected larger for lower temperatures. This level of fluctuation in the gain is negligible and has no

---

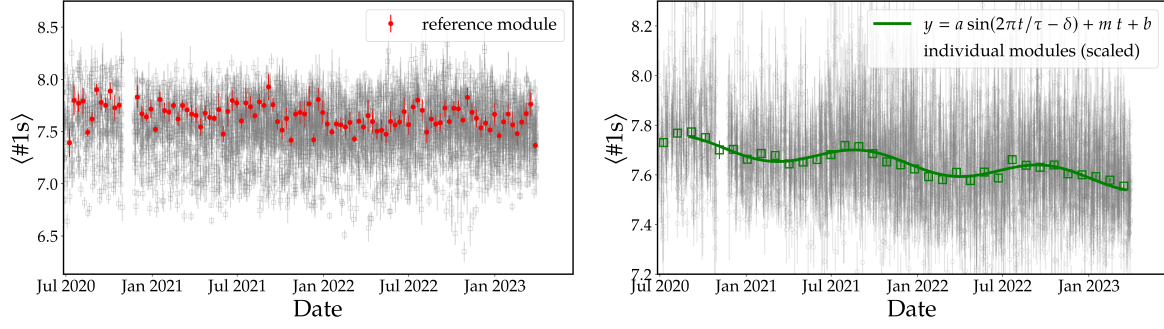[1]We thank Fernando Gollan for providing these measurements.

Figure I.9: *Left:* Raw time series of the #1s for each module. Module-to-module variations can be seen due to gain fluctuations between the modules. Red markers show the time series of the reference module to which all the modules are scaled. *Right:* Scaled time series. Unfilled green markers shows the profile over the whole set of modules. The green line corresponds to the fit of a sinus (seasonal fluctuations) plus linear term (aging).
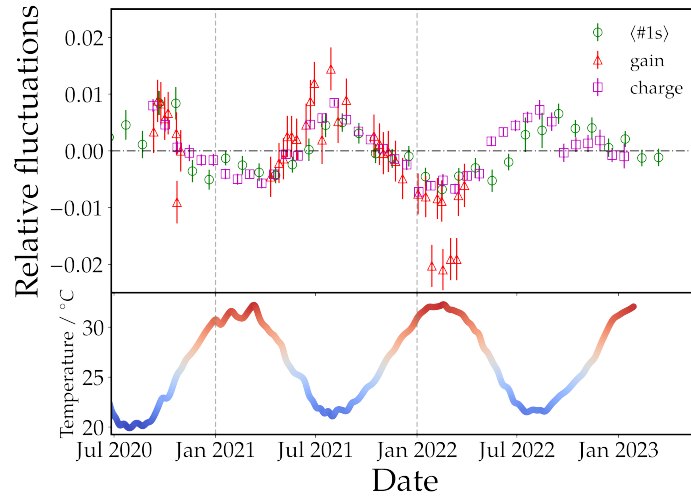

Figure I.10: Magenta (green) markers represent the relative fluctuations of the charge in the ADC trace ($\langle$#1s$\rangle$ in the binary trace) after the linear term associated with aging was subtracted. Red markers show the relative fluctuations of the SiPM gain, obtained as the average gain over all the 64 SiPMs for each measurement. The lower plot displays the average temperature registered by a sensor located in the UMD electronics. Grey dashed vertical lines enclose one year period.

impact on the detector performance. It is however useful to explain the oscillations observed in the binary and ADC signals. For this, the linear term of the model that was fit to the time evolution of the online charge and $\langle$#1s$\rangle$ (right panel of Fig. I.8 and Fig. I.9) was subtracted from the data points. The relative fluctuations of these aging-corrected quantities are also shown in Fig. I.10. It is apparent that the seasonal modulation in the signals are highly consistent with that found in the gain.

I.3 Summary

In this section of the appendix, the detector signals were characterized, and their long-term performance was analyzed.

The impact of fiber attenuation on the signals in binary and ADC mode was assessed using a dataset of three years of air-shower events in Appendix I.1. In binary mode, it was shown that strips with longer fibers, on average, register fewer 1s than strips with shorter

fibers, leading to a difference of approximately 5% between the longest and shortest fibers. As a consequence, strips with longer fibers are slightly less efficient, having on average a lower number of muon patterns, resulting in a difference of approximately 2.5% between the longest and shortest fibers. A fiber effect was also found in ADC mode, where a decrease in the single-muon charge with fiber length was observed, translating into a difference of approximately 10% between the longest and shortest fibers.

In Appendix I.2, the long-term behavior of the signals was evaluated, revealing an aging effect along with a seasonal fluctuation of $\pm 1\%$, the latter being consistent with SiPM gain fluctuations. The aging effect manifests as a decrease of -0.7% per year in the number of 1s and as a -2.5% per year in the charge for the binary and ADC mode, respectively.

Acknowledgments

This work would not have been possible without the help and support of many people.

First and foremost, I would like to thank my supervisors and referees, Juan Manuel Figueira and Ralph Engel, for their guidance and support, for allowing me to write this thesis, and for accepting me into the DDAp, which has been a life-changing experience. I would also like to thank Federico Sanchez, who greatly supported me and generously helped me countless times in revising my writing and coding, especially during my early work with the UMD part of the $\overline{\text{Off}\underline{\text{line}}}$.

I owe my deepest gratitude to all my colleagues at ITeDA, many of whom I consider dear friends. To my office partners, Marina and Rolando, who made the day-to-day atmosphere in the office fun and pleasant, and for their constant support. To my DDAp colleagues from ITeDA—Carmina, Varada, Ezequiel, Gabriel, and Flavia—who were amazing partners throughout this journey. Also to Nicolas Gonzalez, for assisting me in my first steps with $\overline{\text{Off}\underline{\text{line}}}$ generously sharing his codes. To Belen and Fernando, for helping many times, especially during the stressful times before the ICRC.

I am also deeply thankful to the Karlsruhe group. To Markus Roth, for welcoming me into the IAP group and for his advice and support. To David Schmidt, for always being available to discuss and help. To Darko Veberic, for taking a genuine interest in my work and generously helping me numerous times throughout my PhD.

I carry with me fond memories from my stays in Karlsruhe, largely thanks to my wonderful colleagues who made me feel at home. Many thanks to Max (all of them), Steffen, Felix, Tobias, Emily, Sara, Paul, Fiona. I hope our paths continue to cross. Thanks to Tobias for helping me translate the abstract into German and to Fiona for submitting the printed copy of this thesis. Thanks to Max Stadelmaier, for all the fun times, his generosity, and his help with my arrival at both Karlsruhe and ITeDA.

Thanks to Sabine for printing this thesis and assisting with all the administrative matters at KIT. Special thanks to Marie-Christine for helping me many times with paperwork and for always being available to help.

I also want to express my gratitude to all my colleagues in the Pierre Auger Collaboration and to everyone who contributed to this work, many of whom I am surely forgetting.

My deepest thanks goes to my family and friends, who make everything meaningful. To my parents and siblings, for their unconditional love and support, without which none of this would have been possible.

Bibliography

[1] T. P. A. Collaboration, Muons in air showers at the Pierre Auger Observatory: Mean number in highly inclined events, Physical Review D 91 (3) (2015) 032003.

[2] A. Aab, P. Abreu, M. Aglietta, J. M. Albury, I. Allekotte, A. Almela, J. Alvarez-Muñiz, R. Alves Batista, G. A. Anastasi, L. Anchordoqui, et al., Measurement of the fluctuations in the number of muons in extensive air showers with the Pierre Auger Observatory, Physical review letters 126 (15) (2021) 152002.

[3] J. Albrecht, L. Cazon, H. Dembinski, A. Fedynitch, K.-H. Kampert, T. Pierog, W. Rhode, D. Soldin, B. Spaan, R. Ulrich, et al., The Muon Puzzle in cosmic-ray induced air showers and its connection to the Large Hadron Collider, Astrophysics and Space Science 367 (3) (2022) 27.

[4] J. Arteaga Velazquez, A report by the WHISP working group on the combined analysis of muon data at cosmic-ray energies above 1 PeV, PoS ICRC2023 466 (2023).

[5] P. A. Collaboration, A. Aab, P. Abreu, M. Aglietta, I. Al Samarai, I. Albuquerque, I. Allekotte, A. Almela, J. Alvarez Castillo, J. Alvarez-Muñiz, et al., Observation of a large-scale anisotropy in the arrival directions of cosmic rays above 8×10^{18} eV, Science 357 (6357) (2017) 1266–1270.

[6] P. D. Group, R. Workman, V. Burkert, V. Crede, E. Klempt, U. Thoma, L. Tiator, K. Agashe, G. Aielli, B. Allanach, et al., Review of particle physics, Progress of theoretical and experimental physics 2022 (8) (2022) 083C01.

[7] O. Adriani, G. Barbarino, G. Bazilevskaya, R. Bellotti, M. Boezio, E. Bogomolov, L. Bonechi, M. Bongi, V. Bonvicini, S. Borisov, et al., PAMELA measurements of cosmic-ray proton and helium spectra, Science 332 (6025) (2011) 69–72.

[8] H. Ahn, P. Allison, M. G. Bagliesi, L. Barbier, J. Beatty, G. Bigongiari, T. Brandt, J. Childers, N. Conklin, S. Coutu, et al., Energy spectra of cosmic-ray nuclei at high energies, The Astrophysical Journal 707 (1) (2009) 593.

[9] M. Aguilar, D. Aisa, B. Alpat, A. Alvino, G. Ambrosi, K. Andeen, L. Arruda, N. Attig, P. Azzarello, A. Bachlechner, et al., Precision measurement of the proton flux in primary cosmic rays from rigidity 1 GV to 1.8 TV with the Alpha Magnetic Spectrometer on the International Space Station, Physical Review Letters 114 (17) (2015) 171103.

[10] The Telescope Array Coll., Telescope Array Experiment, Nuclear Physics B - Proceedings Supplements 175-176 (2008) 221–226, proceedings of the XIV International Symposium on Very High Energy Cosmic Ray Interactions. `doi:https://doi.org/10.1016/`

```
j.nuclphysbps.2007.11.002.
URL https://www.sciencedirect.com/science/article/pii/S0920563207007992
```

[11] P. A. Collaboration, et al., The Pierre Auger cosmic ray observatory, Nuclear Instruments and Methods in Physics Research Section A: Accelerators, Spectrometers, Detectors and Associated Equipment 798 (2015) 172–213.

[12] T. K. Gaisser, R. Engel, E. Resconi, Cosmic rays and particle physics, Cambridge University Press, 2016.

[13] E. Fermi, On the origin of the cosmic radiation, Physical review 75 (8) (1949) 1169.

[14] A. M. Hillas, The origin of ultra-high-energy cosmic rays, IN: Annual review of astronomy and astrophysics. Volume 22. Palo Alto, CA, Annual Reviews, Inc., 1984, p. 425-444. 22 (1984) 425–444.

[15] M. Dova, Ultra-high energy cosmic rays, arXiv:1604.07584 (arXiv preprint) (2016).

[16] E. Amato, The origin of galactic cosmic rays, International Journal of Modern Physics D 23 (07) (2014) 1430013.

[17] M. Spurio, et al., Particles and astrophysics, Springer, 2014.

[18] K. Greisen, End to the cosmic-ray spectrum?, Physical Review Letters 16 (17) (1966) 748.

[19] G. T. Zatsepin, V. A. Kuzmin, Upper limit of the spectrum of cosmic rays, Soviet Journal of Experimental and Theoretical Physics Letters 4 (1966) 78.

[20] J. W. Cronin, The highest-energy cosmic rays, Nuclear Physics B-proceedings supplements 138 (2005) 465–491.

[21] K. Kotera, A. V. Olinto, The astrophysics of ultrahigh-energy cosmic rays, Annual Review of Astronomy and Astrophysics 49 (1) (2011) 119–153.

[22] W. Heitler, The quantum theory of radiation, Courier Corporation, 1984.

[23] J. Matthews, A Heitler model of extensive air showers, Astroparticle Physics 22 (5-6) (2005) 387–397.

[24] D. Heck, J. Knapp, J. Capdevielle, G. Schatz, T. Thouw, et al., CORSIKA: A Monte Carlo code to simulate extensive air showers (1998).

[25] SJ, Sciutto, AIRES: A system for air shower simulations, Departamento de Fisica Universidad Nacional de La Plata 2 (2002) 6–0.

[26] T. Bergmann, R. Engel, D. Heck, N. Kalmykov, S. Ostapchenko, T. Pierog, T. Thouw, K. Werner, One-dimensional hybrid approach to extensive air shower simulation, Astroparticle Physics 26 (6) (2007) 420–432.

[27] K. Werner, F.-M. Liu, T. Pierog, Parton ladder splitting and the rapidity dependence of transverse momentum spectra in deuteron-gold collisions at the BNL Relativistic Heavy Ion Collider, Physical Review C—Nuclear Physics 74 (4) (2006) 044902.

[28] T. Pierog, I. Karpenko, J. M. Katzy, E. Yatsenko, K. Werner, EPOS LHC: Test of collective hadronization with data measured at the CERN Large Hadron Collider, Physical Review C 92 (3) (2015) 034906.

[29] S. Ostapchenko, QGSJET-II: physics, recent improvements, and results for air showers, in: EPJ Web of Conferences, Vol. 52, EDP Sciences, 2013, p. 02001.

[30] F. Riehn, H. P. Dembinski, R. Engel, A. Fedynitch, T. K. Gaisser, T. Stanev, The hadronic interaction model SIBYLL 2.3 c and Feynman scaling, arXiv preprint arXiv:1709.07227 (2017).

[31] S. A. Bass, M. Belkacem, M. Bleicher, M. Brandstetter, L. Bravina, C. Ernst, L. Gerland, M. Hofmann, S. Hofmann, J. Konopka, et al., Microscopic models for ultrarelativistic heavy ion collisions, Progress in Particle and Nuclear Physics 41 (1998) 255–369.

[32] T. Böhlen, F. Cerutti, M. Chin, A. Fassò, A. Ferrari, P. G. Ortega, A. Mairani, P. R. Sala, G. Smirnov, V. Vlachoudis, The FLUKA code: developments and challenges for high energy and medical applications, Nuclear data sheets 120 (2014) 211–214.

[33] A. A. Halim, P. Abreu, M. Aglietta, I. Allekotte, K. A. Cheminant, A. Almela, J. Alvarez-Muñiz, J. A. Yebra, G. A. Anastasi, L. Anchordoqui, et al., Constraining the sources of ultra-high-energy cosmic rays across and above the ankle with the spectrum and composition data measured at the Pierre Auger Observatory, Journal of cosmology and astroparticle physics 2023 (05) (2023) 024.

[34] J. Abraham, P. Abreu, M. Aglietta, E. Ahn, D. Allard, I. Allekotte, J. Allen, J. Alvarez-Muñiz, M. Ambrosio, L. Anchordoqui, et al., Trigger and aperture of the surface detector array of the Pierre Auger Observatory, Nuclear Instruments and Methods in Physics Research Section A: Accelerators, Spectrometers, Detectors and Associated Equipment 613 (1) (2010) 29–39.

[35] I. Allekotte, A. Barbosa, P. Bauleo, C. Bonifazi, B. Civit, C. Escobar, B. García, G. Guedes, M. G. Berisso, J. Harton, et al., The surface detector system of the Pierre Auger Observatory, Nuclear Instruments and Methods in Physics Research Section A: Accelerators, Spectrometers, Detectors and Associated Equipment 586 (3) (2008) 409–420.

[36] D. Veberic, M. Roth, SD reconstruction, Auger internal note GAP-2005-035 (2005).

[37] A. Aab, P. Abreu, M. Aglietta, J. M. Albury, I. Allekotte, A. Almela, J. A. Castillo, J. Alvarez-Muñiz, R. A. Batista, G. A. Anastasi, et al., Reconstruction of events recorded with the surface detector of the Pierre Auger Observatory, Journal of Instrumentation 15 (10) (2020) P10021.

[38] D. Newton, J. Knapp, A. Watson, The optimum distance at which to determine the size of a giant air shower, Astroparticle Physics 26 (6) (2007) 414–419.

[39] D. Veberic, B. Kegl, R. Engel, M. Roth, Constant Intensity Cut: Unbinned estimation of the Signal Attenuation Function, Auger internal note GAP-2015-065 (2015).

[40] J. Hersil, I. Escobar, D. Scott, G. Clark, S. Olbert, Observations of extensive air showers near the maximum of their longitudinal development, Physical Review Letters 6 (1) (1961) 22.

[41] H. P. Dembinski, B. Kégl, I. C. Mariş, M. Roth, D. Veberič, A likelihood method to cross-calibrate air-shower detectors, Astroparticle Physics 73 (2016) 44–51.

[42] M. Unger, Highlights from the Pierre Auger Observatory (ICRC17), arXiv preprint arXiv:1710.09478 (2017).

[43] J. Abraham, P. Abreu, M. Aglietta, C. Aguirre, E. Ahn, D. Allard, I. Allekotte, J. Allen, P. Allison, J. Alvarez-Muniz, et al., The fluorescence detector of the Pierre Auger Observatory, Nuclear Instruments and Methods in Physics Research Section A: Accelerators, Spectrometers, Detectors and Associated Equipment 620 (2-3) (2010) 227–251.

[44] A. Aab, P. Abreu, M. Aglietta, E.-J. Ahn, I. Al Samarai, I. F. d. M. Albuquerque, I. Allekotte, J. Allen, P. Allison, A. Almela, et al., Depth of maximum of air-shower profiles at the Pierre Auger Observatory: Measurements at energies above $10^{17.8}$ eV, Physical Review D 90 (12) (2014) 122005.

[45] C. Meurer, N. Scharf, HEAT-a low energy enhancement of the Pierre Auger Observatory, arXiv preprint arXiv:1106.1329 (2011).

[46] A. Taboada, Analysis of data from surface detector stations of the AugerPrime Upgrade, in: 36th International Cosmic Ray Conference (ICRC2019), Vol. 36, 2019, p. 434.

[47] G. Cataldi, R. Alves Batista, F. Canfora, S. de Jong, G. De Mauro, H. Falcke, T. Fodran, C. Galea, U. Giaccari, J. Hörandel, et al., The upgrade of the Pierre Auger Observatory with the scintillator surface detector (2022).

[48] A. Castellina, AugerPrime: the Pierre Auger observatory upgrade, in: EPJ Web of Conferences, Vol. 210, EDP Sciences, 2019, p. 06002.

[49] G. A. Anastasi, A. Abdul Halim, H. Abreu, M. Aglietta, T. Bister, A. Bwembya, S. de Jong, M. Emam, H. Falcke, T. Fodran, et al., The dynamic range of the upgraded surface-detector stations of AugerPrime (2023).

[50] E. M. Holt, I. F. d. M. Albuquerque, F. Catalani, V. d. Souza, N. Kemmerich, R. Lang, R. Prado, W. Carvalho, E. M. Santos, C. J. T. Peixoto, Recent results of the Auger engineering radio array (AERA), Proceedings of Science 301 (2017) 492–1.

[51] T. Fodran, P. Abreu, M. Aglietta, J. M. Albury, I. Allekotte, A. Almela, J. Alvarez-Muniz, R. Alves Batista, G. A. Anastasi, L. Anchordoqui, et al., First results from the Auger-Prime Radio Detector, Pos proceedings of science 395 (2022) 1–12.

[52] F. Schluter, P. Abreu, M. Aglietta, J. M. Albury, I. Allekotte, A. Almela, J. Alvarez-Muniz, R. Alves Batista, G. A. Anastasi, L. Anchordoqui, et al., Expected performance of the AugerPrime Radio Detector, Pos proceedings of science 395 (2022) 1–12.

[53] Etchegoyen, Alberto and Pierre Auger Collaboration and others, AMIGA, Auger Muons and Infill for the Ground Array, arXiv preprint arXiv:0710.1646 (2007).

[54] A. M. Botti, Determination of the chemical composition of cosmic rays in the energy region of 5 EeV with the AMIGA upgrade of the Pierre Auger Observatory, Dissertation, Karlsruhe Institute of Technology, Universidad Nacional de San Martin (2019).

[55] A. Pla-Dalmau, A. Bross, V. Rykalin, Extruding plastic scintillator at Fermilab, in: 2003 IEEE Nuclear Science Symposium. Conference Record (IEEE Cat. No.03CH37515), Vol. 1, 2003, pp. 102–104 Vol.1. `doi:10.1109/NSSMIC.2003.1352007`.

[56] M. Platino, M. Hampel, A. Almela, A. Krieger, D. Gorbena, A. Ferrero, G. De La Vega, A. Lucero, F. Suarez, M. Videla, et al., AMIGA at the Auger Observatory: the scintillator module testing system, Journal of Instrumentation 6 (06) (2011) P06006.

[57] M. Hampel, Optoelectrónica con Fotomultiplicadores de Silicio para Detectores de Rayos Cósmicos, Dissertation, Universidad Tecnológica Nacional, Buenos Aires, Argentina (2018).

[58] A. Aab, P. Abreu, M. Aglietta, E. Ahn, I. Al Samarai, I. Albuquerque, I. Allekotte, P. Allison, A. Almela, J. A. Castillo, et al., Muon counting using silicon photomultipliers in the AMIGA detector of the Pierre Auger Observatory, Journal of Instrumentation 12 (03) (2017) P03002.

[59] A. Aab, P. Abreu, M. Aglietta, J. M. Albury, I. Allekotte, A. Almela, J. Alvarez-Muñiz, R. A. Batista, G. A. Anastasi, L. Anchordoqui, et al., Calibration of the underground muon detector of the Pierre Auger Observatory, Journal of instrumentation 16 (04) (2021) P04003.

[60] A. M. Botti, F. Sánchez, M. Roth, A. Etchegoyen, Development and validation of the signal simulation for the underground muon detector of the Pierre Auger Observatory, Journal of Instrumentation 16 (07) (2021) P07059.

[61] A. Aab, P. Abreu, M. Aglietta, E.-J. Ahn, I. Al Samarai, I. Albuquerque, I. Allekotte, P. Allison, A. Almela, J. A. Castillo, et al., Prototype muon detectors for the AMIGA component of the Pierre Auger Observatory, Journal of Instrumentation 11 (02) (2016) P02012.

[62] A. Aab, et al., The Pierre Auger Collaboration, Direct measurement of the muonic content of extensive air showers between 2×10^{17} and 2×10^{18} ev at the Pierre Auger Observatory, The European Physical Journal C 80 (2020) 1–19.

[63] D. Ravignani, A. D. Supanitsky, A new method for reconstructing the muon lateral distribution with an array of segmented counters, Astroparticle Physics 65 (2015) 1–10.

[64] A. Supanitsky, Estimation of the number of muons with muon counters, Astroparticle Physics 127 (2021) 102535.

[65] A. Supanitsky, A. Etchegoyen, G. Medina-Tanco, I. Allekotte, M. G. Berisso, M. C. Medina, Underground muon counters as a tool for composition analyses, Astroparticle Physics 29 (6) (2008) 461–470.

[66] F. Gesualdi, A. D. Supanitsky, Estimation of the number of counts on a particle counter detector with full time resolution, The European Physical Journal C 82 (10) (2022) 925.

[67] J. Neyman, Outline of a theory of statistical estimation based on the classical theory of probability, Philosophical Transactions of the Royal Society of London. Series A, Mathematical and Physical Sciences 236 (767) (1937) 333–380.

[68] G. J. Feldman, R. D. Cousins, Unified approach to the classical statistical analysis of small signals, Physical review D 57 (7) (1998) 3873.

[69] S. Müller, Measurement of the Cosmic Ray Composition with Air Showers Detected by the AMIGA Extensions at the Pierre Auger Observatory, Dissertation, Karlsruhe Institute of Technology, Universidad Nacional de San Martin (2018).

[70] F. Gesualdi, The muon content of atmospheric air showers and the mass composition of cosmic rays, Dissertation, Karlsruhe Institute of Technology, Universidad Nacional de San Martin (2022).

[71] A. Botti, Private Communication (05 2022).

[72] N. Gonzalez, F. Sanchez, J. M. Figueira, On the muon lateral distribution using Underground Muon Detector data, Auger internal note GAP-2020-021 (2020).

[73] M. Perlin, Core-corona hadronization model and its impact on muon content of extensive air showers, Dissertation, Karlsruhe Institute of Technology, Universidad Nacional de San Martin (2021).

[74] D. Ravignani, A. D. Supanitsky, D. Melo, Reconstruction of air shower muon densities using segmented counters with time resolution, Astroparticle Physics 82 (2016) 108–116.

[75] A. Botti, F. Sanchez, Characterization of the signal undershoot in the UMD binary channel, Auger internal note GAP-2021-061 (2021).

[76] I. Maris, The AMIGA infill detector of the Pierre Auger Observatory: performance and first data, in: Proceedings of the 32nd International Cosmic Ray Conference (ICRC). Beijing, China, 2011.

[77] T. Schulz, Q. Luce, M. Roth, D. Schmidt, D. Veberic, Propagating SD Core Uncertainties in Subordinate Reconstructions, Auger internal note GAP-2020-068 (2020).

[78] J. Bellido, I. F. d. M. Albuquerque, F. Catalani, V. d. Souza, N. Kemmerich, R. Lang, R. Prado, W. Carvalho, E. M. Santos, C. J. T. Peixoto, Depth of maximum of air-shower profiles at the Pierre Auger Observatory: measurements above $10^{17.2}$ eV and composition implications, Proceedings of Science 301 (2017) 506–1.

[79] H. Dembinski, M. Roth, Constant Intensity Cut method revisited: Uncertainty calculation with the Bootstrap, Auger internal note GAP-2011-074 (2011).

[80] H. P. Dembinski, Computing mean logarithmic mass from muon counts in air shower experiments, Astroparticle Physics 102 (2018) 89–94.

[81] F. Gesualdi, A. D. Supanitsky, A. Etchegoyen, Muon deficit in air shower simulations estimated from AGASA muon measurements, Physical Review D 101 (8) (2020) 083025.

[82] A. Aab, P. Abreu, M. Aglietta, J. M. Albury, I. Allekotte, A. Almela, J. Alvarez Castillo, J. Alvarez-Muñiz, R. Alves Batista, G. A. Anastasi, et al., Features of the energy spectrum of cosmic rays above 2.5×10^{18} eV using the Pierre Auger Observatory, Physical review letters 125 (12) (2020) 121106.

[83] P. Abreu, M. Aglietta, J. M. Albury, I. Allekotte, A. Almela, J. Alvarez-Muñiz, R. Alves Batista, G. A. Anastasi, L. Anchordoqui, B. Andrada, et al., The energy spectrum of cosmic rays beyond the turn-down around 10^{17} eV as measured with the surface detector of the Pierre Auger Observatory, The European Physical Journal C 81 (2021) 1–25.

[84] A. Yushkov, P. A. Collaboration, et al., Mass Composition of Cosmic Rays with Energies above $10^{17.2}$ eV from the Hybrid Data of the Pierre Auger Observatory, in: 36th International Cosmic Ray Conference, Vol. 358, Sissa Medialab, 2021, p. 482.

[85] H. Dembinski, J. Arteaga-Velázquez, L. Cazon, R. Conceição, J. Gonzalez, Y. Itow, D. Ivanov, N. Kalmykov, I. Karpikov, S. Müller, et al., Report on tests and measurements of hadronic interaction properties with air showers, in: EPJ Web of Conferences, Vol. 210, EDP Sciences, 2019, p. 02004.

[86] D. Soldin, Update on the combined analysis of muon measurements from nine air shower experiments, arXiv preprint arXiv:2108.08341 (2021).

[87] F. Gesualdi, H. Dembinski, K. Shinozaki, D. Supanitsky, T. Pierog, L. Cazon, D. Soldin, R. Conceição, On the muon scale of air showers and its application to the AGASA data, arXiv preprint arXiv:2108.04824 (2021).

[88] D. Ivanov, I. F. d. M. Albuquerque, F. Catalani, V. d. Souza, N. Kemmerich, R. Lang, R. Prado, W. Carvalho, E. M. Santos, C. J. T. Peixoto, Report of the Telescope Array-Pierre Auger Observatory working group on energy spectrum, Proceedings of Science 301 (2017) 498–1.

[89] H. Dembinski, R. Engel, A. Fedynitch, T. Gaisser, F. Riehn, T. Stanev, Data-driven model of the cosmic-ray flux and mass composition from 10 GeV to 10^{11} GeV, arXiv preprint arXiv:1711.11432 (2017).

[90] N. Hayashida, K. Honda, M. Honda, S. Imaizumi, N. Inoue, K. Kadota, F. Kakimoto, K. Kamata, S. Kawaguchi, N. Kawasumi, et al., Muons (>= 1 GeV) in large extensive air showers of energies between $10^{16.5}$ eV and $10^{19.5}$ eV observed at Akeno, Journal of Physics G: Nuclear and Particle Physics 21 (8) (1995) 1101.

[91] A. Glushkov, I. Makarov, E. Nikiforova, M. Pravdin, I. Y. Sleptsov, Muon component of EAS with energies above 10^{17} eV, Astroparticle Physics 4 (1) (1995) 15–22.

[92] H. Dembinski, J. Arteaga-Velázquez, L. Cazon, R. Conceição, J. Gonzalez, Y. Itow, D. Ivanov, N. Kalmykov, I. Karpikov, S. Müller, et al., Report on tests and measurements of hadronic interaction properties with air showers, in: EPJ Web of Conferences, Vol. 210, EDP Sciences, 2019, p. 02004.

[93] Shinozaki, Kenji and Teshima, Masahiro and AGASA Collaboration and others, AGASA results, Nuclear Physics B-Proceedings Supplements 136 (2004) 18–27.

[94] K. Greisen, Cosmic ray showers, Ann. Rev. Nuclear Sci. 10 (1960).

[95] L. Dedenko, T. Roganova, G. Fedorova, Signals in the underground scintillation detectors of the Yakutsk array from muons of extensive air showers, Moscow University Physics Bulletin 66 (2011) 358–362.